

Coupling phenomena in magnonic hybrid heterostructures

Manuel M. Müller

Vollständiger Abdruck der von der TUM School of Natural Sciences der Technischen Universität München zur Erlangung eines Doktors der Naturwissenschaften genehmigten Dissertation.

Vorsitz: Prof. Dr. David Egger

Prüfer*innen der Dissertation:

1. Prof. Dr. Rudolf Gross
2. apl. Prof. Dr. Martin Brandt

Die Dissertation wurde am 27.10.2023 bei der Technischen Universität München eingereicht und durch die TUM School of Natural Sciences am 14.12.2023 angenommen.



TECHNISCHE
UNIVERSITÄT
MÜNCHEN



WALTHER-
MEISSNER-
INSTITUT

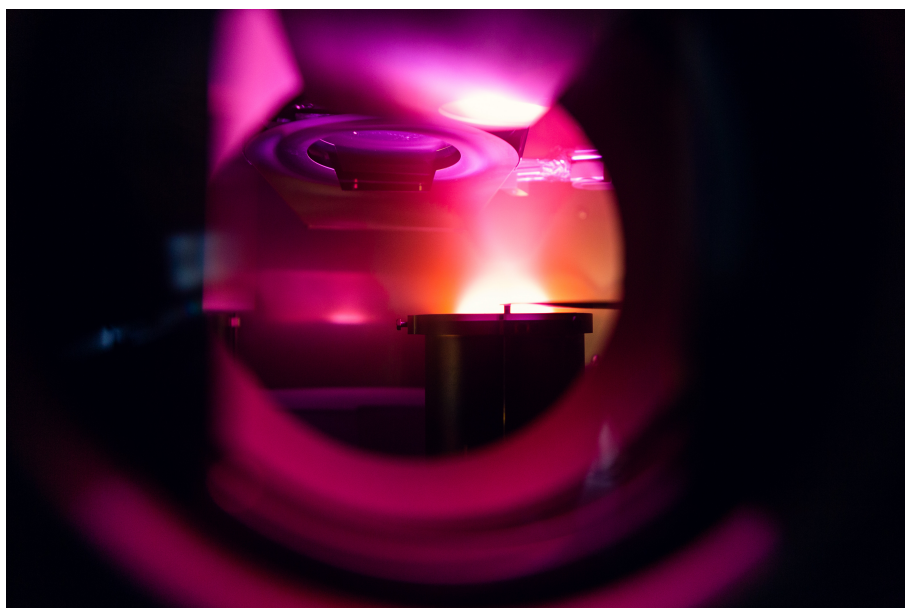


BAYERISCHE
AKADEMIE DER
WISSENSCHAFTEN

Coupling phenomena in magnonic hybrid heterostructures

Dissertation

Manuel M. Müller



Cover image: Copyright BAdW/Kai Neunert (2020)

'Man has always assumed that he is more intelligent than dolphins because he has achieved so much—the wheel, New York, wars and so on – while all the dolphins had ever done was muck about in the water having a good time. But, conversely, the dolphins had always believed that they were far more intelligent than man – for precisely the same reasons.'

— Douglas Adams

To my beloved mother and father

Abstract

The control of magnetization dynamics in ferromagnetic thin films is of key interest in the field of magnonics, where one aims at utilizing spin waves or magnons, the elementary excitations of the magnetic lattice, to store and transport information. Here, a promising method for control is to couple the magnons to other quantized excitations such as photons, phonons or other solid state excitations. To this end, the characterization of the coupling rates between magnons and other elementary excitations as well as the properties of hybridized magnon polaritons are of key interest. If the coupling rate of the coupling system exceeds the loss rates of the two individual subsystems, strong coupling is achieved and a coherent exchange of information between the modes is possible, thus enabling to efficiently manipulate the magnetization dynamics via the solid-state subsystem coupled to it. In this thesis, we employ both broadband ferromagnetic resonance experiments at cryogenic temperatures and microwave resonator spectroscopy to study the magnetization dynamics of various different magnetic thin film/solid state hybrid systems. First, we study the magnetization dynamics of magnetic $\gamma\text{-Fe}_2\text{O}_3$ thin films exchange-coupled to paramagnetic impurities. We find evidence for the presence of nonlinear temperature-dependent magnetization damping processes, that allow us to tune the magnetization damping with temperature. We then investigate the magnetization dynamics of magnetic thin films driven by spin torques generated by interfacial superconductors by analyzing the inductive coupling between superconductor/ferromagnet heterostructure and microwave transducer. Here, we detect large spin torques in the superconducting state, which is of interest for quantum sensing devices. Turning our attention to the coupling of the magnetization with quasiparticle excitations in superconductors, we then characterize the magnon-photon coupling of magnetic field robust superconducting $\text{Nb}_{70}\text{Ti}_{30}\text{N}$ resonators interacting with micropatterned magnetic $\text{Co}_{25}\text{Fe}_{75}$ strip structures. We find evidence for strong coupling. Finally, we investigate the coupling of the magnetic Kittel mode of a $\text{Co}_{25}\text{Fe}_{75}$ thin film layer with transverse acoustic phonons in various substrate materials serving as bulk acoustic resonators. In these hybrid systems, we detect phononic birefringence, which might enable the realization of phononic $\lambda/4$ -plates to transform linear into circularly polarized phonons. These novel findings contribute to a better understanding of magnetization dynamics in

hybrid systems and open up interesting new perspectives for future research in this area.

Kurzfassung

Die Kontrolle der Magnetisierungsdynamik in ferromagnetischen Dünnschichtfilmen ist von großem Interesse im Bereich der Magnonik, die darauf abzielt, quantisierte Spinwellen oder Magnonen, die elementaren Anregungen des magnetischen Gitters, zur Speicherung und Übertragung von Information zu nutzen. Eine vielversprechende Methode ist dabei die Kopplung von Magnonen mit anderen quantisierten Anregungen wie Photonen, Phononen oder anderen Festkörperanregungen. Für diese Zielsetzung ist die genaue Charakterisierung der Kopplungsrate zwischen Magnonen und anderen Elementaranregungen sowie die Untersuchung der Eigenschaften der durch die Kopplung entstehenden Magnon-Polaritonen von großem Interesse. Wenn die Kopplungsrate die Verlustraten der beiden einzelnen Subsysteme übersteigt, wird eine starke Kopplung erreicht und ein kohärenter Informationsaustausch zwischen den Moden ist möglich. Dadurch wird eine effiziente Manipulation der Magnetisierungsdynamik über das daran gekoppelte Festkörpersubsystem ermöglicht. In dieser Arbeit nutzen wir sowohl breitbandige Ferromagnetische Resonanz bei kryogenen Temperaturen als auch Mikrowellenresonatorspektroskopie, um die Magnetisierungsdynamik verschiedener magnetischer Dünnschicht-/Festkörper-Hybridsysteme zu untersuchen. Zunächst untersuchen wir die Magnetisierungsdynamik von ferrimagnetischen γ - Fe_2O_3 -Dünnschichtfilmen, die mit paramagnetischen Verunreinigungen austauschgekoppelt sind, und finden Hinweise auf das Vorhandensein von nichtlinearen temperaturabhängigen Dämpfungsprozessen der Magnetisierung, die es ermöglichen, die Magnetisierungsdämpfung unter Verwendung der Temperatur einzustellen. Anschließend untersuchen wir die Magnetisierungsdynamik von magnetischen dünnen Schichten, die mit in angrenzenden Supraleitern erzeugten Spinströmen wechselwirken, indem wir die induktive Kopplung zwischen Supraleiter/Ferromagnet-Heterostruktur und Mikrowellenleiter analysieren. Hierbei detektieren wir große Spinströme im supraleitenden Zustand, was für Quantensensorik interessant ist. Danach wenden wir uns der Kopplung der Magnetisierung mit Quasiteilchenanregungen zu und charakterisieren die Magnon-Photon-Kopplung von magnetfeld robusten supraleitenden $\text{Nb}_{70}\text{Ti}_{30}\text{N}$ -Resonatoren, die mit mikrostrukturierten magnetischen $\text{Co}_{25}\text{Fe}_{75}$ -Streifenstrukturen wechselwirken, und finden Hinweise auf eine starke Kopplung. Zuletzt untersuchen wir die Kopplung der magnetischen Kittel-Mode einer

Co₂₅Fe₇₅-Dünnschicht mit transversalen akustischen Phononen in verschiedenen Substratmaterialien, die als akustische Resonatoren dienen. In diesen Hybridsystemen detektieren wir phononische Doppelbrechung, was die Realisierung von phononischen $\lambda/4$ -Plättchen zur Umwandlung von linear polarisierten in zirkular polarisierte Phononen ermöglichen könnte. Diese neuen Erkenntnisse tragen zu einem besseren Verständnis der Magnetisierungsdynamik in Hybridsystemen bei und eröffnen interessante neue Perspektiven für zukünftige Forschung auf diesem Gebiet.

Contents

Abstract	v
Contents	ix
1 Introduction	1
2 Phenomenological Description of Magnetization Dynamics	7
2.1 Macrospin model	7
2.1.1 Heisenberg exchange interaction	7
2.1.2 Magnetization	8
2.1.3 Effective field	8
2.1.4 Landau-Lifshitz-Gilbert equation	11
2.2 Ferromagnetic Resonance	13
2.3 Magnetization dynamics in hybrid systems	18
2.3.1 Spin torques in Ferromagnet/Normal metal hybrids	18
2.3.2 Spin pumping mechanism	20
2.3.3 Temperature-dependent magnetic relaxation processes	21
2.3.4 Magnon-Photon coupling	24
2.3.5 Magnon-Phonon coupling	27
3 Experimental Details	29
3.1 Thin film deposition process	29
3.1.1 Operation principle of magnetron sputtering	29
3.1.2 Growth optimization parameters	31
3.1.3 Superbowls sputtering cluster	33
3.1.4 Ultradisk sputtering system	33
3.1.5 Advantages and disadvantages of the Superbowls and Ultradisk sputtering systems	34
3.2 Sample patterning techniques	35
3.3 Experimental procedure	37
3.3.1 Cryogenic ferromagnetic resonance spectroscopy	37
3.3.2 Characterization of superconducting resonators	42
4 Slowly relaxing impurities in maghemite thin films	47
4.1 Physical properties of γ -Fe ₂ O ₃	48

4.2	Thin film deposition and structural characterization	49
4.3	Magnetic properties of maghemite thin films	53
4.3.1	Static magnetic properties	53
4.3.2	Dynamic magnetic properties	54
4.4	Discussion of the non-linear magnetic damping	58
4.5	Summary and Outlook	60
5	Spin torques in Superconductor/Ferromagnet heterostructures	63
5.1	Inductive detection of spin torques	66
5.1.1	Modifications to the inductive detection technique in the superconducting state	68
5.2	Spin torques in NbN/Py-heterostructures	71
5.3	Spin torques in TaN/Py-heterostructures	83
5.3.1	Growth optimization of TaN	84
5.3.2	Broadband ferromagnetic resonance	91
5.4	Summary and Outlook	100
6	Magnon-Photon coupling in superconducting microwave resonators/ ferromagnetic microstructure hybrids	103
6.1	Characterization of superconducting NbTiN planar microwave res- onators	105
6.1.1	Loss mechanisms of superconducting microwave resonators	105
6.1.2	Optimization series of our superconducting resonators . . .	107
6.1.3	Performance of NbTiN resonators at elevated temperatures and at applied magnetic fields	111
6.1.4	Performance of NbTiN resonators at mK temperatures for quantum science applications	114
6.2	Magnon-Photon coupling in thin-film devices	116
6.3	Summary and Outlook	125
7	Magnon-Phonon coupling in bulk acoustic wave resonator/ magnetic thin films hybrids	127
7.1	Chiral phonons and phononic birefringence in CoFe/sapphire . .	129
7.1.1	Qualitative discussion	130
7.1.2	Experimental detection of phononic birefringence	133
7.2	Temperature dependence of magnon-phonon-polarons	141
7.2.1	temperature dependence of the raw $ S_{21} $ -data spectra . . .	142
7.2.2	Frequency and temperature dependence of the magnetic and elastic relaxation rate	143
7.2.3	Frequency- and temperature dependence of the effective coupling rate and cooperativity	147
7.2.4	Study of the tuning of the phononic resonances for sensing applications	149

7.3	Summary and Outlook	151
8	Summary and Outlook	153
8.1	Slowly relaxing impurities in maghemite thin films	154
8.2	Spin torques in Superconductor/Ferromagnet heterostructures . . .	154
8.3	Magnon-Photon coupling in superconducting microwave resonators/- ferromagnetic microstructure hybrids	156
8.4	Magnon-Phonon coupling in bulk acoustic wave resonator/ mag- netic thin films hybrids	157
A	Appendix A: Additional experiments on the magnetic properties of $\gamma\text{-Fe}_2\text{O}_3$	161
A1	Identification of potential slowly relaxing impurities	161
A2	Additional data on magnetic properties of maghemite films	162
A3	Additional FMR-results for $\gamma - \text{Fe}_2\text{O}_3$ thin films	164
B	Appendix B: Sputter deposition parameters	167
B1	Sputter deposition parameters	167
B2	Superbowls	167
B3	Ultradisk	167
C	Appendix C: Determination of the superconducting transition temper- ature	169
D	Appendix D: Raw data for the reduced inductance	171
D1	Reduced inductance at room temperature	171
D2	Reduced inductance in the superconducting state	172
E	Appendix E: Sputter deposition parameters of the TaN thin films	173
E1	N_2/Ar -gas flow ratio series	173
E2	Deposition temperature series	174
E3	Deposition power series	174
E4	Deposition pressure series	175
F	Appendix F: Superconducting NbTiN microwave resonators	177
F1	X-ray diffraction results of NbTiN thin film grown on HF-dipped Si	177
F2	Quality factors of our NbTiN resonators	178
F3	Participation ratios and loss tangents extracted from simulation . .	179
G	Appendix G: Magnetoelastic coupling in CoFe on Al_2O_3 substrates	181
G1	Determination of the parameters describing the magnetization dy- namics in CoFe	181
G1.1	Magnetization dynamics parameters of the CoFe layer as function of temperature	182

G2	Analytical expressions for the velocity splitting of the transverse modes	183
G2.1	Substrate with hexagonal crystallographic order	184
G2.2	Cubic crystallographic order	185
G3	Temperature-dependence of the elastic damping by the Landau-Rumer-mechanism	186
List of Publications		187
Bibliography		189
Acknowledgements		233

'We cannot solve our problems with the same thinking we used when we created them.'

— Albert Einstein

This quotation taken from Albert Einstein, one of the most influential physicists of the 20th century, is frequently cited in science to highlight the paramount importance of testing new ideas to overcome the limitations of existing technological devices by using new material systems, better and more precise device fabrication methods or altogether different physical phenomena. Among a plethora of research directions, this principle can be applied to the miniaturization of silicon transistors for integrated circuits to meet the evergrowing demand of raising computational power of modern information technology. Here increasing current densities, which limit the maximum clock frequencies due to Joule heating, impose a critical limit to transistor miniaturization [1]. This problem raises the demand for new ideas to implement logical circuits. On the material research side, promising approaches for further downscaling of logic devices include the realization of transistors made from two-dimensional materials [2,3], nanowires [4,5] or tunnel field-effect transistors (TFETs), [6,7]. As an alternative to the usage of charge carriers in these unconventional materials, there are approaches, which aim to utilize alternate information carriers such as for example photons in the field photonics [8,9], plasmons in plasmonics [10,11] and polaritons in polaritonics [12]. However, one of the arguably most matured fields in this research direction is that of spintronics, which aims to harness the spin degree of freedom of electrons in a solid system both in combination with and instead of their charge information. Magnetoresistive spintronics effects based on the giant- (GMR) [13–15] and tunneling magnetoresistive effect (TMR) have already found application in the form of magnetic hard disks for information storage, whereas magnetoresistive random access memory (MRAM) devices [16–18] allow for non-volatile data storage at comparable read/write speeds to existing static and dynamic random access memory concepts. This offers a promising venue to tackle the Von Neumann bottleneck [19] by enabling for in-memory computing [20]. Another spintronics-based data storage application are three-dimensional racetrack memory concepts, which aim to store data in the form of magnetic domains or skyrmions to achieve even higher data storage densities [21–24].

Fundamentally, the spintronics devices listed so far simultaneously utilize both charge and spin of electrons in their operation. However, there also exist ideas to exclusively mediate spin information in the form of excitations of the magnetic ground state called spin waves or magnons in the field of magnonics [25–28]. Primary advantages of spin-wave- over existing charge current-based devices

are the intrinsic magnonic frequencies situated in the GHz to THz regime [29], prospects for device miniaturization [30, 31] and vector-based spin-wave computing [28, 32, 33]. One main focal point in the field of magnonics is the identification of new low magnon-propagation loss magnetic materials to reduce energy consumption of magnon-based applications. Within this thesis, we contribute to this field in **Chapter 4** by characterizing the magnetization dynamics parameters of the room-temperature ferrimagnetic insulator spinel ferrite $\gamma\text{-Fe}_2\text{O}_3$ (maghemite) and discuss the feasibility of its nonlinear magnetization damping properties induced by the interaction of its magnetization with paramagnetic impurities for the realization of magnonics devices. Another important aspect of magnonics is the control of magnetization dynamics. Here, potential avenues include the usage of various types of hybrid devices. For instance, magnetization dynamics can be driven via spin-orbit torques [34–38] in ferromagnet/heavy metal bilayer or multilayer structures. While conventional heavy metals such as platinum [39–42] or tantalum [43, 44] are intensively studied material systems, exotic materials and phases have drawn an increasing interest in recent years [45, 46]. In particular, superconductors have been found to exhibit sizable spin torques below T_c [47–50], though conventional approaches for their quantification employing resistive measurements are difficult due to the shunting effect of superconducting materials. This experimental problem has motivated us to study the inverse spin-orbit torques manifesting in superconductor/ferromagnet heterostructures from a different angle by using a phase-sensitive detection technique to measure the inductive coupling between sample and signal transducer in **Chapter 5**. Besides the usage of spin-orbit torques another important perspective for the control of magnetization dynamics is to couple the magnetic systems to other physical systems such as for example photonic [51–54], phononic [55–64] or other magnetic systems [65, 66], where the interactions of the individual quantized subsystem excitations lead to the formation of hybridized modes, the quantized excitations of the coupled system [30]. In this thesis, we hybridize the magnetic systems with two types of excitations: Microwave photons in superconducting resonators made from the magnetic field robust type II superconductor $\text{Nb}_{70}\text{Ti}_{30}\text{N}$ in **Chapter 6** and transverse acoustic phonons propagating in various crystalline substrate materials in **Chapter 7**. Our magnon-photon hybrids achieve strong coupling at temperatures of up to 3 K and hence allow to push magnon-photon devices to higher operation temperatures, whereas our magnon-phonon hybrids exhibit a phononic birefringence paving the way towards the interconversion of linear and circularly polarized phonons.

This thesis is structured as follows:

We begin in **Chapter 2** by establishing the theoretical background required to explain the obtained experimental results of this thesis by introducing the basics of magnetization dynamics in a simple macrospin model, where we introduce the concept and components of the effective magnetic field felt by the sample

magnetization. We then derive the characteristic equation of motion of the magnetization namely the so-called Landau-Lifshitz Gilbert equation, which we solve in the case of uniform precession. Thereby, we obtain an analytical expression for the evolution of the resonance field as function of frequency called Kittel equation, which we further simplify for several experimentally relevant cases. To conclude the theory part of this thesis, we then discuss how the magnetization dynamics in the magnetic macrospin model are modified, when it is coupled to various forms of excitations investigated in this thesis such as paramagnetic impurities, spin torques in superconductor/ferromagnet heterostructures and quasiparticle excitations like photons and phonons.

In **Chapter 3**, we describe the details of the experimental methods used in this thesis. We start with the sample fabrication process via dc magnetron sputtering. Here we discuss the physics of the sputtering process as well as the different deposition parameters, which need to be optimized for the optimal growth of thin films, and detail the used sputtering machines Superbowls and Ultradisk. Furthermore, we detail the fabrication process of superconducting microwave resonators via electron beam lithography and reactive ion etching, which are used for the characterization of magnon-photon hybrids. We then describe, how the finalized heterostructures fabricated by using these methods are characterized via either broadband ferromagnetic resonance at cryogenic temperatures in different experimental geometries in various liquid helium cryostats, whereas the superconducting microwave resonators are studied via microwave resonator spectroscopy at cryogenic and mK temperatures using both liquid helium and dry pulse tube cryostats.

In **Chapter 4**, we characterize the room-temperature ferrimagnetic insulator spinel ferrite $\gamma\text{-Fe}_2\text{O}_3$ (maghemite), which is grown with epitaxial strain on MgO substrates via pulsed laser deposition (PLD), in terms of its epitaxial growth as well as static and dynamic magnetic properties. While high-resolution x-ray diffraction (HR-XRD) experiments confirm the good crystalline quality and coherently strained growth of our thin films, SQUID magnetometry reveals the presence of a sizable density of antiphase boundaries in our $\gamma\text{-Fe}_2\text{O}_3$ thin films. Regarding their dynamic magnetic properties studied by cryogenic broadband ferromagnetic resonance (bbFMR), we detect a small negative effective magnetization M_{eff} , providing further evidence for the presence of a strain-induced perpendicular magnetic anisotropy in our samples. Moreover, we observe a non-linear evolution of the ferromagnetic resonance-linewidth as function of the microwave frequency, which we interpret as the coupling of the sample magnetization with paramagnetic impurities in the so-called slow relaxor mechanism. Its nonlinear damping properties and strain-induced perpendicular anisotropy render $\gamma\text{-Fe}_2\text{O}_3$ an interesting material platform for spintronics devices.

The main results presented in this chapter are published in M. Müller, M. Scheufele, J. Gückelhorn, L. Flacke, M. Weiler, H. Huebl, S. Geprägs, R. Gross, M.

Althammer, *Reduced effective magnetization and damping by slowly relaxing impurities in strained γ -Fe₂O₃ thin films*, *Journal of Applied Physics* **132**, 233905 (2022) [67].

In **Chapter 5**, we move from single magnetic layers to the magnetization dynamics of ferromagnetic materials in multilayered heterostructure samples. In detail, we investigate the injection of quasiparticle spin currents into a superconductor via spin pumping from an adjacent FM layer. To this end, we use NbN/Ni₈₀Fe₂₀(Py)-heterostructures with a Pt spin sink layer and perform cryogenic bbFMR using a coplanar waveguide both as signal detector and microwave transducer. The phase sensitive detection of the microwave transmission signal is used to quantitatively extract the inductive coupling strength between sample and coplanar waveguide, which we interpret in terms of inverse spin-current induced torques, in our heterostructures as a function of both temperature and frequency. In the superconducting state of NbN, we observe a negative σ_d attributed to the quasiparticle-mediated inverse spin Hall effect (QMISHE). Moreover, below T_c we find a large field-like current-induced torque.

Both the theoretical details of the inductive analysis technique as well as the experimental results are published in M. Müller, L. Liensberger, L. Flacke, H. Huebl, A. Kamra, W. Belzig, R. Gross, M. Weiler, M. Althammer, *Temperature-Dependent Spin Transport and Current-Induced Torques in Superconductor-Ferromagnet Heterostructures*, *Physical Review Letters* **126**, 087201 (2021) [68].

To test the validity of our inductive analysis technique, in the second part of this chapter, we optimize the growth of superconducting TaN thin films on SiO₂ substrates via dc magnetron sputtering. This material is of interest for both different fields of quantum technology and superconducting spintronics as it is a magnetic field-robust superconductor with strong spin-orbit interaction. Hence, we naively expect the spin-orbit torques to be enhanced for this material. In a following step, we investigate the impact of the strong spin-orbit interaction in TaN on the inductively detected spin torques in TaN/Py-heterostructures. In the superconducting state of TaN, we again detect a negative damping-like spin torque attributed to the QMISHE of a larger amplitude compared to the results for NbN/Py-bilayers, which we attribute to the stronger spin-orbit interaction in TaN. Furthermore, we again observe the manifestation of a large positive field-like spin torque of unknown origin matching our results for NbN/Py-bilayers. In particular detected the sizable damping-like spin orbit torque in our superconductor/ferromagnet heterostructures is of interest, as it can be used to probe spin currents in emergent quantum materials.

The growth optimization of TaN and FMR-experiments on TaN/Py-heterostructures are published in M. Müller, R. Hoepfl, L. Liensberger, S. Geprägs, H. Huebl, M. Weiler, R. Gross, M. Althammer, *Growth optimization of TaN for superconducting spintronics*, *Materials for Quantum Technology* **1**, 045001 (2021) [69].

Chapter 6 is dedicated to the study of magnon-photon coupling in on-chip magnon-photon hybrid devices with a magnetic strip coupled to superconducting microwave resonators. In a first step, we study the performance of compact lumped element planar microwave Nb₇₀Ti₃₀N (NbTiN) resonators grown on various substrate materials in external in-plane magnetic fields and over a broad temperature regime ranging from mK temperatures to the superconducting transition temperature to characterize their applicability in electron spin resonance, ferromagnetic resonance and quantum applications. Consequently, in a second step, we use our optimized NbTiN resonators for the implementation of on-chip magnon-photon hybrid devices with a magnetic strip fabricated from the metallic ferromagnet Co₂₅Fe₇₅(CoFe) deposited on top of resonators. In our experiments, we investigate two different types of hybrid devices, where the CoFe is (i) coupled either directly to the NbTiN layer and (ii) grown on top of an insulating AlN layer to investigate the impact of a direct ferromagnetic exchange bias on the magnon-photon coupling. While devices from the former type suffer from high magnetic loss rates, samples of the latter type exhibit strong coupling. These results are comparable to state of the art magnon-photon devices and unite the high coupling rate per spin g_0 with the usage of a hard-type-II-superconductor with the perspective to push these devices to higher operating temperatures.

The results of this optimization process for superconducting NbTiN microwave resonators are published in M. Müller, T. Luschmann, A. Faltermeier, S. Weichselbaumer, L. Koch, G.B.P. Huber, H.W. Schumacher, N. Ubbelohde, D. Reifert, T. Scheller, F. Deppe, A. Marx, S. Filipp, M. Althammer, R. Gross, H. Huebl, *Magnetic field robust high quality factor NbTiN superconducting microwave resonators*, [Materials for Quantum Technology](#) **2**, 015002 (2022) [70].

To conclude our experimental results, in **Chapter 7**, we experimentally investigate the magnetoelastic coupling between the ferromagnetic resonance modes in a metallic Co₂₅Fe₇₅ thin film and standing transverse elastic phonon modes in sapphire, silicon and gadolinium gallium garnet by performing bbFMR experiments at cryogenic temperatures. For all these substrate materials, we observe an interaction between two resonant phonon modes with the magnetic Kittel mode. We identify these phonon modes as transverse shear waves propagating with slightly different velocities, and thus all substrates show phononic birefringence. Furthermore, in a second step, we exemplarily study the temperature-dependence of the magnetoelastic coupling of a CoFe thin film with the standing transverse elastic waves of a sapphire substrate as a function of temperature and frequency. We observe a strong decrease in the relaxation rate of the elastic modes for decreasing temperatures and a correspondingly vastly enhanced cooperativity C of the coupled magnon-phonon system. This highlights the importance of performing these experiments at cryogenic temperatures. Magnomechanical devices are discussed as efficient and broadband microwave signal transducers in the classical

and quantum limit, whereas in analogy to optics, phononic birefringence can allow for the controlled conversion between linear and circular phonons

Our initial bbFMR-experiments on ferromagnetic metal/BAW resonator hybrids using various substrate materials and observing the manifestation of phononic birefringence are available on the arxiv as M. Müller, J. Weber, F. Engelhardt, V.A.S.V. Bittencourt, T. Luschmann, M. Cherkasski, S.T.B. Goennenwein, S. Viola Kusminskiy, S. Geprägs, R. Gross, M. Althammer, H. Huebl *Chiral phonons and phononic birefringence in ferromagnetic metal - bulk acoustic resonator hybrids*, [arxiv: 2303.08429](https://arxiv.org/abs/2303.08429), (2023) [71].

Finally, in **Chapter 8**, we summarize the most important results of this thesis and give a brief outlook on future projects in the field of hybrid magnetization dynamics.

Phenomenological Description of Magnetization Dynamics

2

In this chapter, we establish the basic theoretical background required to explain the obtained experimental results of this thesis. We begin by introducing the macrospin model and define the concepts of magnetization vector M and effective field H_{ext} in a single-domain ferromagnet in Sec. 2.1. Thereafter, we define and describe its equation of motion in an external magnetic field, the so-called Landau-Lifshitz-Gilbert equation (LLG). We extend this model by adding an external perpendicular oscillating microwave field and derive its linear response function, the so-called Polder susceptibility $\hat{\chi}_p$ [72] and derive the ferromagnetic resonance (FMR) equation given by the famous Kittel equation [73] in Sec. 2.2. Depending on both sample shape and anisotropy, we then present the used experimentally relevant simplifications of the Kittel equation. In Sec. 2.3, we discuss how the magnetization dynamics of the magnetic macrospin are modified, when it couples to the various excitations of the hybrid devices investigated in this thesis. The presented calculations on the magnetization dynamics of ferromagnetic thin films closely follow the extensive derivations found in Refs. [74–76], whereas the theory for the diverse hybrid devices in this thesis are inspired by contemporary research [34, 77–85].

2.1 Macrospin model

2.1.1 Heisenberg exchange interaction

Ferromagnetism is a quantum-mechanical ordering phenomenon manifesting on a macroscopic scale [86], where the coulomb interaction in combination with the Pauli repulsion principle [87] give rise to an effective spin-spin-interaction of the electrons in a solid. In an atom, the individual electron spins s_i combine to a net atomic spin S . Combined with the orbital angular momentum L , it give rise to the total angular momentum of the atom $J = L + S$, where the respective alignment of L and S is given by Hund's Rules [88]. When neglecting itinerant electrons, the interaction of localized electrons in an insulating material can be modeled with the Heisenberg exchange mechanism [30, 86, 89, 90], where the free energy density of a solid with volume V is defined as

$$F_{\text{ex}} = -\frac{1}{\hbar^2 V} \sum_{j \neq i, i < j} E_{ij} \mathbf{J}_i \cdot \mathbf{J}_j, \quad (2.1)$$

where E_{ij} is the exchange constant and \hbar is the reduced Planck constant [91]. Depending on the sign of E_{ij} , the Heisenberg model can model both a ferromagnetic solid favoring the parallel alignment of the spins for $E_{ij} > 0$ as well as antiferromagnetic solid, where the angular momenta align in an antiparallel order for $E_{ij} < 0$. In Eq.(2.1) the sum is performed over all atoms i and neighboring atoms j , where the constriction $i > j$ prevents the double counting of the atom-neighbor pairs. We note, that the Heisenberg model can be extended to describe the magnetic ordering of itinerant ferromagnets, where the exchange interaction is mediated by conduction electrons [86,92]. In the following discussion, we restrict ourselves to ferromagnetic materials.

2.1.2 Magnetization

The magnetic moment $\boldsymbol{\mu}$ of an individual atom in a solid associated with the total angular momentum \boldsymbol{J} is given by

$$\boldsymbol{\mu} = -g\mu_B \frac{\boldsymbol{J}}{\hbar}, \quad (2.2)$$

where g is the Landé g -factor [93], μ_B is the Bohr magneton [94]. We define the gyromagnetic ratio $\gamma = g\mu_B/\hbar$ as the ratio between an atom's magnetic moment and its angular momentum. Using this definition, we introduce the magnetization \boldsymbol{M} as the macroscopic response observable as the sum of the combined individual magnetic moments of a ferromagnetic volume V

$$\boldsymbol{M} = \frac{1}{V} \sum_{\boldsymbol{\mu}_i \in V} \boldsymbol{\mu}_i. \quad (2.3)$$

This approach is valid due to the large number of magnetic moments per volume ($\simeq 10^{28} \text{ e}^-/\text{m}^3$) [30,95]. In the absence of domains walls or pinned magnetic moments in the ferromagnet, the individual $\boldsymbol{\mu}_i$ align in parallel to each other due to the Heisenberg interaction [see Eq.(2.1)]. Consequently, we can define the macroscopic magnetization vector as $\boldsymbol{M} = M_s \boldsymbol{m}$, where the saturation magnetization M_s is the magnitude of the magnetization vector and the unit vector $\boldsymbol{m} = (m_x, m_y, m_z)$ defines the direction of the unit vector in cartesian coordinates.

2.1.3 Effective field

In equilibrium, the magnetization of a magnetic solid will align in parallel to the orientation of an effective magnetic field [30,96]

$$\mu_0 \boldsymbol{H}_{\text{eff}} = -\left(\frac{\partial}{\partial m_x}, \frac{\partial}{\partial m_y}, \frac{\partial}{\partial m_z}\right) F_m = -\nabla_m F_m, \quad (2.4)$$

where F_m is the free energy density and $\mu_0 \approx 4\pi \cdot 10^{-7} \text{ Vs/Am}$ is the magnetic vacuum permeability. Notably, from Eq.(2.1), it is apparent, that the Heisenberg

exchange governs the alignment of the individual magnetic moment with respect to each other, but does not generate a favored magnetization direction and consequently does not contribute to \mathbf{H}_{eff} .

However the net free energy density F_m comprises several additional free energy contributions F_i , which do give rise to a preferred orientation direction of \mathbf{M} . We define $F_m = \sum_i F_i$.

In the following, we list and define the most relevant contributions to F_m for this thesis.

- **Zeeman energy:**

The magnetization direction can be externally controlled by applying an external magnetic field $\mu_0 \mathbf{H}_{\text{ext}}$ via the Zeeman interaction. The corresponding free energy density is given by [30,75,86]

$$F_{\text{zee}} = -\mu_0 \mathbf{M} \cdot \mathbf{H}_{\text{ext}}. \quad (2.5)$$

We note that only real macroscopic magnetic fields and not fictitious intermolecular fields such as the exchange field contribute to the Zeeman interaction [30,86]. By plugging Eq. (2.5) into Eq. (2.4), we obtain $\mathbf{H}_{\text{zee}} = \mathbf{H}_{\text{ext}}$ as the first contribution to \mathbf{H}_{eff} .

- **Shape anisotropy:**

In this thesis, primarily the magnetization dynamics of magnetic thin films is discussed. The shape of the sample translates to a magnetic anisotropy called the shape anisotropy. Here, the finite magnetization of a magnetic material gives rise to fictitious magnetic charges (north and south poles) at the surface, which are the sources of a stray field H_s outside of the magnetic volume and a demagnetizing field H_d inside the magnetic volume. To minimize the energy associated with these fields, \mathbf{M} will align along a certain direction depending on the shape of the magnetic volume [86,97]. To quantify the contribution of the demagnetization field H_d to H_{eff} , we model our magnetic volume as an ellipsoid with its main axes aligned in parallel to the cartesian coordinate axes for the sake of simplicity. In this case, the free energy density contribution of the shape anisotropy takes the form [30,98]

$$F_d = -\frac{\mu_0}{2} \mathbf{M} \hat{N} \mathbf{M}, \quad (2.6)$$

where the demagnetization tensor can be written as

$$\hat{N} = \begin{pmatrix} N_{xx} & 0 & 0 \\ 0 & N_{yy} & 0 \\ 0 & 0 & N_{zz} \end{pmatrix}. \quad (2.7)$$

Here, the N_{ii} represent the diagonal demagnetization factors along the cartesian axes, which fulfill the relation $N_{xx} + N_{yy} + N_{zz} = 1$. For a given sample shape, the N_{ii} can be determined using the equations given in Ref. [99]. We insert Eq. (2.6) into Eq. (2.4) to determine the demagnetization field \mathbf{H}_d

$$\mu_0 H_d = -\mu_0 \hat{N} M. \quad (2.8)$$

The thin films discussed in this work can be modeled as thin disks with $N_{\perp} \simeq 1$ perpendicular to the thin film surface and $N_{\parallel} \simeq 0$ in the film plane.

- **Magnetocrystalline anisotropy:**

In a crystalline magnetic solid, the magnetocrystalline anisotropy leads to a minimum of the free energy density in specific directions which we call easy axes. The energy difference between the hard and easy axes direction can be expressed by $\mu_0 M H_{\text{ani}}$, that is, in terms of an anisotropy field H_{ani} that points along a certain crystallographic direction depending on the crystal symmetry [75,86,100,101]. This phenomenon originates from the coupling of the net orbital angular momentum L of the valence electrons of 3d-transition or 4f-rare earth metals to the crystal structure to minimize the Coulomb energy. Due to the coupling of L to the net spin S of the material induced by spin-orbit coupling, S is also coupled to the crystal structure. As a consequence, it is energetically favorable for S to point along a particular crystallographic axis [86,100]. Consequently, for different alignments of the magnetic moments μ_i , the overlapping of their quantum-mechanical wave functions is also different giving rise to an energetic splitting in the Heisenberg exchange interaction energy and electrostatic exchange energy of the electrons [86]. Depending on the underlying crystalline lattice of the magnetic volume, the magnetocrystalline contribution to the free energy F_{mc} will take different forms [30,86]. However, as this thesis predominantly discusses the magnetization dynamics of polycrystalline magnetic thin films, in the following, we will neglect the contribution of magnetocrystalline anisotropy fields H_{mc} to H_{eff} .

- **Uniaxial anisotropy:**

In a uniaxial anisotropy, the magnetic free energy density F_m is minimized or maximized along one distinct axis and isotropic in the plane perpendicular to it. In contrast to the effective field contributions discussed thus far, there are several different physical mechanism that can give rise to an uniaxial anisotropy, such as magnetocrystalline anisotropy [86], shape anisotropy, large spin-orbit interaction from a heavy metal material interfaced with a ferromagnet [102–105] as well as induced from an elastic strain σ induced at the interface of the ferromagnet [67,106–108]. In the following, we summarize all uniaxial effective field contributions, which do not originate from

shape anisotropy or magnetocrystalline anisotropy as an uniaxial anisotropy H_u . To obtain an expression for the uniaxial anisotropy contribution to the magnetic free energy density F_u , we apply a phenomenological model with directional cosines. To this end, we write down a Taylor series for $F_u(\mathbf{m})$ in terms of the energy penalty $(1 - \mathbf{m} \cdot \mathbf{u})$ payed by \mathbf{m} for being tilted away from \mathbf{u} by the angle ϑ [$\mathbf{m} \cdot \mathbf{u} = |\mathbf{m}||\mathbf{u}|\cos(\vartheta)$] [86]

$$F_u = K_u[1 - (\mathbf{u} \cdot \mathbf{m})^2] + \mathcal{O}[K_2^{\text{uni}}(\mathbf{u} \cdot \mathbf{m})^4] \quad (2.9)$$

Here K_u is the uniaxial anisotropy constant, K_2^{uni} is the second order anisotropy constant and \mathbf{u} the unit vector along the easy axis direction. In Eq. (2.9), we use only even terms in our Taylor series as we set $F_u(\mathbf{m}) = F_u(-\mathbf{m})$ to model easy axis anisotropy (Note, that the case $F_u(\mathbf{m}) \neq F_u(-\mathbf{m})$ describes easy direction anisotropy). Neglecting the higher order magnetization term, in case $K_u > 0$, Eq. (2.9) describes a system with an uniaxial \mathbf{u} -direction easy axis anisotropy, whereas for the case $K_u < 0$, the \mathbf{u} -axis is a magnetic hard axis [86, 92]. We note, that a strain-induced uniaxial easy axis will play a key role for the understanding of the magnetization dynamics of $\gamma\text{-Fe}_2\text{O}_3$ in Ch. 4.

By inserting Eq. (2.9) into Eq. (2.4), we obtain for the resulting uniaxial anisotropy contribution H_u to \mathbf{H}_{eff} [75, 92]

$$\mu_0 \mathbf{H}_u = \frac{2K_u}{M_s} \mathbf{u}. \quad (2.10)$$

Finally, we obtain the effective magnetic field H_{eff} as the sum of all the previously listed contributions resulting in

$$\mathbf{H}_{\text{eff}} = \mathbf{H}_{\text{ext}} + \mathbf{H}_d + \mathbf{H}_u = \mathbf{H}_{\text{ext}} - \hat{N}\mathbf{M} + H_u \mathbf{u}. \quad (2.11)$$

2.1.4 Landau-Lifshitz-Gilbert equation

As previously established, the magnetic moments $\boldsymbol{\mu}$ of isolated atoms are related to the atomic angular momentum \mathbf{J} via Eq. (2.2). We define the macroscopic magnetic moment $\boldsymbol{\mu}_{\text{ges}} = V\mathbf{M}$, where V is the sample volume. The total angular momentum of the sample \mathbf{L}_{ges} is then given by [86]

$$\mathbf{L}_{\text{ges}} = -\frac{\boldsymbol{\mu}_{\text{ges}}}{\gamma}. \quad (2.12)$$

In a classical picture, the effective field \mathbf{H}_{eff} exerts a torque $\boldsymbol{\tau}$ on the magnetization \mathbf{M} in the form

$$\boldsymbol{\tau} = \frac{d\mathbf{L}_{\text{ges}}}{dt} = -\frac{V}{\gamma} \frac{\partial \mathbf{M}}{\partial t} = -\boldsymbol{\mu}_{\text{ges}} \times \mu_0 \mathbf{H}_{\text{eff}}. \quad (2.13)$$

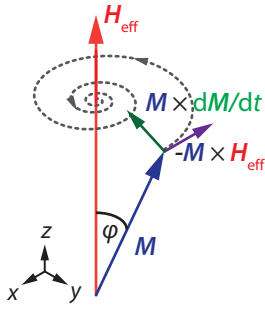


Fig. 2.1. – Schematic depiction of the magnetization dynamics in the macrospin model. Adapted from Ref. [30].

In real physical systems, there exist various relaxation mechanisms for M such as the magnon-phonon relaxation mechanism [110–113], two-magnon scattering processes [114–116] and intrinsic damping processes from electronic intraband and interband transitions [117, 118]. To obtain a more realistic model, Gilbert introduced a phenomenological material-dependent Gilbert damping parameter α to Eq. (2.14) [119] to account for the loss of angular momentum in the magnetization dynamics and proposed the Landau-Lifshitz-Gilbert (LLG)-equation

$$\frac{dM}{dt} = -\underbrace{\gamma M \times \mu_0 H_{\text{eff}}}_{\text{precession}} + \frac{\alpha}{M_s} \underbrace{M \times \frac{dM}{dt}}_{\text{damping}}. \quad (2.15)$$

We note that the Gilbert damping term constitutes a small perturbation in Eq. (2.15) as the values for α in real physical systems typically are in the $10^{-5} \leq \alpha \leq 10^{-2}$ -range. Hence the temporal evolution of the magnetization dynamics $\frac{dM}{dt}$ is primarily governed by the magnetization precession term $M \times \mu_0 H_{\text{eff}}$. As a consequence, the Gilbert damping term $M \times \frac{dM}{dt}$ points perpendicularly to both the magnetization M and the magnetization precession term $M \times \mu_0 H_{\text{eff}}$ and thus faces towards the rotation axis, effectively reducing the precession cone angle φ as a function of time. The resulting trajectory for M is a spiral motion around H_{eff} , as schematically depicted in Fig. 2.1, until M has relaxed into its equilibrium position parallel to H_{eff} . The system can hence be understood in analogy to a damped harmonic oscillator in classical mechanics [30].

This torque hence forces μ_{ges} to precess around H_{eff} with an angular frequency ω .

With this, the dynamic equation of motion of M known as the Landau-Lifshitz equation [109] can be derived by rewriting Eq. (2.13) in terms of the magnetization M

$$\frac{dM}{dt} = -\gamma M \times \mu_0 H_{\text{eff}}. \quad (2.14)$$

Eq. (2.14) describes the magnetization dynamics in an idealized unattenuated case, where M continuously precesses around H_{eff} at a constant cone angle φ . In real physical systems, there exist various relaxation mechanisms for M such as the magnon-phonon relaxation mechanism [110–113], two-magnon scattering processes [114–116] and intrinsic damping processes from electronic intraband and interband transitions [117, 118]. To obtain a more realistic model, Gilbert introduced a phenomenological material-dependent Gilbert damping parameter α to Eq. (2.14) [119] to account for the loss of angular momentum in the magnetization dynamics and proposed the Landau-Lifshitz-Gilbert (LLG)-equation

2.2 Ferromagnetic Resonance

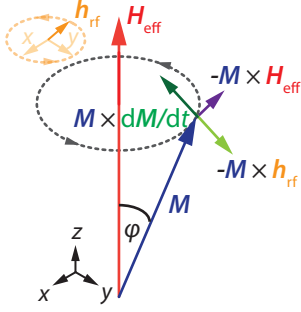


Fig. 2.2. – Schematic depiction of ferromagnetic resonance, where an additional driving torque ($\mathbf{M} \times \mathbf{h}_{\text{rf}}$) by the oscillating field \mathbf{h}_{rf} compensates the damping torque ($\mathbf{M} \times d\mathbf{M}/dt$).

In the previous section, we have discussed the magnetization dynamics of a magnetic sample with magnetization \mathbf{M} exposed to a static external magnetic field \mathbf{H}_{ext} . We found, that \mathbf{M} will start to precess around \mathbf{H}_{ext} and due to a finite damping eventually relax in parallel to it. In this section, we extend on this model by introducing an additional oscillating driving field $\mathbf{h}_{\text{rf}}(t)$ perpendicular to the external static field \mathbf{H}_{ext} as illustrated in Fig. 2.2, which exerts an additional torque $\mathbf{M} \times \mathbf{h}_{\text{rf}}$ on the magnetization. This system can then be modeled as a driven, damped harmonic oscillator. Consequently, we expect to observe a resonant enhancement of the precession cone angle φ , when the driving frequency of $\mathbf{h}_{\text{rf}}(t)$ matches the precession frequency ω of \mathbf{M} and the displacement of $\mathbf{M} \times \mathbf{h}_{\text{rf}}$ caused by the external drive resonantly counteracts the damping

($\mathbf{M} \times d\mathbf{M}/dt$). The following derivations will closely follow the compact overviews provided by previous works in Refs. [30,92,120–122], which are in turn based on the extensive derivations found in Refs. [75,76,96].

We model the dynamically driven magnetization dynamics by deriving the response function of the magnetization \mathbf{M} of an ellipsoidal sample, which is exposed to a constant external magnetic field applied along the z -axis ($\mathbf{H} = H_{\text{ext}}\mathbf{z}$) and dynamically driven by an oscillatory field $\mathbf{h}_{\text{rf}}(t) = (h_{\text{rf},x}(t), h_{\text{rf},y}(t), 0)^\top$ in the x - y -plane (see Fig. 2.2). We assume, that its ellipsoidal symmetry axes point along the cartesian axes in Fig. 2.2 so that its demagnetization tensor is diagonal with the components N_{xx} , N_{yy} and N_{zz} . Furthermore, we define a generalized uniaxial anisotropy vector $\mathbf{u} = (u_x, u_y, u_z)^\top$. Adding $\mathbf{h}_{\text{rf}}(t)$ to the effective field in Eq. (2.11), we obtain

$$\begin{aligned} \mathbf{H}_{\text{eff}} &= \mathbf{H}_{\text{ext}} + \mathbf{H}_d + \mathbf{H}_u + \mathbf{h}_{\text{rf}}(t) \\ &= \begin{pmatrix} -N_{xx}M_x(t) + u_x H_u \\ -N_{yy}M_y(t) + u_y H_u \\ H_{\text{ext}} - N_{zz}M_z + u_z H_u \end{pmatrix} + \begin{pmatrix} h_{\text{rf},x}(t) \\ h_{\text{rf},y}(t) \\ 0 \end{pmatrix}. \end{aligned} \quad (2.16)$$

Here, we account for the effect of the excited magnetization dynamics in the x - y -plane on the demagnetization field via the time-dependent $N_{ii}M_i(t)$ -terms. This simplification can be made under the assumptions of magnetization dynamics with a small precession cone angle φ , where $M_{x,y} \ll M_z$ and $|\mathbf{h}_{\text{rf}}| \ll |\mathbf{H}_{\text{ext}}|$. Furthermore, in Eq. (2.16) we use a fixed magnitude of the magnetization vector $|\mathbf{M}| = M_s$, which points in parallel to \mathbf{H}_{eff} [30,123]. In this simplified approach,

the magnetization \mathbf{M} can be expressed as the sum of a time-independent part \mathbf{M}_0 and a time-dependent response $\mathbf{M}_{\text{rf}}(t)$ as

$$\mathbf{M} = \mathbf{M}_0 + \mathbf{M}_{\text{rf}}(t) = \begin{pmatrix} M_x(t) \\ M_y(t) \\ M_s \end{pmatrix}. \quad (2.17)$$

We use a harmonic ansatz to model the magnetization dynamics $\mathbf{M}_{\text{rf}}(t)$ in an oscillating magnetic field $\mathbf{h}_{\text{rf}}(t)$

$$\begin{aligned} \mathbf{h}_{\text{rf}}(t) &= (h_{\text{rf},x}, h_{\text{rf},y}, 0)^\top \cdot e^{i\omega t} \\ \mathbf{M}_{\text{rf}}(t) &= (M_{\text{rf},x}, M_{\text{rf},y}, 0)^\top \cdot e^{i\omega t} \end{aligned} \quad (2.18)$$

and insert Eqs. (2.16)-(2.18) into the LLG-equation in Eq. (2.15) resulting in an expression of the form

$$\begin{pmatrix} h_{\text{rf},x} \\ h_{\text{rf},y} \end{pmatrix} = \hat{\chi}_{\text{P}}^{-1} \begin{pmatrix} M_{\text{rf},x} \\ M_{\text{rf},y} \end{pmatrix}, \quad (2.19)$$

where the Polder susceptibility $\hat{\chi}_{\text{P}}$ [72] describes the linear response of $\mathbf{M}_{\text{rf}}(t)$ to an external perturbation $\mathbf{h}_{\text{rf}}(t)$.

Here, $\hat{\chi}_{\text{P}}$ is of the form [92]

$$\hat{\chi}_{\text{P}} = \begin{pmatrix} \chi_{xx} & \chi_{xy} \\ \chi_{yx} & \chi_{yy} \end{pmatrix} = \frac{\mu_0 M_s}{\text{Det}(\hat{\chi}_{\text{P}}^{-1})} \begin{pmatrix} A_{11} & \frac{i\omega}{\gamma\mu_0} \\ -\frac{i\omega}{\gamma\mu_0} & A_{22} \end{pmatrix} \quad (2.20)$$

with the diagonal entries

$$\begin{aligned} A_{11} &= H_{\text{ext}} + (N_{yy} - N_{zz}) \cdot M_s - (u_y - u_z) \cdot H_u + \frac{i\omega\alpha}{\gamma\mu_0} \\ A_{22} &= H_{\text{ext}} + (N_{xx} - N_{zz}) \cdot M_s - (u_x - u_z) \cdot H_u + \frac{i\omega\alpha}{\gamma\mu_0}. \end{aligned} \quad (2.21)$$

The Polder susceptibility $\hat{\chi}_{\text{P}}$ is a complex function ($\hat{\chi}_{\text{P}} = \hat{\chi}' + i\hat{\chi}''$) consisting of a dispersive real part $\hat{\chi}'$ and a dissipative imaginary part $\hat{\chi}''$. The characteristic behavior of the susceptibility components χ' and χ'' as a function of external magnetic field \mathbf{H}_{ext} for the case of a magnetic thin film sample without uniaxial anisotropy in an external magnetic field $H_{\text{ext}} \parallel z$ ($u_x = u_y = u_z = N_{xx} = N_{yy} = 0$ and $N_{zz}=1$) at a frequency $f = \omega/2\pi = 10$ GHz and using the magnetic parameters for thin film Permalloy [124, 125] ($\text{Ni}_{80}\text{Fe}_{20}$, Py) ($\mu_0 M_s = 1.0$ T, $g = 2.1$ and $\alpha = 0.006$) is illustrated in Fig. 2.3(a). In order to obtain the resonance field H_{res} as a function of frequency $f_{\text{res}} = \omega_{\text{res}}/2\pi$, we solve the real part of $\text{Det}(\hat{\chi}_{\text{P}}) \stackrel{!}{=} 0$ in

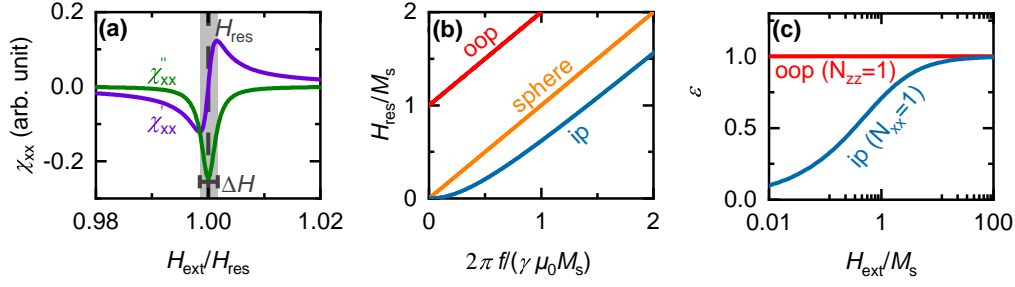


Fig. 2.3. – (a) Real and imaginary part of the Polder susceptibility $\hat{\chi}_P$ for $f = \omega/2\pi = 10$ GHz, $\mu_0 M_s = 1.0$ T, $g = 2.1$, $\alpha = 0.006$ as function of external magnetic field \mathbf{H}_{ext} . The gray dashed line indicates the resonance field H_{res} and the gray colored area represents the resonance linewidth ΔH . (b) Resonance field H_{res} as function of f derived from Eq. (2.22) for a spherical sample (yellow) and a thin film in ip- and oop-geometry. (c) Ellipticity ϵ calculated using Eq. (2.31) as function of H_{ext} for an ip- ($N_{xx} = 1$) and oop-configuration ($N_{zz} = 1$).

Eq. (2.20) for H_{res} . The resulting solution called the Kittel equation [73] is given by [92]

$$H_{\text{res}} = -\frac{1}{2}(N_{xx} + N_{yy} - 2N_{zz})M_s + \frac{1}{2}(u_x + u_y - 2u_z)H_u + \sqrt{\left(\frac{2\pi f}{\gamma\mu_0}\right)^2 + \left(\frac{[(N_{yy} - N_{xx})M_s - (u_y - u_x)H_u]}{2}\right)^2}. \quad (2.22)$$

This equation allows to determine the resonance frequency for samples with varying shapes by adjusting N_{ii} as well as for different uniaxial anisotropy field magnitudes H_u and directions \mathbf{u} . For the results in this thesis, in particular the case of a perpendicular magnetic anisotropy (PMA) will be relevant. Hence, for the sake of simplicity, we set $\mathbf{u} = (0, 0, 1)^\top$.

In the following, we will discuss the dispersion of Eq. (2.22) in three experimentally relevant cases:

- **Sphere:**

For a spherical sample, the diagonal demagnetization factors are equal ($N_{xx} = N_{yy} = N_{zz} = 1/3$) and hence the shape anisotropy contribution cancels out in Eq. (2.22) resulting in

$$H_{\text{res}} = \frac{2\pi f}{\gamma\mu_0} - H_u. \quad (2.23)$$

- **Thin film out-of-plane (oop):**

For a magnetic thin film exposed to a magnetic field applied along the surface normal ($\mathbf{H}_{\text{ext}} \propto \mathbf{z}$) with layer thickness \ll lateral dimension, we

approximate the demagnetization factors as $N_{xx} = N_{yy} = 0$ and $N_{zz} = 1$. For this case, the Kittel equation takes the form

$$H_{\text{eff}} = H_{\text{res}} - M_{\text{eff}} = \frac{2\pi f}{\gamma\mu_0}, \quad (2.24)$$

where we define $M_{\text{eff}} = M_s - H_u$ as the effective magnetization.

- **Thin film in-plane (ip):**

For a magnetic thin film exposed to a magnetic field applied in the sample plane without a loss of generality, the shape anisotropy takes the form $N_{xx} = 1$ and $N_{yy} = N_{zz} = 0$. Consequently, Eq. (2.22) can be simplified to

$$H_{\text{res}} = -H_u - \frac{1}{2}M_s + \sqrt{\left(\frac{2\pi f}{\gamma\mu_0}\right)^2 + \left(\frac{M_s}{2}\right)^2}. \quad (2.25)$$

To account for the potential presence of in-plane uniaxial anisotropies, we use a modified version of Eq. (2.25) in Ch. 5

$$H_{\text{res}} = -H_u^{\text{oop}} - \frac{1}{2}M_{\text{eff}} + \sqrt{\left(\frac{2\pi f}{\gamma\mu_0}\right)^2 + \left(\frac{M_{\text{eff}}}{2}\right)^2}. \quad (2.26)$$

The Kittel equation for these three cases for $H_u = 0$ is plotted in Fig. 2.3(b). A sizable finite H_u in Fig. 2.3(b) would result in a shift of the dispersion curves along the y -axis.

Apart from determining an analytical expression for the resonance field H_{res} as a function of frequency f using the Kittel equation via Eq. (2.22), the Polder susceptibility $\hat{\chi}_p$ also allows to determine the dissipative behavior of the ferromagnetic precession in its imaginary part. By solving the imaginary part of $\text{Det}(\hat{\chi}_p) \stackrel{!}{=} 0$ using Eq. (2.20), we obtain an expression for the fanning out of the ferromagnetic resonance linewidth ΔH given as the full-width at half-maximum of the ferromagnetic resonance as function of frequency

$$\Delta H = 2\frac{2\pi f\alpha}{\gamma\mu_0}. \quad (2.27)$$

We note, that Eq. (2.27) holds irrespective of sample shape and anisotropy as well as measurement geometry. The material-dependent Gilbert damping parameter α can hence be obtained by studying ΔH as function of f . In real ferromagnetic resonance experiments, ΔH may not intersect $\Delta H = 0$ at $f = 0$ but exhibit an additional offset in ferromagnetic resonance linewidth called the inhomogeneous line broadening H_{inh} caused by spatial variations of the sample and experimental parameters. Hence, a more realistic dispersion in $\Delta H(f)$ is given by

$$\Delta H = H_{\text{inh}} + 2 \cdot \frac{2\pi f \alpha}{\mu_0 \gamma}. \quad (2.28)$$

There exist several potential reasons for the manifestation of a non-zero H_{inh} in experiments ranging from measurement setup misalignment issues, thermal heating effects from the microwave drive over inhomogeneities in the sample to two-magnon scattering processes [126]. In rough terms it can be taken as a measure of the thin film homogeneity in our experiments [92] as the used broadband ferromagnetic resonance approach outlined in Ch. 3 probes the integrated response of the sample area underneath the microwave drive.

Having derived explicit expressions for the resonance field and linewidth, we now discuss the magnitude of the individual Polder susceptibility components in Eq. (2.20). Under the assumption $\alpha \ll 1$ we can express the resonant amplitude of the off-diagonal elements of $\hat{\chi}_{\text{p}}$ in Eq. (2.20) as [83]

$$|\chi_{yx}(\omega_{\text{res}})| = |\chi_{xy}(\omega_{\text{res}})| \approx \frac{M_s}{2\Delta H}. \quad (2.29)$$

The Polder susceptibility in Eq. (2.20) can then be approximated as

$$\hat{\chi}_{\text{p}} \approx \chi_{\text{yx}} \begin{pmatrix} i\epsilon & -1 \\ 1 & \frac{i}{\epsilon} \end{pmatrix}, \quad (2.30)$$

where

$$\epsilon = \left| \frac{M_{\text{rf},x}}{M_{\text{rf},y}} \right| \approx \sqrt{\frac{H_{\text{ext}} + (N_{yy} - N_{zz}) \cdot M_s - (u_y - u_z) \cdot H_u}{H_{\text{ext}} + (N_{xx} - N_{zz}) \cdot M_s - (u_x - u_z) \cdot H_u}} \quad (2.31)$$

is a measure for the ellipticity $f = 1 - \epsilon$ of the precession [83]. Neglecting uniaxial anisotropy ($H_u = 0$), we plot ϵ as function of H_{ext}/M_s in Fig. 2.3 for the magnetic field applied in the oop-direction ($N_{xx} = N_{yy} = 0, N_{zz} = 1$) (red line) and in the ip-direction along the x -axis ($N_{yy} = N_{zz} = 0, N_{xx} = 1$) (blue line). We note, that the magnetization precession of a magnetic thin film is circular ($\epsilon = 1$) for the magnetic field applied in the oop-direction, but exhibits a finite ellipticity, when applied in the in-plane direction. For sufficiently large external fields $H_{\text{ext}}/M_s \gg 1$, the magnetization precesses circularly ($\epsilon \rightarrow 1$) irrespective of sample orientation with respect to the external field.

2.3 Magnetization dynamics in hybrid systems

In the model derived above, the magnetization dynamics of a homogeneously magnetized magnetic ellipsoid with rotational axes along the cartesian axes has been derived and simplified further for the case of magnetic thin films in different geometries. In the following, we discuss, how the coupling of the thin film magnetization dynamics is modified, when it interacts with the various different excitations in the hybrid samples investigated in this thesis such as for example phononic excitations or paramagnetic impurities. In detail, we first introduce the coupling between the magnetization dynamics in a ferromagnetic layer and charge currents in an adjacent normal metal layer via spin torques and the the injection of angular momentum into thin film layers adjacent to the magnetic layer via spin pumping necessary for the interpretation of the results in Ch. 5. The presented derivations are based on Refs. [34, 83–85]. Thereafter, we discuss how the magnetization dynamics of magnetic thin films are affected by the coupling to paramagnetic impurities via the so-called slow-relaxor and valence exchange mechanism as detected for the γ -Fe₂O₃ thin films in Ch. 4 closely following the derivations in Refs. [81, 82]. Finally, we will discuss the conceptually similar fundamentals of both magnon-photon- and magnon-phonon coupling discussed in chapters 6 and 7. Presented calculations for the magnon-photon-coupling are adapted from the calculations presented in Refs. [78–80], whereas our derivations for the magnon-photon coupling strength are inspired by Ref. [77].

2.3.1 Spin torques in Ferromagnet/Normal metal hybrids

When normal metal (NM) films are attached to ferromagnetic (FM) films, the magnetization dynamics are altered due to a finite coupling between the two constituents. The coupling can lead to an additional driving or damping of the magnetization dynamics, which can be described by additional torques. We can distinguish between so-called field-like spin torques, which act in the same way as a magnetic driving field by counteracting the damping, and so-called damping-like spin torques, which are exactly opposite to the field-like torque acting as an additional damping process [34, 83, 84]. Both torques can be represented by two additional magnetic field contributions: the field-like contribution \mathbf{H}_f pointing along \mathbf{H}_{eff} and the damping-like contribution \mathbf{H}_d in parallel to $\mathbf{M} \times \mathbf{H}_{\text{eff}}$.

There are several physical origins for these additional torques. If we create a perturbation in the NM film by driving a charge current J_c through it, we generate both an Oersted field and a spin current via the Spin Hall effect (SHE) [35, 36], both of which generate additional field-like and damping-like spin torques in the adjacent FM layer. Consequently, the driving of a charge current in NM also has a finite effect on the magnetization dynamics in the FM.

On the other hand, if we drive magnetization dynamics in the FM layer by applying an AC magnetic field, the Oersted fields of drive and dynamics will also

induce eddy currents in the adjacent NM layer. Moreover, the magnetization dynamics induced in the FM layer will lead to the injection of a dynamic spin current J_s into the NM layer, as will be discussed in greater detail in the next section 2.3.2. Via the inverse SHE [127, 128], this spin current will generate a charge current in the NM layer. Both effects cause a damping of the magnetization dynamics in the FM, which can be described by additional damping-like spin torques. Hence, the reciprocal effect, i.e. the driving of the magnetization dynamics in a FM has a finite effect on the charge current flowing in the NM. In literature the processes, where a charge current in the NM induces a torque on the magnetization in the adjacent FM layer are commonly denoted as 'spin torques', whereas the reciprocal effect, where magnetization effects in the FM layer generate a charge current in the NM layer are called 'inverse spin torques' [34, 83, 84]. This relation between spin torques and inverse spin torques is illustrated in Fig. 2.4.

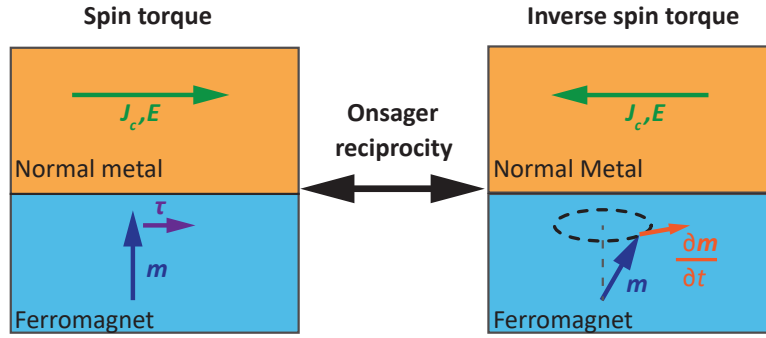


Fig. 2.4. – Spin torque and inverse spin torque in ferromagnet/normal metal heterostructures. For spin torques, a charge current J_c driven by an applied electric field E in the NM layer with thickness d_{NM} gives rise to a torque τ acting on the magnetization M of the adjacent FM layer with layer thickness d_{FM} . In the reciprocal process, a dynamically precessing magnetization $\partial M/\partial t$ in the FM layer induces an electric field E in the NM layer, which in turn drives a charge current J_c . Adapted from Ref. [120].

In a linear response model, the cross-coupling between torques τ and charge current densities J_c driven by the magnetization dynamics $\partial m/\partial t$ in the FM layer and an applied dc electric field E in the NM layer is given by [83, 84]

$$\begin{pmatrix} \tau \\ J_c \end{pmatrix} = \left[\hat{t} \circ \begin{pmatrix} m \times & -m \times \\ n \times & -n \times \end{pmatrix} \right] \begin{pmatrix} \partial m/\partial t \\ n \times E \end{pmatrix} \quad (2.32)$$

$$\hat{t} = \begin{pmatrix} -\alpha/\gamma M_s & \sigma_{\text{ST}}\hbar/(2ed_{\text{FM}}) \\ \sigma_{\text{ST}}\hbar/[2e(d_{\text{FM}} + d_{\text{NM}})] & \sigma_{\text{NM}} \end{pmatrix},$$

where, m and n are unit vectors pointing along the magnetization and surface normal, the d_{NM} and d_{FM} denote the layer thicknesses of the NM and FM layer, respectively and σ_{NM} is the conductivity of the NM layer. Furthermore, we have introduced the spin torque conductivity σ_{ST} in units of $(\Omega\text{m})^{-1}$ as the scaling parameter of the spin torques. The spin torque conductivity is a complex quantity $\sigma_{\text{ST}} = \sigma_f + i\sigma_d$ with the real part σ_f corresponding to the added contribution of

all field-like spin torques and the imaginary part σ_d representing the sum of all damping-like torques. Note, that in the case $\sigma_{ST} = 0$, charge currents \mathbf{J}_c in the normal metal and magnetization torques $\boldsymbol{\tau}$ in the ferromagnetic layer are uncoupled and the ordinary Gilbert damping torque in the LLG equation (2.15) $\boldsymbol{\tau} = -(\alpha/\gamma)\partial\mathbf{M}/\partial t$ and the ohmic relation $\mathbf{J}_c = \sigma_{NM}\mathbf{E}$ are restored. For the NM/FM-heterostructures discussed in this thesis, we attribute σ_f to the sum of the spin torque conductivity contributions of the ordinary Faraday effect σ_F and of the inverse Rashba Edelstein effect σ_{iREE} [129] resulting in $\sigma_f = \sigma_{iREE} - \sigma_F$ [83,84]. Importantly, it is impossible to disentangle these contributions via symmetry arguments [83,130]. On the other hand, in our hybrid NM/FM-heterostructures, the damping-like torque is related to the SHE via $\Theta_{SH}T = \sigma_d/\sigma_{NM}$, where T is the interface transparency for spins at the NM/FM-interface. We note that σ_{NM} , σ_{ST} and α can strictly only be assumed to be isotropic in the case of polycrystalline FM and NM layers [83]. In crystalline materials, these quantities need to be replaced by tensors in Eq. (2.32).

2.3.2 Spin pumping mechanism

In the previous section 2.2, we have outlined, how the various magnetization dynamics parameters can be extracted from the frequency-dependence of the ferromagnetic resonance field $\mu_0 H_{res}$ and linewidth $\mu_0 \Delta H$. As the various sources for magnetization damping are often not known, the phenomenological Gilbert damping parameter α has been introduced. It constitutes a measure of the total dissipation of angular momentum by all the various loss mechanisms in the magnetic materials such as for example eddy current damping [123,131], radiative damping [132], or two-magnon scattering [114–116]. As already mentioned above, interfacing a magnetic thin film with an adjacent normal metal layer gives rise to an additional loss channel for α via the injection of an angular momentum in the form of a dynamic spin current density \mathbf{J}_s into the adjacent normal metal layer. This process is called spin pumping [85]. The spin current density injected across the interface is given by

$$\mathbf{J}_s = \frac{\hbar}{4\pi} \left(\underbrace{\text{Re}(G_{\uparrow\downarrow})\mathbf{M} \times \frac{d\mathbf{M}}{dt}}_{\text{damping-like}} - \underbrace{\text{Im}(G_{\uparrow\downarrow})\frac{d\mathbf{M}}{dt}}_{\text{field-like}} \right), \quad (2.33)$$

where $G_{\uparrow\downarrow}$ is the spin-mixing conductance, which is a material- and interface-dependent parameter that describes the transport of spins non-collinear to the magnetization of the ferromagnetic layer [133]. The spin-pumping mechanism acts on the magnetization dynamics as an additional spin torque in the LLG in the form $\boldsymbol{\tau}_s = \gamma/(M_s d_{FM})\mathbf{J}_s$, where d_{FM} is the layer thickness of the FM layer. Here, the first term of Eq. (2.33) corresponds to an additional damping-like term in the LLG, whereas the second term has the symmetry of a field-like contribution to the

precession of M . As the imaginary part of the spin-mixing conductance $G_{\uparrow\downarrow}$ is typically negligibly small [36], spin pumping is primarily discussed in terms of its damping-like contribution as an enhanced damping α_{SP} in the LLG given by [134]

$$\alpha_{\text{SP}} = \frac{g\mu_{\text{B}}}{4\pi M_{\text{s}}} G_{\uparrow\downarrow} \frac{1}{d_{\text{FM}}}. \quad (2.34)$$

The net Gilbert damping can hence be written as the sum of the intrinsic contribution α_0 and the spin-pumping contribution α_{SP}

$$\alpha = \alpha_0 + \alpha_{\text{SP}}. \quad (2.35)$$

As α_{SP} is inversely proportional to the layer thickness of the FM, samples with low d_{FM} are required to detect the effect of spin pumping. Hence, to experimentally determine the spin-mixing conductance $G_{\uparrow\downarrow}$, the net Gilbert damping α of a series of ferromagnet/normal metal samples with varying low d_{FM} is typically studied [40, 132, 135, 136]. Moreover, via the iSHE, this spin current injected via spin pumping is converted into a charge current in the adjacent NM layer and thereby contributes as a damping-like torque conductivity σ_{d} in Eq. (2.32), which can be detected via the inductive analysis technique [84] presented in Ch. 5.

2.3.3 Temperature-dependent magnetic relaxation processes

The temperature dependence of the magnetization dynamics of magnetic materials can be instructive to study the hybridization of magnetic excitations with other solid-state excitations [137, 138] or exotic spin textures, which manifest primarily at cryogenic temperatures [30, 139]. In particular for the ferromagnetic resonance linewidth ΔH of the ferrimagnetic insulator yttrium iron garnet ($\text{Y}_3\text{Fe}_5\text{O}_{12}$, YIG), the temperature-dependence exhibits one or several local maxima for certain temperatures T [140–142]. These features are attributed to several different temperature-dependent magnetic relaxation processes generated by ionic impurities introduced in the magnetic thin film during its growth process [81, 100, 143]. There are several theoretical models for these magnetic relaxation processes, which then manifest at different temperatures and excitation frequencies. In the following, we will introduce the mechanisms relevant for the magnetization dynamics of $\gamma\text{-Fe}_2\text{O}_3$ in Ch. 4 of this thesis: (i) The slowly-relaxing impurity mechanism [82, 140, 144–146] and (ii) the valence-exchange mechanism [100, 147, 148].

- **Slowly-relaxing impurity:**

In the slowly-relaxing impurity model, the energy levels of substitutional ionic impurities effectively constitute a disordered magnetic subsystem in the crystal structure to which the host magnetic material can couple via the Heisenberg exchange interaction (see Sec. 2.1). The ionic energy levels of the

impurities are periodically modulated by the precession of M as the strength of the exchange coupling depends on the relative orientation of M and the impurity magnetic moments. This modulation leads to a net energy transfer from the magnetic subsystem to the impurity system, when the impurities relax towards the thermal equilibrium [81]. This process is illustrated in Fig. 2.5(a) and (b). As a result, the thermal population is redistributed

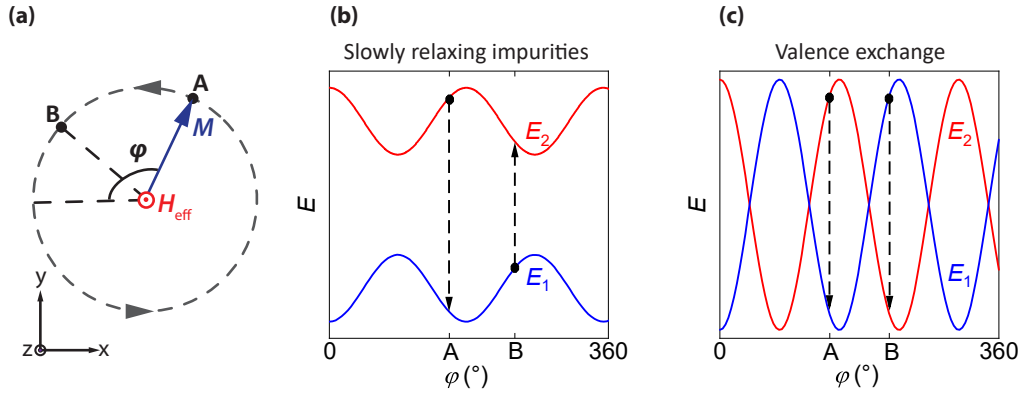


Fig. 2.5. – (a) Magnetization precession around the effective field in the x - y -plane (see Fig. 2.3). The angle φ denotes the polar orientation of M in the x - y -plane. The points A and B denote two exemplary magnetization orientations. (b) Energy variation of the two lowest energy levels of the slowly-relaxing impurity as function of φ . (c) Energy variation of the two lowest energy levels of the additional electron exchanged between the two neighboring lattice sites in the valence-exchange mechanism as function of φ . Adapted from Refs. [81, 143].

between the two energy levels E_1 and E_2 . For the magnetization orientation marked by position A in Fig. 2.5(a), the energy splitting between E_2 and E_1 oscillates as function of φ causing a redistribution between the equilibrium occupations N_{E_i} of the two energy levels with ions transitioning to E_1 and transferring energy to the lattice in the process [81]. For the magnetization at position B, the equilibrium population of the ions shifts towards level E_2 and hence energy is absorbed from the lattice. The thermal relaxation time of the ions is given by τ and is typically in the \simeq ps-range. When the magnetization is driven in the GHz-range by the frequency ω , a maximum energy transfer to the lattice is achieved for $\omega\tau = 1$ giving rise to a peak in the FMR-linewidth as a function of ω . The strong temperature-dependence of this process results from the population distribution of the two energy levels being given by

$$\frac{N_{E_2}}{N_{E_1}} = \exp\left(\frac{E_2 - E_1}{k_B T}\right), \quad (2.36)$$

where k_B is the Boltzmann constant. As a consequence, the slowly-relaxing impurity process is strongly temperature- and frequency-dependent. For the slowly relaxing impurity mechanism, the temperature-dependent peak

in $\Delta H(T)$ usually manifests at cryogenic temperatures in the range $10 \text{ K} \leq T \leq 50 \text{ K}$ [140–142].

In the presence of slowly relaxing impurities and assuming a uniform uniaxial out-of-plane anisotropy field H_u parallel to the applied static magnetic field, the total dispersion of the ferromagnetic resonance and the change of linewidth with frequency can then be expressed as [82, 146]

$$\mu_0 H_{\text{res}} = \mu_0 M_{\text{eff}} + \frac{hf}{g\mu_B} [1 + \text{Im}(\alpha_{\text{slow}}(f))] \quad (2.37)$$

$$\mu_0 \Delta H = \mu_0 H_{\text{inh}} + 2 \cdot \frac{hf}{g\mu_B} [\alpha + \text{Re}(\alpha_{\text{slow}}(f))]. \quad (2.38)$$

Here, the slowly-relaxing impurity contribution is given by $\alpha_{\text{slow}}(f)$ [82]

$$\alpha_{\text{slow}}(f) = CF(T) \left[\frac{\tau}{1 + (2\pi f\tau)^2} - i \frac{2\pi f\tau^2}{1 + (2\pi f\tau)^2} \right], \quad (2.39)$$

where the constant C is given by [82, 146]

$$C = \frac{g\mu_B N_{\text{slow}}}{8M_s \hbar k_B T} \left[\left(\frac{\partial E_{\text{slow}}}{\partial \phi} \right)^2 + \left(\frac{\partial E_{\text{slow}}}{\partial \theta} \right)^2 \right]. \quad (2.40)$$

In Eq. (2.40), N_{slow} represents the concentration of the slowly relaxing impurities and E_{slow} is the spin splitting of the paramagnetic impurity energy levels induced by the exchange field of the magnetically ordered layer. The angular derivatives of E_{slow} (where θ and ϕ are the azimuthal and polar angles with respect to the magnetic field axis along z , respectively) are a consequence of the anisotropic exchange coupling of the impurity atoms with the ferromagnetic moment [82]. The function $F(T)$ describes the temperature dependence of the damping contribution by the slowly relaxing impurities and can be expressed as

$$F(T) = \text{sech}^2 \left(\frac{E_{\text{slow}}}{k_B T} \right). \quad (2.41)$$

- **Valence-exchange model:**

The so-called valence-exchange or charge-transfer mechanism [100, 147, 148] manifests itself if mixed-valent ions are present in the ferromagnetic sample (i.e. Fe^{2+} or Fe^{4+} ions in YIG with nominal only Fe^{3+} -ions). In this case electrons can hop between the different valence lattice sites. This hopping mediates a net energy transfer from the dynamically precessing magnetization to the crystal lattice and can thereby increase the damping. This process is illustrated in Fig. 2.5(c). Here, 1 and 2 denote two neighboring lattice sites exchanging the additional valence electron. Depending on the alignment of the magnetization M in Fig. 2.5(a), the energy at sites 1 and

2 are periodically modulated and their thermal equilibrium population depends on φ . At position A, an extra electron at site 2 will hop to site 1 by transferring its excess energy $E_2 - E_1$ to the lattice. Conversely, at magnetization position B, the electron will hop back to its initial site 2 by again transferring the energy $E_2 - E_1$ to the lattice [81]. In analogy to the slowly-relaxing-impurity mechanism, the maximum energy is transferred from the magnetic subsystem to the lattice, when the thermal relaxation rate of the electrons $1/\tau_e$, where τ_e is the relaxation time, matches the frequency of the precessing M . Notably, this mechanism results in the same peak-like frequency dependence to the FMR linewidth in Eq.(2.38) with the characteristic relaxation time τ_e . In contrast to the slowly relaxing impurity mechanism, the temperature-dependent peaks in ΔH induced by the valence exchange mechanism manifests at elevated temperatures in the range $100 \text{ K} \leq T \leq 400 \text{ K}$ [147, 148]. A temperature-dependent study of $\Delta H(T)$ hence enables to disentangle these two temperature-peak processes.

2.3.4 Magnon-Photon coupling

In the following, we will discuss the two conceptually similar process of magnon-photon and magnon-phonon coupling. Considering the coupling of two particular modes of the phonon and magnon system, in a classical description we can model both modes as two harmonic oscillators with resonance frequencies f_i and loss rates κ_i coupled to oneanother with the effective coupling rate g_{eff} . If the resonance frequencies of the two resonators are tuned to cross each other via an external control parameter, they can hybridize and avoid each other in a characteristic anticrossing feature in the case of strong coupling $g_{\text{eff}} > \kappa_1, \kappa_2$ [30]. Using this simple analogy, we model the magnon-photon coupling between a magnetically ordered system and a superconducting microwave resonator. This is illustrated in Fig. 2.6(a). The microwave photons oscillate inside a superconducting microwave resonator with resonance frequency f_r determined by the resonator's inductance L and capacitance C at a loss rate κ_r given as the sum of the internal and external loss rates κ_{int} and κ_{ext} , respectively. The magnonic excitations of the ferromagnetic material are resonantly excited at a frequency f_{mag} tunable via an external magnetic field \mathbf{H}_{ext} according to the Kittel equation [Eq. (2.22)] and decay at a rate of κ_s proportional to the FMR-linewidth ($\kappa_s = \pi\gamma\mu_0\Delta H$). In this system, the coupling between the magnonic and the phononic subsystem is mediated by dipolar interaction [30, 78]. Hence, applying an external magnetic field allows to tune f_{mag} to cross f_r to observe magnon-photon coupling. This mechanism has been extensively studied in different coupling regimes i.e. for various ratios of g_{eff}, κ_s and $\kappa_{\text{int}} + \kappa_{\text{ext}}$ [30, 149–151].

Using a quantum mechanical description and neglecting dissipative terms, the

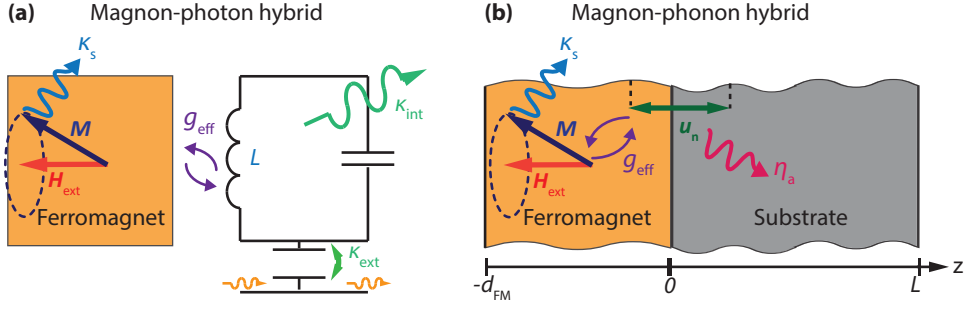


Fig. 2.6. – Illustration of the coupling between bosonic excitations and magnonic modes in coupled resonator/ferromagnet hybrid systems. (a) Schematics of the magnon-photon coupling. The magnetization precessing with resonance frequency f_{mag} (Kittel mode) and loss rate κ_s inductively couples with the effective coupling rate g_{eff} to the electromagnetic modes of a superconducting LC -resonator with resonance frequency f_r . The total resonator loss rate is given by the sum of the internal and external loss rates κ_{int} and κ_{ext} . (b) Schematics of the magnon-phonon coupling. The magnetization precessing with resonance frequency f_{mag} and loss rate κ_s couples magnetoelastically with the elastic modes of the substrate with the effective coupling rate g_{eff} . As the substrate can be viewed as a bulk acoustic wave (BAW) resonator, in particular the coupling to quantized standing-wave BAW excitations (phonons) with resonance frequency f_r is of interest. The BAW resonator loss rate is given by the acoustic loss rate η_a .

Hamiltonian of the undriven magnon-photon hybrid system can in a rotating wave approximation be expressed as [65, 78, 152–155]

$$H_{\text{cp}} = \underbrace{hf_r a^\dagger a}_{\text{Resonator}} + \underbrace{hf_{\text{mag}} \sum_{i=1}^N b_i^\dagger b_i}_{\text{Magnet}} + \underbrace{\frac{hg_{\text{eff}}}{2\pi} (ab^\dagger + a^\dagger b)}_{\text{Coupling}}, \quad (2.42)$$

where (a^\dagger, a) is the generation and annihilation operators of photons in the microwave resonator and the operators $(b^\dagger = 1/g_{\text{eff}} \sum_{i=1}^N b_i^\dagger, b = 1/g_{\text{eff}} \sum_{i=1}^N b_i)$ describe the creation and annihilation of a collective spin excitation. The net coupling strength $g_{\text{eff}} = \sqrt{\sum_{i=1}^N g_i^2}$ normalizes the creation and annihilation operators, where g_i is the coupling rate of a microwave photon to a magnetic moment at lattice site i [155]. For the coupling to excitations in 3d-metals, assume identical coupling rates of photons to all magnetic moments ($g_i = g_0$) and obtain $g_{\text{eff}} = g_0 \sqrt{N}$. In Eq. (2.42), the first term represents the energy of a microwave photon in the uncoupled resonator and likewise the second term that of a magnetic excitation in the magnetic sample, where N is the number of spins in the magnetic sample [30, 78]. The third term describes the coupling between the two excitations.

In real physical systems, we account for magnetic and microwave loss rates by introducing the complex resonator frequencies [155, 156] in Eq. (2.42)

$$f_r \rightarrow \tilde{f}_r = f_r - i\kappa_r/(2\pi), \quad f_{\text{mag}} \rightarrow \tilde{f}_{\text{mag}} = f_{\text{mag}} - i\kappa_s/(2\pi). \quad (2.43)$$

Furthermore, we add an external drive H_{drive} of the form

$$H_{\text{drive}} = -i\hbar\eta(a - a^\dagger), \quad (2.44)$$

where η is the coupling rate between microwave resonator and external drive to Eq. (2.42). By solving the thereby modified Hamiltonian and calculating its temporal dynamics, we then obtain an analytical expression for the expected complex transmission parameter T of this system as [78–80]

$$T(f) \propto \frac{\kappa_{\text{ext}}/(2\pi)}{i(f - f_r) - \kappa_r/(2\pi) + \frac{[g_{\text{eff}}/(2\pi)]^2}{i(f - f_{\text{mag}}) + \kappa_s/(2\pi)}}. \quad (2.45)$$

Following Eq. (2.42), the eigenmodes of the coupled magnon-photon hybrid system are given by [79]

$$[i(f_r - f) + \kappa_r/(2\pi)] \cdot [i(f_{\text{mag}} - f) + \kappa_s/(2\pi)] = [g_{\text{eff}}/(2\pi)]^2. \quad (2.46)$$

We solve Eq. (2.46) by f and obtain the two solutions for the coupled magnon-photon system

$$\tilde{f}_{\text{mp}}^\pm = \frac{f_r + f_{\text{mag}}}{2} - i\frac{\kappa_r + \kappa_s}{4\pi} \pm \sqrt{\left(\frac{f_r - f_{\text{mag}}}{2} - i\frac{\kappa_r - \kappa_s}{4\pi}\right)^2 + (g_{\text{eff}}/2\pi)^2}. \quad (2.47)$$

The real and imaginary part of Eq. (2.47) represent the resonance position f_{mp} and linewidth κ_{mp} of the hybrid mode, respectively. In the case $f_i \gg \kappa_i$ for both uncoupled magnonic and resonator subsystems, f_{mp} and κ_{mp} are given by

$$f_{\text{mp}}^\pm = \frac{f_r + f_{\text{mag}}}{2} \pm \frac{\sqrt{(f_r - f_{\text{mag}})^2 + (g_{\text{eff}}/\pi)^2}}{2}, \quad (2.48)$$

$$\frac{\kappa_{\text{mp}}^\pm}{2\pi} = \frac{\kappa_r + \kappa_s}{4\pi} \pm \frac{\kappa_r - \kappa_s}{4\pi} \frac{f_r - f_{\text{mag}}}{\sqrt{(f_r - f_{\text{mag}})^2 + (g_{\text{eff}}/\pi)^2}}. \quad (2.49)$$

Consequently, we can experimentally study the magnon-photon coupling in our samples by fitting the measured resonance frequency f_{mp}^\pm and linewidth κ_{mp}^\pm of the coupled magnon-photon hybrid system to Eqs. (2.48) and (2.49), respectively.

2.3.5 Magnon-Phonon coupling

In our experiments, we study magnon-phonon coupling between the fundamental Kittel mode of a ferromagnetic thin film and the elastic standing waves of a crystalline substrate material serving as a bulk acoustic wave resonator. In resonance, due to magneto-elastic coupling the homogeneous ferromagnetic resonance mode generates a strain field in the FM with the same frequency and helicity as the Kittel mode. Due to elastic coupling at the interface to the substrate, this strain field couples to the BAW resonator modes of the substrate. For the geometry in our experiments, the BAW modes correspond predominantly to transverse acoustic shear waves with orthogonal polarizations [112]. As depicted in Fig. 2.6(b), the propagating shear waves meet reflective boundary conditions imposed by the finite thickness of the substrate L plus magnetic thin film d_{FM} and thus we expect the formation of standing waves. For a substrate thickness of $L \simeq 500 \mu\text{m}$ this corresponds to a mode spacing in the MHz range for transverse acoustic modes propagating in the substrate with velocities $v_t \simeq 1 \text{ km/s}$. As we excite the FMR in the magnetic layer with frequencies in the $\simeq 10 \text{ GHz}$ range, we operate this BAW resonator in the high-overtone regime. Here, the resonance frequency of an elastic standing wave mode with mode number n can be well approximated by [157]

$$f_n = \frac{n}{2 \left(\frac{d_{\text{FM}}}{\bar{v}_t} + \frac{L}{v_t} \right)}, \quad (2.50)$$

where d_{FM} is the thickness of the CoFe thin film and \bar{v}_t denotes the transverse phonon velocity of the magnetic thin film. Whenever the frequency of the FMR is resonant with one of the standing wave modes of the BAW, we can efficiently excite the elastic mode via magnetoelastic coupling [55, 56, 77, 158, 159]. At these frequencies we thus expect a modification of the FMR resonance features. Due to resonance with the acoustic modes at frequencies f_n , the FMR absorption line shows a frequency-periodic modification when measured over a broad frequency regime [77, 158, 159]. The periodicity is given by the free spectral range $f_{\text{FSR}} = f_1$.

To determine the net effective coupling rate g_{eff} between the transverse elastic waves and the magnetic Kittel mode, we describe our FM/BAW resonator system by a circularly polarized elastic wave, which is coupled to the magnetic Kittel mode. As discussed in detail in Refs. [77, 160] the systems of coupled damped harmonic resonators can be described via

$$\begin{aligned} (f - f_{\text{mag}} + i \frac{\kappa_s}{2\pi}) m^+ &= \frac{g_{\text{eff}}}{4\pi} u_n^+ + \zeta h^+ \\ (f - f_n + i \frac{\eta_a}{2\pi}) u_n^+ &= \frac{g_{\text{eff}}}{4\pi} m^+. \end{aligned} \quad (2.51)$$

Here, f_{mag} is the magnetic resonance frequency, the f_n is the resonance frequency of the elastic standing wave using Eq. (2.50) and η_a is the loss rate of the elastic system. The variables m^+ and u_n^+ are the circularly polarized magnetization and

elastic wave amplitudes, respectively. Note that in our experiments the chirality of m and u is given by the oscillating driving field of the CPW h^+ , which is coupled inductively to m^+ at the coupling rate ζ . We solve Eq. (2.51) for m^+ and obtain

$$m^+ = -\zeta h^+ \frac{[f - f_n + i\eta_a]/(2\pi)}{[f - f_n + i\eta_a/(2\pi)][f - f_{\text{mag}} + i\kappa_s/(2\pi)] + g_{\text{eff}}^2/(16\pi^2)}. \quad (2.52)$$

We can rewrite this expression as

$$m^{x,y} = \frac{-\zeta h^{x,y}}{(f - f_{\text{mag}}) - g_{\text{eff}}^2/(16\pi^2 C(f))(f - f_n) + i \cdot [\kappa_s/(2\pi) + g_{\text{eff}}^2 \eta_a / (32\pi^3 C(f))]}, \quad (2.53)$$

where we have defined $C(f) = (f - f_n)^2 + [\eta_a/(2\pi)]^2$. The imaginary part in the denominator of Eq. (2.53) can be interpreted as a modified magnetic relaxation rate $\tilde{\kappa}_s$ in the presence of magnetoelastic coupling given by

$$\tilde{\kappa}_s = \kappa_s + \frac{\eta_a g_{\text{eff}}^2 / (4\pi^2)}{4[(f - f_n)^2 + \eta_a^2 / (4\pi^2)]} \quad (2.54)$$

In resonance with the phononic modes, we obtain

$$\tilde{\kappa}_s(f = f_n) = \kappa_s + \frac{g_{\text{eff}}^2}{4\eta_a} \quad (2.55)$$

We see that the magnetic damping is increased by the finite coupling to the acoustic resonator with damping rate η_a . We solve Eq. (2.55) by the effective coupling rate g_{eff} and obtain

$$g_{\text{eff}} = 2\sqrt{\eta_a(\tilde{\kappa}_s(f = f_n) - \kappa_s)} = \sqrt{2\eta_a\gamma[\mu_0(\Delta H(f = f_n) - \Delta H_0)]}. \quad (2.56)$$

Hence, in our experiments, the effective coupling rate between Kittel mode and BAW resonator substrate can be determined from the modification of the FMR-linewidth ΔH at those frequencies, where the Kittel mode is in resonance with the n^{th} elastic mode of the BAW resonator ($f = f_n$).

In this Chapter, we present detailed information on the experimental methods performed in this thesis. Starting with the growth of thin film heterostructures using magnetron sputter deposition in Ch. 3.1, we proceed with the description of the nanofabrication of the planar superconducting resonator samples in Ch. 3.2. Finally, we describe the experimental setup and measurement techniques used for the characterization of our hybrid samples in Ch. 3.3.

3.1 Thin film deposition process

This section is dedicated to the growth process of thin film multilayers for the hybrid heterostructures discussed in Chs. 5, 6 and 7. The heterostructures are deposited by dc magnetron sputtering by using the Superbowl and Ultradisk sputtering machines of the Walther-Meißner-Institute. As the growth of several materials has been optimized throughout the course of this thesis (see Refs. [69, 161–163]), we also provide an overview of the relevant deposition parameters, which have been optimized to obtain tailored material properties.

3.1.1 Operation principle of magnetron sputtering

In the following, we will briefly describe the growth of metallic thin films for the heterostructures investigated in this thesis. The following explanations are based on textbooks on the topic of sputtering deposition from Refs. [164–166]. Sputtering describes the process of removing surface atoms from a target material by ion bombardment. The dislodged surface atoms move to the substrate surface and condense there, contributing to the growth of solid thin films on the substrate. The physical mechanism is illustrated in Fig. 3.1(a). High energy ions with energies in the $\simeq (0.1 - 1)$ keV-range are accelerated towards the target material, collide with it in collision cascades [168, 169] leading to the ejection of atoms or even small material clusters. The number of removed surface atoms depends on the energy of ions, the relation of their mass to the mass of the target material atoms for an optimal momentum transfer and on the composition of the target. Ions with a comparable mass to the target material are required to obtain an optimal sputtering yield Y , defined as the ratio between the sputtered atoms N_a and the incident ions N_i ($Y = N_a / N_i$) [167] and a sufficiently low threshold energy E_{th} for the onset of the sputtering process [170]. To this end, we utilize an inert Argon gas, which is ionized and accelerated towards the target by applying a dc voltage $V \simeq 100$ V to the target material and an anode ring. This process is illustrated in Fig. 3.1(b). To allow for sputtering deposition of materials at elevated growth

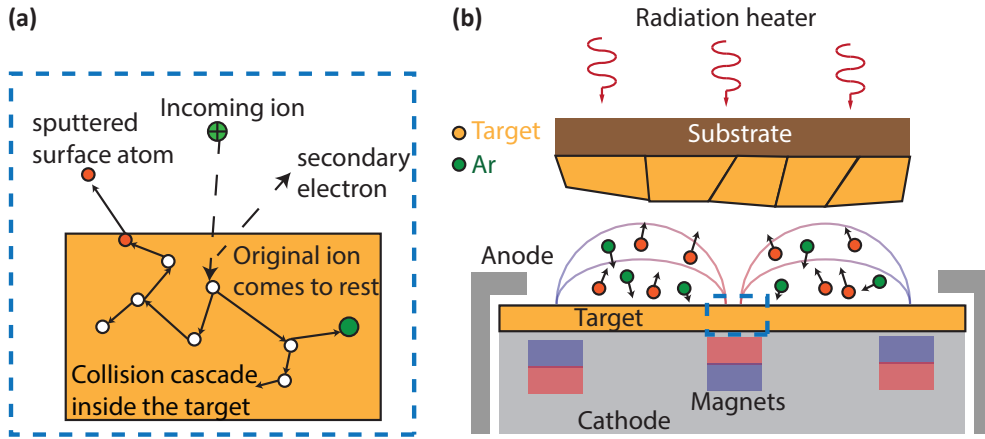


Fig. 3.1. – (a) Physical mechanism of sputtering. The incident incoming Ar ions cause a cascade of collisions in the target material that triggers the injection of both surface atoms and secondary electrons. The schematic sketch was recreated from Fig. 1. in Ref. [167]. (b) Schematic illustration of the magnetron sputtering process. Ar atoms are ionized in the electric field applied between anode and cathode and are accelerated towards the target material igniting a plasma state. The permanent magnets below the target confine secondary electrons, which increases the ionization efficiency and therefore the plasma density and deposition rates.

rates on the substrate requires low inert gas pressures to avoid the scattering of the ejected target particles with the incoming ions and background gas particles. To this end, we employ magnetron sputtering to trap ejected secondary electrons, emitted during the ion collision process, in a transversal magnetic field generated by permanent magnets mounted underneath the target [see Fig. 3.1(b)]. The transverse magnetic field generated by the magnets exerts a Lorentz force on the electrons and thereby forces them on a helical path on their way towards the anode ring [122]. Consequently, the emitted secondary electrons complete many gyrations and hence traverse a much longer path in the space between the target material and the anode ring. Thereby the ejected electrons can ionize more primary ions for sputtering allowing to perform sputter deposition processes at pressures $\leq 10^{-2}$ mbar. As indicated in Fig. 3.1(a), the thin films grown by sputter deposition are typically polycrystalline consisting of many crystalline or even fully epitaxial grains rather than a single crystal across the whole substrate. However, in our deposition systems, the sample can be heated with a radiation heater to promote textured growth of our thin film and to influence the size of grains.

3.1.2 Growth optimization parameters

To ensure optimal growth conditions for the desired material, there are several deposition parameters which need to be optimized:

- **Deposition rate r_{depo} :**

The rate at which material is deposited on the substrate is an important parameter to obtain optimal growth of our thin films. For instance, it impacts the structural properties of the thin film such as the surface roughness and crystalline quality but can also have direct influence on the functional properties such as the electrical [171], optical [172] or magnetic [173] characteristics of the respective materials. The main deposition parameters that allow to adjust r_{depo} are: (i) The target-to-substrate distance d , (ii) the deposition power P_{depo} , (iii) the deposition pressure p_{depo} and (iv) the configuration of the target with respect to the substrate (face-to-face, off-axis, confocal). As these parameters can vary strongly for different sputtering machines, the deposition rate r_{depo} can be viewed as the most universal parameter, when comparing deposition recipes of different sputtering machines.

- **Process temperature T_{depo} :** A radiation heater mounted on top of the manipulator enables to heat the substrates to temperatures of up to 800°C before, during, and after deposition. Target atoms and clusters sputter-deposited on a heated substrate exhibit an enhanced mobility resulting in the conglomeration of smaller size grains into larger sized structures [174], which improves the crystalline growth of the material. However, high deposition temperatures can also break molecular bonds in the deposition of compounds [175] and give rise to unwanted chemical reactions between substrate and deposited thin films [137, 176] or between individual materials in a heterostructures [177].

- **Deposition power P_{depo} :**

In sputter deposition, the deposition power P_{depo} used in the sputtering process also has a profound impact on the sputtering deposition [178, 179] as it controls either the charge current or voltage applied between anode and cathode during deposition based on the mode of operation of the power source. In sputtering deposition, the current at the DC source controls the number of Ar ions impacting on the target surface and thereby directly contribute to r_{depo} , whereas the target voltage governs the respective kinetic energies of the Ar ions, which influences the average sputter particle size and kinetic energy and can consequently impact both r_{depo} and thin film surface roughness.

In the sputter deposition systems used in this work, the used DC power supplies of the Superbowls sputtering system are operated in the constant power mode, whereas those of the Ultradisk sputtering system are operated

in the constant current mode. In the constant current mode, the deposition power is increased by increasing the sputtering current of the magnetron target, proportional to the gas ion current on the target surface. Furthermore, we know from our deposition runs in the Superbowls sputtering system, that raising the deposition power primarily increases the deposition current. Therefore in our growth optimization processes in both sputtering chambers, P_{depo} predominantly controls the number of Ar ions impacting on the target surface thereby contribute to r_{depo} but not the respective kinetic energies of the Ar ions, which influences the average sputter particle size and kinetic energy.

- **Deposition pressure p_{depo} and target-substrate distance d :**

The inert gas pressure during deposition p_{depo} affects the mean free path l of the particles ejected from the target material surface. In combination with the target-sample distance d , this enables to control the size S of the particle complexes sputtered on the sample surface as l is inversely proportional to S [180]. The deposition of smaller particle complexes can improve the surface roughness of the deposited films [181].

- **Target configuration:**

The sputtering devices used for this work allow for two different target configurations with respect to the substrate: The **face-to-face**(ftf)- and the **tilt-in**(ti)-configuration. As the name suggests, in the ftf-configuration, the target and magnetron are aligned in a confocal orientation. Hence, the target material impact on the substrate surface at a right angle traversing a minimum distance d and thereby transferring the maximum kinetic energy on the substrate material at the maximum deposition rate r_{depo} . As outlined previously, a high deposition rate can be advantageous for certain materials, however, it is detrimental to the smoothness of the substrate/material interface and gives rise to a higher surface roughness compared to a deposition at an angle β [182, 183] in the ti-configuration. Likewise to a deposition at an elevated target-substrate distance d , particles sputtered from a target at an angle traverse a longer path before reaching the sample surface and thereby inflict less damage on the substrate surface.

- **Ratio of inert and reactive gas flow in reactive sputtering processes x :** The deposition compound materials like oxides or nitrides from an elemental target require the injection of a reactive gas in addition to the inert gas during sputtering. The reactive gas forms radicals in the ion plasma, which react with the sputtered target material to form the desired compound [165]. To enable the growth at the desired stoichiometric composition in the deposited compound material, the ideal gas flow ratio of inert and reactive gas needs to be determined. Furthermore, in reactive sputtering processes, hysteretic

behavior in the target voltage due the free radicals of the reactive gas reacting with both the ejected target particles as well as the target itself need to be accounted for [161, 162, 184–186].

3.1.3 Superbowls sputtering cluster

The UHV Sputter Utensil Performing Everything Required for Best, Optimized, World Leading Samples (Superbowls) by *Bestec* enables to fabricate complex multilayer heterostructures made from both ferromagnetic and superconducting materials. Here, the spatial separation of superconducting and ferromagnetic target materials in the SP2- and SP4-chamber allows to minimize cross-contamination of the targets. The Superbowls deposition cluster is depicted in Fig. 3.2(a). For superconductor/ferromagnet-heterostructures with clean interfaces, an in-situ transfer of the sample from one chamber to the other via the Loadlock is possible. The SP2 chamber contains two 3"-magnetrons and one 2"-magnetron. Two magnetrons can be tilted into a confocal configuration to enable the simultaneous deposition from up to three targets. To clean samples before deposition, the SP2-chamber also contains an Ar-ion milling source. The SP4 chamber consists of eight tillable 2"-magnetrons, which are aligned in two confocal deposition clusters allowing to deposit an alloy comprising of up to four materials and can be operated both with a dc and a rf power source. Both chambers have a high purity Argon- and a Nitrogen-gas inlet to enable reactive sputtering deposition.

3.1.4 Ultradisk sputtering system

Besides the Superbowls sputtering cluster, the second UHV sputtering system used in this work is the Unlimited Legendary Tool for Reliable Achievements in the Deposition of Integrated Superconducting Komponenten (Ultradisk) by *Mantis* schematically illustrated in Fig. 3.2(b). Intended for the deposition of superconducting materials on areas of up to 4" in diameter for wafer-size superconducting quantum circuits, this deposition chamber comprises of six clusters with a total of eleven magnetrons, which can be operated both with a dc and a rf power source. The clusters one, three and five each contain one 4"-inch target, whereas the clusters two four and six allow for a tilted deposition to enable material alloying. Like the Superbowls system, the Ultradisk is equipped with an Ar ion milling gun for substrate cleaning as well as gas inlets for both argon and nitrogen gas for reactive sputtering.

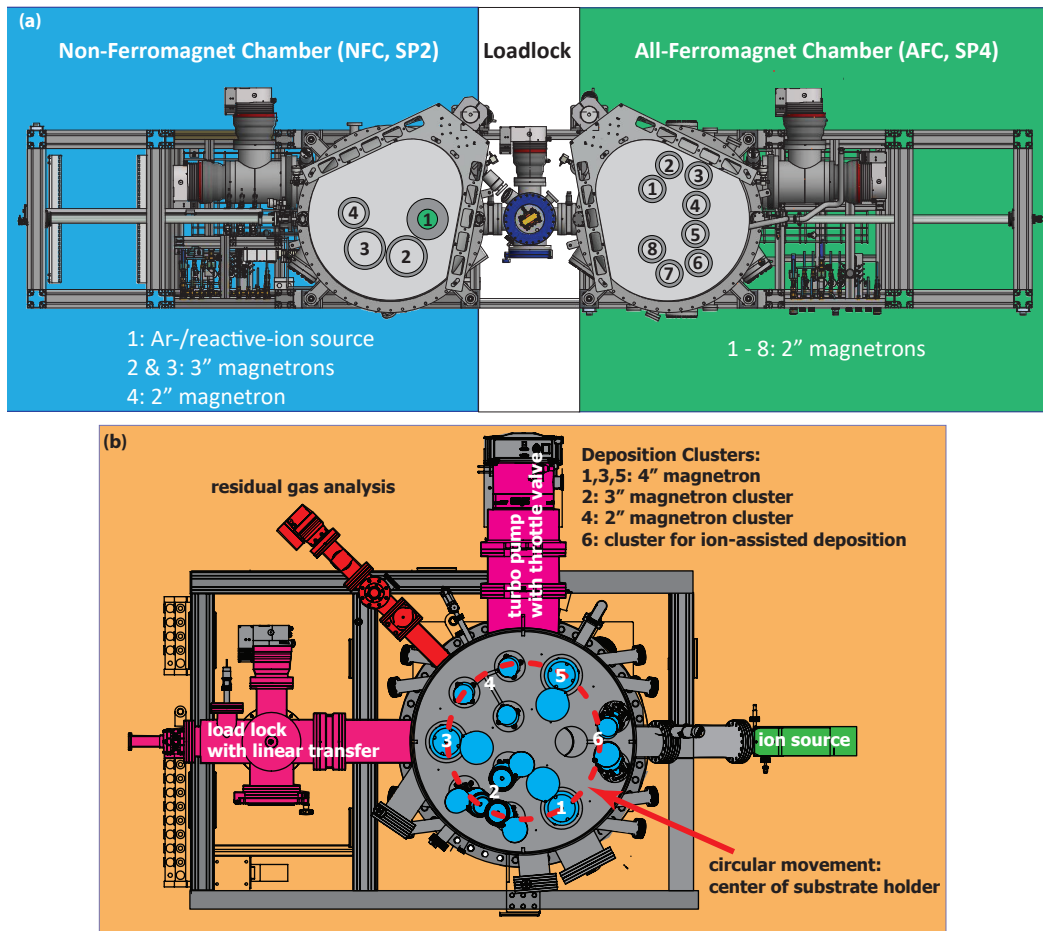


Fig. 3.2. – Sketch of the Superbowls (a) and Ultradisk (b) sputtering systems. Adapted from Refs. [185](a) and [186](b).

3.1.5 Advantages and disadvantages of the Superbowls and Ultradisk sputtering systems

Depending on the task at hand, both sputtering systems have their unique strengths and weaknesses. Hence, they were used for the different topics discussed in this thesis. The Superbowls cluster is optimally suited for the in-situ deposition of multilayer structures of both superconducting and ferromagnetic materials and was hence used for the deposition of the SC/FM-heterostructures in Ch. 5. On the other hand, the ability to fabricate many samples in a single deposition run by using a 4"-target and the absence of ferromagnetic impurities render the Ultradisk advantageous for the fabrication of high quality NbTiN thin films for superconducting resonators in Sec. 6. Finally for the study of magnon-phonon coupling in Ch. 7 the require magnetic thin films were deposited in the Superbowls system. A comprehensive overview of the main advantages and disadvantages of the two sputtering systems is given in Tab. 3.1.

	Superbowls	Ultradisk
Advantages:	-Larger deposition rates due to lower d_{depo} -Growth of Superconductor/-Ferromagnet heterostructures possible	-No FM contaminants -Fabrication of many samples in a single deposition run
Disadvantages:	-Potential FM contaminants	-No FM materials

Tab. 3.1. – Advantages and disadvantages of the Superbowl- and Ultradisk sputtering systems.

EBL process parameters	
resist	CSAR 6200.18
spin coating	8000 rpm, 1 min
bakeout	150°C, 1 min
base dose	2.2 C m ⁻²
post-bakeout	130°C, 1 min
developer	AR 600-546
development time	60 sec
RIE process parameters	
etching gas ratio	20 SF ₆ /7.2 Ar
rf power	100 W
gas pressure	2 × 10 ⁻² mbar
etching time	2 × 65 s
wait time	7 min in an Ar-atmosphere
Resist removal	
remover	AR 600-71
removal time	2 min

Tab. 3.2. – Summary of the EBL process-, RIE- and resist removal parameters for the fabrication of superconducting NbTiN resonators grown on Si substrates.

3.2 Sample patterning techniques

The magnon-photon coupling experiments in Ch. 5 require NbTiN thin films grown on Si substrates, which are patterned into superconducting resonators via electron beam lithography (EBL), subsequent reactive ion etching (RIE) and finally the removal of the resist layer. The resist processing parameters for these process steps are listed in Tab. 3.2.

In the following, we will detail the procedure for each step:

- **EBL process:**

The NbTiN thin film samples are first cleaned in acetone and isopropanol (IPA) in an ultrasonic bath. Afterwards, they are spin coated with a resist layer and baked on a hotplate to reduce the concentration of solvent in the

resist mask. The resist exposure is performed with the *NanoBeam nB5 system* from *NanoBeam Ltd.*, which is operated at a beam voltage of 80 kV using the lowest available beam current of $\simeq 2.2$ nA to obtain the best possible feature accuracy. Thereafter, a hard bake is performed to improve the durability of the resist for the reactive ion etching process. As a final step, we develop the resist in the suitable chemical solution. We use a positive resist and hence the exposed areas of the resist are removed by the developer, while the the unexposed areas remain almost unaffected. After the desired time, the developing reaction is stopped by rinsing the sample twice in IPA. The desired resonator layout has hereby been transferred to the resist layer.

- **RIE process:**

To remove the NbTiN from the exposed areas of the patterned sample, we perform a RIE process using a *Plasmalab 80 Plus* system from *Oxford Instruments* with a reactive plasma of a mixture of SF₆ and Ar gas. The etching process is split into two identical etching steps to avoid overheating of the sample and the crosslinking of the resist layer. Between the two etching steps, the sample is cooled in a pure Ar-atmosphere.

- **Resist removal:**

Finally, after etching the NbTiN from the exposed areas, the protective resist layer is removed in the ultrasonic bath using a suitable remover chemical. Like the resist development step, the removal process is stopped by rinsing the sample twice in IPA.

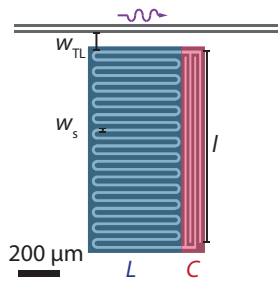


Fig. 3.3. – Illustration of the superconducting resonator layout used in this thesis. Adapted from Ref. [70].

The resonator layout used in this work is shown in Fig. 3.3. NbTiN thin films with a layer thickness of $d = 150$ nm are grown on Si substrates using reactive dc magnetron sputtering in a mixed Ar/N₂-atmosphere with a gas flow ratio of 36.2/3.8, a deposition temperature of $T_{\text{depo}} = 500$ °C, a pressure of $p_{\text{depo}} = 5$ μbar, and a deposition power of $P = 95$ W using a 4" Nb₇₀Ti₃₀ target. These thin films are then patterned into capacitively shunted planar meander-type resonators consisting of an interdigitated finger capacitor with capacitance C (red) shunting

a meandering inductor with inductance L (blue). The individual fingers have a length of $l = 720$ μm and a width of $w_s = 15$ μm. These dimensions are the result of a resonator characterization series in Ref. [186], where the geometry of the fabricated resonators was varied. The investigated chip layout includes a microwave transmission line patterned at a distance $w_{\text{TL}} = 40$ μm from all resonators, which is coupled to the multiple lumped element resonators (LER)

each with a different capacitance C to shift their resonance frequencies f_r . This configuration allows for a multiplexed readout scheme of the resonator quality factors Q .

3.3 Experimental procedure

The main experimental techniques performed in this work are broadband ferromagnetic resonance spectroscopy and the performance characterization of planar superconducting resonators. The details of these techniques are outlined in the following.

3.3.1 Cryogenic ferromagnetic resonance spectroscopy

The general experimental setup for cryogenic broadband ferromagnetic resonance spectroscopy (bbFMR) consists of three main components: A superconducting magnet cryostat, a vector network analyzer (VNA) and a coplanar waveguide (CPW). A schematic illustration of the experimental setup is shown in Fig. 3.4(a). The sample is placed face-down on a coplanar waveguide (CPW) on a copper holder at the end of a RF measurement dipstick. Both ends of the CPW are attached to microwave cables in the dipstick which are in turn connected to a broadband microwave source, in this case a vector network analyzer (VNA) [see Fig. 3.4(b)]. Additional DC wires for a temperature sensor and a resistive heater allow to control the sample temperature. The dipstick is then placed in the variable temperature insert (VTI) of a superconducting magnet cryostat as illustrated in Fig. 3.4(a). The liquid helium cryostat utilizes the flow of liquid helium through an adjustable needle valve to cool the sample space in the pumped VTI enabling temperatures in the range ($2\text{ K} \leq T \leq 300\text{ K}$). Three different superconducting magnet cryostat have been used for the experiments performed in this thesis (the magnetic field geometry is defined with respect to the coordinate system given in Fig. 3.4(b)):

1. The **Chaos** cryostat, a 3D-vector magnet consisting of three superconducting Helmholtz coils reaching magnetic field strengths of up to $\mu_0 H_{\text{ext}} = 2.5\text{ T}$ in the b - c -plane and up to $\mu_0 H_{\text{ext}} = 6\text{ T}$ in the a -direction. This cryostat was used for the BBFMR-experiments in chapters 4 and 5.
2. The **Moria** cryostat, a superconducting split coil with a field strength of up to $\mu_0 H_{\text{ext}} = 7\text{ T}$ with the possibility to rotate the sample in the b - c -plane via an electronic stepper motor. Due to its capability to apply large magnetic fields in the vertical direction c , it was used to characterize the magnetoelastic coupling of CoFe thin films to bulk acoustic resonances in the substrate crystal in Ch. 7.

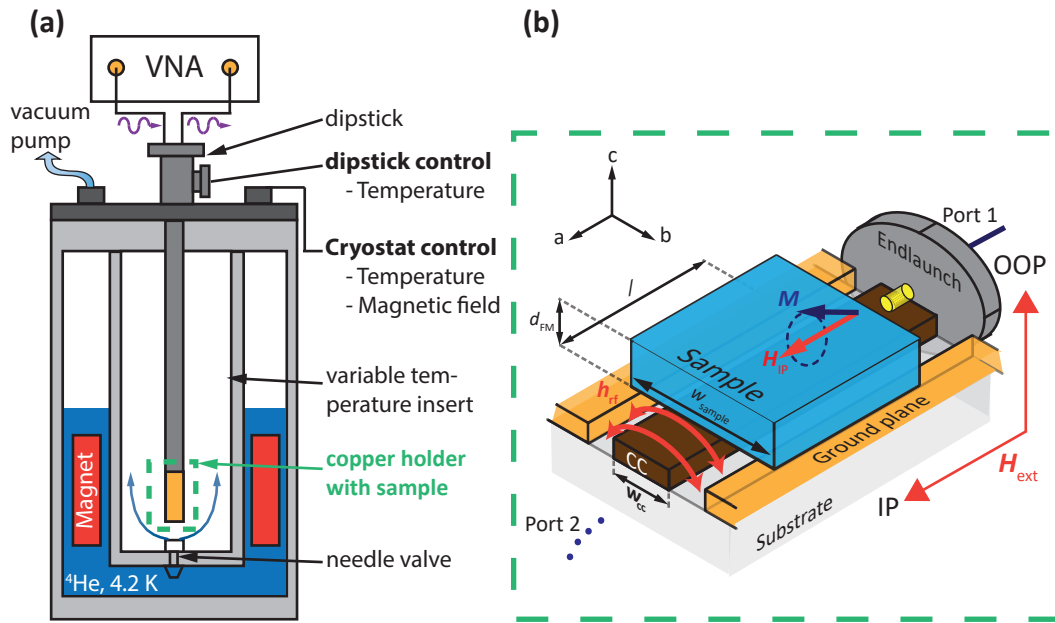


Fig. 3.4. – (a) Schematic illustration of the measurement setup for BBFMR at cryogenic temperatures. The dipstick is inserted into the variable temperature insert (VTI), where the sample temperature can be varied between 2 K and 300 K. The external magnetic field H_{ext} is created by superconducting (vector) magnets inside the helium tank. Adapted from Ref. [187]. (b) Sample holder mounted at the end of the dipstick. The sample is placed face-down on a CPW, which is in turn connected to the ports of a vector network analyzer via microwave cables attached to the endlaunch connectors. A microwave signal generated by the VNA is coupled into the center conductor, where it induces an oscillating magnetic field h_{rf} , which drives the magnetization within the sample. Adapted from Ref. [120].

3. The **17T** cryostat, a superconducting solenoid capable of large field strengths of up to $\mu_0 H = 17\text{ T}$ along the a -direction. This setup has been primarily used for the characterization of superconducting resonators in Ch. 5.

In this thesis, the magnetization dynamics of our hybrid thin film devices are characterized by performing broadband ferromagnetic resonance spectroscopy, which allows to study magnetization dynamics of thin film samples $> 1\text{ nm}$ over a large bandwidth of frequencies $\simeq 50\text{ GHz}$ [82]. Here, the thin film sample is placed face-down on a CPW as illustrated in Fig. 3.4(b). The electromagnetic wave propagates along the CPW. Due to the interaction of the associated rf magnetic field with the sample placed on top of the CPW, a frequency-dependent change of the transmission and reflection coefficient of the CPW is induced, which can be measured by a VNA. By measuring the complex scattering parameters S_{ij} ($i, j=1,2$) as a function of frequency, all parameters determining the FMR signal can be deduced. A vector network analyzer is used as the broadband microwave source and detector. In our experiments, the used *Keysight N5225B* VNA is capable to generate and detect microwave signals in the range ($10\text{ MHz} \leq f \leq 50\text{ GHz}$). Additionally, the usage of VNA's allows for the phase sensitive study of the FMR

and thereby to obtain information on field- and damping-like spin-orbit torques (SOT) by employing the inductive analysis technique outlined in Ref. [84] as done in Ch. 5. In our experiments, the ferromagnetic resonance in the magnetic layer is excited by a microwave signal generated at port 1 of the VNA and coupled into the CC of the CPW with a width of $w_{cc} \simeq 60 \mu\text{m}$ via microwave cables mounted on the dipstick, which are attached to the endlaunch connectors on the sample holder. The thereby generated dynamic magnetic driving field \mathbf{h}_{rf} in the b - c -plane can be approximated by modeling the CC as a rectangular slab using the Karlqvist equations [188]

$$\begin{aligned} h_b(b, c, t) &= \frac{1}{\pi} h_0(t) \left[\arctan \left(\frac{b + \frac{w_{cc}}{2}}{c} \right) - \arctan \left(\frac{b - \frac{w_{cc}}{2}}{c} \right) \right] \\ h_c(b, c, t) &= \frac{1}{2\pi} h_0(t) \ln \left(\frac{(b + \frac{w_{cc}}{2})^2 + c^2}{(b - \frac{w_{cc}}{2})^2 + c^2} \right). \end{aligned} \quad (3.1)$$

Here $h_0(t) = I(t)/2w_{cc}$ is the dynamics field amplitude at the center of the CC ($b = c = 0$). The generated oscillating magnetic field drives the precession of the sample's magnetization \mathbf{M} . In resonance due to Faraday's law, \mathbf{M} induces a dynamic voltage V_{ind} driving currents, which oppose the microwave driving currents. This process leads to the absorption of microwave power, which is detected in the transmitting signal entering port 2 of the VNA. The voltage induced in the CPW is given by

$$V_{\text{ind}} = -\frac{\partial \Phi(t)}{\partial t}, \quad (3.2)$$

where the dynamic magnetic flux $\Phi(t)$ is induced from the precessing magnetization $\mathbf{M}(t)$ of our thin film sample driven by the dynamic driving field $\mathbf{h}_{\text{rf}}(t)$. Hence, an analytic expression for $\Phi(t)$ can be obtained by using Eq. (3.1), the definition $\mathbf{M}(t) = \hat{\chi}_{\text{p}} \mathbf{h}_{\text{rf}}(t)$ from Eq. (2.19) and integrating over the sample volume on top of the CC V' [92]

$$\begin{aligned} \Phi(t) &= \frac{\mu_0}{I(t)} \iiint_{V'} \mathbf{h}_{\text{rf}}(b, c, t) \hat{\chi}_{\text{p}} \mathbf{h}_{\text{rf}}(b, c, t) \text{d}a \text{d}b \text{d}c \\ &= \frac{\mu_0 l}{I(t)} \iint_{A'} h_b^2(b, c, t) \chi_{bb} (1 - \delta_{bH}) + h_c^2(b, c, t) \chi_{cc} (1 - \delta_{cH}) \text{d}b \text{d}c, \end{aligned} \quad (3.3)$$

where l is the sample length on top of the CC and A' the sample area above it. We account for the different measurement geometries with the Kronecker delta terms $\delta_{iH} = 1$ for $\mathbf{i} \parallel \mathbf{H}_{\text{ext}}$ ($\mathbf{i} = \mathbf{a}, \mathbf{b}, \mathbf{c}$) and $\delta_{iH} = 0$ for $\mathbf{i} \perp \mathbf{H}_{\text{ext}}$ (i.e. only the driving field components, which are perpendicular to \mathbf{H}_{ext} can drive the magnetization dynamics and contribute to the dynamic flux). Note, that in Eq. (3.3) we can neglect the odd term in h_b due to symmetry. In the thin film limit $d_{\text{FM}} \ll w_{cc}$, we can simplify Eq. (3.3) by using $h_{b,c}(b, c) = h_{b,c}(b, 0)$. Furthermore, we assume that the width w_{sample} of the sample is large compared to that of the CC ($w_{\text{sample}} \gg w_{cc}$)

and integrate from $-\infty$ to ∞ in the b -direction. Under these assumptions, the dynamic flux $\Phi(t)$ simplifies to [92]

$$\Phi(t) = \mu_0 I(t) \frac{ld_{\text{FM}}}{4w_{\text{cc}}} [\chi_{bb}(1 - \delta_{bH}) + \chi_{cc}(1 - \delta_{cH})]. \quad (3.4)$$

The magnetic flux Φ is related to the inductance $L_0 = \Phi(t)/I(t)$, which quantifies the mutual inductive coupling between sample and CPW¹. It is given by

$$L_0 = \mu_0 \frac{ld_{\text{FM}}}{4w_{\text{cc}}} [\chi_{bb}(1 - \delta_{bH}) + \chi_{cc}(1 - \delta_{cH})]. \quad (3.5)$$

Having quantified the inductive coupling between thin film sample and CPW, we now describe, how to detect L in our bbFMR experiments using a VNA. The complex transmission parameter S_{21} recorded by port 2 of the VNA is defined as

$$S_{21} = \frac{V_2}{V_1} = \frac{|V_2|}{|V_1|} e^{i(\phi_2 - \phi_1)}, \quad (3.6)$$

where V_i are the measured complex voltages with magnitude $|V_i|$ and phase ϕ_i of the respective port i . It consists of the background S_{21}^0 caused by microwave- and cable-losses from the setup, which are modeled as a complex linear function of the form $S_{21}^0 = A + B \cdot H_{\text{ext}}$, where A and B are complex constants, to account for the magnetic-field dependence of these losses and a change of transmission ΔS_{21} caused by the FMR of the sample in resonance.

$$\Delta S_{21} = \frac{S_{21} - S_{21}^0}{S_{21}}, \quad (3.7)$$

The inductive coupling between sample and CPW gives rise to contribution $i2\pi f L_0$ in series to the impedance $Z_0 = 50 \Omega$ of the empty CPW. In a voltage-divider model, the net change in transmission of the loaded CPW can be expressed as [189]

$$\Delta S_{21} = \frac{1}{2} \frac{-i2\pi f L_0}{Z_0 - i2\pi f L_0} \approx -\frac{i\pi f L_0}{Z_0}, \quad (3.8)$$

under the assumption $2\pi f L_0 \ll Z_0$, which is valid in our case ($f \simeq 50$ GHz and $L_0 \simeq 10^{-15}$ H). In Eq. (3.8), the factor $1/2$ is required, as the complex voltage V_2 is measured between CPW and port 2 and not between port 1 and port 2.

¹In literature, a mutual inductance is commonly denoted with the variable M . However, to avoid confusion with the sample magnetization and to be consistent with the formalism outlined in Refs. [83,84], we denote the mutual inductive coupling between sample and CPW with L_0 .

Using Eqs. (3.8) and (3.7), we obtain a general expression for $S_{21}(f, H_{\text{ext}})$

$$\begin{aligned}
S_{21}(f, H_{\text{ext}}) &= S_{21}^0(f)(1 + \Delta S_{21}) = S_{21}^0(f) \cdot \left(1 - e^{i\phi} \frac{i\pi f L_0}{Z_0}\right) \\
&= S_{21}^0(f) \left(1 - i \frac{\pi f \mu_0 l d_{\text{FM}}}{4Z_0 w_{\text{cc}}} e^{i\phi} [\chi_{bb}(f, H_{\text{ext}})(1 - \delta_{bH}) + \chi_{cc}(f, H_{\text{ext}})(1 - \delta_{cH})]\right) \\
&= S_{21}^0(f) - iAe^{i\phi} [\chi_{bb}(f, H_{\text{ext}})(1 - \delta_{bH}) + \chi_{cc}(f, H_{\text{ext}})(1 - \delta_{cH})].
\end{aligned} \tag{3.9}$$

Here, we have introduced the constant $A = \pi f \mu_0 l d_{\text{FM}} / (4Z_0 w_{\text{cc}})$, which comprises all the geometrical and setup parameters and a phase shift in the microwave signal by ϕ , that accounts for the phase change of the signal when traversing the microwave circuit

Depending on the orientation of the CC along \mathbf{a} with respect to the external magnetic field \mathbf{H}_{ext} , we can differentiate between three measurement geometries for bbFMR:

- $\mathbf{H}_{\text{ext}} \parallel \mathbf{a}$ (ip):

In the case $\mathbf{H}_{\text{ext}} \parallel \mathbf{a}$, the coordinate system in Fig. 3.4 can be mapped onto the one in the schematic depiction of the FMR in Fig. 2.2 via $\mathbf{a} \rightarrow \mathbf{z}$, $\mathbf{b} \rightarrow \mathbf{y}$ and $\mathbf{c} \rightarrow \mathbf{x}$. Here, using the generalized expression for the components of $\hat{\chi}_{\text{p}}$ from Eq. (2.30), $S_{21}(f, H_{\text{ext}})$ takes the following form

$$\begin{aligned}
S_{21}(f, H_{\text{ext}}) &= S_{21}^0(f) - iAe^{i\phi} [\chi_{yy}(f, H_{\text{ext}}) + \chi_{xx}(f, H_{\text{ext}})] \\
&= S_{21}^0(f) + Ae^{i\phi} \chi_{yx}(f, H_{\text{ext}}) \left[\epsilon + \frac{1}{\epsilon} \right].
\end{aligned} \tag{3.10}$$

As apparent from Eq. (3.10), both driving field components $h_{\text{rf},b}$ and $h_{\text{rf},c}$ contribute to the magnetization dynamics giving rise to an enhanced signal magnitude in ΔS_{21} , which renders this ip-configuration of particular interest to characterize magnetic thin films.

- $\mathbf{H}_{\text{ext}} \parallel \mathbf{b}$ (ip):

For $\mathbf{H}_{\text{ext}} \parallel \mathbf{b}$, the coordinate system mapping between our measurement and FMR toy model is $\mathbf{a} \rightarrow \mathbf{x}$, $\mathbf{b} \rightarrow \mathbf{z}$ and $\mathbf{c} \rightarrow \mathbf{y}$. Consequently, Eq. (3.9) can be simplified to

$$\begin{aligned}
S_{21}(f, H_{\text{ext}}) &= S_{21}^0(f) - iAe^{i\phi} \chi_{yy}(f, H_{\text{ext}}) \\
&= S_{21}^0(f) + Ae^{i\phi} \chi_{yx}(f, H_{\text{ext}}) \frac{1}{\epsilon}.
\end{aligned} \tag{3.11}$$

We note, that this ip-configuration is undesirable for the characterization of magnetic thin films with a high M_s as the large ellipticity ($\epsilon \gg 1$, $f \gg 0$)

will strongly reduce the detected signal magnitude in the VNA [note, that in Eq. (2.31), $\epsilon > 1$ for $N_{xx} = N_{zz} = 0$, $N_{yy} = 1$ (thin film limit) and $H_u \ll M_s$].

- $\mathbf{H}_{\text{ext}} \parallel \mathbf{c}$ (oop):

Finally, for the oop-configuration, we can map the coordinate systems of our measurement setup and FMR toy model via $\mathbf{a} \rightarrow \mathbf{x}$, $\mathbf{b} \rightarrow \mathbf{y}$ and $\mathbf{c} \rightarrow \mathbf{z}$. Consequently, Eq. (3.12) takes the form

$$\begin{aligned} S_{21}(f, H_{\text{ext}}) &= S_{21}^0(f) - iAe^{i\phi} \chi_{xx}(f, H_{\text{ext}}) \\ &= S_{21}^0(f) + Ae^{i\phi} \chi_{yx}(f, H_{\text{ext}})\epsilon. \end{aligned} \quad (3.12)$$

Note, that in general in our experiments, we can assume a circular magnetization precession with $\epsilon = 1$ in our thin films [note, that in Eq. (2.31), $\epsilon \approx 1$ for $N_{xx} = N_{yy} = 0$, $N_{zz} = 1$ (thin film limit) and $H_u \ll M_s$].

The magnetization dynamics of our hybrid thin films is hence studied by recording S_{21} in magnetic resonance for a broad range of frequencies and fitting it to either Eq. (3.10), (3.11) or (3.12) depending on the direction of the applied external field \mathbf{H}_{ext} and thereby extracting the resonance field $H_{\text{res}}(f)$ and linewidth $\Delta H(f)$, which are in turn fitted to Eq. (2.26) or (2.24) depending on the measurement geometry and Eq. (2.28), respectively. There are two different experimental approaches to conduct bbFMR: The "field-swept"-mode, where a fixed VNA-frequency f is applied [continuous wave mode (CW)] and S_{21} is recorded with a fine magnetic field resolution, while sweeping H_{ext} through H_{res} or in the "frequency-swept"-mode by recording S_{21} with a fine frequency resolution around f_{res} at a fixed H_{ext} . Unless otherwise stated, the experiments in this thesis are performed in the "field"-swept mode with a high resolution in H_{ext} rather than f , as for the low FMR signal magnitudes of magnetic thin films, a low IF-bandwidth [IFBW] of the VNA is required to reliably detect the FMR, meaning a "frequency-swept"-mode with a high resolution in frequency would be too time-consuming. Moreover, for most FMR investigations only a very rough frequency resolution over a broad frequency range is needed.

3.3.2 Characterization of superconducting resonators

The superconducting lumped element resonators fabricated in this work can be viewed as a LC -circuit with capacitance C and inductance L as shown in the electrical schematic in Fig. 3.5(a) and the layout shown in Fig. 3.3. The resonance frequency is defined as [190, 191]

$$f_r = \frac{1}{2\pi\sqrt{LC}}. \quad (3.13)$$

In our used layout (see Fig. 3.3), L and C are chosen corresponding to a resonance frequency of $f_r \simeq 5$ GHz.

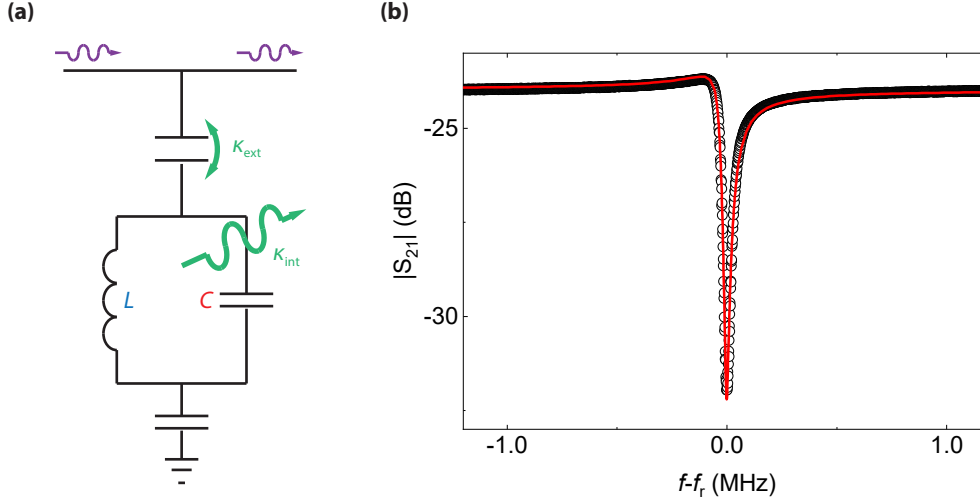


Fig. 3.5. – (a) Electrical schematic of a lumped element resonator. The LC circuit is capacitively coupled to the microwave feedline. The loss rates κ_{ext} and κ_{int} quantify the external and internal loss rates of the resonator. Adapted from Ref. [190]. Exemplary resonance feature in the microwave transmission spectrum $|S_{21}(f)|$ of a single resonator fabricated from NbTiN grown on Si and measured at $T = 2.2$ K at a microwave power corresponding to the high power regime. The red continuous line indicates a fit to the data using Eq. (3.18).

The performance of a resonator is characterized by the quality factor Q , which is defined as $2\pi \times$ the ratio of the energy stored in the electromagnetic mode E_{tot} and the energy lost per cycle P_{loss}/ω_r given by the total loss rate κ_r of the resonator [190, 191]. Hence it can be expressed as²

$$Q = \frac{E_{\text{tot}}}{P_{\text{loss}}/\omega_r} = \frac{\pi f_r}{\kappa_r} = \frac{\omega_r}{2\kappa_r}. \quad (3.14)$$

As is apparent from the electrical schematic in Fig. 3.3, the total loss rate κ_r is the sum of the external losses κ_{ext} from the environment (i.e. the microwave strip line) and the internal losses κ_{int} induced by quasiparticle excitations [192, 193], the coupling of the resonator to two-level systems (TLS) [194–196] as well as from resistive, dielectric or radiative losses [197]

$$\kappa_r = \kappa_{\text{ext}} + \kappa_{\text{int}}. \quad (3.15)$$

κ_{ext} and κ_{int} are related to the internal and external quality factor via

$$Q_{\text{int}} = \frac{\pi f_r}{\kappa_{\text{int}}}, \quad Q_{\text{ext}} = \frac{\pi f_r}{\kappa_{\text{ext}}}. \quad (3.16)$$

²Noe, that we here define κ_r as half width at half maximum (HWHM) of the resonator. Hence, we define $Q = \frac{\omega_r}{2\kappa_r}$. In literature, κ_r is sometimes also defined as the full width at half maximum (FWHM) resulting in the definition $Q = \frac{\omega_r}{\kappa_r}$.

The total quality factor Q can hence be rewritten as

$$Q = \left(\frac{1}{Q_{\text{ext}}} + \frac{1}{Q_{\text{int}}} \right)^{-1}. \quad (3.17)$$

The microwave resonators fabricated in this work are typically operated in the critically coupled regime ($Q_{\text{int}} \simeq Q_{\text{ext}}$) [197] to allow for the characterization of our resonator performance using the ‘circle fit method’ [198]. To this end, the finalized chips are mounted on a gold plated oxygen free high thermal conductivity copper sample box and inserted into a variable temperature insert in a liquid helium cryostat or into the mK sample stage of a He₃/He₄ dilution fridge. The two ends of the central feed line are then connected to the two ports of a VNA. We then record the complex transmission parameter $S_{21}(f)$ close to their respective resonance frequencies f_r . The superconducting resonators are characterized in terms of their quality factors by fitting the recorded $S_{21}(f)$ -spectra with the ‘circle fit method’ [198] using

$$S_{21}(f) = \underbrace{ae^{i\beta}e^{-2\pi if\tau}}_{\text{environment}} \underbrace{\left[1 - \frac{(Q/|Q_{\text{ext}}|)e^{i\phi}}{1 + 2iQ(f/f_r - 1)} \right]}_{\text{ideal resonator}}. \quad (3.18)$$

The prefactors in front of the square brackets account for the attenuation and phase shifts attributed to the microwave circuit. Specifically, the attenuation is given by the constant a , the phase shift by β , and the electrical delay due to the finite length of the wiring by τ . The expression within the square brackets describes the response of the resonator itself, including an additional correction $e^{i\phi}$ to account for potential asymmetries induced by spurious input- and output impedance or standing waves. We note that expanding Q_{ext} to the complex plane allows one to account for differences in impedance between the resonator and the feedline. In addition, f and f_r denote the VNA driving frequency and resonator resonance frequency, respectively.

Exemplary raw data for $|S_{21}(f)|$ of a NbTiN resonator in resonance is shown in Fig. 3.5(b). The resonator is fabricated from NbTiN deposited on a highly resistive Si substrate and is measured at $T = 2.2$ K at a microwave power corresponding to the high power regime. The red continuous line indicates a fit to the data via the ‘circle fit method’ using Eq. (3.18). We extract a resonance frequency of $f_r = 4.924$ GHz as well as the quality factors $Q = (84.3 \pm 0.6) \cdot 10^3$, $Q_{\text{int}} = (207.8 \pm 3.8) \cdot 10^3$ and $Q_{\text{ext}} = (141.9 \pm 0.1) \cdot 10^3$.

Two principle setups have been used for the characterization of our superconducting microwave resonators:

- For the statistical analysis of our resonators as well as for the experiments performed at elevated temperatures ($2.2 \text{ K} \leq T \leq 13 \text{ K}$) and external magnetic fields ($0 \text{ mT} \leq \mu_0 H_{\text{ext}} \leq 500 \text{ mT}$), our mounted resonators were installed

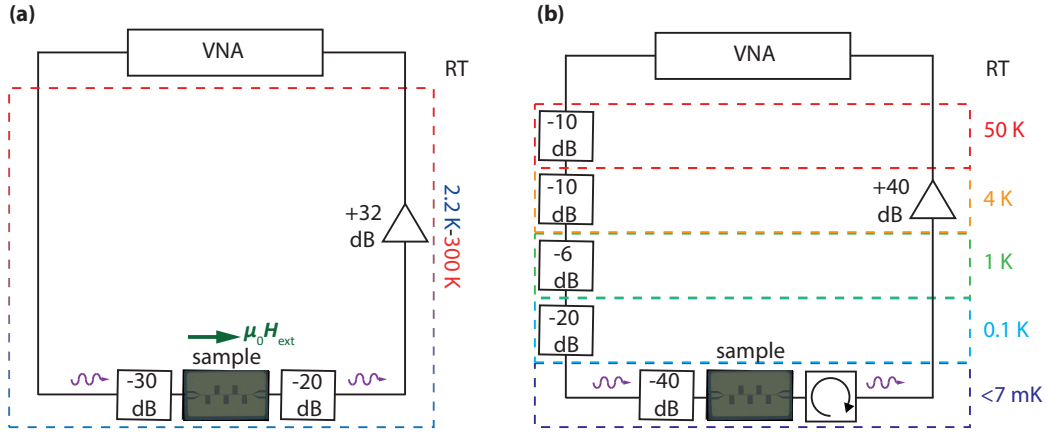


Fig. 3.6. – (a) Schematic of the microwave circuit of the measurement setup. The green arrow indicates the direction of the applied in-plane magnetic field $\mu_0 H_{\text{ext}}$. (b) Microwave setup for experiments at mK temperatures.

in the VTI of a liquid helium magnet cryostat (see Sec. 3.3.1). Fig. 3.6(a) schematically depicts the microwave transmission setup employed for these experiments. To reduce room temperature thermal noise, the input signal is attenuated by 30 dB close to the SMA connector of the sample box. At the output connector, we use a 20 dB attenuator to suppress the formation of standing waves as well as a cryogenic HEMT amplifier (gain: +32 dB).

- For the mK experiments, we used a Bluefors LD-400 dry dilution refrigerator. The used microwave circuitry is depicted in Fig. 3.6(b). To suppress room temperature noise photons from reaching the sample under investigation, the incoming signal is attenuated by a set of attenuators on the various temperature stages. On the output side, we use a cryogenic circulator mounted on the mK stage to suppress the formation of standing waves. The outgoing signal is then amplified by +40 dB by a cryogenic HEMT amplifier mounted at the 4 K stage. For this setup, we measure ≈ 10 dB cable losses from the microwave cables at $f \simeq 5$ GHz.

Slowly relaxing impurities in maghemite thin films

Magnetic insulators, where magnons carry spin information, are the basis for the implementation of logic circuits using angular momentum transport [199] in the emerging fields of magnonics [25, 26], spin-caloritronics [200], and spin-orbitronics [201]. The most commonly used material platform in all of these research fields is yttrium iron garnet ($\text{Y}_3\text{Fe}_5\text{O}_{12}$, YIG), particularly because its low Gilbert damping $\alpha \simeq 10^{-5}$ [141, 202, 203] is the key parameter for the implementation of spin-wave-based devices, as it allows for the generation of spin waves with propagation lengths up to the millimeter regime and at frequencies ranging from the GHz to the THz regime [204, 205]. However, apart from its exceptional damping properties, YIG has major drawbacks regarding its integration into more complex heterogeneous magnonic devices as it requires high deposition and annealing temperatures and paramagnetic gadolinium gallium garnet ($\text{Gd}_3\text{Ga}_5\text{O}_{12}$) substrates for its optimal growth, rendering alternative magnetic insulators with low Gilbert damping desirable. To this end, an emergent material platform are ferrites with a spinel structure such as nickel ferrite (NFO, NiFe_2O_4) [206], nickel zinc aluminum ferrite (NiZnAlFO , $\text{Ni}_{0.65}\text{Zn}_{0.35}\text{Al}_{0.8}\text{Fe}_{1.2}\text{O}_4$) [207], magnesium aluminum ferrite (MAFO, $\text{MgAl}_{0.5}\text{Fe}_{1.5}\text{O}_4$) [208] and aluminum-doped ferrites (FAO, $\gamma\text{-Fe}_{2-x}\text{Al}_x\text{O}_3$) [209]. They are both compatible with conventional substrate materials such as MgO and exhibit a low Gilbert damping $\alpha \simeq 10^{-3}$ in the bulk limit [206, 208]. The desire for alternative insulating magnetic materials to YIG has motivated us to characterize the room-temperature ferrimagnetic insulator, namely spinel-type ferrite $\gamma\text{-Fe}_2\text{O}_3$ (maghemite), in terms of its epitaxial growth as well as static and dynamic magnetic properties. The growth of high-quality $\gamma\text{-Fe}_2\text{O}_3$ thin films is challenging as this phase is metastable and tends to easily transform into antiferromagnetic hematite ($\alpha\text{-Fe}_2\text{O}_3$), which is the equilibrium phase above 350°C [210, 211]. To obtain pure $\gamma\text{-Fe}_2\text{O}_3$, we deposit our thin films in the presence of epitaxial strain on MgO substrates using pulsed laser deposition (PLD). We then confirm the good crystalline quality and coherently strained growth of our thin films by performing high-resolution x-ray diffraction (HR-XRD). Furthermore, we study the static magnetic properties of our samples via SQUID magnetometry. Finally, we investigate the dynamic magnetic properties of our thin film samples via cryogenic bbFMR (see Sec. 3.3.1). In these experiments, we detect a small negative effective magnetization M_{eff} , providing further evidence for the presence of a strain-induced perpendicular magnetic anisotropy in our samples. The presence of a sizable PMA at room-temperature renders $\gamma\text{-Fe}_2\text{O}_3$ particularly desirable for both spintronics applications [212, 213] and for

all-electrical magnon transport experiments [106, 199, 214, 215] as the PMA has been found to reduce non-viscous contributions to damping (see Sec. 2.2). Here, the thin film deposition via pulsed laser deposition (PLD) and characterization via HR-XRD have been done by Monika Scheufele in the course of her Master's thesis [216], whereas the author has performed the SQUID magnetometry and cryogenic bbFMR experiments as well as the data analysis procedure of the FMR data.

Regarding the temperature dependence of $M_{\text{eff}}(T)$, we observe a sign change from negative to positive values with decreasing temperature, which indicates a transition of the magnetic anisotropy in our maghemite thin films from an oop easy-axis to an in-plane (ip) easy-plane orientation. Furthermore, we also observe a non-linear behavior in the FMR linewidth $\Delta H(f)$ as a function of the microwave frequency f , which can be well interpreted in terms of the temperature-dependent magnetic relaxation process (see Sec. 2.3.3) induced by Fe^{2+} -impurities in our thin films.

This chapter is organized as follows: In Sec. 4.1, we discuss the crystalline structure of $\gamma\text{-Fe}_2\text{O}_3$. Thereafter we describe the growth and structural characterization of our thin films in Section 4.2. In Section 4.3 we then focus on the static and dynamic magnetic properties of our $\gamma\text{-Fe}_2\text{O}_3$ films before discussing the presence of the non-linear damping mechanisms present in our $\gamma\text{-Fe}_2\text{O}_3$ in Section 4.4. Finally, in Section 4.5 we summarize our key findings.

The $\gamma\text{-Fe}_2\text{O}_3$ thin films, which are investigated in this chapter, have been grown via pulsed laser deposition (PLD) and characterized via HR-XRD by Monika Scheufele in the course of her Master's thesis [216].

The main results presented in this chapter are published in M. Müller, M. Scheufele, J. Gückelhorn, L. Flacke, M. Weiler, H. Huebl, S. Geprägs, R. Gross, M. Althammer, *Reduced effective magnetization and damping by slowly relaxing impurities in strained $\gamma\text{-Fe}_2\text{O}_3$ thin films*, *Journal of Applied Physics* **132**, 233905 (2022) [67].

4.1 Physical properties of $\gamma\text{-Fe}_2\text{O}_3$

The physical properties of various iron oxide phases have been described in Refs. [95, 216]. Here, we briefly summarize the relevant magnetic properties of $\gamma\text{-Fe}_2\text{O}_3$ found in these references.

Depending on the degree of Fe vacancy disorder, $\gamma\text{-Fe}_2\text{O}_3$ can crystallize either into a cubic lattice or a tetragonal inverse spinel superstructure with $c \simeq 3a$ [217], where $a \simeq 0.833$ nm [218] is the ip lattice constant and c is the oop lattice constant. The crystal lattice of $\gamma\text{-Fe}_2\text{O}_3$ is shown in Fig. 4.1. The Fe^{3+} ions (green spheres in Fig. 4.1) are located on octahedral and tetrahedral sites and are surrounded by O^{2-} ions (blue spheres in Fig. 4.1) [216]. In the tetragonal state, Fe^{3+} vacancies (large bright green spheres in Fig. 4.1) show an ordered arrangement on one

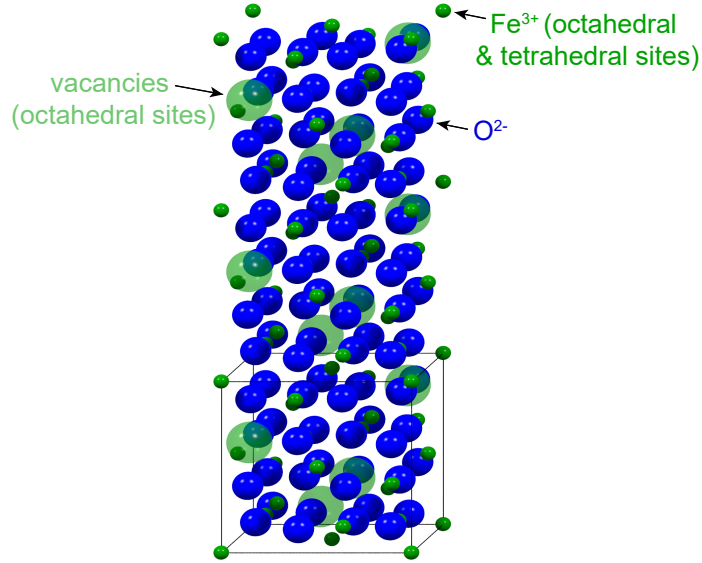


Fig. 4.1. – Tetragonal unit cell of $\gamma\text{-Fe}_2\text{O}_3$. Fe^{3+} ions are represented as green spheres, O^{2-} as blue spheres and vacancies by the larger green semitransparent spheres. The oop lattice constant c is three times the ip lattice constant a . In case of disordered vacancy sites, $\gamma\text{-Fe}_2\text{O}_3$ appears in a cubic structure (unit cell indicated by black lines). Taken from Ref. [216].

particular octahedral lattice site, whereas in the cubic state, they are randomly distributed on the octahedral sites in the crystal [219]. The unit cell of the cubic lattice comprises eight formula units of the form $\text{Fe}_A^{3+}(\text{Fe}_{5/3}^{3+}\square_{1/3})_B\text{O}_4^{2-}$, where \square denotes the vacancies, the index A the tetrahedral and the index B the octahedral sites [216, 220]. Therefore, the vacancy sites reduce the net positive charge per unit cell and thereby give rise to charge neutrality in $\gamma\text{-Fe}_2\text{O}_3$. The Fe^{3+} -ions with net spin quantum number $S = 5/2$ on the octahedral and tetrahedral lattice sites interact with each other and form two magnetic sublattices, which in turn couple in an antiparallel configuration. As more tetrahedral sites A than octahedral sites B are occupied by Fe^{3+} -ions, the resulting magnetic order in $\gamma\text{-Fe}_2\text{O}_3$ is ferrimagnetic with a Curie temperature of $T_c = 950\text{ K}$ [221] and an expected net magnetization of $\mu_0 M_s \simeq 0.5\text{ T}$ at room temperature [95, 222].

4.2 Thin film deposition and structural characterization

The $\gamma\text{-Fe}_2\text{O}_3$ thin films investigated in this study are grown via pulsed laser deposition on MgO (001) substrates at a deposition temperature of $T_{\text{depo}} = 320\text{ }^\circ\text{C}$, a pure oxygen pressure of $p_{\text{O}_2} = 25\text{ }\mu\text{bar}$, a laser fluence at the stoichiometric, polycrystalline $\alpha\text{-Fe}_2\text{O}_3$ target of $\rho_L = 2.5\text{ J/cm}^2$ and a laser pulse repetition frequency of $f = 2\text{ Hz}$ resulting in a growth rate of $r \simeq 0.3\text{ nm/s}$. Due to the lattice mismatch between the substrate and the thin film, the pseudomorphically grown $\gamma\text{-Fe}_2\text{O}_3$ thin films exhibit tensile strain within the film plane. In our

experiments, we study two maghemite thin films of different thickness (45.0 nm and 52.6 nm) but comparable static and dynamic magnetic properties. Since the larger layer thickness of the latter thin film allowed for a better signal-to-noise ratio in the cryogenic bbFMR experiments, we only present the dynamic magnetic properties of the thicker film in the main text and show those of the thinner film in the Appendix A. To determine the phase, in which our thin films are grown, we perform a wide range $2\theta - \omega$ x-ray diffraction scan on the 45.0 nm thick $\gamma\text{-Fe}_2\text{O}_3$ film. The resulting XRD intensity I as a function of the detector angle 2θ is plotted in Fig. 4.2(a). We observe reflection peaks in intensity from the spinel $\gamma\text{-Fe}_2\text{O}_3$

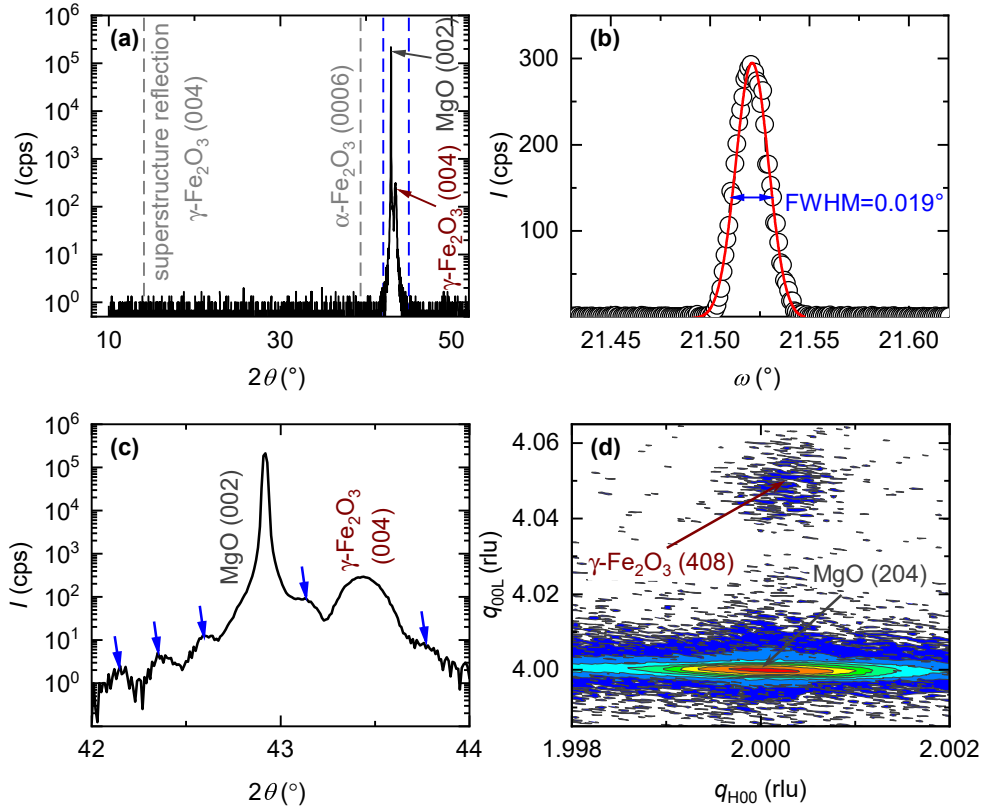


Fig. 4.2. – (a) Wide range $2\theta - \omega$ x-ray diffraction scan of the 45.0 nm thick $\gamma\text{-Fe}_2\text{O}_3$ film grown on a (001) oriented MgO substrate. We observe crystalline reflections from the spinel $\gamma\text{-Fe}_2\text{O}_3$ (004) structure as well as the (002)-reflection from MgO. No superstructure from the tetragonal phase of $\gamma\text{-Fe}_2\text{O}_3$ nor reflections from undesired iron oxide impurity phases such as hematite ($\alpha\text{-Fe}_2\text{O}_3$) are visible (gray dashed lines indicate their expected positions). The blue dashed lines indicate the 2θ range plotted in panel (c). (b) Rocking curve of the $\gamma\text{-Fe}_2\text{O}_3$ (004)-reflection. The red line indicates a Gaussian fit to the raw data. We extract a narrow full-width at half maximum (FWHM) of $\text{FWHM} = (0.0194 \pm 0.0002)^\circ$. (c) Zoom in on the overview $2\theta - \omega$ XRD scan in panel (a). Laue oscillations of the $\gamma\text{-Fe}_2\text{O}_3$ (004)-reflection are visible (blue arrows). (d) Reciprocal space mapping around the asymmetrical MgO (204) and $\gamma\text{-Fe}_2\text{O}_3$ (408) reflections. The units are given in reciprocal lattice units (rlu) with respect to the MgO substrate. From the thin film reflection at $q_{H00} = 1.99998$ rlu and $q_{00L} = 4.0463$ rlu, we determine an epitaxial strain of $\epsilon_{xx} = 1.1\%$ in the film plane and $\epsilon_{zz} = -0.05\%$ out of the film plane.

(004) phase as well as from the (002)-reflection of the MgO substrate. However, we

observe no superstructure reflection from the tetragonal phase of $\gamma\text{-Fe}_2\text{O}_3$ nor from additional iron oxide phases such as hematite [see gray dashed lines in Fig. 4.2(a)]. The blue dashed lines indicate the range of angles for the x-ray diffraction data plotted in Fig. 4.2(c). From Fig. 4.2(a), we infer that in our thin films the $\gamma\text{-Fe}_2\text{O}_3$ unit cell grows in the cubic phase on four MgO unit cells resulting in an expected lattice mismatch of $\epsilon = (2a_{\text{MgO}}^{\text{bulk}} - a_{\gamma\text{-Fe}_2\text{O}_3}^{\text{bulk}}) / 2a_{\text{MgO}}^{\text{bulk}} = 1.1\%$ using the bulk lattice constants $a_{\gamma\text{-Fe}_2\text{O}_3}^{\text{bulk}} = 0.8332\text{ nm}$ [218] and $a_{\text{MgO}}^{\text{bulk}} = 0.4212\text{ nm}$ [223]. In Fig. 4.2(b), we show the extracted rocking curve of the $\gamma\text{-Fe}_2\text{O}_3(004)$ -reflection to a Gaussian fit and extract a full-width at half maximum (FWHM) of $\text{FWHM} = (0.0194 \pm 0.0002)^\circ$, which demonstrates a good crystalline growth. Fig. 4.2(c) depicts a zoomed-in view of the 2θ - ω scan in panel (a). We observe Laue oscillations (blue arrows) around the (004)-reflection of $\gamma\text{-Fe}_2\text{O}_3$, indicating the coherent growth of $\gamma\text{-Fe}_2\text{O}_3$ on MgO (001). From the 2θ position of the $\gamma\text{-Fe}_2\text{O}_3(004)$ reflection at $2\theta = 43.44^\circ$, we calculate the oop lattice constant to $c = 0.8327\text{ nm}$.

In order to also determine the ip lattice constant $a_{\gamma\text{-Fe}_2\text{O}_3}$ of our thin films, a reciprocal space mapping around the maghemite (408) reflection is performed and shown in Fig. 4.2(b). We observe the (408) reflection of $\gamma\text{-Fe}_2\text{O}_3$ at $q_{\text{H00}} = 1.99998$ reciprocal lattice units (rlu) and $q_{00\text{L}} = 4.0463$ rlu, yielding the lattice constants $a_{\gamma\text{-Fe}_2\text{O}_3} = 0.8423\text{ nm}$ and $c_{\gamma\text{-Fe}_2\text{O}_3} = 0.8326\text{ nm}$. The latter is in excellent agreement with the value extracted from the position of the (004) $\gamma\text{-Fe}_2\text{O}_3$ -reflection in panel (c). From the measured in-plane lattice constant we derive an epitaxial strain in the thin film plane of $\epsilon_{xx} = 1.1\%$, in agreement with our naive initial assumption using the bulk lattice constants of MgO and $\gamma\text{-Fe}_2\text{O}_3$. This observation indicates that our thin films are fully epitaxially strained. The out-of-plane strain is determined to $\epsilon_{zz} = -0.05\%$. This value is significantly lower than expected under the naive assumption that maghemite exhibits the same Poisson ratio as hematite ($\nu \approx 0.12$) [224], which would result in an oop-strain of $\epsilon_{zz} = -2\epsilon_{xx} / (1 - \nu) = -2.5\%$. As our $\gamma\text{-Fe}_2\text{O}_3$ thin films exclusively show crystalline reflections from the cubic phase, we expect the Fe^{3+} vacancies in our $\gamma\text{-Fe}_2\text{O}_3$ thin films to be randomly distributed throughout our thin films [217] and hence do not alter the oop-strain. Therefore, we attribute the unexpectedly low out-of-plane strain and the correspondingly large increase of the unit cell volume of $\Delta V / V \simeq 1.0\%$ to an oxygen deficiency in our maghemite thin films. The oxygen deficiency results from the fact that the film can significantly reduce the lattice strain and hence the elastic energy by incorporating less oxygen. Regarding existing literature, in Ref. [225], a comparable change in lattice constant for the spinel ferrite $\text{NiFe}_2\text{O}_{4-\delta}$ has been observed and could be correlated to an oxygen deficiency of $\delta = 0.0355$. Consequently, we assume a comparable oxygen deficiency for our $\gamma\text{-Fe}_2\text{O}_3$ thin films.

As a further probe for the pure and singular growth of the $\gamma\text{-Fe}_2\text{O}_3$ phase in our samples, we measure the temperature dependence of the electrical resistivity

ρ on our unpatterned thin films using the Van-der-Pauw method [226]. The resulting $\rho(T)$ for the 45.0 nm thick γ - Fe_2O_3 thin film is plotted in Fig. 4.3(a).

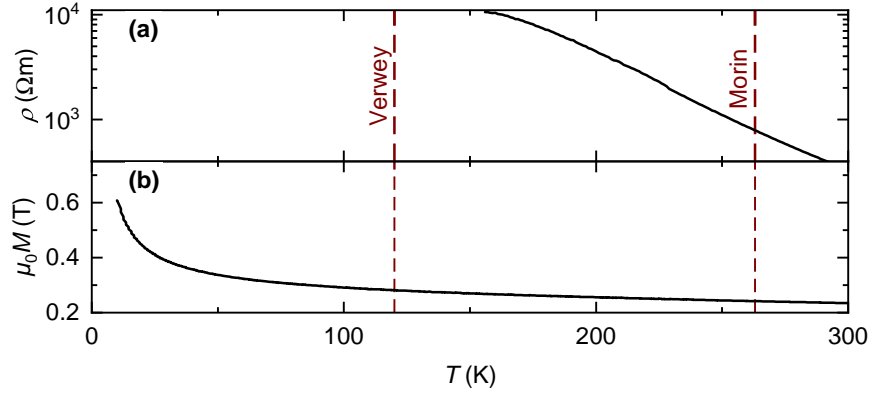


Fig. 4.3. – (a) Temperature dependence of the electrical resistivity ρ of a 45.0 nm thick γ - Fe_2O_3 sample. Below $T = 155$ K, the resistivity of the investigated film exceeds the range of our measurement scheme. Hence, below $T = 155$ K, ρ is above the detection limit. (b) Temperature dependence of the magnetization M of the same film measured at an external field of $\mu_0 H_{\text{ext}} = 0.5$ T. The film was previously cooled in a magnetic field of 7 T to saturate its magnetization. The increase of the magnetization below 50 K is caused by paramagnetic impurities within the MgO substrate. The brown dashed lines mark the temperatures of the Morin and Verwey transition in α - Fe_2O_3 and Fe_3O_4 , respectively.

We observe a smooth evolution with temperature in the sample resistivity $\rho(T)$ and no evidence for the Morin phase transition [227] ($T = 263$ K) from the undesired hematite (α - Fe_2O_3)-phase. Due to the good insulating properties of our samples, the thin film resistivity for $T < 155$ K exceeds the experimental detection limit. Hence, using this method we cannot probe for the presence of magnetite (Fe_3O_4) as the temperature of its phase transition, called the Verwey transition [228], is at $T = 120$ K. As an alternative probe, we measure the magnetization M of our sample at an external magnetic field $\mu_0 H_{\text{ext}} = 0.5$ T applied within the film plane via SQUID magnetometry. The resulting $M(T)$ is plotted in Fig. 4.3(b). We observe a smooth evolution in $M(T)$ throughout the entire investigated temperature range from $T = 5$ K to $T = 300$ K and in particular, no abrupt changes at the temperatures of the Morin- and Verwey transition as indicated by the dark red dashed lines. The observed strong increase in $M(T)$ for temperatures $T < 50$ K can be attributed to the magnetic response of paramagnetic impurities within the MgO substrate. To summarize the results of our XRD and transport experiments, we demonstrate the growth of single-phase γ - Fe_2O_3 thin films of highly crystalline quality. However, the reduced oop-strain ϵ_{zz} indicates a finite density of oxygen vacancies, which will be important for discussing the magnetization dynamics of our γ - Fe_2O_3 thin films in the subsequent section 4.3.

4.3 Magnetic properties of maghemite thin films

4.3.1 Static magnetic properties

To characterize the static magnetic properties of our samples, we measure magnetic hysteresis $M(H_{\text{ext}})$ curves via SQUID magnetometry with the external magnetic field H_{ext} applied both in ip- and oop-direction. The resulting hysteresis curves of the 45.0 nm thick maghemite sample are shown in Fig. 4.4 for the ip (black circles) and oop (red circles) geometry.

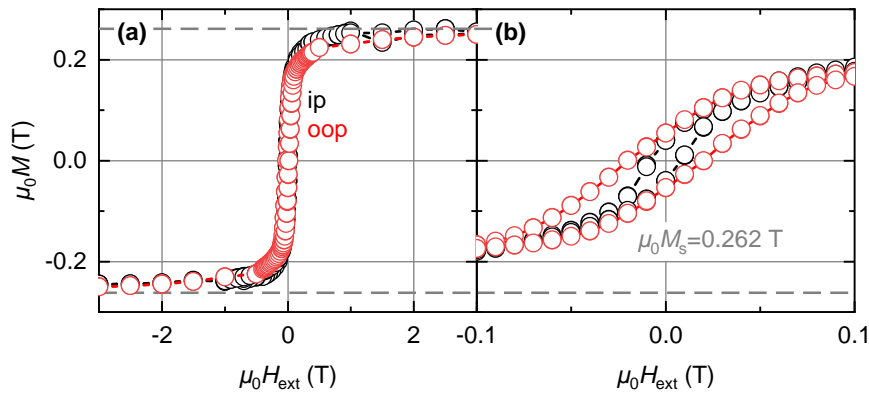


Fig. 4.4. – (a) Room-temperature magnetization as function of applied magnetic field curves recorded via SQUID magnetometry for $\gamma\text{-Fe}_2\text{O}_3$ thin films measured in ip (black) and oop (red) geometry. (b) Zoomed-in view of the magnetic hysteresis curve shown in (a) for the field range $-0.1 \text{ T} \leq \mu_0 H_{\text{ext}} \leq 0.1 \text{ T}$. The horizontal, gray dashed lines mark the saturation magnetization of $\mu_0 M_s = 0.262 \text{ T}$.

Here, we have subtracted a diamagnetic linear background contribution to M from the MgO substrate. In panel (a), we plot the whole examined magnetic field range $-3 \text{ T} \leq \mu_0 H_{\text{ext}} \leq 3 \text{ T}$, whereas in panel (b), we show a magnified view of the field range $-0.1 \text{ T} \leq \mu_0 H_{\text{ext}} \leq 0.1 \text{ T}$. Notably, we observe in panel (b) a hysteretic behavior in $M(H)$ in both ip and oop geometry. Along the magnetic hard axis in the oop-geometry, we attribute the observed magnetic hysteresis in $M(H_{\text{ext}})$ to the pinning of domain walls induced by the presence of a finite density of so-called antiphase boundaries (APBs) [206, 229, 230] in our $\gamma\text{-Fe}_2\text{O}_3$ thin films. APBs are formed, when crystalline regions with different symmetry merge and couple antiferromagnetically during film growth [231, 232]. This causes domain wall pinning and thus a large external magnetic field is required to align the orientation of all of the individual magnetic domains along the magnetic field direction (cf. Ref. [233]). Notably, APBs are commonly observed in iron oxide thin films with spinel crystal symmetry [206, 234]. In our SQUID magnetometry measurements the contribution of APBs to M is difficult to quantify, as it can be masked by the diamagnetic contribution from the MgO substrate at large H_{ext} .

For the saturation magnetization, we extract $\mu_0 M_s = 0.262 \text{ T}$, which is only about half of the expected bulk value from literature $\mu_0 M_s \simeq 0.5 \text{ T}$ [95, 222].

However, the saturation magnetization of $\gamma\text{-Fe}_2\text{O}_3$ thin films has been found to sensitively depend on the fabrication method and the thin film quality. As an example, reduced values of M_s have been reported for $\gamma\text{-Fe}_2\text{O}_3$ thin films grown on MgO substrates via molecular beam epitaxy ($\mu_0 M_s = 0.339$ T) [229]. Likewise to the hysteretic magnetic behavior in oop-geometry, we attribute the strongly reduced M_s in our thin films to the pinning of domain walls by antiphase boundaries.

4.3.2 Dynamic magnetic properties

To study the dynamic magnetic properties of our $\gamma\text{-Fe}_2\text{O}_3$ samples, we perform cryogenic bbFMR experiments (see Sec. 3.3.1). For the bbFMR experiments in this chapter, we record the complex microwave transmission parameter S_{21} for fixed microwave frequencies in the range $5\text{ GHz} \leq f \leq 43.5\text{ GHz}$ as a function of the static applied magnetic field H_{ext} in the oop geometry [see Fig. 3.4(a)] to suppress two-magnon scattering [114–116] using a VNA. Exemplary raw data for the recorded net change in the complex transmission parameter ΔS_{21} induced by the FMR in $\gamma\text{-Fe}_2\text{O}_3$ at $T = 300$ K and $f = 15$ GHz is shown in Fig. 4.5 for the real (a) and imaginary part (b). The data is calculated from the raw S_{21} data using Eq. (3.7) as a function of external magnetic field H_{ext} . The complex ΔS_{21} data is fitted to the Polder susceptibility $\hat{\chi}_p$ [continuous lines in panels (a) and (b)] via Eq. (2.30) to extract the resonance field H_{ext} [blue dashed line in panels (a) and (b)] and the linewidth ΔH [light blue box in panels (a) and (b)] as a function of f . The resulting FMR field and linewidth evolution $H_{\text{res}}(f)$ and $\Delta H(f)$ is plotted in Fig. 4.5(c) and (d), respectively.

For the FMR linewidth $\Delta H(f)$ in Fig. 4.5(d), we observe a non-linear $\Delta H(f)$ dependence showing a distinct cusp feature in the intermediate frequency range ($10\text{ GHz} \leq f \leq 20\text{ GHz}$). A cusp-feature $\Delta H(f)$ indicates the presence of one or multiple temperature-dependent magnetic relaxation processes in our $\gamma\text{-Fe}_2\text{O}_3$ thin films, where a peak-like feature in $\Delta H(f)$ can manifest, when energy is resonantly transferred from the dynamically precessing magnetization to the lattice (see Sec. 2.3.3).

In the following, we interpret this feature in $\Delta H(f)$ as caused by the slowly-relaxing impurity mechanism. From energy-dispersive x-ray spectroscopy (EDS) experiments performed on our samples shown in Appendix A1, we observe no traces of any impurity contamination in our thin films. However, an alternative plausible candidate are unpaired Fe^{2+} -ions [147, 235–237] caused by the oxygen deficiency in our samples (see Sec. 4.2). Indeed, a finite concentration of Fe^{2+} -ions in $\gamma\text{-Fe}_2\text{O}_3$ nanocrystals has been observed via x-ray absorption spectroscopy in Ref. [219]. In the presence of slowly relaxing impurities and assuming a uniform uniaxial out-of-plane anisotropy field H_u , the total dispersion of the ferromagnetic resonance and the change of linewidth with frequency in oop-

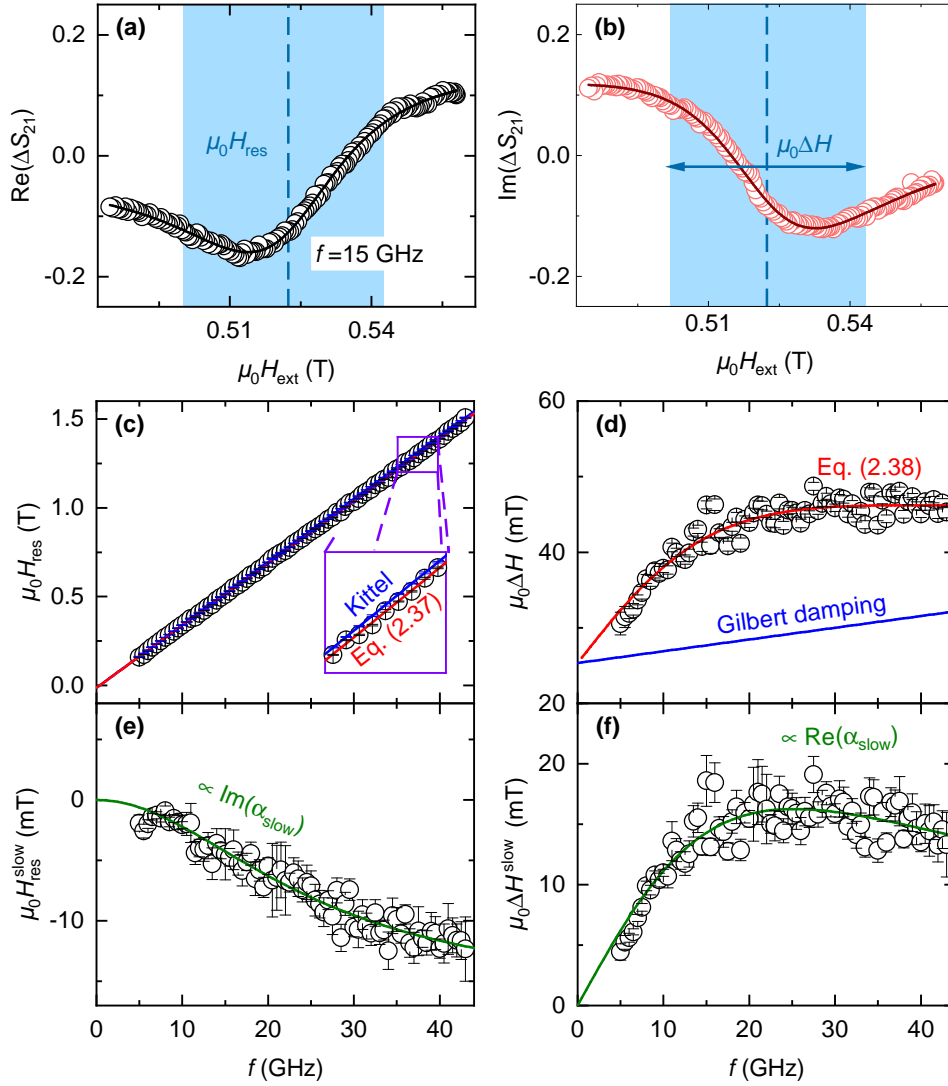


Fig. 4.5. – Exemplary raw and processed data for the room temperature oop bbFMR experiment of the 52.6 nm thick γ -Fe₂O₃ thin film. (a) and (b) depict raw data for the real and imaginary part of ΔS_{21} as function of H_{ext} at $f = 15$ GHz. The continuous lines represent fits to the Polder susceptibility, whereas the dashed line and colored box represent the resonance field H_{res} and linewidth ΔH , respectively. (c) Extracted resonance field H_{res} together with a fit following Eq. (2.37) (red line). The inset displays an apparent small difference between the linear Kittel contribution (blue line) and the total fit (red line). (d) Raw data of the extracted resonance linewidth ΔH together with a fit following Eq. (2.38) (red line). The linear-in-frequency term in Eq. (2.38) is the Gilbert damping (blue line). (e) Slowly relaxing impurity contribution to the resonance field $H_{\text{res}}^{\text{slow}}$ obtained by subtracting the Kittel contribution (blue line) from the raw data for H_{res} in panel (c) together with a fit to $\text{Im}(\alpha_{\text{slow}})$ according to Eq. (2.39) (green line). (f) Slowly relaxing impurity contribution to the resonance linewidth $\Delta H^{\text{slow}}(f)$ extracted by subtracting the linear Gilbert contribution (blue line) from the raw data for ΔH in panel (d) together with a fit to $\text{Re}(\alpha_{\text{slow}})(f)$ according to Eq. (2.39) (green line).

geometry is given by Eqs.(2.37) and (2.38), where we account for the slow-relaxor mechanism via the additional contribution $\propto \alpha_{\text{slow}}$ to H_{res} and ΔH , which is defined in Eq. (2.39). The continuous red lines in Fig. 4.5(c) and (d) represent a simultaneous fit to Eqs. (2.37) and (2.38) including the slowly relaxing impurity parameters, whereas the blue continuous lines represent the background to H_{res} and ΔH in the absence of the slow-relaxor mechanism. In Fig. 4.5(e) and (f), we plot the extracted isolated slow-relaxor contribution to the FMR resonance field and linewidth as function of f . Here, the green lines represent the real and imaginary part of α_{slow} following Eq. (2.39). While the imaginary part of $\alpha_{\text{slow}}(f)$ in Fig. 4.5(c) only weakly modifies the FMR resonance frequency and could be misinterpreted as a modified g -factor, the real part of $\alpha_{\text{slow}}(f)$, shown in Fig. 4.5(d), can qualitatively reproduce the cusp-feature in the FMR linewidth. We account for the slight impact of the slow-relaxor mechanism on $H_{\text{res}}(f)$ by performing a global fit for both $H_{\text{res}}(f)$ and $\Delta H(f)$ using the same shared parameters. Here, we use a temperature-independent g -factor $g = 2.022$, which matches previous results for maghemite nanopowders [238], to reduce the number of free fitting parameters. The fitted magnetization dynamics and parameters describing the slowly relaxing impurities for the fit to the data presented in Fig. 4.5 are $\mu_0 M_{\text{eff}} = (-12.4 \pm 2.1)$ mT, $\alpha = (2.2 \pm 1.5) \cdot 10^{-3}$, $CF(T) = (2.9 \pm 0.6)$ GHz and $\tau = (6.3 \pm 2.5)$ ps. These values also represent the room-temperature data points in the Fig. 4.6. Notably, we fit a low negative effective magnetization M_{eff} , which indicates a dominant oop easy-axis anisotropy with $\mu_0 H_u < \mu_0 M_s \approx 0.3$ T for our maghemite thin films. We attribute the observed large H_u despite the relatively low oop strain ($\epsilon_{zz} = -0.05\%$, see Sec. 4.2), to the presence of a strong magnetoelastic coupling, which is common for epitaxial spinel ferrite thin films [207,239,240]. In the Appendix A2, we present additional room temperature FMR-results of three different $\gamma\text{-Fe}_2\text{O}_3$ thin films. For the magnetization dynamics in all of these films, we observe a comparable behavior to the data displayed in Fig. 4.5 with a reduced effective magnetization and non-linear behavior in ΔH as function of frequency. This indicates an universal origin of the observed strain induced magnetic anisotropy and the slowly relaxing impurity contribution to the resonance linewidth.

In Fig. 4.6, we present the magnetization dynamics and slow-relaxor parameters of the 52.6 nm thick maghemite thin film. The data is obtained by fitting the H_{res} and ΔH values derived from our bbFMR experiments using Eqs. (2.37) and (2.38) as a function of temperature T . In panel (a), we observe a small negative effective magnetization $\mu_0 M_{\text{eff}} \approx -12$ mT at room temperature, which gradually increases with decreasing temperature and changes sign at $T_{\text{cross}} \approx 200$ K [brown dashed line in Fig. 4.6(a)]. We attribute the strong temperature-dependence and sign change in M_{eff} to be governed by the reduction in the strain-induced anisotropy contribution H_u due to the reduced strain between MgO and $\gamma\text{-Fe}_2\text{O}_3$ with decreasing temperature. We note, that this reduction in strain is expected from literature, as iron oxides exhibit a larger thermal

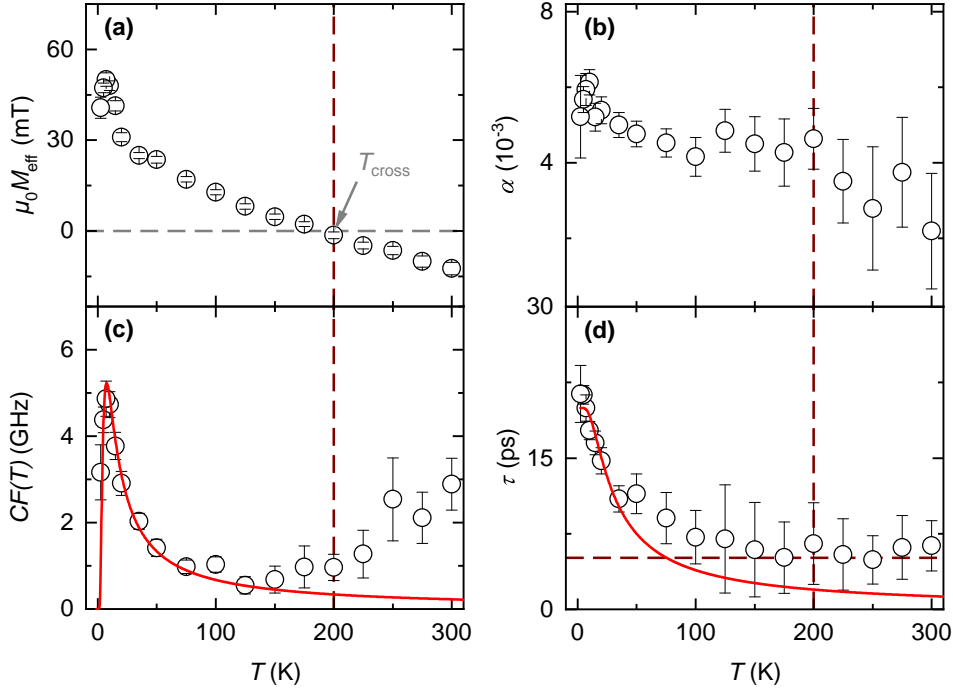


Fig. 4.6. – Magnetization dynamics- and slowly relaxing impurity parameters of the 52.6 nm thick maghemite sample as a function of temperature T . (a) Effective magnetization M_{eff} and (b) Gilbert damping parameter α as function of T . (c) Magnitude of slowly relaxing impurity contribution $CF(T)$ together with a theoretical fitting curve for $CF(T)$ (red line) following the product of Eqs. (2.40) and (2.41). We extract $E_{\text{slow}} = (0.50 \pm 0.04)$ meV and $C \cdot T = (66 \pm 4)$ GHz·K. (d) Relaxation time τ as function of T . The red line represents a fit to Eq. (4.1). We extract $E_A = (3.3 \pm 0.6)$ meV and $\tau_0 = (19.9 \pm 0.1)$ ps.

expansion coefficient [241] compared to that of MgO [242]. In parallel to a change in interfacial strain, the saturation magnetization M_s of maghemite increases with decreasing temperature [243] and contributes to the observed rise in $\mu_0 M_{\text{eff}}$ with decreasing T . However, from the low change in magnitude with reduced T in Ref. [243][$M_s(300 \text{ K}) \approx 0.9 M_s(0 \text{ K})$], we expect this contribution to be too small to single-handedly describe the observed increase in $M_{\text{eff}}(T)$ in panel (a). For the temperature-dependence of the Gilbert damping, plotted in Fig. 4.6(b), we observe a light but continuous increase in α with decreasing temperatures. In the same way as the Gilbert damping of the 45.0 nm thick $\gamma\text{-Fe}_2\text{O}_3$ thin film presented in the Appendix A2, the increase in α with decreasing temperatures coincides with the sign change in M_{eff} . This correspondence indicates that the change in anisotropy from easy-axis to easy-plane in our samples enhances the Gilbert damping in our $\gamma\text{-Fe}_2\text{O}_3$ thin films. Regarding the characteristic parameters of the slowly relaxing impurities in Fig. 4.6(c), we observe a maximum in $CF(T)$ at $T \simeq 7$ K followed by a decrease in magnitude for $CF(T)$ with rising temperatures up to $T = 150$ K. Surprisingly, for higher T , the magnitude of $CF(T)$ increases again and this trend continues up to room temperature. The observed peak-behavior at low T is characteristic for temperature-dependent magnetic relaxation processes (see Sec. 2.3.3). Furthermore, we observe a good agreement for the experimental data

of $CF(T)$ in Fig. 4.6(c) with a fit to the product of Eqs. (2.40) and (2.41) (red line) for low temperatures ($T \leq 50$ K). From this fit, we obtain the slow-relaxor parameters $E_{\text{slow}} = (0.50 \pm 0.04)$ meV and $C \cdot T = (66 \pm 4)$ GHz·K, which are comparable to values reported in previous publications on slowly relaxing impurities [82, 244]. A potential mechanism to explain the increase in $CF(T)$ for $T > 150$ K is the valence-exchange mechanism (see Sec. 2.3.3) as will be discussed in detail in the following Section 4.4. Finally, for the temperature-dependence of the relaxation time τ in Fig. 4.6(d), we observe a constant τ for elevated temperatures $T > 100$ K and a strong increase in τ below 100 K. Assuming the predominant relaxation of the slowly relaxing impurities via a single particle Orbach process [245] with activation energy E_A , we fit the extracted τ for temperatures below 100 K using

$$\tau = \tau_0 \cdot \tanh\left(\frac{E_A}{2k_B T}\right). \quad (4.1)$$

From the resulting fit [red line in Fig. 4.6(d)], we obtain $E_A = (3.3 \pm 0.6)$ meV and $\tau_0 = (19.9 \pm 0.1)$ ps, which correspond well to the slow-relaxor excitation energies in Refs. [244, 246]. For elevated temperatures, we observe a deviation between fitting curve and raw data in Fig. 4.6(d) due to the increasing impact of Raman- and two-quasiparticle Orbach processes [245, 247], which exhibit different temperature dependencies than that of single-particle Orbach processes in Eq. (4.1). In the Appendix A1, the fitting results for τ of Fig. 4.6(d) are compared to those of the 45 nm thick maghemite film, where we observe a comparable magnitude and evolution with temperature for both $CF(T)$ and τ and thereby confirm that the temperature dependence of the magnetization dynamics and slow relaxor parameters in Fig. 4.6 are representative for our $\gamma\text{-Fe}_2\text{O}_3$ thin films.

4.4 Discussion of the non-linear magnetic damping

In the previous data, we have found that the magnetization dynamics of our $\gamma\text{-Fe}_2\text{O}_3$ thin films can be well described with the slowly-relaxing impurity mechanism for low temperatures $T \leq 50$ K and assume a valence-exchange mechanism to manifest at higher temperatures. However, there are various variety of other non-linear magnetization damping mechanisms, which we will discuss in the following and provide arguments for why we can rule them out in our $\gamma\text{-Fe}_2\text{O}_3$ thin films.

We begin our discussion with the magnetization damping caused by the scattering of the uniform magnetization mode ($k = 0$) with optical phonons according to the Kasuya-LeCraw-mechanism [248, 249] or with optical magnons as described by the Kolokolov-L'vov-Cherepanov process [202]. However, these processes give rise to a contribution to the FMR-linewidth that is approximately linear in frequency and temperature for intermediate temperatures ($150 \text{ K} \leq T \leq 350 \text{ K}$) [203] and can hence not explain the observed non-linear features in FMR

linewidth ΔH at elevated temperatures [see Fig. 4.6(c)]. Similarly, a non-linear damping contribution can arise due to two-magnon scattering [114–116]. However, this process does not exhibit a strong temperature dependence [74,249] and is also expected to be suppressed in oop-geometry. Hence, we assume the contribution of two-magnon scattering to the damping to be negligible for our samples.

As an alternative explanation for the non-linear frequency dependence of ΔH in our experiments, damping effects induced by the perpendicular magnetic anisotropy may play a role. In this context, a non-linear $\Delta H(f)$ dependence can be induced by a non-collinear distribution of uniaxial anisotropies with an average angle β around the out-of-plane direction. This scenario has been described with the so-called anisotropy dispersion model by Krysztofik *et al.* in Ref. [250]. However, in contrast to our results, they observe a convex shape for the $\Delta H(f)$ dependence of strained YIG on yttrium aluminum garnet ($\text{Y}_3\text{Al}_5\text{O}_{12}$, YAG) substrates with a negative slope in $\Delta H(f)$, such that we can also rule out an angular distribution in magnetic anisotropies around the sample normal as the origin of the non-linear $\Delta H(f)$ dependence in the high-temperature regime.

Finally, we note that there exists a temperature-dependent magnetic relaxation process that gives rise to a non-linear evolution in $\Delta H(f)$ at elevated temperatures ($100 \text{ K} \leq T \leq 400 \text{ K}$ [147,148]), namely the so-called valence-exchange or charge-transfer mechanism [74,147,148]. As detailed in Sec. 2.3.3, this effect manifests itself if mixed-valent ions are present in the ferromagnetic thin film (i.e. Fe^{2+} or Fe^{4+} ions in YIG with nominal only Fe^{3+} -ions). In this case, electrons can hop between the different valence lattice site and thereby mediate a net energy transfer from the dynamically precessing magnetization to the crystal lattice, which increases the magnetization damping. Notably, this mechanism results in the same peak-like frequency dependence to the FMR linewidth [147] $\Delta H_{\text{ct}} \propto \omega\tau_{\text{ct}}/[1 + (\omega\tau_{\text{ct}})^2]$ as predicted by the slowly relaxing impurity model [see Eq.(2.39)]. However, it exhibits a different characteristic timescale τ_{ct} , representing the electron hopping time. Fortunately, its impact on the FMR-linewidth can be distinguished from that of slowly relaxing impurities, as it has been found to manifest itself at temperatures above room temperature, for example, above $T \simeq 370 \text{ K}$ in YIG [147,236]. In our $\gamma\text{-Fe}_2\text{O}_3$ samples, the electron hopping mechanism would then take place between the Fe^{3+} -ions and the unpaired Fe^{2+} -ions induced by the oxygen deficiency.

To discuss the impact of the valence-exchange mechanism on the magnetization damping of our $\gamma\text{-Fe}_2\text{O}_3$ thin films, we plot in Fig. 4.7 the FMR linewidth ΔH recorded at $f = 15 \text{ GHz}$ for the 52.6 nm thick maghemite film as function of temperature T . The red dashed line represents the slowly relaxing impurity contribution to the FMR linewidth following the real part of Eq.(2.39) together with a theory curve (red line) using the fitted parameters to $CF(T)$ and τ from Fig. 4.6(c) and (d). In the low temperature regime ($T < 50 \text{ K}$), the peak-like feature in Fig. 4.7 can be well described by our slowly relaxing impurity model, while the gradual increase in ΔH at elevated temperatures mirrors our observations for the

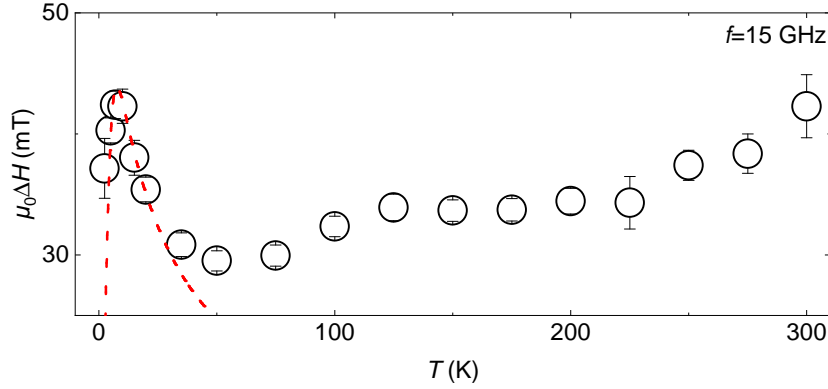


Fig. 4.7. – FMR linewidth ΔH recorded at $f = 15$ GHz of the 52.6 nm thick maghemite film as a function of temperature T . The red dashed line represents the slowly relaxing impurity contribution to the FMR linewidth following the real part of Eq. (2.39) using the extracted fitting parameters from fits to $CF(T)$ and τ in Fig. 4.6(c) and (d).

slowly relaxing impurity constant $CF(T)$ in Fig. 4.6(c). This correspondence indicates that the increase in ΔH is generated by a non-linear magnetization damping contribution [see also the decrease in α with rising T in Fig. 4.6(b)]. Furthermore, it is worth mentioning that the increase in FMR linewidth at $T > 150$ K coincides with a decrease in sample resistivity ρ [see Fig. 4.3(a)] and thereby with the increased thermally induced hopping probability of the electrons available for the valence-exchange mechanism. Based on these experimental hints, we suspect that the observed increase in FMR linewidth ΔH and slowly-relaxing impurity constant $CF(T)$ at higher temperatures $T > 100$ K up to room temperature originates from the valence-exchange mechanism caused by electron hopping between Fe^{2+} and Fe^{3+} ions in $\gamma\text{-Fe}_2\text{O}_3$. We do not observe the characteristic temperature peak in ΔH for the valence-exchange model, as we have performed FMR measurements only up to room temperature in our thin films.

4.5 Summary and Outlook

In this chapter, we investigate the static and dynamic magnetic properties of epitaxially strained $\gamma\text{-Fe}_2\text{O}_3$ thin films grown on MgO substrates by performing SQUID magnetometry and temperature dependent bbFMR experiments. XRD measurements demonstrate the pseudomorphic growth of $\gamma\text{-Fe}_2\text{O}_3$ with a tensile in-plane epitaxial strain of $\epsilon_{xx} = 1.1\%$ and an unexpectedly small out-of-plane strain of $\epsilon_{zz} = -0.05\%$. The latter suggests an oxygen deficiency in our samples. Room temperature SQUID magnetometry experiments show hysteretic magnetization curves for the magnetic field applied in both the ip and oop direction with a saturation magnetization of $\mu_0 M_s = 0.262$ T, which is only about half of the literature value $\mu_0 M_s \simeq 0.5$ T for bulk material [222, 251]. This indicates the presence of a sizable density of antiphase boundaries. Regarding the magnetization dynamics, we find that the conventional Gilbert damping mechanism

including an inhomogeneous linewidth broadening is not sufficient to describe the observed non-linear frequency dependence of the FMR linewidth $\Delta H(f)$. We model the observed peak in $\Delta H(f)$ by accounting for the coupling of the sample magnetization with an ensemble of paramagnetic impurities using the so-called slow-relaxor model. Here, the presence of a finite density of Fe^{2+} ions is the most plausible candidate for the impurities [147, 235–237]. This is in agreement with the observed increased unit cell of our samples. To characterize the slow-relaxing impurity mechanism in our samples, we then study the magnetization dynamics and parameters describing the slowly relaxing impurities as a function of temperature by performing cryogenic bbFMR (see Sec. 3.3.1). For the effective magnetization $M_{\text{eff}}(T)$, we find a crossover from an oop easy-axis to an ip easy-plane anisotropy, which we attribute to the reduced strain in $\gamma\text{-Fe}_2\text{O}_3$ on MgO for reduced temperatures. Regarding the slowly relaxing impurity contribution, we observe the predicted temperature-dependent magnetic relaxation behavior at low T . Furthermore, for elevated temperatures ($T > 150$ K), we measure an unexpected increase of the linewidth with increasing temperature, which is induced by a non-linear magnetization damping process. We attribute this increase to electrons hopping between Fe^{2+} and Fe^{3+} ions in our oxygen-deficient films, which gives rise to an additional temperature-dependent magnetic relaxation process called the valence-exchange mechanism.

Our thorough characterization of the slowly-relaxing impurity mechanism as function of temperature and frequency in $\gamma\text{-Fe}_2\text{O}_3$ provides input for the theoretical understanding of magnetization damping induced by the magnetic coupling to slowly relaxing impurities. The controlled non-linear magnetization damping is of interest for magnetization damping engineering of magnetic materials for example to enhance the magnetic damping for magnetic sensor applications [82]. Moreover, the observed PMA in maghemite is of interest for energy efficient data storage devices based on magnetic textures such as magnetic bubbles, chiral domain walls, and magnetic skyrmions [212, 213]. Finally, the strain-induced near-zero effective magnetization of maghemite renders it a promising material platform for future magnonics applications of magnetically ordered insulators [106, 199, 214, 215].

Spin torques in Superconductor/Ferromagnet heterostructures

In the last chapter, we have investigated the impact of the coupling of the magnetization of a magnetic thin film to a disordered ensemble of paramagnetic impurities and its effect on the magnetization dynamics. On a more general level it is interesting to ask the question, how the magnetization dynamics in magnetic thin films is affected by the interaction with the excitations of adjacent solid state phases, such as for example topological phases [65, 66, 252], charge ordered phases [253–255] or superconductivity [49, 256, 257]. Using the Superbowls sputtering machine (see Sec. 3.1.5), we are able fabricate heterostructures consisting of magnetically ordered materials and materials showing various other ordering phenomena. This allows us to realize systems where the magnetization dynamics is coupled to excitation of other solid-state phases. In this chapter, we address the question how the magnetization dynamics in magnetic thin films is affected by coupling it to an adjacent superconducting film.

In the following, we will provide a rough overview of selected aspects of superconductivity, which are relevant for the interpretation of the presented results. A more detailed discussion on this phenomenon can be found for example in Refs. [86, 258–260]. Superconductivity describes a macroscopic quantum phenomenon leading to zero electrical resistance and perfect diamagnetism below a superconducting transition temperature T_c . Superconducting materials are thus capable of carrying large persistent electric charge currents without measurable resistance. This has enabled their technical application in high-field superconducting magnets used for example in magnetic resonance imaging [261, 262] and tapes used for efficient energy transmission applications [263–265].

In simple terms, superconductivity is mediated by an attractive interaction of electrons via the virtual exchange of phonons. In this simple picture [86], an electron moving in a superconducting material attracts the positively charged ions from the underlying material lattice. This elastic distortion of the lattice gives rise to a localized positive potential well, which survives for a finite time τ given by the inverse of the characteristic phonon frequency ω_D of the material. In turn, this leads to a retarded attractive interaction for a second nearby electron and hence to an attractive electron-electron interaction. Due to a maximum overlap of the momentum states in the reciprocal space [86], the retarded interaction mechanism favors -in the simplest case- the pairing of electrons with opposite momentum k called Cooper-pairs [86, 266]. These Cooper pairs can form over large distances d

ranging between $10 \text{ nm} \leq d \leq 1000 \text{ nm}$ depending on the phononic relaxation time τ of the atoms in the host lattice. For temperatures below T_c , the Cooper pairs form a coherent state which can be described by a macroscopic wave function $\Psi(\mathbf{r}, t)$ with amplitude $|\Psi_0(\mathbf{r}, t)|$ and phase $\theta(\mathbf{r}, t)$:

$$\Psi(\mathbf{r}, t) = |\Psi_0(\mathbf{r}, t)| \cdot e^{i\theta(\mathbf{r}, t)}. \quad (5.1)$$

The superconducting condensate can carry a finite supercurrent without any dissipation. In the simplest case, the Cooper pairs forming the condensate are spin singlet pairs and therefore the supercurrent is not expected to carry any angular momentum. This immediately raises the following interesting questions: What happens if we inject a finite spin current into a superconductor? How is the superconductor affected by such spin current? Can a finite spin current be transported across a superconductor? The latter question has given rise to the field of superconducting spintronics [267–269]. As already mentioned, ordinary superconductors favor the formation of *s*-wave Cooper pairs with a symmetric orbital function and antisymmetric spin wave function $|\uparrow\downarrow\rangle$ leading to a net zero spin current of the condensate. However, both superconducting quasiparticle excitations [48, 50, 270–272] and spin-triplet Cooper pairs [267, 273] generated for example by spin-orbit interaction in heavy metals in contact to superconductors [49, 274, 275] are expected to carry spin currents with reduced dissipation compared to the normal state. Furthermore, superconducting vortices are theoretically discussed as carriers of spin information [276–278]. In recent years, the charge-to-spin current interconversion mechanisms and the associated spin-orbit torque effects in the superconducting state have been of great interest as they may allow us to control of magnetization dynamics with superconducting materials and thereby to reduce dissipative effects. The pioneering experiments in this direction were dc transport experiments in superconducting lateral spin valve structures, which reported changes in the spin signal and spin decay length³ λ_s [282–284] in the superconducting state.

However, more recent experiments [49, 256, 257, 285–288] have instead put emphasis on investigating the magnetization dynamics of a ferromagnetic metal (FM) layer in contact to a superconducting layer (SC). Here, changes of either the FMR-linewidth ΔH or the Gilbert damping α below T_c allow us to investigate spin injection into superconductors via spin pumping [49, 256, 257, 285, 286, 288]. These experiments have detected a variety of different features in the magnetization damping in superconductor/ferromagnet-heterostructures below T_c ranging from a monotonic reduction in the Gilbert damping α due to a freeze-out of

³Note that as the spin transport is diffusive in nature and captured by a spatial variation of its chemical potential, this quantity is sometimes referred to as a “spin diffusion length” in literature (see for example Refs. [257, 279, 280]). However, this terminology is to be contrasted with the diffusion of conserved particles, such as a gas diffusing into or out of a particular volume and hence we deem the term “spin decay length” to be a more descriptive term of the physics at play [281].

quasiparticles (QP) mediating the spin transport [256] over the manifestation of a quasiparticle coherence peak in α for temperatures slightly below T_c [257], to an enhanced FMR-linewidth ΔH attributed to enhanced spin pumping properties in the superconducting state mediated by spin-triplet Cooper pairs [49]. To clarify the origin of these competing results, we have performed an in-depth systematic study of the magnetization dynamics of several different FM/SC-heterostructures as a function of temperature above and below T_c and have additionally performed an investigation of the linear spin-orbit-torques present in these multilayers by performing bbFMR experiments in combination with the phase sensitive detection of the microwave transmission signal. This approach allows us to simultaneously detect the electrical ac currents due to magnetization dynamics, which manifest in these heterostructures due to inverse spin torques (iST) as well as classical electrodynamics (i.e. Faraday's law) [84]. By employing this technique, we are able to simultaneously quantify the impact of an adjacent SC film on both the magnetization dynamics (e.g. FMR linewidth) and the field- and damping-like σ^{ST} in SC/FM heterostructures. For the latter, we have modified the inductive coupling analysis reported in Ref. [84] to account for the altered transport properties of the SC layer. In this way, we have developed a new powerful method to study nonequilibrium spin transport in SCs, which is presented in Sec. 5.1. The experimental results for the bbFMR analysis of SC/FM-heterostructures are presented in Sec. 5.2. Both the theoretical details of the inductive analysis technique as well as the experimental results are published in

M. Müller, L. Liensberger, L. Flacke, H. Huebl, A. Kamra, W. Belzig, R. Gross, M. Weiler, M. Althammer, *Temperature-Dependent Spin Transport and Current- Induced Torques in Superconductor-Ferromagnet Heterostructures*, *Physical Review Letters* **126**, 087201 (2021) [68].

An emerging direction within the field of superconducting spintronics is the investigation of superconductors with large spin-orbit interaction (SOI) [289–294] or in proximity to heavy metals [49, 286]. This approach allows to study how SOI affects the superconducting and spin transport properties. Besides the generation of spin-triplet supercurrents [289, 290], theoretical predictions include the generation of supercurrents by Rashba-type spin-orbit interaction [37, 295], the generation of Majorana quasiparticles [296–298] and supercurrent-induced spin torques [299]. Motivated by the large SOI induced by Ta [44, 280], we have also performed a growth optimization of superconducting TaN deposited via reactive dc magnetron sputtering, a material which otherwise finds application in corrosion-resistive coatings [300, 301] and as a diffusion barrier against Cu [302–304]. Using the large SOI TaN as a SC layer, we again investigate the magnetization dynamics of TaN/FM-heterostructures as a function of temperature using bbFMR spectroscopy combined with the inductive analysis technique to extract the inverse current-induced torques of the bilayers. The obtained results are then compared to those of Sec. 5.2. The growth optimization of TaN in Sec. 5.3

is the result of the Bachelor thesis performed by Raphael Hoepfl [162] under the guidance of the author, which resulted in the publication M. Müller, R. Hoepfl, L. Liensberger, S. Geprägs, H. Huebl, M. Weiler, R. Gross, M. Althammer, *Growth optimization of TaN for superconducting spintronics*, *Materials for Quantum Technology* **1**, 045001 (2021) [69].

5.1 Inductive detection of spin torques

In section 2.3.1, we have established, that in NM/FM-bilayers, magnetization dynamics in the FM layer due to magnetic resonance can generate charge currents with a density \mathbf{J}_c in the adjacent NM layer via both field-like and damping-like inverse spin torque effects. The ac component of \mathbf{J}_c inductively couples to the CPW and thereby gives rise to an additional inductance [83,84]

$$L_J = -L_{12} \frac{J_a}{J_0}, \quad (5.2)$$

where J_a is the ac charge current density flowing in the NM layer along the CPW in Fig. 3.4, J_0 is the magnitude of the charge current density flowing in the CPW and L_{12} is the mutual inductance between the FM/NM-bilayer sample and CPW, which can be modeled as two parallel current carrying sheets with length l and width w_{cc} and separation δ [305]

$$L_{12} = \frac{\mu_0 l}{4\pi} \left[1 + 2 \ln \left(\frac{2l}{w_{cc}} \right) \right]. \quad (5.3)$$

in the limit $\delta \ll w_{cc}$. Consequently, we define the net total inductance as

$$L_{\text{tot}} = L_0 + iL_J, \quad (5.4)$$

with the inductance of the sample L_0 from Eq. (3.5). From Eq. (2.32), we can find an explicit expression for J_a using the geometry from Fig. 3.4

$$J_a = -\text{sgn} \cdot w_{cc} \cdot \frac{\hbar}{2e} \mathbf{a} \cdot \left[\mathbf{c} \times \frac{\partial \mathbf{m}}{\partial t} \sigma_f - \mathbf{c} \times \left(\mathbf{m} \times \frac{\partial \mathbf{m}}{\partial t} \right) \sigma_d \right]. \quad (5.5)$$

Here $\text{sgn} = \pm 1$ accounts for the current direction given by the stack sequence of the NM/FM-heterostructure ($\text{sgn} = +1$ for substrate/NM/FM-stacking order and $\text{sgn} = -1$ for substrate/FM/NM-stacking order) as shown in Fig. 5.1(a). We combine Eqs. (5.2), (5.4) and (5.5) to obtain the total reduced inductance

$$\begin{aligned} \tilde{L}_{\text{tot}} &= \frac{L_{\text{tot}}}{[\chi_{bb}(1 - \delta_{bH}) + \chi_{cc}(1 - \delta_{cH})]} = \\ &= \mu_0 \frac{ld_{\text{FM}}}{4w_{cc}} + i \cdot \text{sgn} \cdot \frac{\hbar w_{cc} L_{12} \mathbf{a} \cdot \left[\mathbf{c} \times \frac{\partial \mathbf{m}}{\partial t} \sigma_f - \mathbf{c} \times \left(\mathbf{m} \times \frac{\partial \mathbf{m}}{\partial t} \right) \sigma_d \right]}{2eI_0 [\chi_{bb}(1 - \delta_{bH}) + \chi_{cc}(1 - \delta_{cH})]}. \end{aligned} \quad (5.6)$$

From Eq. (5.6), we see, that the first contribution to \tilde{L}_{tot} from the inductance of the FM layer has a frequency independent and strictly real component and the second contribution is a complex frequency-dependent function, which critically depends on the measurement geometry and magnitude as well as symmetry of the inverse spin torques. For the magnetization unit vector, we use the expression⁴

$$\mathbf{m} = \frac{1}{M_s} \begin{pmatrix} [\chi_{xx}h_x(1 - \delta_{xa} - \delta_{xc}) + \chi_{xy}h_y(1 - \delta_{ya} - \delta_{yc})]e^{i2\pi ft} \\ [\chi_{yx}h_x(1 - \delta_{xa} - \delta_{xc}) + \chi_{yy}h_y(1 - \delta_{ya} - \delta_{yc})]e^{i2\pi ft} \\ M_s \end{pmatrix}. \quad (5.7)$$

defined in Sec. 2.2. Here, we again account for the different driving field components contributing in the three measurement geometries in Fig. 3.4 with the terms $(1 - \delta_{ia})$. Additionally we have to consider that any linear response (\mathbf{m} and \mathbf{J}_c) due to the c -direction driving field component is antisymmetric if mirrored along the ac -plane. Thus, currents induced by h_c do not contribute to the inductance. Hence, we further simplify Eq. (5.7) by adding the terms δ_{xc} and δ_{yc} .

In the following, we extend the model in Ref. [84] and derive explicit expressions for \tilde{L}_{tot} for the three different measurement geometries defined in section 3.3.1 based on the coordinate system shown in Fig. 3.4 by inserting Eq. (5.7) into Eq.(5.6).

- $\mathbf{H}_{\text{ext}} \parallel \mathbf{a}$ (ip, $\mathbf{a} \rightarrow \mathbf{x}$, $\mathbf{b} \rightarrow \mathbf{z}$, $\mathbf{c} \rightarrow \mathbf{y}$):

For the ip-geometry $\mathbf{H}_{\text{ext}} \parallel \mathbf{a}$, Eq. (5.7) takes the form

$$\begin{aligned} \tilde{L}_{\text{tot}} &= \mu_0 \frac{ld_{\text{FM}}}{4w_{\text{cc}}} + i \cdot \text{sgn} \cdot f \cdot \frac{hw_{\text{cc}}L_{12}h_y [i\sigma_{\text{f}}\chi_{yy} + i\sigma_{\text{d}}\chi_{yx}]}{2eI_0[\chi_{xx} + \chi_{yy}]} \\ &= \mu_0 \frac{ld_{\text{FM}}}{4w_{\text{cc}}} + \text{sgn} \cdot f \cdot \frac{hL_{12} [-\sigma_{\text{f}} + i\sigma_{\text{d}}\epsilon(f)]}{4eMs[\epsilon^2(f) + 1]}, \end{aligned} \quad (5.8)$$

where we have used $h_y = I_0/(2w_{\text{cc}})$ and $\chi_{yx} = i\chi_{xx}/\epsilon(f) = i\chi_{yy}\epsilon(f)$. By studying the net inductive coupling \tilde{L}_{tot} as function of frequency over a broad frequency bandwidth $\simeq (20 - 30)$ GHz and fitting it to Eq. (5.8), we can hence extract the field- and damping-like spin torque conductivities. However, we need to account for the evolving ellipticity via $\epsilon(f)$ as function of f , by inserting $H_{\text{ext}} = H_{\text{res}}(f)$ in Eq. (2.31).

- $\mathbf{H}_{\text{ext}} \parallel \mathbf{b}$ (ip, $\mathbf{a} \rightarrow \mathbf{x}$, $\mathbf{b} \rightarrow \mathbf{y}$, $\mathbf{c} \rightarrow \mathbf{z}$):

For the other possible ip-geometry $\mathbf{H}_{\text{ext}} \parallel \mathbf{b}$, Eq. (5.7) can be simplified to

$$\tilde{L}_{\text{tot}} = \mu_0 \frac{ld_{\text{FM}}}{4w_{\text{cc}}}. \quad (5.9)$$

Notably, in this ip-geometry, the contribution of the spin torques to \tilde{L}_{tot} vanishes. This can be easily understood, as the inverse spin torque currents

⁴Here, we again map the coordinate system (\mathbf{x} , \mathbf{y} and \mathbf{z}) of the magnetization dynamics from Fig. 2.2 onto that of the sample on the CPW (\mathbf{a} , \mathbf{b} and \mathbf{c}) in Fig. 3.4(b).

in this geometry are driven by the oop-component of the rf driving field h_c , which can not give rise to an inductance.

- $H_{\text{ext}} \parallel c$ (oop, $a \rightarrow y, b \rightarrow z, c \rightarrow x$):

Finally, in the oop-geometry, due to the circular magnetization precession ($\epsilon = 1$), the spin-orbit torque conductivities are linearly proportional to f via

$$\tilde{L}_{\text{tot}} = \mu_0 \frac{ld_{\text{FM}}}{4w_{\text{cc}}} + \text{sgn} \cdot f \cdot \frac{hL_{12} [-\sigma_f + i\sigma_d]}{4eM_S} \quad (5.10)$$

allowing for the simple detection of the spin torque conductivities.

Irrespective of the used geometry, the reduced inductance can be obtained from the change of the complex microwave transmission parameter in resonance ΔS_{21} by replacing L_0 by L_{tot} in Eq. (3.8) and solving by \tilde{L}_{tot} .

5.1.1 Modifications to the inductive detection technique in the superconducting state

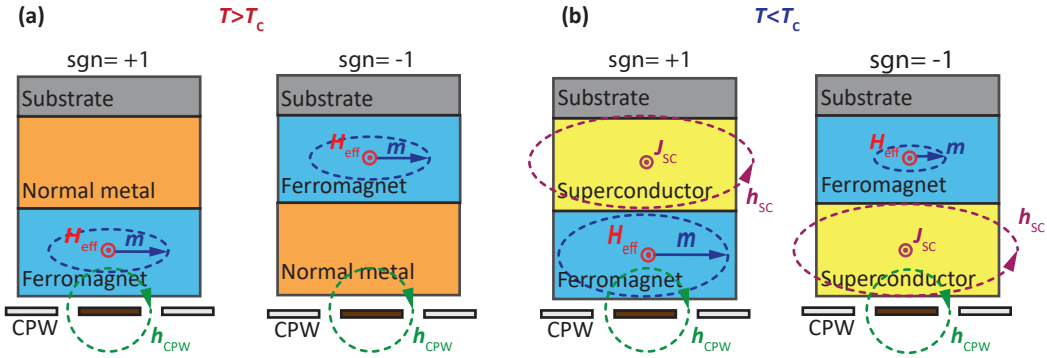


Fig. 5.1. – Illustration of the individual rf-driving field components $h_{\text{rf},i}$ driving the magnetization dynamics in substrate/SC/FM heterostructures ($\text{sgn} = +1$) and in substrate/FM/SC heterostructures ($\text{sgn} = -1$) above (a) and below (b) the superconducting transition temperature T_c . In the normal state [panel (a)] for $T > T_c$, the magnetization dynamics in the ferromagnet is asymmetrically driven from its top side by the driving field of the CPW h_{CPW} . As the driving field components from eddy currents flowing in the thin film superconductor, are negligible in the normal state, the magnetization precession magnitude m is independent of the stack sequence. In the superconducting state [panel (b)], for $T < T_c$, superconducting image currents create an additional driving field contribution h_{SC} and either enhance ($\text{sgn} = +1$) or reduce ($\text{sgn} = -1$) the net total driving field h_{rf} and correspondingly the precession amplitude of m . Figure is based on Ref. [122].

When replacing the normal metal layer in our NM/FM-heterostructures with a superconductor, the model by Berger et al. [84] needs to be modified to account for the unusual properties of superconductors, when exposed to both static and dynamic external magnetic fields in our FMR experiments. In detail, superconductors are perfect diamagnets ($\chi = -1$) that fully expel an external field with the magnetic field H_{ext} from their interior over a characteristic length scale

known as the London penetration depth λ_L [86, 306], which is typically in the $(10 \text{ nm} \leq \lambda_L \leq 100 \text{ nm})$ -range. This effect is known as the Meißner effect [307]. As the expulsion of \mathbf{H}_{ext} is associated with an energy cost, the formation of Cooper pairs of electrons in superconductivity is only energetically favorable up to a certain threshold known as the critical field magnitude H_c . There exists, however, type-II of superconductors, which avoids the energy cost associated with the magnetic field expulsion by forming a mixed state above a lower critical field. In this mixed state the superconductor contains so-called vortices which carry the magnetic flux $\Phi = \Phi_0 = h/2e$ and have a normal core. As a consequence, type II-superconductors are more resilient to external magnetic fields withstanding external oop magnetic fields of up to 50 T. In our experiments, we perform bbFMR in the ip-geometry $\mathbf{H}_{\text{ext}} \parallel \mathbf{a}$ to avoid the formation of normal state vortices in the SC layer in FMR experiments ($N_{xx}, N_{yy} \approx 0$) and thereby detect a larger effect from a SC layer, which is only weakly penetrated by vortices in the sample plane, while simultaneously being able to inductively detect the spin torque conductivities in the normal and superconducting state [see Eq. (3.10)]. When studying the FMR amplitude A in SC/FM-heterostructures in the superconducting state, we indirectly observe the superconducting Meißner effect. Depending on the stack sequence, A is either enhanced in the case $\text{sgn} = +1$ for substrate/SC/FM heterostructures or reduced for $\text{sgn} = -1$ for substrate/FM/SC heterostructures. This is due to the fact, that for substrate/SC/FM heterostructures, rf Meißner currents in the SC layer mirror the external driving field of the CPW \mathbf{h}_{CPW} [308] and thus lead to a net enhanced rf driving field \mathbf{h}_{rf} , whereas in the latter case for substrate/FM/SC heterostructures, the SC is 'sandwiched' between FM and CPW and hence its Meißner screening currents generate a driving field that counteracts \mathbf{h}_{CPW} . This effect is schematically illustrated in Fig. 5.1. The enhancement of A can be well explained by superconducting image charge currents repelling the oscillatory driving field of the CPW \mathbf{h}_{rf} . Moreover, we note that the CPW detects only the upper half of the flux Φ_{dyn} generated by the precessing macrospin \mathbf{M} of the FM layer in the normal state. However, for the stack sequence substrate/SC/FM ($\text{sgn} = +1$), this fraction is enhanced below T_c as the underlying superconductor also expels the lower half of Φ_{dyn} from its interior via image currents and thereby essentially enhances the flux felt by the CPW. Consequently in the superconducting state the magnetization of the FM layer is not only driven with twice the net driving field \mathbf{h}_{rf} , which overall enhances the precession amplitude A by a factor of 4, but the CPW also detects twice the net flux generated by the dynamically precessing \mathbf{M} . As a result an overall enhancement in FMR signal of up to 8 times is possible. We note that this effect is not restricted to superconductors and can likewise also be observed for NM/FM-heterostructures, when the NM layer is a good electric conductor giving rise to pronounced eddy screening currents. In Ref. [308], a 7-fold increase in FMR-amplitude has been observed in thick Au/Co-heterostructures. Therefore, the enhanced FMR ampli-

tude in NM/FM-heterostructures compared to bare FM layers incorporating both thick and highly conductive NM layers might enable the characterization of even thinner FM potentially down to VdW monolayer materials such as $\text{Cr}_2\text{Ge}_2\text{Te}_6$, which are of interest for integrated spintronics devices [309–311]. In our experiments, substrate/SC/FM-heterostructures with $\text{sgn} = +1$ are used to benefit from the enhanced A in the SC state. Experiments on inverted stack sequences with $\text{sgn} = -1$ yielded bad fitting results in the superconducting state due to the strongly reduced inductive coupling, when the SC screens the FM layer from the driving field of the CPW [122]. The greatly altered inductive coupling strength of SC/FM-heterostructures in the SC state compared to the normal state requires a modification of Ref. [84], where a constant \tilde{L}_0 between FM and NM irrespective of stacking order and sample conductivity is assumed. From Eqs. (3.3) and (5.8), we note that the inductive coupling between FM layer and CPW \tilde{L}_0 scales quadratically with the net oscillatory driving field amplitude h_{rf} , whereas the inductive coupling to the NM/SC-layer \tilde{L}_J is only linearly proportional to h_{rf} . Thus, we normalize our spin torques $\sigma_{\text{ST}}^{\text{SC}}$ in the SC state to a constant \tilde{L}_0 detected in the normal state by adding the normalization factor $E^{1/2}$, where E is the enhanced inductive coupling between sample and CPW in the SC state, to \tilde{L}_J in Eq. (5.8). Another modification to the model of Berger et al., [84] required in the SC state stems from the contribution of Faraday currents σ_{F} to σ_{ST} as σ_{F} is reciprocally proportional to the effective surface impedance Z_{eff} of the heterostructure via

$$\sigma_{\text{F}} = \frac{e\mu_0 M_s d_{\text{FM}}}{\hbar Z_{\text{eff}}(f)}. \quad (5.11)$$

In the normal state, Z_{eff} is assumed to be constant with frequency [84] for the sake of simplicity. Superconductors, however, exhibit a surface impedance, which is strongly frequency-dependent. For Z_{eff} , we use [86]

$$Z_{\text{eff}}(f) = 4\mu_0^2 \pi^2 \lambda_{\text{eff}}^3 \sigma_0 \frac{n_n}{n} - i \cdot \mu_0 2\pi f \lambda_{\text{eff}} \quad (5.12)$$

Here, σ_0 is the normal state electric conductance of the SC layer, n_n/n is the fraction of the normal-conducting phase below T_c and $\lambda_{\text{eff}} = \lambda_{\text{L}}^2/d_{\text{SC}}$ is the thin film London penetration depth [312]. In the following, we neglect the real part of Eq. (5.12), which is a valid approximation for frequencies in the low to intermediate GHz range. To account for the frequency-dependent surface impedance of superconductors, we insert the imaginary part of Z_{eff} from Eq. (5.12) in Eq. (5.11) resulting in

$$\sigma_{\text{F}} = i \cdot \frac{eM_s d_{\text{FM}} \cdot d_{\text{SC}}}{\hbar f \lambda_{\text{L}}^2}. \quad (5.13)$$

As the inverse proportionality of σ_{F} to f in Eq. (5.13) cancels out with the linearly f -scaling of the spin torque conductivities in Eq. (3.10), in the superconducting state Faraday currents create an offset \tilde{L}_{F} in the imaginary part in the superconducting

state, which scales as function of temperature with the London penetration depth λ_L^2 .

Taking the enhanced inductive coupling and frequency-dependent surface impedance in the superconducting state into account, the net reduced inductive coupling between substrate/SC/FM-heterostructure (sgn = +1) and CPW in the ip-geometry $\mathbf{H}_{\text{ext}} \parallel \mathbf{a}$ takes the form

$$\tilde{L}_{\text{tot}} = \begin{cases} \tilde{M}_0 E + i \cdot \frac{\tilde{L}_F}{[\epsilon^2(f)+1]} + f \cdot C \sqrt{E} \frac{-\sigma_f + i\sigma_d \epsilon(f)}{[\epsilon^2(f)+1]}, & \text{for } T \leq T_c, \\ \tilde{L}_0 + f \cdot C \frac{[-\sigma_f + i\sigma_d \epsilon(f)]}{[\epsilon^2(f)+1]}, & \text{for } T > T_c. \end{cases} \quad (5.14)$$

Here, we have introduced the constant inductive coupling constant $C = hL_{12}/4eMs$ and E is the dimensionless enhancement factor. We note, that the field-like torque conductivities σ_{iREE} and σ_F scale differently with frequency in the SC state allowing for their separate determination below T_c , whereas they can not be disentangled via symmetry arguments in the normal state (see Sec. 2.3.1). However, in the superconducting state, additional contributions to σ_f can manifest for example from supercurrent-induced spin orbit torques [299] or the theoretically proposed vortex spin Hall effect [276]. Hence, we also denote the net field-like spin torques in the superconducting state as σ_f .

5.2 Spin torques in NbN/Py-heterostructures

Our SC/FM-heterostructures are deposited on Si (001) substrates with a 1 μm thick thermally grown SiO_2 -capping layer in the Superbowls sputtering machine (see Sec. 3.1.5). For our initial study [68], we chose NbN as our superconducting layer due to its resilience to external magnetic fields ($\mu_0 H_{c2} \leq 15 \text{ T}$ [86]) and high superconducting transition temperature of up to $T_c = 16.8 \text{ K}$ [313–315]. These properties render NbN an ideal candidate for bbFMR at cryogenic temperatures as it offers both a large margin in experimentally accessible temperatures between $T = 2 \text{ K}$ and T_c and also in the magnitude of the applied external field H_{ext} , which directly translates to the bandwidth of applicable driving frequencies f in bbFMR [122]. We grew NbN both on the bare substrate and on Pt to investigate its spin pumping properties. Here, we chose the alloy $\text{Ni}_{80}\text{Fe}_{20}$ (Permalloy, Py) for its resilient magnetic properties irrespective of the base layer, it is grown on. Lastly, we deposited a thin capping layer of Ta on our FM to protect it from oxidization. The respective sputtering parameters of the individual materials are listed in the Appendix in Tab. B1. While the thickness of NbN (16 nm) and Py (6 nm) are constant, the Pt, acting as a spin sink, is varied in thickness and position within the layer sequence. The stack sequences of the four samples A-D investigated in our initial study are illustrated in Fig. 5.2. Note, that all samples are grown in the stacking order substrate/SC/FM corresponding to sgn = +1 in Eq. (5.5).

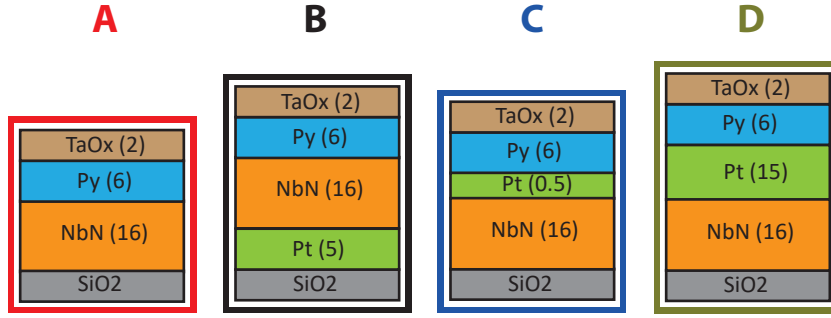


Fig. 5.2. – Layer stack of samples investigated in this thesis. Numbers show the layer thicknesses in nm. For bbFMR, they are mounted face-down on top of a coplanar waveguide.

Sample	A	B	C	D
T_c [K]	11.5	9.0	10.0	10.2

Tab. 5.1. – Superconducting transition temperature T_c of the samples investigated in this study.

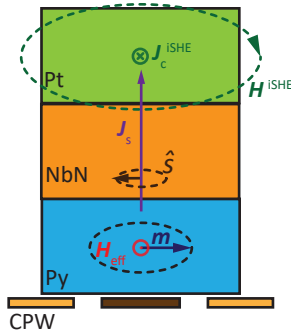


Fig. 5.3. – Schematic illustration for the generation of the charge current density J_c^{iSHE} by ac iSHE. The ac flux $\Phi^{\text{iSHE}} \propto \mathbf{H}^{\text{iSHE}}$ generated by J_c^{iSHE} is coupled into the CPW. Note, that in this figure, the aspect ratio between sample thickness and center conductor width of the CPW is distorted.

The layer thickness $d_{\text{SC}} = 16$ nm of NbN was chosen to be as thin as possible, while maintaining a reasonable T_c . The superconducting transition temperatures of the samples are listed in Tab. 5.1. The contactless method, with which T_c is determined from the complex scattering parameter S_{21} is explained in the Appendix C.

For the FM layer, the thickness of Py $d_{\text{FM}} = 6$ nm was selected to ensure a good signal-to-noise ratio. For these samples, we perform bbFMR experiments in the ip-geometry $\mathbf{H}_{\text{ext}} \parallel \mathbf{a}$ in Fig. 3.4(b) and characterize the magnetization dynamics parameters and spin-torque conductivities as function of temperature around T_c using the Chaos cryostat (see Sec. 3.3.1). For the frequency bandwidth, we chose the range ($10 \text{ GHz} \leq f \leq 36 \text{ GHz}$) at a VNA output power of 1 mW, such that all dynamics are in the linear response regime.

To describe the physics at play in our samples, we begin by discussing the spin pumping in sample configuration B. In the normal state for $T > T_c$, the resonantly precessing magnetization of the Py layer pumps a spin current density J_s across the Py/NbN interface ($T > T_c$) and through the NbN into the adjacent Pt layer as illustrated in Fig. 5.3. In the Pt layer, J_s is absorbed and converted into a charge current with density J_c via the iSHE, where we assume vanishing iSHE contributions from the SC-layer due to the small spin Hall angle of NbN [279]. On

the one hand, this spin pumping effect causes damping and manifests itself as an additional broadening of the FMR (see Sec. 2.3). On the other hand, the ac charge current density \mathbf{J}^{iSHE} generated by the iSHE generates an ac magnetic field which is inductively coupled into the CPW and thus can be detected as a non-zero σ_d in \tilde{L} . Here, it is important to note, that in Fig. 5.3, the aspect ratio between sample thickness and center conductor width of the CPW is distorted. In our experiments, the NbN and Py layers are very thin in the nm-range. Hence, flux induced by the iSHE in the Pt layer Φ^{iSHE} can be efficiently coupled into the CPW.

In contrast, sample configuration A serves as a reference sample, where we expect negligible effects of spin pumping and the iSHE due to the missing Pt layer. In sample C, we insert a very thin Pt interlayer between SC and FM, which is expected to both enhance the spin torque conductivities in the SC state and potentially induce an exchange field in the SC to promote the formation of spin-triplet Cooper pairs [49, 274]. Finally, in sample D, the angular momentum injected from the Py layer is pumped directly into and absorbed in the Pt layer. Consequently, we expect to observe both an enhanced Gilbert damping and σ_d , irrespective of the state of the SC layer. Hence, in this sample, the SC and FM layer can be viewed as uncoupled.

The ferromagnetic resonance field $H_{\text{res}}(f)$, linewidth $\Delta H(f)$ as well as real and imaginary part of the reduced inductive coupling $\tilde{L}(f)$ recorded for sample B are plotted in Fig. 5.4 for temperatures slightly below ($T \approx 0.8T_c$) and above ($T \approx 1.2T_c$) the superconducting transition temperature of the NbN layer.

The raw data for $H_{\text{res}}(f)$, $\Delta H(f)$ and $\text{Re}/\text{Im}[\tilde{L}(f)]$ of the other samples A, C and D in both the normal- and superconducting state is presented in the Appendix Sec. D. The magnetization dynamics parameters are extracted by fitting the raw data in panels (a) and (b) with Eq. (2.26) and the data in panels (c) and (d) with Eq. (2.28), whereas the spin-torque conductivities are extracted by fitting the raw data with the real (e), (f) and imaginary part (g), (h) of Eq. (5.14). For $H_{\text{res}}(f)$, we use the modified ip-Kittel fit in Eq. (2.26) to allow for an oop-anisotropy induced by superconducting Meißner currents as observed in Refs. [287, 316]. The fitted g -factor, effective magnetization M_{eff} , out-of-plane magnetic anisotropy field $H_{\text{ani}}^{\text{oop}}$ and inhomogeneous line broadening H_{inh} of the four samples A-D around T_c as function of the reduced temperature are shown in Fig. 5.5.

From Fig. 5.5 panels (a) and (b), we find that both the g -factor and effective magnetization M_{eff} are comparable for all samples and are unaffected by the onset of superconductivity. The values of $g \approx 2.1$ and $\mu_0 M_{\text{eff}} \approx 0.97 \text{ T}$ are comparable with literature values for Py [124, 125, 137, 317, 318]. Notably, we observe a slightly larger g -factor for the samples C and D with a direct Py/Pt-interface, which we attribute to the small field-like contribution of $\text{Im}(G_{\uparrow\downarrow})$ in Eq. (2.33). As the effective magnetization $\mu_0 M_{\text{eff}}$ in Fig. 5.5(b) is comparable to literature values for $\mu_0 M_s$ [124, 125, 317], we can rule out the presence of an in-plane magnetic anisotropy in our samples. For the out-of-plane anisotropy field $H_{\text{ani}}^{\text{oop}}$ in Fig. 5.5(c),

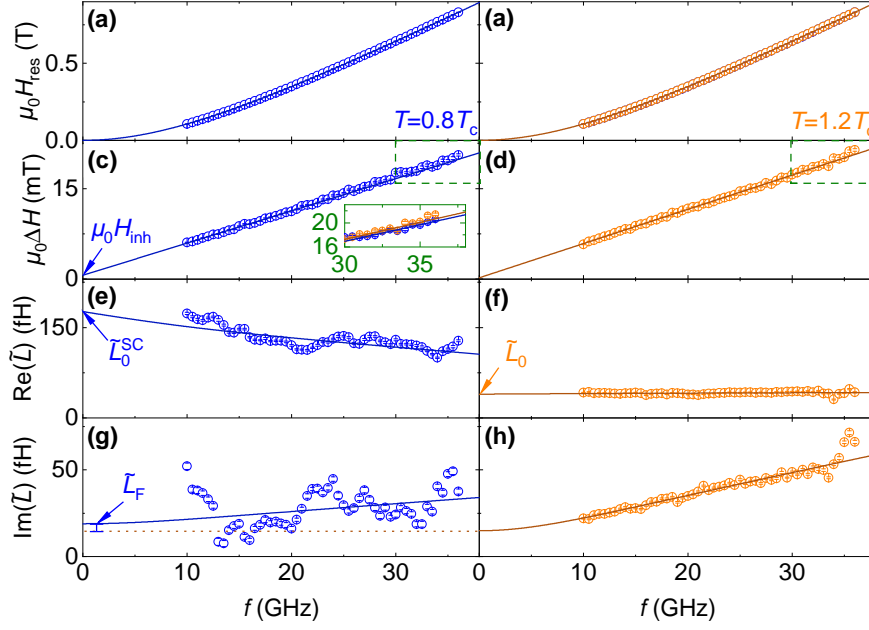


Fig. 5.4. – Resonance field $H_{\text{res}}(f)$ and linewidth $\Delta H(f)$ as well as reduced inductive coupling $\text{Re}(\tilde{L})$ and $\text{Im}(\tilde{L})$ for sample B for temperatures slightly below and above T_c together with the fitting curves according to Eq. (2.26) [(a) and (b)], Eq. (2.28) [(c) and (d)] and Eq. (5.14) [(e)–(h)]. The green dashed box and inset in panel (c) indicates the reduction in ΔH in the superconducting state as the orange data points representing the magnetic linewidth above T_c are situated above the blue data points of the magnetic linewidth below T_c . The dark orange dotted line in panel (g) represents the normal state offset in $\text{Im}(\tilde{L})$.

we observe small positive values in particular for the samples C and D with a direct Py/Pt-interface induced by the spin-orbit interaction in Pt [102–105] (see Sec. 2.1). In the superconducting state, a small increase in $H_{\text{ani}}^{\text{oop}}$ is observed for samples A, B and D due to the field induced by the superconducting Meißner currents, which is in agreement to the findings in Refs. [287, 316]. The low magnitude of the change in $H_{\text{ani}}^{\text{oop}}$ is attributed to the small thickness of the NbN layer. For sample C, $H_{\text{ani}}^{\text{oop}}$ remains roughly constant as function of T , which indicates that the oop-contribution of Pt dominates compared to that of the superconducting Meißner currents. We observe in Fig. 5.4(c) a slightly reduced FMR-linewidth ΔH below T_c , which together with an enhanced inhomogeneous broadening H_{inh} translates into a reduced Gilbert damping contribution α in the superconducting state (see inset in Fig. 5.4). The temperature dependence of α is discussed in great detail together with the damping-like inverse spin torque conductivity in the interpretation of Fig. 5.7. The inhomogeneous linewidth broadening H_{inh} as a function of reduced temperature for all samples is plotted in Fig. 5.5(d). We detect the manifestation of a sizable H_{inh} in the superconducting state, which is likely caused by an incoherent precession of M at the FM/SC-interface as proposed in Ref. [287]. The non-constant H_{inh} as function of T demonstrates the necessity to study the evolution of the FMR-linewidth ΔH over a large frequency range to

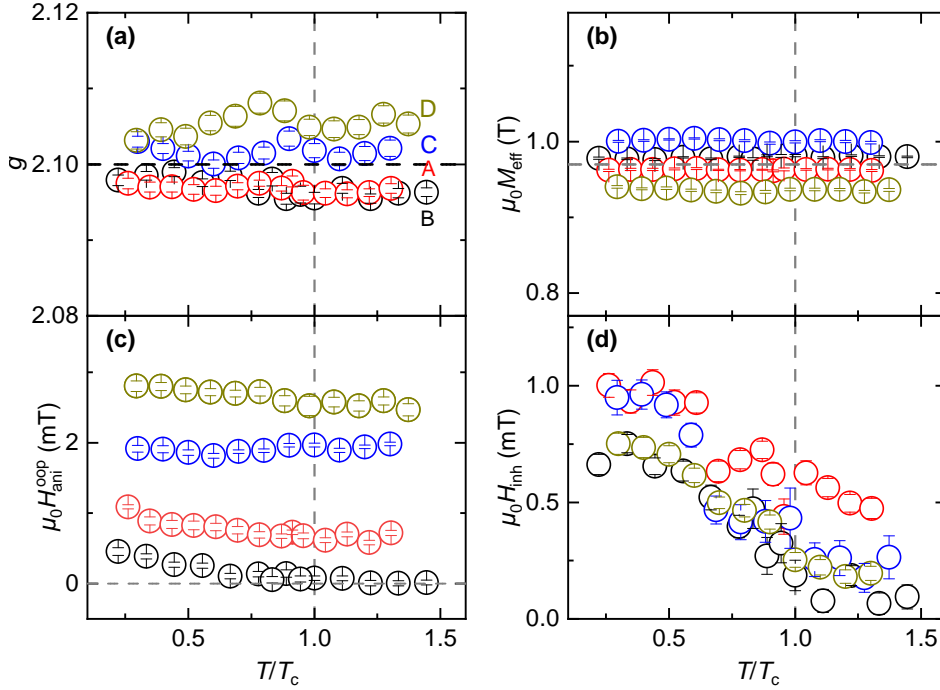


Fig. 5.5. – Temperature dependence of the magnetization dynamics parameters for the samples A-D. Both the g -factor in (a) and the effective magnetization M_{eff} in (b) exhibit no changes in the superconducting state. (c) The out-of-plane magnetic anisotropy field $H_{\text{ani}}^{\text{oop}}$ increases due to a magnetic out-of-plane field contribution from the induced Meißner fields in the superconducting state. (d) The change of the inhomogeneous FMR linewidth broadening H_{inh} in the superconducting state is attributed to the non-uniform magnetization precession.

reliably study the spin pumping properties of superconducting materials as will be later exemplified in the discussion of Fig. 5.8.

In contrast to the minor changes in resonance field and linewidth in Fig. 5.4(a)-(d), for the reduced inductive coupling \tilde{L} we observe a dramatic change below T_c a large increase in magnitude in panels (e) and (g) compared to their normal state counterparts in panels (f) and (h) due to superconducting image currents enhancing the net total driving field h_{rf} and correspondingly the precession amplitude of m [see Fig. 5.1(b)]. The enhancement factor $E \approx 4.5$ can be extracted from the y-axis intercept of \tilde{L} via $\tilde{L}_0^{\text{SC}}/\tilde{L}_0$ [see Eq. (5.14)]. Apart from the significantly enhanced inductive coupling in \tilde{L}_0 , we also observe an altered frequency-evolution of $\tilde{L}(f)$ in panels (a)-(d). In the normal state, we observe a negligible slope in $\text{Re}(\tilde{L})$ in panel (f), indicating the presence of only weak field-like σ_f . For metallic NbN, this is expected, as it is neither a good conductor causing sizable Faraday currents nor a material with large spin-orbit interaction giving rise to charge currents from the iREE. In the superconducting state, however, we observe a large negative slope in $\text{Re}(\tilde{L})$, which will be discussed in detail in the following subsection. For the imaginary part of \tilde{L} above T_c in panel (h), we detect a sizable positive slope from charge currents generated by the iSHE in the Pt layer 5.3. This result indicates, that substantial spin currents can be transmitted across the 16 nm thick NbN layer.

This is in agreement with literature predicting a spin decay length of $\lambda_{\text{sd}} = 14$ nm in NbN [279]. Below T_c , the slope in panel (g) is reduced, which demonstrates the altered spin transport properties in the superconducting state. In our fitting routine, we allow for a y -axis intercept in the imaginary part $\text{Im}(\tilde{L})$ instead of applying a rotational matrix with the angle β to the data as performed in Ref. [84]. Below T_c , we expect this offset to increase due to Faraday currents [Eq. (5.13)] giving rise to the inductive contribution \tilde{L}_F . In our experimental data, we hence define \tilde{L}_F as the change in $\text{Im}(\tilde{L}_0)$ in the superconducting state [see Fig. 5.4(g)]. To get a qualitative picture for the evolution of the reduced inductances \tilde{L}_0 and $\tilde{L}_J(f)$ from the inductive coupling of the CPW with the FM layer and to the NbN and Pt layer, we fit \tilde{L} in Fig. 5.4(e)-(h) with

$$\begin{aligned}\tilde{L}(f) &= \tilde{L}_0 + \tilde{L}_J(f) \\ &= \tilde{L}_0 + \frac{f}{\epsilon^2(f) + 1} \cdot [\text{Re}(\Delta\tilde{L}_J) + i \cdot \text{Im}(\Delta\tilde{L}_J)\epsilon(f)].\end{aligned}\quad (5.15)$$

Here, we define $\Delta\tilde{L}_J$ as the linear frequency dependence of \tilde{L}_J , which corresponds to the contribution to \tilde{L} of the inverse spin torques [see Eq. (5.14)]. The real (triangles) and imaginary part (squares) of the fitted \tilde{L}_0 and \tilde{L}_J are plotted for sample B as a function of reduced temperature in Fig. 5.6(a) and (b), respectively.

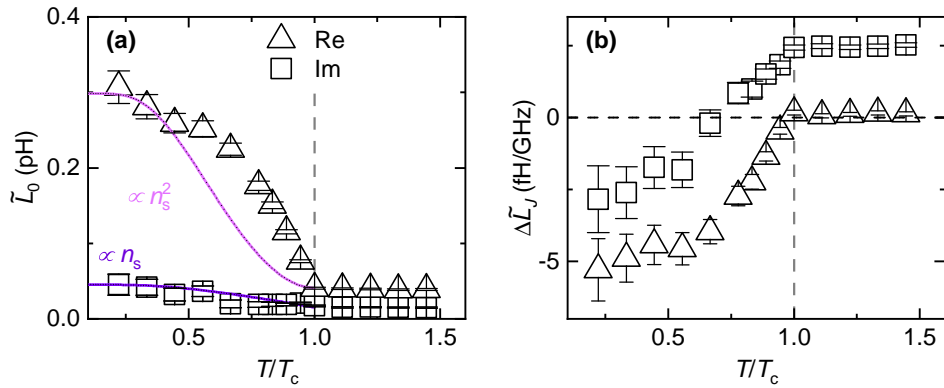


Fig. 5.6. – Reduced inductive coupling parameters for sample B plotted as a function of reduced temperature around T_c . In (a), we plot the real (triangles) and imaginary (squares) parts of the inductive coupling offset \tilde{L}_0 . In (b), we show real (triangles) and imaginary part (squares) of the complex linear frequency dependence $\Delta\tilde{L}_J$ of the reduced inductance \tilde{L} . The colored lines indicate the scaled Cooper pair density n_s following BCS-theory and the error bars originate from fitting the extracted raw data for \tilde{L} with Eq. (5.15).

Compared to \tilde{L}_0 at $T > T_c$, we observe in Fig. 5.6(a) a strongly enhanced inductive coupling strength $\text{Re}(\tilde{L}_0)$ between the FM layer and CPW in the SC state due to the enhanced FMR amplitude, that gradually increases with decreasing T . A net enhancement factor of $E \approx 7$ is observed for the lowest experimentally accessible temperature. This result is compatible with the FMR-amplitude enhancement observed for the FMR in Co, when using thick and highly conductive

Au seedlayers in Ref. [308]. In a naive picture, the temperature dependence of $\text{Re}(\tilde{L}_0)$, can be mapped to that of the superconducting image currents $\mathbf{J}_{\text{SC}}(T)$ via

$$\mathbf{J}_{\text{SC}}(T) = -2en_s(T) \cdot \mathbf{v}_s, \quad (5.16)$$

where e is the electron charge, n_s is the superconducting Cooper pair density and \mathbf{v}_s is the Cooper pair drift velocity in the superconducting state. Since these image currents give rise to a net driving field \mathbf{h}_{rf} that quadratically scales with \tilde{L}_0 according to Eq. (3.3), we expect that the enhancement in \tilde{L}_0 also scales quadratically with n_s . We model n_s^2 following BCS-theory [319,320] (For details see Ref. [122]), via

$$n_s(T) = n_n/2[1 - Y(T)], \quad (5.17)$$

where n_n is the normal state electron density and $Y(T)$ is the Yosida function

$$Y(T) = \frac{1}{D(E_F)} \sum_{\mathbf{k}} -\frac{\partial f(E_{\mathbf{k}})}{\partial E_{\mathbf{k}}}. \quad (5.18)$$

Here, $D(E_F)$ is the density of states at the Fermi energy and $f(E_{\mathbf{k}})$ is the Fermi-Dirac distribution of quasiparticles with energy $E_{\mathbf{k}}$. The square of the particle density n_s^2 is shown as a pink line in Fig. 5.6(a). We find that the predicted temperature dependence of $\tilde{L}_0(T)$ scales more strongly with T than what is observed experimentally. We attribute this disparity to the rising contribution of the superconducting kinetic inductance L_k to \tilde{L}_0 for elevated temperatures [321]. In analogy to $\text{Re}(\tilde{L}_0)$, we observe an increase in $\text{Im}(\tilde{L}_0)$ in the superconducting state, while $\text{Im}(\tilde{L}_0) \approx 0$ in the normal state for $T > T_c$. This increase in $\text{Im}(\tilde{L}_0)$ in the SC state is expected to appear due to the complex surface impedance $Z_{\text{eff}}(\omega)$ in the superconducting state [see Eq. (5.14)]. As the London penetration depth λ_L is related to the superconducting Cooper pair density via $\lambda_L^2 \propto 1/n_s$ (see London equations [86,306]) and $\tilde{L}_F \propto 1/\lambda_L^2$ [see Eq. (5.13)], we model the enhancement in $\text{Im}(\tilde{L}_0)$ in the superconducting state with a theory curve to $n_s(T)$ following Eq. (5.17) in Fig. 5.6(a) (purple line) and observe a good agreement with our raw data. We now turn to the linear contribution $\Delta\tilde{L}_J$ shown in Fig. 5.6(b). Note that $\Delta\tilde{L}_J \neq 0$ is observed when electrical ac currents are generated in the NM/SC-layers by the magnetization dynamics $\mathbf{m}(t)$ in the FM and the real and imaginary part of $\Delta\tilde{L}_J$ are respectively attributed to the manifestation of field- and damping-like inverse spin torques. We find that both $\text{Re}(\Delta\tilde{L}_J)$ (triangles) and $\text{Im}(\Delta\tilde{L}_J)$ (squares) change sign and exhibit large negative values in the superconducting state. This result indicates the modification of both field- and damping-like spin torque conductivities σ_d and σ_f in the superconducting state, which are linearly proportional to the real and imaginary part of $\Delta\tilde{L}_J$. The extracted damping-like and field-like current-induced torques σ_d and σ_f derived for the four samples in Fig. 5.2 are plotted in Figs. 5.7 and 5.9, respectively. In Fig. 5.7(a), we observe large

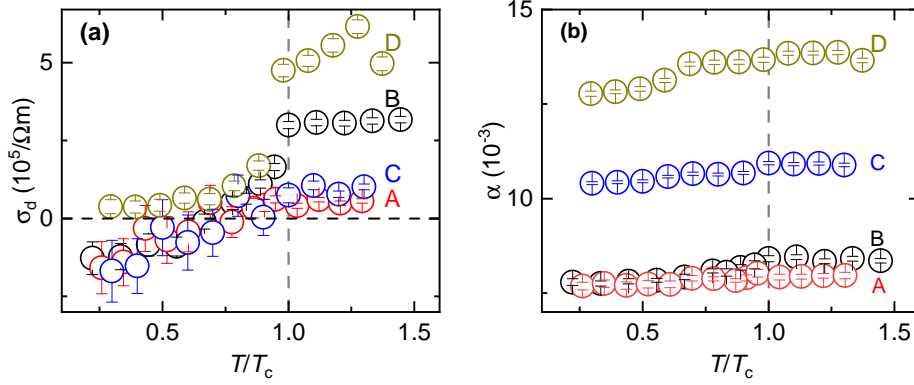


Fig. 5.7. – (a) Damping-like spin torque conductivity σ_d plotted as a function of T/T_c . In the normal state, the samples B and D containing a thick Pt layer exhibit a large positive σ_d due to the iSHE in Pt. Below T_c , all samples show a very similar decay of σ_d with decreasing T irrespective of Pt spin sink layer. (b) Temperature dependence of the Gilbert damping α in the SC state as a function of T/T_c . The apparent decrease of α is due to the suppression of spin pumping into the SC due to the freeze-out of thermally excited quasiparticles. The error bars originate from fitting the extracted raw data for \tilde{L} with Eq. (5.14) (a) and Eq. (2.27) for $\Delta H(f)$ (b).

σ_d values for the samples B and D in the normal state for $T > T_c$ as expected from the iSHE in Pt. In contrast, sample A (NbN/Py bilayer) exhibits only a small positive σ_d despite the negative spin Hall angle in NbN [47,279], which has been confirmed for our NbN thin films in Ref. [322]. We attribute this observation to a small contribution of the Py layer to the iSHE. This contribution to σ_d dominates in the normal state compared to that of the NbN layer due to its higher conductivity. For sample C, we detect a low σ_d , indicating the reduction in the spin-to-charge current conversion due to the low thickness of the Pt layer in sample C. Overall, the normal state results can be consistently understood in a picture where the Pt layer acts as a spin sink and efficiently converts spin- into charge currents. The NbN layer takes a passive role as a spin transparent layer, which does itself not give rise to a detectable contribution to σ_d .

In the superconducting state, σ_d rapidly decreases below T_c and eventually reaches a similar slightly negative value for samples A, B, and C, while staying slightly positive for sample D. There are two effects that affect σ_d in the SC state: First, there is a strongly modified spin transport carried by thermally excited quasiparticles in the SC [50,257] and, second, there is an electrical shunting effect of charge currents by the SC [323,324]. We again start our discussion with the physics at play in sample B. Here, the injected spin current has to pass the SC layer to reach the Pt layer, such that altered spin transport properties in the SC play an especially important role in this sample. In contrast, in sample A, angular momentum is injected exclusively into the superconducting NbN layer and we only expect the detection of a non-zero σ_d in the superconducting state in the presence of a sizable iSHE. Similarly, for sample C, as we do not observe a sizable iSHE from the thin Pt layer in the normal state, we also expect dominant spin

injection into the NbN layer. Finally, in sample D, the dominant source of iSHE in the normal state is the Pt-layer and no spin current can reach the SC due to the small spin decay length $\lambda_S \simeq 4 \text{ nm}$ [40] in Pt. Hence, sample D serves as a reference sample, where no spin current is pumped into the superconductor. In this picture. The small negative values of σ_a in samples A, B and C below T_c are consistent with the quasiparticle mediated inverse spin Hall effect (QMISHE) in superconductors [325–328], whereas the reduced positive σ_a of sample D is attributed to a superconducting shunting effect of the charge currents generated by the iSHE [323, 324]. In Ref. [47] the QMISHE in NbN has been observed via non-local dc transport measurements utilizing non-local lateral spin injection devices as a significantly enhanced iSHE voltage for reduced T . In our bbFMR experiments, we instead detect a saturation of σ_a towards negative values for $T \mapsto 0 \text{ K}$. This discrepancy can be explained by the different applied detection techniques:

We detect the flux generated by the dynamic J_c (caused by the spin-to-charge current conversion via the QMISHE) as a change in inductive coupling strength between NbN layer and CPW, whereas Wakamura *et al.* [47] measured the accumulation of electron- and hole-like quasiparticles on opposite sides of a superconducting NbN strip as a voltage signal. For nonlocal devices the spin Hall resistance ΔR_{SH} generated by quasiparticles is proportional to both quasiparticle resistance ρ_{qp} and spin Hall angle Θ_{SH} . Following Refs. [47, 329], ρ_{qp} is obtained by normalizing the normal state longitudinal resistance ρ_{long} to the amount of quasiparticles populated above the superconducting gap Δ at a certain temperature T , which is given by the Fermi distribution $f_0(\Delta(T))$ resulting in

$$\rho_{\text{qp}} = \rho_{\text{long}} / [2f_0(\Delta(T))]. \quad (5.19)$$

Here ρ_{long} is the normal state longitudinal resistivity along the NbN strip. From Eq. 5.19, the increase in ρ_{qp} for low temperatures immediately becomes apparent, as $f_0(\Delta(T))$ decreases with the increasing superconducting gap $\Delta(T)$. The spin Hall angle Θ_{SH} on the other hand comprises extrinsic contributions from both side jump (SJ) [330]- and skew scattering [331] (SS) as well as intrinsic effects [332]. By taking all these three contributions into account, the Hall resistivity ρ_{SH} can be expressed as

$$\rho_{\text{SH}} = a\rho_{\text{long}} + b\rho_{\text{long}}^2, \quad (5.20)$$

where a and b are proportionality constants quantifying the impact of skew scattering (a) and SJ-scattering plus intrinsic effects (b), respectively. As established in Sec. 2.3.1, the spin Hall angle is defined as the ratio between spin Hall and longitudinal resistance $\Theta_{\text{SH}} = \rho_{\text{SH}} / \rho_{\text{long}}$. Consequently, in the normal state, it takes the form

$$\Theta_{\text{SH}} = a + b\rho_{\text{long}} \quad (5.21)$$

resulting in a linear function with respect to ρ_{long} . To account for the enhanced longitudinal resistance in the case of quasiparticle charge transport in superconductors, we replace ρ_{long} in Eq. (5.21) with the QP resistance ρ_{qp} from Eq. (5.19). Consequently, the intrinsic and side-jump contributions to Θ_{SH} diverge with ρ_{qp} for decreasing T in the SC state. As a result, in non-local spin current experiments, a dramatically enhanced spin Hall resistance $\Delta R_{\text{SH}} \propto \rho_{\text{qp}} \Theta_{\text{SH}}$ as observed by Wakamura *et al.* is in agreement with theoretical predictions. In our experiments on the other hand, we measure the flux generated by charge currents generated by the QMiSHE (J_c^{iSHE}) instead of ΔR_{SH} (the open circuit voltage). The corresponding damping-like σ_d is related to the spin Hall angle via $\sigma_d \propto \Theta_{\text{SH}}/\rho_{\text{qp}}$ following Ref. [84]. Consequently, the divergent ρ_{qp} cancels out, leading to a net constant value for σ_d . This theoretical prediction is in agreement with our results for σ_d in Fig. 5.7, which appear to saturate at slightly negative values for $T \rightarrow 0$ K. Furthermore, in this picture, the negative sign of σ_d can be attributed to the negative spin Hall angle in NbN [47, 279]. In summary, by using existing theoretical models for the quasiparticle-mediated inverse spin Hall effect (QMiSHE), we can satisfactorily explain our results for the damping-like σ_d in samples A-C below T_c . Deviations in the detected quantitative magnitude of this effect from results of Wakamura *et al.* in Ref. [47] originate from the different applied detection methods. For sample D, we observe no negative σ_d as the spin currents are absorbed in the Pt layer and the transition into the superconducting state NbN has no influence on this absorption. However, we do observe a strong reduction in σ_d , which indicates that the adjacent NbN nonetheless alters the spin-to-charge current conversion process in Pt. We attribute this reduction in σ_d to a shunting process of the NbN layer, which reduces the charge current density J_c^{iSHE} in Pt and as a result also σ_d . Likewise, a strong reduction in the detected magnitude of the iSHE in Pt due to shunting effects when brought into contact with highly conductive Cu has been reported in Refs. [323, 324]. Here, we observe an analogue shunting effect for superconductors, giving rise to the same strong suppression of the iSHE.

To support the validity of our inductive analysis technique and the interpretation of our results, we compare the damping-like σ_d to the extracted Gilbert damping α of the Py layer, which is plotted as a function of T/T_c in Fig. 5.7(b). Due to the spin pumping contribution α_{SP} to α [see Eq. (2.35)], the Gilbert damping also directly probes spin current transport in our heterostructures. The magnitude of α for sample A well matches literature values for the damping of Py thin films [124, 125, 137, 317, 318] and hence serves as our reference sample in the absence of spin pumping into Pt. Consequently, the larger α of samples B-D can be attributed to spin pumping into their respective Pt layers. Consequently, we observe a substantial spin pumping contribution from Pt for all temperatures for samples C and D due to the direct Py/Pt-interface. For sample B, where the spin currents must transmit the NbN layer to enter the Pt, however, we observe for temperatures $T < T_c$, that the magnitude of α approaches the values of our

reference sample A. This suggests the strong suppression of spin pumping into Pt in the superconducting state in agreement to the results of Bell *et al.* [256]. Furthermore, similarly to Refs. [49,274], we detect an enhancement in the net FMR linewidth ΔH in the SC state at low frequencies in our samples as apparent in Fig. 5.8(a) and (b), where we plot both ΔH at $f_0 = 10$ GHz and Gilbert damping α for sample B as function of T/T_c . We find that ΔH increases, while α is reduced below T_c . Hence we do also observe changes in $\Delta H(T)$ in the superconducting

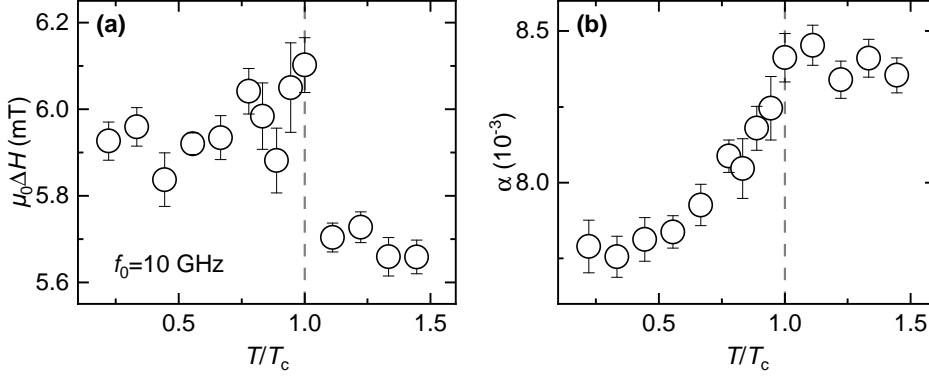


Fig. 5.8. – (a) FMR linewidth ΔH at $f_0 = 10$ GHz as function of reduced temperature for sample B. (b) Gilbert damping α of sample B as function of reduced temperature.

state in agreement to the changes observed by Jeon *et al.* (cf. Fig. 5.8), but differ in the interpretation of this result. We attribute the reduction of α in Fig. 5.8(b) to the SC blocking spin currents in agreement with Ref. [256], whereas Jeon *et al.* [49,274] attribute the increasing $\Delta H(T)$ in the superconducting state to an enhanced spin pumping contribution mediated by spin-triplet Cooper pairs. In sample C, the slight reduction of α below T_c in Fig. 5.7(b) results from the blocking of spin currents at the NbN/Pt-interface, whereas for sample D it is attributed to the SC shunting effect reducing the dissipation of angular momentum generated by the iSHE in the Pt layer. Even below T_c , the values for α of both samples C and D remain substantially larger than that of the reference sample A as the spin pumping at the Py/Pt-interface is not affected by the superconducting NbN on the other side of the Pt layer.

To summarize our results of Fig. 5.7, we observe in σ_d a shunting effect of the superconducting layer and evidence for the quasiparticle-mediated iSHE, which corroborates a recent report [47]. The reduced Gilbert damping in the superconducting state demonstrates that spin current transport through the SC in FM/SC/Pt-heterostructures is blocked below T_c in agreement with the findings in Ref. [256], while the spin pumping in FM/Pt/SC layers is only weakly affected by the SC transition. The direct detection of dissipative spin currents via SOT in Fig. 5.7(a) is thus consistent with their indirect detection via FMR damping α in 5.7(b).

Apart from the damping-like σ_d , originating from the iSHE, we can simultaneously extract σ_f generated by Faraday currents and field-like inverse spin orbit

torques in both the normal- and superconducting state. We plot the extracted σ_f for our samples in Fig. 5.9(a). Above T_c , we detect negative values for samples B, C

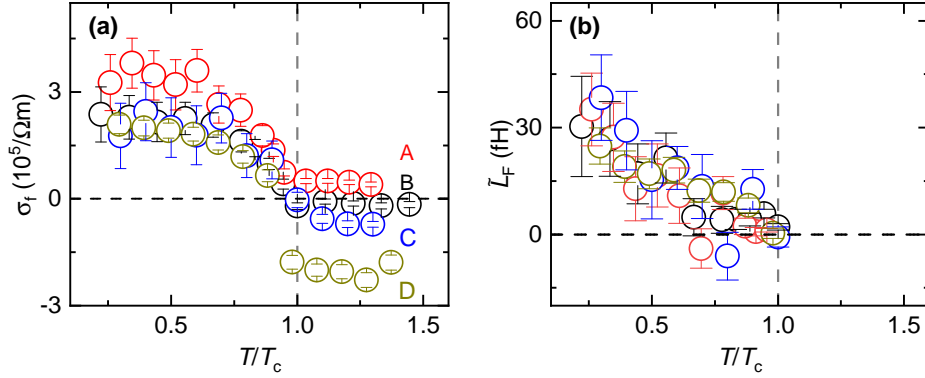


Fig. 5.9. – (a) Field-like spin torque conductivity σ_f plotted as a function of T/T_c . Due to a complex surface impedance $Z_{\text{eff}}(\omega)$ in the SC, the Faraday contribution σ_f^F creates an offset in $\text{Im}(\tilde{L})$ and only affects σ_f above T_c . (b) Change in $\text{Im}(\tilde{L})$ in the SC state due to SC Faraday currents labeled \tilde{L}_F . The error bars in (a) & (b) originate from fitting the extracted raw data for (\tilde{L}) with Eq. (5.14).

and D, attributed to sizable Faraday currents in Pt in agreement with the findings by Berger *et al.* [84] as well as a small positive σ_f for sample A, which indicates a small iREE manifesting in the NbN/Py-interface in the normal state. In the superconducting state, all samples exhibit a substantial positive field-like σ_f that gradually increases with decreasing T . Furthermore, we find that the observed behavior of all samples is nearly independent of the inclusion and position of the Pt layer. For $T < T_c$, Faraday currents in the SC do not contribute to the slope of $\text{Re}(\tilde{L})$ (and thus σ_f) but generate an offset \tilde{L}_F in $\text{Im}(\tilde{L})$ [see Eq. (5.14)]. This extracted offset is plotted as function of reduced temperature in Fig. 5.9(b). Consequently, the similar magnitudes in $\sigma_f(T)$ of our samples below T_c can be understood as in the superconducting state, the Faraday currents manifest themselves in \tilde{L}_F , as the superconductor acts as an inductor instead of as a resistor [see Eq. 5.12]. In Fig. 5.9, the magnitudes in \tilde{L}_F are similar for all samples, which is expected as they all contain NbN with nominally the same layer thickness. Furthermore, we note that the positive σ_f for $T < T_c$ in Fig. 5.9(a) exhibits the opposite sign compared to that expected from Faraday currents [84]. The observed sizable σ_f for $T \mapsto 0\text{ K}$ can also neither be attributed to the inverse Rashba-Edelstein effect [37, 38] nor the electromagnetic proximity effect [333, 334] at the SC/FM-interface, as the observed phenomenon is seemingly independent of the materials interfacing the superconductor and does also not require a direct contact between SC and FM layer. Having ruled out the common sources of field-like current-induced torques, we can merely speculate about its origin in our samples. Potential candidates to generate σ_f in these samples are the coherent motion of vortices in an rf-field [335, 336] as well as the impact of Meißner screening currents on the magnetization dynamics due to either spin-triplet superconductivity [274] or non equilibrium effects [337].

To summarize our initial study [68], we have adapted the inductive detection method introduced in Ref. [84] to study the field-like- and the reduction of damping-like current-induced torques in FM/SC hybrids below T_c . Our observations on the damping-like current-induced torques are consistent with a shunting effect of the SC and quasiparticle-mediated iSHE in NbN [47]. Notably, the spin transport into superconductors is mediated predominantly by quasiparticles in our heterostructures and we find, that features in the FMR-linewidth ΔH associated with spin-triplet superconductivity in Refs. [49,274] can result from the increased inhomogeneous linewidth broadening H_{inh} in the superconducting state. Hence a careful study of ΔH as function of frequency is required to study the spin transport in superconductors. The observed sizable field-like current-induced torque below T_c does not originate from Faraday currents or interfacial inverse spin torques. This still unexplained observation raises interesting questions regarding the theoretical understanding of spin current transport in FM/SC-hybrids. The inductive analysis method established here enables the study of manifold theoretically proposed exotic phenomena of SC/FM-hybrids like the generation of supercurrents by Rashba-spin orbit interaction [37,295], supercurrent-induced spin orbit torques [299] or the theoretically proposed vortex spin Hall effect [276]. Notably, by using our method, these studies can be performed without any need to pattern the samples.

5.3 Spin torques in TaN/Py-heterostructures

Our initial results on NbN/Py-heterostructures including Pt [68] reconcile the seemingly contradictory effects of the works of Bell *et al.* [256] and Jeon *et al.* [49] with the observation of the blocking of spin current transport through superconductors in both α and σ_d . However, in an overview article on the field of superconducting spintronics [268], authored by one of the co-authors of Ref. [49], it was pointed out that the expected generation of spin-triplet Cooper pairs by the exchange field in the Pt layer is expected to be hindered by the short coherence length of NbN ($\xi_0 \simeq 5 \text{ nm}$ [257]) used in our case as compared to the elementary Nb they have used ($\xi_0 \simeq 30 \text{ nm}$ [49]). While this argument may be valid, we note that the investigated NbN/Pt/Py-heterostructure sample C in Sec. 5.2 should have nonetheless enabled the generation and detection of spin-triplets [68]. Nonetheless, we decided to further study the impact of spin-orbit interaction in superconductors on their spin transport properties and repeated our bbFMR experiments using a heavy spin-orbit interaction superconductor, where its spin-orbit field should directly enable the generation of spin-triplets without the need to additionally include a Pt layer in the sample stack. To this end, we select the superconducting material TaN, motivated by the large SOI induced by elementary Ta [44,280] as well as its robustness to external magnetic fields $\mu_0 H_{c2} \simeq 14 \text{ T}$ [338] and experimentally accessible superconducting

transition temperature $T_c \simeq (8 - 10)$ K [338–341]. In a first step, we optimize the growth of superconducting TaN thin films on SiO₂ substrates via reactive dc magnetron sputtering with regards to their superconducting properties in Sec. 5.3.1. To investigate the impact of SOI on the inverse spin-torque conductivities in SC/FM-hybrids, we then use this optimized deposition recipe and analyze the magnetization dynamics of both normal state and superconducting TaN/Py-bilayers as a function of temperature via broadband ferromagnetic resonance spectroscopy in combination with the previously established inductive analysis technique and compare the obtained results with our previous study on NbN/Py-bilayers [68] in Sec. 5.3.2.

5.3.1 Growth optimization of TaN

In order to determine the optimum growth conditions of TaN, we deposit 60 nm thick TaN thin films on a thermally oxidized Si (100) substrates by reactive dc magnetron sputtering in a mixed Ar/N₂-atmosphere using the Superbowls sputtering machine (see Sec. 3.1.5) and systematically vary the deposition parameters listed in Sec. 3.1.2. To determine both the resistivity and the superconducting transition temperature T_c of our TaN thin films, we perform 4-point electrical transport measurements using the Van-der-Pauw method [226] as a function of temperature in the range $3\text{ K} \leq T \leq 300\text{ K}$ using the 17T cryostat (see Sec. 3.3.1). Exemplary data for the resistivity ρ as a function of temperature for our TaN thin films is shown in Fig. 5.10(a).

Here, the gray dashed vertical line represents the extracted superconducting transition temperature $T_c = (T_1 + T_2)/2$ as the mean value between the temperatures where ρ takes on 90% [$\rho(T_1)/\rho_{\text{NC}}=90\%$] and 10% [$\rho(T_2)/\rho_{\text{NC}}=10\%$] of its normal state value ρ_{NC} at $T = 7\text{ K}$. This particular film has been grown at a gas flow ratio N₂/Ar=0.35, a deposition temperature $T_{\text{depo}} = 500^\circ\text{C}$, a deposition pressure $p_{\text{depo}} = 5\ \mu\text{bar}$, and a sputtering power $P = 30\text{ W}$, resulting in a superconducting transition temperature $T_c = 4.97\text{ K}$. The light blue background in Fig. 5.10(a) represents the superconducting transition width $\Delta T_c = T_1 - T_2 = 1.26\text{ K}$. Additionally, to gain insight into the chemical composition of our TaN thin films, we perform x-ray reflectometry experiments (XRR) on them as exemplary displayed in Fig. 5.10(b). By fitting the raw data for the detected x-ray intensity I using the *Leptos*-fitting software utilizing a simulated annealing optimization procedure [342], we can extract both the layer thickness d_{SC} and volume density D_V of our TaN thin films. In particular, the latter parameter provides insight into the sample stoichiometry as the various Ta- and N-rich TaN_{1±δ} phases exhibit a different D_V . In particular, volume densities $D_V < 13.0\text{ g/cm}^3$ are associated with N-rich TaN_{1±δ} phases, whereas TaN with volume densities in the range $(13.0 \leq D_V \leq 14.7)\text{ g/cm}^3$ are attributed the cubic TaN-phase (c-TaN) and Ta-rich TaN_{1±δ} phases exhibit a higher $D_V > 14.7\text{ g/cm}^3$ [300]. In literature, primarily the

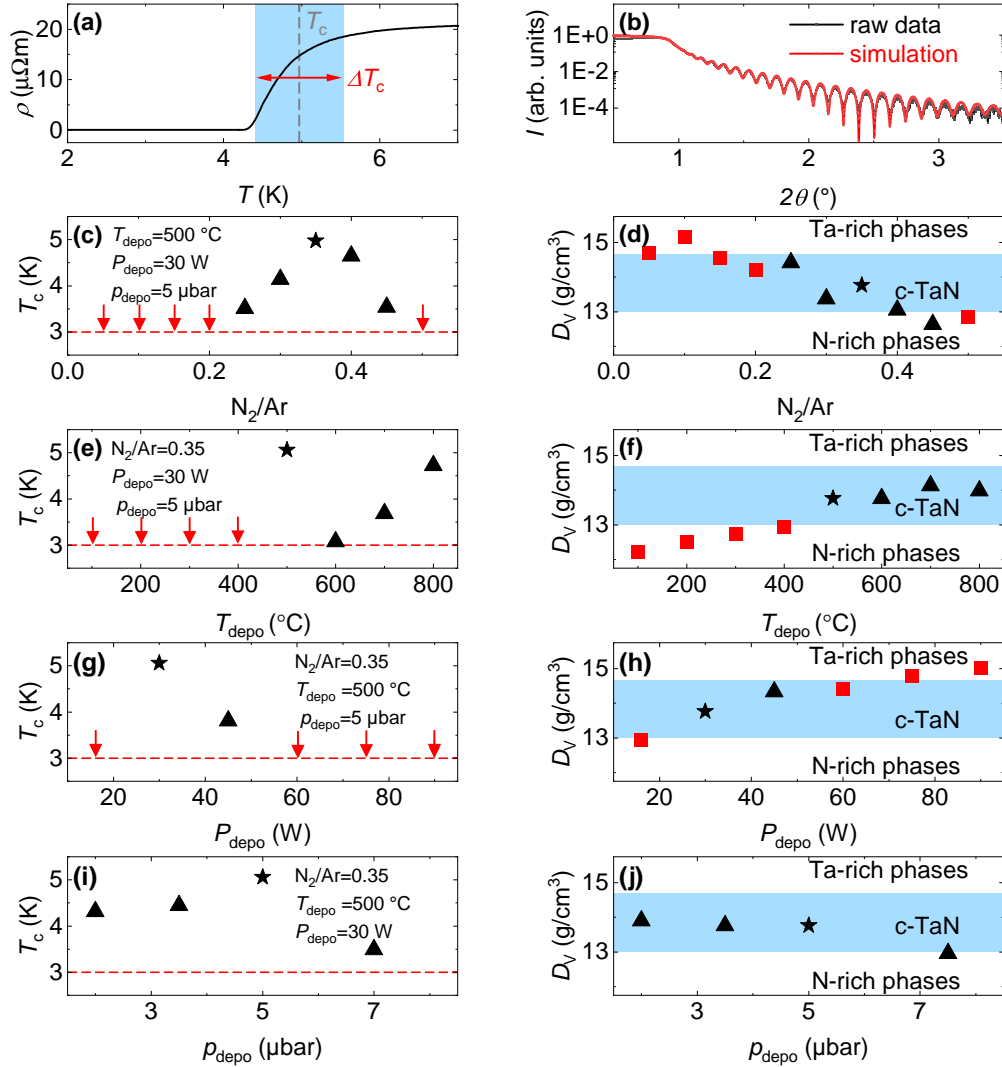


Fig. 5.10. – (a) Exemplary plot of the resistivity ρ versus temperature T of our TaN thin films together with the extracted superconducting transition temperature T_c (vertical dashed line) and transition width ΔT_c (blue region). (b) Exemplary x-ray reflectometry data (black) and simulation curve (red) allowing to extract the volume density D_V of the TaN thin films. (c), (d) Superconducting transition temperature T_c and volume density D_V of the TaN thin films as a function of the N_2/Ar -flow ratio during deposition. (e), (f) T_c and D_V as a function of the deposition temperature T_{depo} . (g), (h) T_c and D_V as a function of the deposition power P_{depo} . (i), (j) T_c and D_V as a function of the deposition pressure p_{depo} . Within each series, the sample with the highest T_c is highlighted with a star symbol. Samples not showing full superconductivity above $T = 3$ K are represented by red arrows in panels (c), (e) (g) and (i) as well as red squares in panels (d), (f) (h) and (j).

cubic c-TaN-phase is expected to give rise to superconductivity [340]. Note that in the fabricated films, these three principal phases may be present in parallel, with varying volume fractions, since in our experiments we only can determine the average volume density. However, we can expect a high fraction of our thin films to be in the TaN phase corresponding to the measured D_V . For all the TaN thin films grown in our optimization study, we observe superconducting transition widths in the range $\Delta T_c \simeq 1$ K with no systematic dependence on the respective deposition parameters (see Appendix E). This broad transition range indicates the presence of a mixture of $\text{TaN}_{1\pm\delta}$ -phases in our thin films. Additional x-ray diffraction experiments on the TaN on SiO_2 samples exhibited no detectable crystalline reflections. For the XRR spectra of the TaN thin film in Fig. 5.10(b), we find a layer thickness $d_{\text{TaN}} \approx 64$ nm and $D_V \approx 13.8$ g/cm³ in agreement with the expected density for cubic TaN [300]. From our XRR experiments, we find that the layer thicknesses d_{TaN} of all samples in our growth optimization range between 54 nm and 66 nm, which greatly exceeds the superconducting coherence length of TaN $\xi_0 \simeq 9$ nm [343]. In this range of layer thicknesses, we hence expect that the small fluctuation in d_{TaN} among the samples does not affect T_c . The respective deposition parameters, superconducting transition temperatures T_c , transition widths ΔT_c , and volume densities D_V for all the TaN films deposited in the growth optimization study are listed in Appendix E. As a first growth optimization parameter, we vary the N_2/Ar gas flow ratios during deposition and deposit TaN-films at a deposition temperature of $T_{\text{depo}} = 500^\circ\text{C}$ and a total pressure of $p = 5$ μbar , a deposition power of $P_{\text{Depo}} = 30$ W. The resulting T_c as function of N_2/Ar gas flow ratio is plotted in Fig. 5.10(c). We exclusively find $T_c > 3$ K for gas flow ratios in the range ($0.25 \leq \text{N}_2/\text{Ar} \leq 0.45$). Samples that did not exhibit full superconductivity above $T = 3$ K are displayed by red arrows Fig. 5.10(c). For this initial step of our optimization series, we find a maximum of $T_c = 4.97$ K at a gas flow ratio of $\text{N}_2/\text{Ar} = 0.35$. Notably, this ratio is significantly higher compared to reports in literature [338–340, 344], where the maxima in the T_c at gas flow ratios in the range ($0.1 \leq \text{N}_2/\text{Ar} \leq 0.15$). This difference can have various reasons such as a different distance between target and substrate in the Superbowls sputtering machine as well as different values of the kinetic energy of the Ta-atoms during the sputtering process due to varying sputtering power P and target bias voltage. The volume density D_V of the TaN thin films grown in this series are plotted as function of the N_2/Ar gas flow ratio in Fig. 5.10(d). We identify three principal regimes with different $\text{TaN}_{1\pm\delta}$ stoichiometry in agreement with Ref. [300]. In particular, we find that the D_V of the non-superconducting TaN thin films for low and high N_2 -concentration correspond to the expected volume densities of Ta- and N-rich phases, respectively. The intermediate range ($13.0 \leq D_V \leq 14.7$) g/cm³ is attributed to the cubic TaN-phase (c-TaN) [300]. Having identified an optimal N_2/Ar gas flow ratio of 0.35 in the first step of our growth optimization series, we next vary the sample temperature during deposi-

tion T_{depo} of TaN films grown at a deposition power of $P_{\text{depo}} = 30$ W, a deposition pressure of $p_{\text{depo}} = 5$ μbar , and $N_2/\text{Ar}=0.35$. The resulting T_c as function of T_{depo} is plotted in Fig. 5.10(e). We find that superconducting TaN thin films with a $T_c > 3$ K are obtained only for elevated deposition temperatures $T_{\text{depo}} > 400^\circ\text{C}$. The volume density D_V plotted in Fig. 5.10(f) suggests that this threshold in T_{depo} coincides with the transition of our samples from the N-rich $\text{TaN}_{1\pm\delta}$ -phase to the c-TaN phase, suggesting, that a finite T_{depo} is required to enable the growth of TaN on the substrate in the energetically preferable c-TaN-phase. For $T_{\text{depo}} > 500^\circ\text{C}$, we observe no systematic changes in T_c with T_{depo} and hence chose to proceed our growth optimization with $T_{\text{depo}} = 500^\circ\text{C}$ as this parameter yielded the highest T_c and to avoid the thermally induced breaking of molecular nitrogen bonds [175]. For the next optimization step, we vary the deposition power P_{depo} using the optimized $T_{\text{depo}} = 500^\circ\text{C}$, $N_2/\text{Ar}=0.35$ and a deposition pressure $p_{\text{depo}} = 5$ μbar . The resulting T_c and D_V as function of P_{depo} are plotted in Fig. 5.10(g) and (h). We find that only two TaN thin films deposited in the intermediate power range $30\text{ W} \leq P_{\text{depo}} \leq 45\text{ W}$ exhibit a $T_c > 3$ K. The volume density D_V of these two films in Fig. 5.10(h) is situated within the expected density range for cubic TaN and we observe a continuous rise in D_V with increasing P_{depo} due to the enhanced removal rate of elementary Ta from the target surface at a fixed nitrogen concentration and consequently the growth of TaN in the Ta-rich phase. From our deposition power series, we find an optimal T_c for $P_{\text{depo}} = 30$ W. As the last step of our optimization series, we study the effect of the deposition pressure p_{depo} on our growth process and deposit TaN at $N_2/\text{Ar}=0.35$, $T_{\text{depo}} = 500^\circ\text{C}$, $P_{\text{depo}} = 30$ W, while varying p_{depo} . We again plot the superconducting T_c and volume density D_V as a function of deposition pressure in Fig. 5.10(i) and (j). We observe nearly constant T_c and D_V for deposition pressures $p_{\text{depo}} \leq 5$ μbar . At $p_{\text{depo}} = 7$ μbar , the reduced T_c and D_V indicate the preferred growth of N-rich $\text{TaN}_{1\pm\delta}$ phases resulting from their increased mean free path in the sputtering plasma [167], which becomes prominent at high deposition pressures. An optimum in T_c is observed at $p_{\text{depo}} = 5$ μbar . In summary, our optimal deposition parameters for superconducting cubic c-TaN are: $N_2/\text{Ar}=0.35$, $T_{\text{depo}} = 500^\circ\text{C}$, $P_{\text{depo}} = 30$ W and $p_{\text{depo}} = 5$ μbar resulting in a maximum $T_c = 4.97$ K as listed in the appendix B1.

We note that this maximum T_c value is comparable to literature values for TaN grown on SiO_2 in Ref. [341], where $T_c = 6$ K has been achieved for c-TaN films grown via infrared pulsed laser deposition. However, TaN is known to exhibit higher superconducting transition temperatures of up to $T_c = 10.2$ K on crystalline substrates such as Al_2O_3 (sapphire) [338,339] and MgO [340,341], where films with a better texture can be achieved. To determine the optimal T_c of our thin films, we deposit a 60 nm thick TaN layer on a c-plane sapphire substrate using our optimized growth recipe ($N_2/\text{Ar}=0.35$, $T_{\text{depo}} = 500^\circ\text{C}$, $P_{\text{depo}} = 30$ W and $p_{\text{depo}} = 5$ μbar). The resistivity of this thin film is plotted in Fig. 5.11(a).

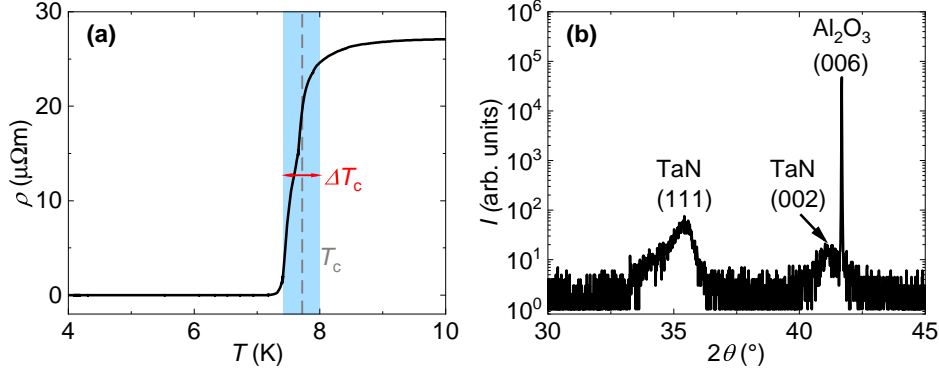


Fig. 5.11. – Resistive transition $\rho(T)$ (a) and x-ray-diffraction pattern (b) of a 60 nm thick TaN film grown on a c-plane Al_2O_3 -substrate. The gray dashed line in panel (a) indicates the superconducting $T_c = 7.72$ K and the red arrow and blue background represent the superconducting transition width $\Delta T_c = 0.56$ K.

We observe a superconducting transition at $T_c = 7.72$ K, which is almost 3 K higher as well as a narrower transition width of $\Delta T_c = 0.56$ K compared to TaN grown on SiO_2 . Furthermore, in x-ray diffraction experiments in Fig. 5.11(b), we observe the (111) and (002) reflections of the cubic c-TaN phase [341, 345]. These results demonstrate a strong correlation between crystalline quality and high T_c in our samples. Our observed optimum $T_c = 7.72$ K on sapphire is still $\simeq 2$ K lower compared to Refs. [338, 339] but comparable to the results in Ref. [340, 341]. We attribute this variation to the different crystalline quality of the TaN thin films grown with varying deposition methods and the limited capabilities of reactive sputter deposition in this regard. We note, however, that the achieved $T_c = 4.97$ K of TaN on SiO_2 is sufficient to compare the inverse spin torques of superconducting TaN in TaN/Py-heterostructures to our results of NbN/Py-heterostructures from the previous section 5.2.

Regarding the net resistivity values of our TaN thin films grown for different deposition parameters, we have observed a large spread in ρ between the individual thin films (cf. Ref. [162]). We attribute this to the different measurement geometries of our TaN thin films as we did not pattern them into a specific geometry to save time and simply performed 4-point measurements in Van-der-Pauw-geometry. However, we can identify the different $\text{TaN}_{1\pm\delta}$ -phases from the temperature evolution of $\rho(T)$. This is exemplified in Fig. 5.12, where we plot the resistivity of three TaN thin films of the N_2/Ar -gas flow series grown in the Ta-rich phase at $\text{N}_2/\text{Ar}=0.20$ (red dots), the N-rich phase $\text{N}_2/\text{Ar}=0.50$ (blue dots) and in the c-TaN-phase at $\text{N}_2/\text{Ar}=0.35$ (black dots) at using the deposition parameters $T_{\text{depo}} = 500^\circ\text{C}$, $P_{\text{depo}} = 30$ W and $p_{\text{depo}} = 5$ μbar .

For the sample in the N-rich $\text{TaN}_{1\pm\delta}$ -phase, we observe in Fig. 5.12 an increasing ρ with decreasing T , which is commonly associated with variable range hopping (VRH) [346, 347] in disordered systems due to the semiconducting properties of N-rich TaN phases [348]. We fit the measured $\rho(T)$ with a VRH function

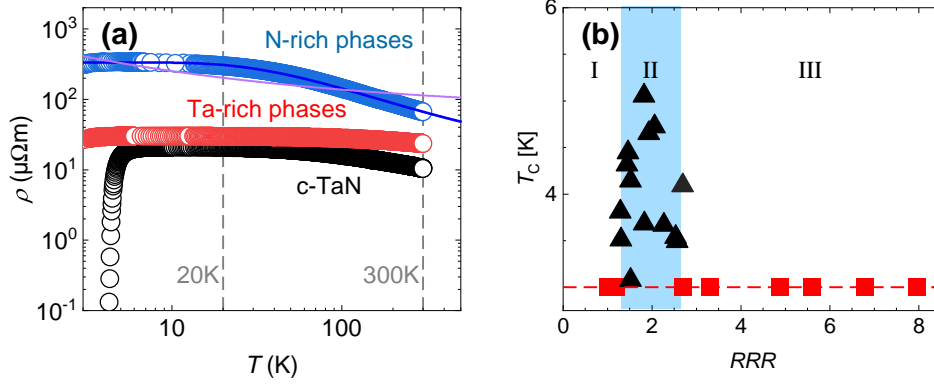


Fig. 5.12. – (a) Resistivity ρ as a function of temperature T for TaN thin films grown in the N-rich (blue), Ta-rich (red) and c-TaN phase in the range from cryogenic temperatures to RT. The violet line represents a fit to the VRH model $\rho(T) = \rho_0 \exp(T_0/T)^{1/4}$ and the dark blue line is a fit to $\rho = \rho_0 \exp(E_g/2k_B T)$. Dashed gray lines mark the temperatures 20 K and 300 K. (b) Superconducting transition temperature of our TaN thin films as function of their RRR-ratio [$RRR = \rho(20 \text{ K}) / \rho(300 \text{ K})$]. The roman numbers indicate the different TaN phases. The Ta-rich and N-rich phases are represented by the ranges I and III, respectively. The superconducting TaN thin films grown in the c-TaN phase in range II for the range ($1.2 \leq RRR \leq 2.7$) are highlighted with a blue background.

$\rho(T) = C \exp[(T_0/T)^{1/4}]$ [346, 347][see purple line in Fig. 5.12(a)] and extract $C = 63 \pm 2 \mu\Omega\text{m}$ and $T_0 = 37 \pm 2 \text{ K}$. Though these fitting parameters are situated within the expected range of values for disordered semiconductors [349, 350], we find, that the VRH model does not properly describe the observed temperature dependence in $\rho(T)$ for the N-rich $\text{TaN}_{1\pm\delta}$ -sample over the entire temperature range. However, we achieve a good fit using an Arrhenius function of the form $\rho(T) = \rho_0 \exp(E_g/2k_B T)$ [351, 352] [see blue line in Fig. 5.12(a)], where E_g is the energy of the semiconducting bandgap and ρ_0 is the resistance in the intrinsic conduction limit, and extract a low bandgap of $E_g \approx (9.0 \pm 0.1) \text{ meV}$. The increasingly insulating properties with rising N_2/Ar -gas flow ratio during deposition is confirmed in Ref. [162]. For the TaN thin film grown in the Ta-rich phase (red data points), we observe in Fig. 5.12(a) a weak temperature dependence in the resistivity demonstrating its enhanced metallic character. Finally, for the resistivity of the TaN thin film grown in the c-TaN phase, we observe a slight rise in $\rho(T)$ with reduced temperatures, which is however weaker than for the TaN thin film grown in the N-rich phase, and the onset of the superconducting phase for temperatures below 5 K. The different temperature evolution in $\rho(T)$ for the three thin films in Fig. 5.12(a) indicates, that the different $\text{TaN}_{1\pm\delta}$ -phases exhibit a characteristic behavior in $\rho(T)$. To test this hypothesis, we determine the RRR-ratio of our TaN thin films defined as $RRR = \rho(20 \text{ K}) / \rho(300 \text{ K})$. In Fig. 5.12(b), we plot the superconducting T_c of all TaN thin films grown for the optimization study as a function of the RRR-ratio. We can clearly identify the three different $\text{TaN}_{1\pm\delta}$ -phases: (I) the Ta-rich phase for $RRR < 1.2$, (II) the c-TaN phase, containing the superconducting samples with a $T_c > 3 \text{ K}$, in the range $1.2 \leq RRR \leq 2.7$ and

(III) the N-rich phase for $RRR > 2.7$. The TaN thin film grown with our optimized recipe is situated in the middle of the superconducting region at $RRR \approx 1.8$. The observed RRR -range of the c-TaN phase is in agreement with literature [338,341]. Hence, the observed electrical transport properties of our samples allows to clearly identify the three main phases of TaN.

To confirm the robustness of our TaN thin films to an in-plane external magnetic field $\mu_0 H_{\text{ext}} \simeq 1$ T, required for our bbFMR experiments in the (10-50) GHz frequency-range, we analyze the magnetic field dependence of their superconducting transition temperature T_c . To this end, we study the resistivity ρ as a function temperature for our optimized TaN thin film ($N_2/Ar=0.35$, $T_{\text{depo}} = 500^\circ\text{C}$, $P_{\text{depo}} = 30$ W and $p_{\text{depo}} = 5$ μbar) grown on SiO_2 for fixed in-plane magnetic fields in the range $0\text{ T} \leq \mu_0 H_{\text{ext}} \leq 12$ T. The resulting $\rho(T)$ curves for varying $\mu_0 H_{\text{ext}}$ are shown in Fig. 5.13(a). We observe a reduction in T_c as well as an increase of the superconducting transition width ΔT_c with increasing $\mu_0 H_{\text{ext}}$.

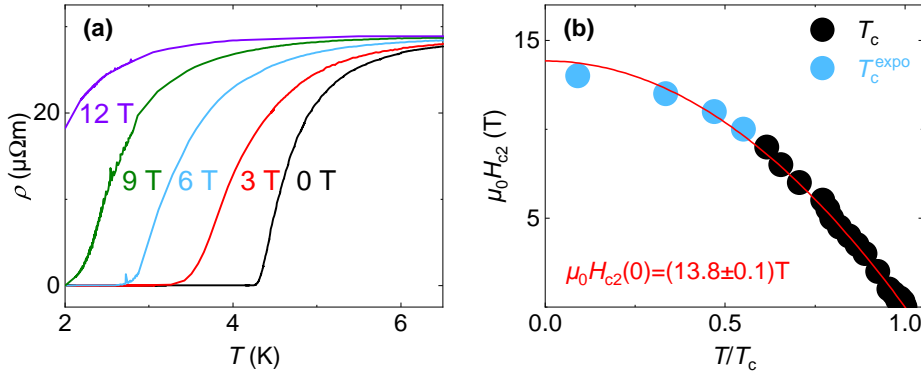


Fig. 5.13. – (a) Resistivity ρ as a function of temperature T of the optimally grown TaN on SiO_2 thin film for varying external in-plane magnetic fields $\mu_0 H_{\text{ext}}$. (b) Extracted critical field $\mu_0 H_{c2}(T)$ (black and blue dots) as a function of reduced temperature T/T_c together with a fit to $\mu_0 H_{c2}(T)$ using Eq. (5.22). The blue data points represent the linearly extrapolated T_c for high external magnetic fields, where the TaN thin film did not exhibit full superconductivity within the experimentally accessible temperature range.

In Fig. 5.13(b) we plot the applied in-plane field $\mu_0 H_{\text{ext}}$ interpreted in this context as the superconducting critical field H_{c2} as function of the normalized temperature $T_c(\mu_0 H_{\text{ext}})/T_c(0)$. Here, we note, that this direct relation between H_{ext} and H_{c2} is only a rough estimate, as it is impossible in our experiments to align the thin film normal of our sample exactly along the applied external magnetic field and consequently the field-induced motion of superconducting vortices may give rise to a resistive transition below the true H_{c2} of the superconductor. For external fields $\mu_0 H_{\text{ext}} > 9$ T, the T_c are in the temperature regime below the lowest experimentally accessible temperature. Here, we to obtain their estimate values by performing a linear extrapolation. The thereby estimated T_c are represented in Fig. 5.13(b) as light blue dots. To obtain an estimate for the upper critical field H_{c2}

of our TaN thin films, we fit the data for $\mu_0 H_{c2}(T)$ in Fig. 5.13(b) to the empirical dependence [86]

$$\mu_0 H_{c2}(T) = \mu_0 H_{c2}(T = 0 \text{ K}) \left[1 - \left(\frac{T}{T_c} \right)^2 \right], \quad (5.22)$$

and find $\mu_0 H_{c2}(T = 0 \text{ K}) = (13.8 \pm 0.1) \text{ T}$. This value is in good agreement with the literature value $\mu_0 H_{c2} = 14 \text{ T}$ reported in Ref. [338] for TaN grown on sapphire substrates demonstrating the state-of-the-art robustness to external magnetic fields in the experimentally accessible T-range and thereby the excellent suitability for bbFMR experiments of our TaN thin films.

5.3.2 Broadband ferromagnetic resonance

Having found an optimal growth recipe for superconducting TaN on SiO₂ and demonstrated its robustness to external in-plane magnetic fields in the 1 T-range, we fabricate SC/FM heterostructures using TaN and repeat the measurement procedure performed for NbN/Py-heterostructures in Sec. 5.2. To this end, we in situ deposit 6 nm of Py on 60 nm thick TaN films grown on SiO₂. The Py layer is again covered with a protective TaOx cap layer to avoid oxidization. For this study, we characterize two TaN/Py-bilayer structures: (i) sample E is a TaN/Py bilayer, where the TaN layer is grown using the optimal deposition parameters ($N_2/Ar=0.35$, $T_{\text{depo}} = 500^\circ\text{C}$, $P_{\text{depo}} = 30 \text{ W}$ and $p_{\text{depo}} = 5 \mu\text{bar}$) and (ii) sample F is a TaN/Py bilayer where the growth parameters of TaN ($N_2/Ar=0.1$, $T_{\text{depo}} = 500^\circ\text{C}$, $P_{\text{depo}} = 30 \text{ W}$ and $p_{\text{depo}} = 5 \mu\text{bar}$) are chosen such that it doesn't exhibit a superconducting transition in the experimentally studied temperature range. The difference in the growth parameters of samples E and F is the lower N_2/Ar gas flow ratio in sample F, which favors the formation of non-superconducting Ta-rich TaN_{1±δ} phases. Sample F can hence be viewed as the reference sample allowing us to verify whether the experimentally observed signatures in our bbFMR experiments can be assigned to the formation of a superconducting phase in the TaN.

The resistivities ρ of samples E and F using the Van-der-Pauw method as function of temperature are shown in Fig. 5.14.

For sample E, we find a superconducting $T_c=4.7 \text{ K}$, demonstrating, that the superconducting properties of TaN are only weakly affected by the ferromagnetic exchange interaction at the TaN/Py-interface. As expected, for sample F, we observe no superconducting transition in the investigated temperature range. We find a RRR ratio of RRR= 0.94 and 0.91 for samples E and F, respectively. We attribute the RRR < 1 in our bilayers to the fractional charge transport in the Py layer, where a reduced resistivity at cryogenic temperatures has been observed in Ref. [353]. The lower ρ in sample F compared to sample E is attributed to its more metallic character due to its higher Ta-content. By modelling the TaN/Py-bilayer

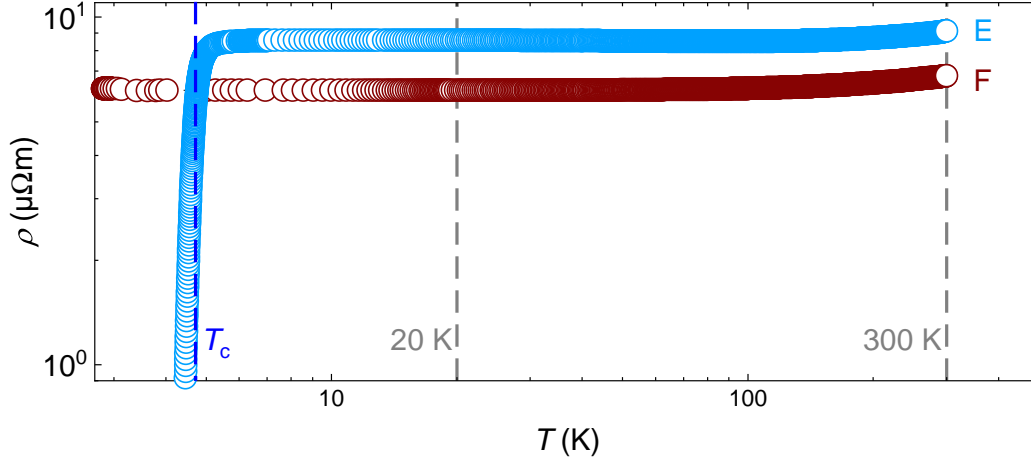


Fig. 5.14. – Resistivity ρ of the TaN/Py bilayers E and F as a function of temperature T in the range from cryogenic temperatures to RT. The dark blue line represents the superconducting T_c , whereas gray dashed lines indicate the temperatures 20 K and 300 K. $T_c=4.7$ K is observed for sample E, whereas sample F remains in the normal state in the investigated temperature range.

as a parallel resistor network and assuming the resistance of the c-TaN thin film in sample E to be $\rho_{\text{TaN}} \approx 28 \mu\Omega\text{m}$ at cryogenic temperatures (see Fig. 5.13), we can estimate the resistivity of the Py layer to be $\rho_{\text{Py}} \approx 12 \mu\Omega\text{m}$. This value is an order of magnitude higher compared to literature values [353] due to the relative uncertainty in the determination of the sheet resistance of the used Van-der-Pauw method. We can however state, that the resistivity of the Py layer is lower than that of the TaN layer and hence shunting effects of the iSHE can manifest in the used TaN/Py-bilayers.

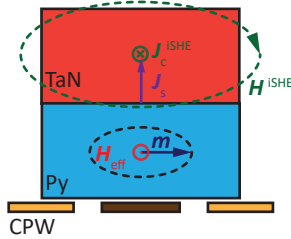


Fig. 5.15. – Schematic illustration for the generation of the charge current density J_c^{iSHE} by the ac iSHE in the normal state in samples E and F. The ac flux $\Phi^{\text{iSHE}} \propto H^{\text{iSHE}}$ generated by J_c^{iSHE} is coupled into the CPW. Note, that in this figure, the aspect ratio between sample thickness and center conductor width of the CPW is distorted.

In analogy to Sec. 5.2, we perform bbFMR experiments on the samples E and F in the ip-geometry $H_{\text{ext}} \parallel a$ in Fig. 3.4(b) and characterize both their magnetization dynamics parameters and spin-torque conductivities as function of temperature using the Chaos cryostat (see Sec. 3.3.1). Again, we use the frequency range ($10 \text{ GHz} \leq f \leq 36 \text{ GHz}$) and record the complex microwave transmission parameter S_{21} of the CPW with the mounted samples as function of the external magnetic field H_{ext} at a microwave power of 1 mW corresponding to the linear regime. As the TaN layer in the normal state exhibits a large spin-orbit interaction, the physics at play in samples E and F is in analogy to that of sample B in Sec. 5.2 illustrated in Fig. 5.3 with the only difference being, that in this case, the SC layer also

simultaneously serves as the spin sink layer as shown in Fig. 5.15. The magnetization dynamics excited in the Py layer pumps a spin current density J_s into the adjacent TaN layer, where it is absorbed and converted into a charge current J_c^{iSHE} via the iSHE. On the one hand, this process manifests itself as an additional contribution to the Gilbert damping α of the FMR [85] and, on the other hand, in the frequency-dependence of the inductive coupling between sample and CPW [84].

The resulting magnetization dynamics parameters consisting of g -factor, effective magnetization M_{eff} , out-of-plane magnetic anisotropy field $H_{\text{ani}}^{\text{oop}}$ and inhomogeneous line broadening H_{inh} of the two TaN/Py-samples E and F recorded at cryogenic temperatures are plotted as a function of the reduced temperature in Fig. 5.16. As sample F does not exhibit superconductivity within the experimentally investigated temperature-range, we divide the T of the data points for this sample to the T_c of sample E. We plot the magnetization dynamics parameters and inverse spin torque conductivities of samples E and F as a function of reduced temperature to allow for their comparison with the results for the NbN/Py-heterostructures in Sec. 5.2.

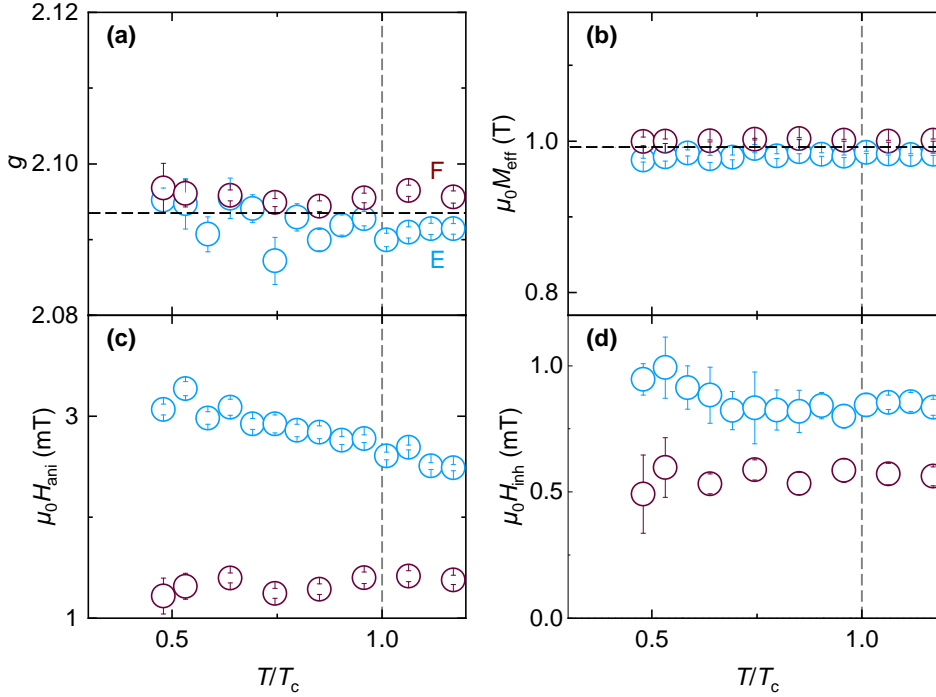


Fig. 5.16. – Temperature dependence of the magnetization dynamics parameters for the TaN/Py samples E and F. Both the g -factor in (a) and the effective magnetization M_{eff} in (b) exhibit no changes in the superconducting state. (c) The out-of-plane magnetic anisotropy field $H_{\text{ani}}^{\text{oop}}$ of sample E increases due to a magnetic out-of-plane field contribution from the induced Meissner fields in the superconducting state. (d) Inhomogeneous broadening H_{inh} as function of reduced temperature.

We find, that just like for our NbN/Py-heterostructures, the g -factor and effective magnetization M_{eff} in Fig. 5.16 panels (a) and (b) are comparable for both samples unaffected by the onset of superconductivity in sample E. The values

for M_{eff} and g -factor for samples E and F are comparable to those of samples A-D demonstrating the growth of Py on both TaN and NbN with equally good properties in the absence of in-plane anisotropy contributions ($M_{\text{eff}} = M_s$). For the out-of-plane anisotropy field $H_{\text{ani}}^{\text{oop}}$ in Fig. 5.16(c), we observe positive values in the mT-range in particular for sample E. While it is tempting to again attribute this $H_{\text{ani}}^{\text{oop}}$ to the presence of spin-orbit interaction in analogy to samples C and D, the different magnitude of $H_{\text{ani}}^{\text{oop}}$ in samples E and F indicates the presence of an additional oop anisotropy contribution. We suspect the manifestation of a small magnetocrystalline anisotropy (see Sec. 2.1) from a crystalline texturing of our thin films. The varying magnitude in $H_{\text{ani}}^{\text{oop}}$ can then be understood as the Ta-rich TaN in sample F primarily crystallizes in the hexagonal Ta_5N_6 -phase [354], whereas the superconducting TaN in sample E crystallizes in the cubic c -TaN phase. For sample E, in the superconducting state, a small increase in $H_{\text{ani}}^{\text{oop}}$ is observed comparable in magnitude to what has been observed for samples A, B and D in Fig. 5.16(c) despite the larger layer thickness of the superconductor in sample E. This finding appears to indicate that additional mechanisms to the superconducting Meißner currents must contribute to $H_{\text{ani}}^{\text{oop}}$ in the SC/FM/SC-trilayers in Refs. [287, 316], where shifts of the Kittel mode in the $\simeq 100$ mT range have been observed. In a recent work [355], Mikhail Silaev has postulated that the Anderson-Higgs mechanism mediated by Meißner currents in SC/FM/SC-trilayers generate a mass for the magnons in the sandwiched FM layer and thereby a spectrum gap in the magnons, which manifests as a shift in the Kittel mode. As this mechanism requires SC/FM/SC-trilayer heterostructures, it represents a plausible scenario as to why no significant $H_{\text{ani}}^{\text{oop}}$ are observed in our samples even when using samples with thick superconducting layers and sizable Meißner currents. Finally, for the inhomogeneous linewidth broadening H_{inh} plotted in Fig. 5.16(d), we observe a small H_{inh} in the normal state for both samples and a slight increase for sample E in the superconducting state in agreement to our results for samples A-D in Fig. 5.5(d). Overall, the magnetization dynamics parameters for our two TaN/Py-heterostructures in Fig. 5.16 are comparable to those of the four studied NbN/Py-heterostructures in Fig. 5.5. Furthermore, sample E exhibits the same characteristic changes in $H_{\text{ani}}^{\text{oop}}$ and H_{inh} , demonstrating the universality of these effects for all superconducting materials in SC/FM-heterostructures.

Having studied the temperature dependence of the magnetization dynamics parameters of the two TaN/Py bilayer samples E and F, we now discuss their extracted inverse damping-like and field-like current-induced torques σ_d and σ_f , which are plotted in Figs. 5.17 and 5.19, respectively. Again, we have chosen to plot the Gilbert damping parameter α together with σ_d as both parameters are associated with spin transport at the TaN/Py-interface.

In Fig. 5.17(a), we observe a sizable positive and temperature-independent σ_d for both samples E and F in the normal state. This contribution comprises the combined iSHE effects of both the Py and TaN layers in our samples. We

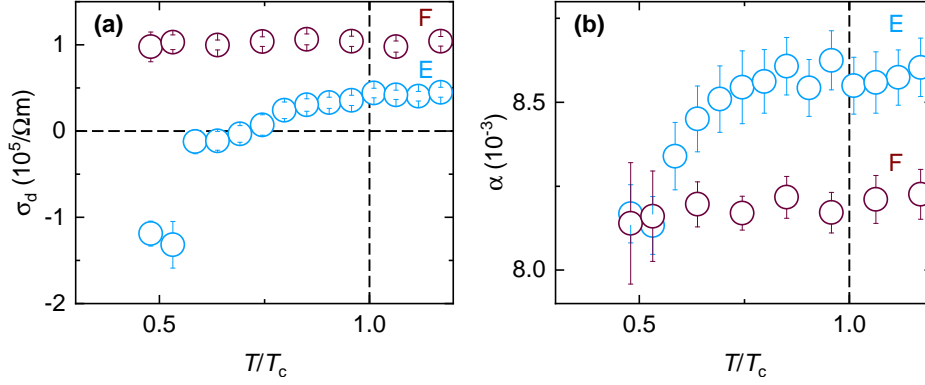


Fig. 5.17. – (a) Damping-like spin torque conductivity σ_d plotted as a function of T/T_c . A positive σ_d is detected in both samples in the normal state. In the SC state, the σ_d of sample A decays to negative values. (b) Gilbert damping parameter α for both the superconducting (light blue, E) and normalconducting (dark red, F) TaN/Py-bilayers. The apparent decrease of α in the SC state is due to the suppression of spin pumping into the SC due to the freeze-out of thermally excited quasiparticles. The error bars originate from fitting the extracted raw data for \tilde{L} with Eq. (5.14) (a) and Eq. (2.27) for $\Delta H(f)$ (b).

have previously observed similar positive σ_d for the NbN/Py-bilayer sample A in Sec. 5.2 despite the negative spin Hall angle in NbN [47, 279]. Hence, we assume, that the contribution of Py to σ_d dominates due to the higher conductivity of the Py layer and we can not quantify the magnitude of the spin Hall angle of TaN in the normal state. However, we can state that the various TaN phases exhibit different SHA as evident from the larger positive σ_d of sample F containing primarily Ta-rich phases like Ta₂N. In a recent work, a negative spin Hall angle of $\Theta_{\text{SH}} = -0.039$ has been found for superconducting c-TaN at room temperature by Swatek *et al.* [356]. From the calculated band structure of TaN using density functional theory calculations, they further claim, that the spin Hall effect in TaN stems primarily from intrinsic effects from gapless Dirac nodes and high-degeneracy points along high-symmetry k -points in the bandstructure, which are absent in pure Ta. In this light, the reduced positive σ_d of sample E can be attributed to a negative contribution of c-TaN due to its negative spin Hall angle compared to the TaN of sample F grown in the Ta-rich phase, which is hence expected to exhibit a Θ_{SH} with a lower magnitude. In the superconducting state, the σ_d of sample E first decreases towards approximately zero with decreasing temperature due to a superconducting shunting effect of the TaN layer as previously detected in Sec. 5.2 and takes negative values with a rising magnitude for lower temperatures in agreement with the quasiparticle mediated inverse spin Hall effect (QMISHE) [68, 357] due to the negative spin Hall angle of c-TaN [356]. Notably, the σ_d of sample F remains constant for all experimentally investigated temperatures and the observed behavior in σ_d of sample E can hence be unambiguously attributed to the onset of superconductivity in TaN. We attribute the abrupt increase in magnitude of the negative σ_d for $T \leq 2.75$ K to a non-uniform superconducting transition of the TaN layer, with its fraction, that is in contact with the Py layer

transitioning only for temperatures below 2.75 K. This is supported by analyzing the net inductive coupling between FM and CPW in the presence of Meißner currents in Fig. 5.18, where we plot the enhancement of \tilde{L}_0 of sample E as a function of reduced temperature.

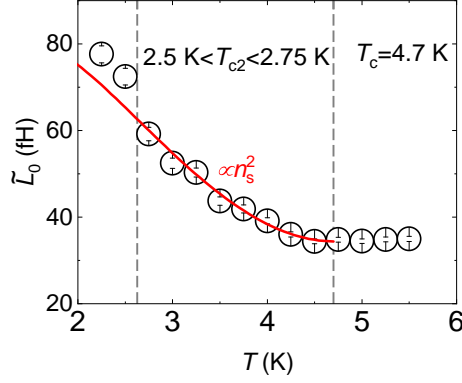


Fig. 5.18. – Offset of the real part of the reduced inductive coupling between sample and CPW \tilde{L}_0 together with the BCS superconducting Cooper pair density n_s^2 as a function of temperature T . In the SC state, Meißner currents mirror the net oscillatory driving field \mathbf{h}_{rf} of the CPW. A second SC transition at ($2.5 < T_{c2} < 2.75$) K becomes apparent in the abrupt further enhancement of \tilde{L}_0 below 2.75 K.

We observe in Fig. 5.18 a very good agreement between $n_s^2(T)$ and $\tilde{L}_0(T)$ as compared to the NbN/Py-heterostructures in Fig. 5.6(a), where we had attributed the observed disparity between $n_s^2(T)$ and $\tilde{L}_0(T)$ due to a contribution of the large kinetic inductance $L_k \propto \lambda_L^2$ in NbN. As TaN is expected to have a smaller London penetration depth compared to NbN ($\lambda_L \simeq 20$ nm [343]), the contribution of L_k to \tilde{L}_0 is much weaker in Fig. 5.18 and we hence observe a good agreement between raw data and theory prediction. Below $T \leq 2.75$ K we observe an abrupt increase in \tilde{L}_0 attributed to the additional contribution of image currents by the fraction of TaN, which is in direct contact to the FM layer. From its notable deviation from the expected behavior following $n_s^2(T)$, we can attribute this deviation to a second SC transition of the TaN thin film. For ($2.75 \text{ K} < T < T_c$), we thus assume that sample E does not exhibit a direct SC/FM-contact and hence we predominantly observe the SC shunting effect of the iSHE in the Py/TaN-bilayer in Fig. 5.17(a). For lower T , the entire TaN layer becomes superconducting and the established direct SC/FM-contact enables the SC quasiparticles to contribute to the spin transport via the QMiSHE. We note, that the direct contact of a SC to a FM material can have a significant effect on the superconducting T_c [358–360]. Note, that in Sec. 5.2, the QMiSHE has only been observed for samples A-C, which exhibit a direct contact (samples A and B) or close proximity (sample C) between SC and FM and could be fully suppressed in sample D by the insertion of a thick Pt spin-sink layer between the SC and FM. Hence, the interpretation of our results is consistent with the results for the NbN/Py-heterostructures in Sec. 5.2.

Again, our results for σ_d can be directly compared to the Gilbert damping parameter α of our TaN/Py-heterostructures, which is plotted in Fig. 5.17(b). In the normal state, we observe a larger α for sample E than in sample F, which is consistent with our previous assumption, that the cubic c-TaN in sample E acts as a stronger spin sink layer with a larger Θ_{SH} . For temperatures below the superconducting T_c of sample E, α remains constant for sample F. In contrast for sample E, α decreases towards lower temperatures at first gradually and then below 2.75 K abruptly drops to a low fixed value of $\alpha = 8.2 \cdot 10^{-3}$. This reduction in the α of sample E below T_c is in agreement with the results for the NbN/Pt/Py-heterostructure sample D in Fig. 5.7 of Sec. 5.2, where we have attributed the reduction in α in the superconducting state to the superconducting shunting effect of spin currents. Here, we note that as the spin transport by thermally excited quasiparticles in the superconductor is expected to give rise to a decay in α in a convex shape following the density of thermally excited quasiparticles $1 - (T/T_c)^4$ [361] [see samples A and B in Fig. 5.17(b)], whereas for sample E α decays in a concave shape, we attribute the reduction in α in sample E to the non-uniform superconducting transition of its TaN layer and the superconducting shunting effect rather than quasiparticle spin transport. From Fig. 5.17(b), we note that a strong reduction in α with decreasing T from quasiparticle spin transport manifests only for temperatures below 2.75 K, which corroborates our assumptions of a second superconducting transition of the TaN fraction, that interfaces the Py layer.

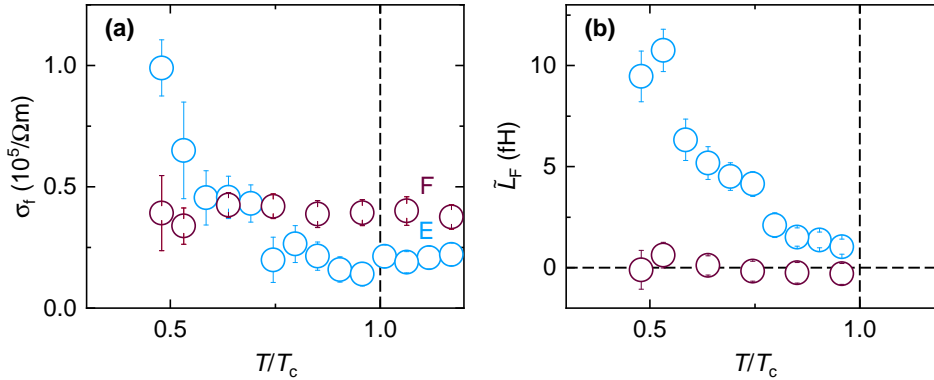


Fig. 5.19. – (a) Field-like spin torque conductivity σ_f plotted as a function of T/T_c . We observe a small positive σ_f for both samples in the normal state attributed to the iREE. In the SC state, σ_f in sample E rises to large positive values. (b) Change in $\text{Im}(\tilde{L})$ in the SC state due to SC Faraday currents labeled \tilde{L}_F . The error bars in (a) & (b) originate from fitting the extracted raw data for (\tilde{L}) with Eq. (5.14). Magnetization dynamics parameters and spin torque conductivities as function of reduced temperature.

In Fig. 5.19(a), we plot the extracted field-like inverse spin torque conductivity σ_f as function of reduced temperature for samples E and F. We observe small positive values in the normal state that are compatible with the iREE [37, 38], as the Faraday effect would give rise to negative σ_f in the substrate/NM/FM-stack sequence ($\text{sgn} = +1$) [84]. Similar σ_f values have been detected in Pt/Py-

bilayers [84]. The higher magnitude in σ_F of sample F compared to sample E can be understood from its higher conductivity in Fig. 5.14 via $\sigma_F \propto \sigma_{\text{int}}$ [84], where σ_{int} is the conductivity of the TaN/Py interface. In the superconducting state of sample E, we observe a large increase in σ_f with decreasing T . The observation of a field-like σ_f in the superconducting state is in agreement with our previous results on NbN/Py-heterostructures in Sec. 5.2. We note that the strong increase in σ_f below $T = 2.75$ K provides further evidence for the presence of a second superconducting transition for $T \leq 2.75$ K, though this effect evidently does not require direct SC/FM-contact [see Fig. 5.19(a)]. From this result, we infer that the magnitude of σ_f depends on the superconducting Cooper pair density n_s . The detected enhancement in σ_f in the superconducting state for both NbN/Py- and TaN/Py-heterostructures demonstrates that the underlying effect is universal. We speculate on its precise origin in the discussion of Fig. 5.20. In Fig. 5.19(b), we plot the contribution of Faraday currents to $\text{Im}(\tilde{L}_0)$ in the superconducting state \tilde{L}_F as function of reduced temperature. We observe a steep increase in sample E, whereas $\text{Im}(\tilde{L}_0)$ of sample F remained close to zero throughout the investigated temperature range. The magnitude of \tilde{L}_F in sample E is a factor of ≈ 3 smaller than what has been observed for our NbN/Py-heterostructures in Fig. 5.19(b) despite the lower London penetration depth $\lambda_L \simeq 20$ nm of TaN [343] compared to NbN. This result seems to indicate a reduced superconducting Cooper pair density $n_s \propto 1/\lambda_L^2$ in our TaN/Py hybrid compared to the NbN/Py-samples. This is corroborated by the reduced FMR amplitude enhancement in the superconducting state evident from Fig. 5.18.

To understand the impact of the enhanced spin-orbit interaction in TaN compared to NbN on the inverse spin-orbit torque conductivities, we plot in Fig. 5.20 the damping-like σ_d (a) and field-like σ_f (b) inverse spin-torque conductivities of the SC/Py-bilayer samples A and E as function of reduced temperature. For the damping-like σ_d in panel (a), we find comparable positive magnitudes in the normal state indicating, that σ_d is dominated by the Py layer in the normal state due to its higher conductivity. In the superconducting state, at $T/T_c \simeq 0.5$ the magnitude of σ_d in the TaN/Py-bilayer is larger compared to that of the NbN/Py-bilayer in agreement with the experimentally found larger negative Θ_{SH} of TaN ($\Theta_{\text{SH}} \approx -0.039$ [356]) compared to that of NbN ($\Theta_{\text{SH}} \approx -0.011$ [279]). For lower temperatures, the σ_d of sample A decays further and seemingly reaches a constant value in agreement with theory predictions (see Sec. 5.2). Note, that these low T/T_c -values are experimentally not accessible for the sample E due to the reduced T_c of TaN. In Fig. 5.20(b), we observe for the field-like σ_f of our samples in the normal state a slightly larger positive value for sample A compared to sample E, which we attribute to the higher conductivity of NbN compared to TaN and the corresponding larger σ_{int} in combination with the iREE. In the superconducting state, the observed increase in σ_f is much stronger for sample A as compared to sample E. Furthermore, for sample A, σ_f reaches a constant

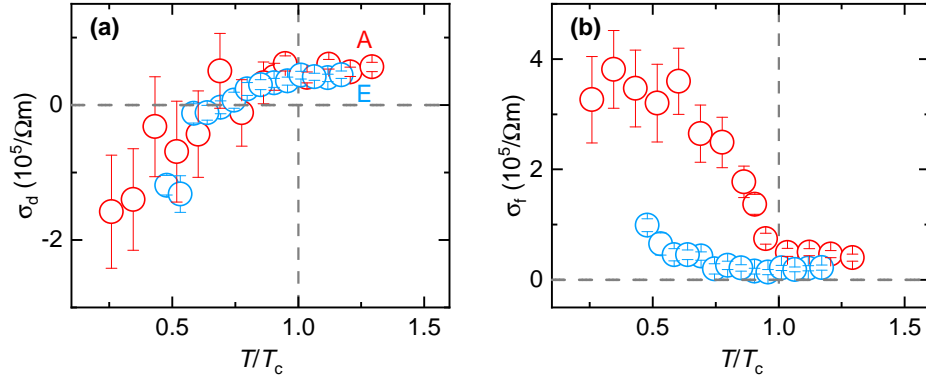


Fig. 5.20. – Inverse spin torque conductivities of the NbN/Py- and TaN/Py-bilayer samples A and E as function in the superconducting state of reduced temperature. (a) Damping-like spin torque conductivity σ_d plotted as a function of T/T_c . A positive σ_d is detected in both samples in the normal state. In the SC state, the σ_d for both samples reach negative values for a low reduced temperature. (b) Field-like spin torque conductivity σ_f plotted as a function of T/T_c . A much stronger enhancement in σ_f below T_c is observed in sample A compared to sample E.

value at $T/T_c \approx 0.6$, while increasing continuously with reducing temperatures for sample E. This observation can be related to the non-uniform superconducting transition in sample E, which clearly demonstrates that σ_f strongly depends on the superconducting Cooper pair density. In light of these results, we interpret the strongly enhanced σ_f in the superconducting state of sample A to currents induced by the dynamic field-like currents in superconductors as theoretically proposed in Refs. [295,362].

To summarize our experimental findings in this section, we have optimized the reactive dc magnetron sputtering deposition for superconducting TaN thin films on SiO₂ and have achieved films with a superconducting T_c of up to 5 K and a critical field of $\mu_0 H_{c2}(T = 0) = (13.8 \pm 0.1)$ T. Using our optimized deposition recipe, we fabricated TaN/Py-bilayers and performed broadband ferromagnetic resonance experiments in combination with our inductive analysis technique as a function of temperature and compare our results to our findings with those in Sec. 5.2. We find that in the superconducting state α decreases due to the freeze-out of thermally excited quasiparticles and a finite QMiSHE manifests in σ_d . Overall the results of bbFMR spectroscopy are in good agreement to those in our previous study on NbN/Py-bilayers [68] and demonstrate the universality of the observed behavior for the σ_{ST} for SC/FM-hybrids. In comparison to the NbN/Py-hybrids, our TaN/Py-heterostructures exhibit a larger σ_d due to the larger spin Hall angle in TaN and a much lower magnitude in σ_f , which hints to the crucial impact of the superconducting Cooper pair density to σ_f , which strongly indicates that the observed enhancement in σ_f is related to superconducting field-like currents as theoretically proposed in Refs. [295,362].

5.4 Summary and Outlook

In summary, the goal of the research discussed in this chapter was to study the dynamic spin transport into superconductors in SC/FM-heterostructures. Here, recent experiments [49, 256, 257, 285–288] have reported a diverse range of different effects for the magnetization damping in the superconducting state ranging from a monotonic reduction in the Gilbert damping α due to a freeze-out of quasiparticles (QP) mediating the spin transport [256] over the manifestation of a quasiparticle coherence peak in α for temperatures slightly below T_c [257] to an enhanced FMR-linewidth ΔH mediated by spin-triplet Cooper pairs [49]. These competing results have motivated us to study these hybrid systems from a different angle by studying the inductive coupling between sample and CPW as a function of frequency. By incorporating this inductive analysis technique in the established data analysis procedure based on the work of Berger *et al.* [84] and accounting for the modified FMR-properties in the superconducting state, we have developed a data analysis procedure to simultaneously study both the magnetization dynamics parameters and inverse spin torques of our SC/FM-hybrids as detailed in Sec. 5.1. Notably, in particular the damping-like inverse spin torque conductivity σ_d allows to study the iSHE and hence constitutes a measure for the spin pumping mechanism at the interface that can be related and compared to the recorded Gilbert damping parameter α . We have studied the magnetization dynamics and inverse spin torque conductivities of several SC/FM-heterostructures using the superconductor NbN and including heavy metal Platinum layers between either SC and FM or SC and substrate to investigate the modified spin injection into Pt in the superconducting state as well as the impact of its exchange field and the proposed generation of spin-triplet Cooper pairs on the spin transport properties of superconductors [49].

The results in Sec. 5.2 revealed the manifestation of a small out-of-plane anisotropy field $H_{\text{ani}}^{\text{OP}}$ induced by superconducting Meißner currents in agreement to the observations in Refs. [287, 316]. In our case, the magnitude is decreased, hinting at the necessity to use SC/FM/SC-trilayers to observe a large effect [355]. For the Gilbert damping α , we observe a decrease in the superconducting state, indicating the blocking of spin currents in superconductors due to the manifesting energy gap Δ in the superconducting state in agreement with the findings by Bell *et al.* [256]. Notably, our results can nonetheless reproduce the enhanced FMR-linewidth ΔH in the superconducting state observed and attributed to spin transport by spin-triplet Cooper pairs by Jeon *et al.* [49] as the inhomogeneous linewidth increases in the superconducting state thus generating a net FMR-linewidth increase for low driving frequencies. This blocking of spin currents is also apparent in the damping-like spin-torque conductivity σ_d as we observe a strong reduction with reducing temperature of the large positive σ_d from the iSHE in SC/FM-hybrid samples containing Pt. For low temperatures $T \ll T_c$,

we instead observe the manifestation of a negative σ_d in agreement with the quasiparticle-mediated iSHE in NbN [47]. For the field-like σ_f , we have observed an unexpectedly large positive contribution in the superconducting state, which seems to be independent of material interfaces in our hybrids and does not require a direct SC/FM-interface ruling out the contribution of the inverse Rashba-Edelstein effect [38]. While this effect remained unexplained in our initial study, the follow-up work on TaN/Py-heterostructures discussed later in this section has allowed us to shed some light on the physics at play for this effect. Our initial study on NbN/Py-heterostructures containing Pt [68] has allowed to reconcile the seemingly contradictory effects of the works of Bell *et al.* [256] and Jeon *et al.* [49] with the observation of the blocking of superconducting spin currents in both α and σ_d . Simultaneously, we demonstrate the contactless detection of the quasiparticle inverse spin Hall effect in agreement with Ref. [47]. Motivated by the proposal in Ref. [268], that the absence of FMR features associated with spin-triplet Cooper pairs in our initial experiments [68] could be attributed to the short coherence length of NbN ($\xi_0 \simeq 5$ nm [257]), we decided to further study the impact of spin-orbit interaction in superconductors on their spin transport properties and repeated our bbFMR experiments using the heavy spin-orbit interaction superconductor TaN, where the spin-orbit field generated by TaN should directly enable the generation of spin-triplets without the need to additionally include a Pt layer in the sample stack.

To this end, we have optimized the reactive sputter deposition process for the growth of TaN and studied the magnetization dynamics parameters and inverse spin torque conductivities σ_{ST} of TaN/Py-heterostructures in Sec. 5.3. Our optimized recipe yielded a superconducting T_c of up to 5 K on SiO₂ and a critical field of $\mu_0 H_{c2}(T = 0) = (13.8 \pm 0.1)$ T comparable to literature values [338, 341]. The TaN/Py-bilayer grown using this optimized growth recipe exhibited a very similar behavior in its magnetization dynamics compared to the NbN/Py-heterostructures in Sec. 5.2. Notably, despite the expected large spin-orbit interaction in TaN, a reduction in the Gilbert damping α in the superconducting state was also observed for the TaN/Py-heterostructures. Interestingly, for the damping-like spin torque conductivity σ_d a larger negative contribution at a fixed T/T_c has been observed as compared to NbN attributed to the QMiSHE due to the larger spin Hall angle in TaN [356]. Furthermore, the observed field-like σ_f manifesting in the superconducting state exhibited much lower values compared to the NbN/Py-bilayers, indicating the crucial impact of the superconducting Cooper pair density to σ_f . This observation points to charge currents with a field-like symmetry generated directly in the superconductor as proposed in Refs. [295, 362]. Future experiments are required to identify the precise physical mechanism giving rise to the enhanced σ_f in our heterostructures.

Our presented experiments have enabled to investigate the spin transport in superconductors from a new perspective by adding the inverse spin torque con-

ductivities as parameters for its study. Despite our best efforts, the enhancement of spin transport by spin-triplet Cooper pairs has remained elusive in our experiments both on SC/FM-hybrids containing Pt as well as for the superconductor with strong spin-orbit interaction TaN. Notably, the reduction in α in the superconducting state of SC/FM-hybrids observed in our experiments has recently been confirmed by Refs. [363,364]. The damping-like σ_d in the superconducting state represents an alternative detection technique for the study of the QMiSHE in superconductors to the spin-current injection experiments in Ref. [47], which does not require sample patterning. The observed large σ_f in the superconducting state raises interesting questions regarding the theoretical understanding of spin current transport in SC/FM hybrids. Our experimental findings point to the flux of frequency-dependent charge currents in the superconducting state apart from the superconducting Meißner currents. Such intrinsic charge currents in superconductors in the presence of spin-orbit interaction have been proposed in Refs. [295,362]. An attempt to demonstrate the control of the magnetization in the Py layer via superconducting spin torques has been performed in Ref. [122], where it was found, that the required currents to generate sizable effects in the FM layer exceed the superconducting critical current I_c . Instead, our future research aims to observe a modulation of the properties of magnetization dynamics by charge-current induced spin torques in the superconducting state using the micro-focused frequency-resolved magneto-optic Kerr effect (μ FR-MOKE) technique outlined in Refs. [30,365] at cryogenic temperatures.

Magnon-Photon coupling in superconducting microwave resonators/ferromagnetic microstructure hybrids

In the previous chapters, we have investigated, how magnetization dynamics in magnetic thin films are modified by coupling it to fluctuators caused by disordered magnetic impurities (See Ch. 4) and elementary excitations in superconductors (See Ch. 5). In the following, we will study the coupling of the quantized excitations of the spin lattice (magnons) in ferromagnets couple to other excitations such as the quantized elastic modes of the crystal lattice (phonons) or the quantized modes of electromagnetic resonators (photons). We will see that the finite coupling leads to hybridized modes. We begin with the investigation of the coupling between magnons in ferromagnetic thin films and photons in superconducting microwave resonators. High quality superconducting microwave resonators are central building blocks for today's quantum science and technology. This particularly includes quantum information processing with superconducting circuit elements [366–368] as well as the realization of single photon detectors [369–371]. Furthermore, they represent an important enabling technology for a variety of quantum devices such as quantum limited microwave amplifiers [372–374] and also play a key role in hybrid quantum systems like nano-electromechanical systems [375], cavity magnonic systems [78, 376, 377] and hybrids based on the spin-photon interaction [378–381]. One particular advantage of superconducting resonators is the possibility to achieve high and ultra-high quality factors Q in planar designs e.g. in the form of lumped-element or coplanar waveguide resonators [382–384]. This means that photons can be stored for a long time within the small mode volume of such resonators leading to strong and even ultra-strong light matter interaction.

While aluminum and niobium are the most commonly used materials in superconducting quantum technology, superconductors with higher critical temperatures T_c and high upper critical field exist and are discussed as temperature- and magnetic field-robust alternatives for hybrid devices. Note that the higher T_c translates into a larger superconducting gap. Altogether, this offers an enhanced robustness against magnetic fields and better performance at 'elevated' temperatures due to the correspondingly lower density of thermally induced quasiparticles. This furthermore allows one to push hybrid quantum systems to elevated temperatures and frequencies [385, 386]. Here, the compound niobium

titanium nitride (NbTiN) is a prime candidate, known as a hard type II superconductor with a transition temperature of up to $T_c = 17$ K [313, 387, 388] a large upper critical field. The expected good resonator performance over both large magnetic field- and temperature ranges motivate us to optimize the fabrication of NbTiN resonators for electron spin resonance (ESR) and ferromagnetic resonance (FMR) experiments in the strong coupling regime [78, 382]. The results of this optimization process for superconducting NbTiN microwave resonators, presented in section 6.1, are published in

M. Müller, T. Luschmann, A. Faltermeier, S. Weichselbaumer, L. Koch, G.B.P. Huber, H.W. Schumacher, N. Ubbelohde, D. Reifert, T. Scheller, F. Deppe, A. Marx, S. Philipp, M. Althammer, R. Gross, H. Huebl, *Magnetic field robust high quality factor NbTiN superconducting microwave resonators*, *Materials for Quantum Technology* **2**, 015002 (2022) [70].

Having optimized the fabrication of superconducting NbTiN planar microwave resonators, in Sec. 6.2, we use them as a platform for the implementation of on-chip magnon-photon hybrid devices with a magnetic strip fabricated from the metallic ferromagnet $\text{Co}_{25}\text{Fe}_{75}$ (CoFe) deposited on top of the inductive element of our meander-shaped superconducting planar microwave NbTiN resonators. As a ferromagnetic material, CoFe is selected, due to its resilient growth properties via sputtering deposition, high spin density [65] and ultralow Gilbert damping [135, 389, 390], whereas our NbTiN resonators, besides their demonstrated excellent robustness to external magnetic fields and elevated temperatures, are quasi-onedimensional cavities and therefore exhibit smaller mode volumes compared to macroscopic microwave cavities. This allows for the coupling of magnons with long-lived and concentrated photons in the resonator [79]. In our experiments, we investigate two types of hybrid devices, where the CoFe is (i) coupled either directly to the NbTiN layer and (ii) grown on top of an insulating AlN layer, spatially separating the CoFe from the NbTiN, to investigate the impact of a direct ferromagnetic exchange bias on the magnon-photon coupling. Magnon-photon hybrid devices of the latter type exhibit strong coupling with an effective magnon-photon coupling rate of $g_{\text{eff}}/(2\pi) = (120 \pm 4)$ MHz resulting in an estimated coupling rate per magnetic moment μ_B of $g_0/(2\pi) \approx 223$ Hz, which together with the loss rates of microwave resonator κ_r and magnetic thin film κ_s translates to a cooperativity of $C = g_{\text{eff}}^2/(\kappa_r\kappa_s) \approx 136$ at a temperature of $T = 3$ K. These results are comparable to the best state of the art magnon-photon devices from Refs. [79, 80] and unite the high g_0 of Ref. [80] with the usage of a hard-type-II-superconductor as done in Ref. [79] and hence demonstrate the suitability of NbTiN as a material platform to implement magnon-photon hybrid devices.

For the resonators, which are directly exchange-coupled, we observe a magnon-photon coupling in the Purcell-enhanced regime [149] due an increased magnetic relaxation rate κ_s for the CoFe layer, which has been directly grown on

top of the NbTiN resonator. The results of our magnon-photon hybrid devices will be published in a manuscript, that is still in preparation at the time of the writing of this thesis.

S. Yoshii, M. Müller, P. Oehrl, J. Franz, M. Althammer, R. Gross, M. Masashi, H. Huebl, *Manuscript title pending* (202X).

6.1 Characterization of superconducting NbTiN planar microwave resonators

In this section, we present the investigation of the quality factors for thin-film NbTiN lumped element microwave resonators from a materials perspective and compare the achieved quality factors for various substrate configurations. Furthermore, we characterize the performance of our resonators under experimentally relevant conditions for ESR and FMR experiments at applied external in-plane magnetic fields and elevated temperatures. Finally, we test their suitability for quantum science applications by quantifying their Q_{int} under optimal conditions, when cooled down to mK temperatures and using appropriate radiative and magnetic flux shielding in the Bluefors LD-400 dry dilution refrigerator (see Sec. 3.3).

6.1.1 Loss mechanisms of superconducting microwave resonators

The various loss mechanisms of superconducting microwave resonators constitute a large area of research subject to intensive study in the field of quantum physics. Here, we will only give a very brief overview on the most important loss mechanisms necessary for the understanding of the presented results, which is based on contemporary review articles and PhD theses [192,391–393]. The internal quality factor Q_{int} of our superconducting NbTiN resonators is limited by the combined contribution of all loss mechanisms present in the system. Loss channels for superconducting resonators include losses from trapped superconducting vortices [394,395], radiative losses [396], thermally excited quasiparticles [192,193] and the coupling to parasitic modes of the used sample box or transmission line [397]. For the experiments in the 17T cryostat (see Sec. 3.3), pronounced losses are expected in particular from vortices induced by flux coupled into the resonator via the superconducting coils of the magnet as well as from thermally enhanced quasiparticles at the experimentally accessible temperatures $T \leq 2.2$ K. In contrast, for the mK-experiments, the used Bluefors LD-400 dry dilution refrigerator (see Sec. 3.3) allows for experiments in the mK-range with shielding from external radiation and magnetic fields allowing to avoid these loss mechanisms. Hence, much higher quality factors are expected in our mK-experiments. Furthermore, the used resonator sample boxes have been designed to exhibit different resonant

box mode frequencies from the NbTiN superconducting resonators at $f \simeq 5$ GHz. Apart from the resonator loss channels listed so far, two level systems (TLS) with an energy splitting corresponding to f_T can interact coherently with the electric field of the resonator and enable an energy transfer from the resonator to the phonon bath. Thereby TLS constitute an additional loss channel in superconducting circuits [398]. Hence, the magnitude of the TLS-induced losses strongly depend on the microwave power P driven through the feedline [195, 391, 399, 400]. In our experiments, these TLS are present primarily in the amorphous oxide-layers at the resonator interfaces: (i) the interface between the superconducting metal layer and the air (MA), (ii) the interface between the substrate and metal (MS) and in the areas, where the metal has been removed via etching (iii) between substrate and air (SA). These three interfaces are illustrated in Fig. 6.1(a).

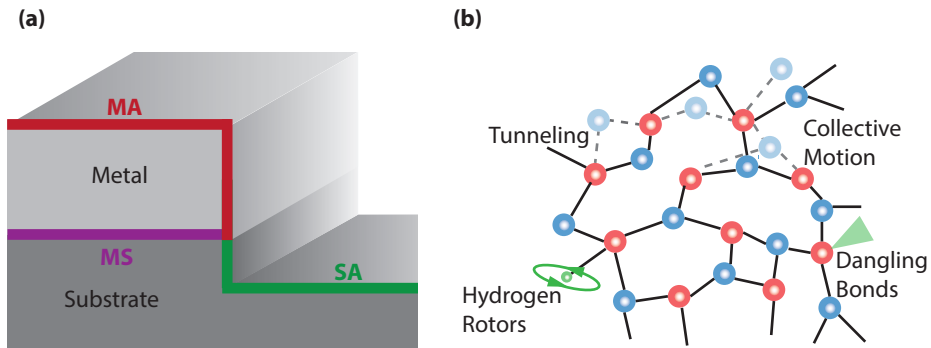
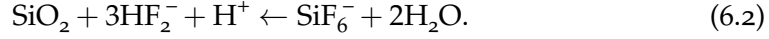


Fig. 6.1. – (a) Amorphous host interfaces of the TLS: Green lines indicate the metal-air interface (MA), violet lines represent the metal-substrate interface (MS) and green lines are the substrate-air interface (SA). (b) Possible physical mechanisms for TLS at the amorphous interfaces. Adapted from Ref. [391].

Despite extensive research [192, 196, 392, 401, 402], the precise microscopic mechanism that gives rise to TLS in amorphous solids remains elusive. Proposed mechanisms discussed in literature are illustrated in Fig. 6.1(b). The most heavily discussed mechanism is the existence of a bi-stable configuration of the atoms in the amorphous solid, where atoms can tunnel between the two configurations at a certain oscillation frequency [391]. Other proposed mechanisms for TLS include hydrogen interstitials [403], dangling bonds [404] and the interaction of tunneling electrons with collective phonon modes [405]. We note, that in contrast to the other listed intrinsic resonator loss mechanisms, the contribution of TLS is independent on the used setup and can be strongly reduced by removing the amorphous SiO_2 from the MS and SA interfaces as well as potential metallic oxides such as Nb_2O_5 - and TiO_2 from the SA and MA interfaces. In our experiments, we remove the surface oxides by performing a buffered oxide etch (BOE) using a $\sim 7:1$ mixture of hydrofluoric acid (HF, 6.5 wt%) and ammonium fluoride (34.8 wt%). HF ionizes in water via the reactions [404, 406]



and removes the SiO₂ layer following



The HF treatment thereby results in a hydrogen passivized surface, which temporarily protects the silicon surface from reoxidization [404, 407]. To avoid an overabundance of H⁺, the electrolytic ammonium fluoride buffer is used as a source of F⁻ ions to stabilize the ratio of F⁻ ions and H⁺ ions, which greatly increases the etch rate of SiO₂ (≈ 2 nm/s for a BOE 5:1 mixture ratio [392, 406]). In our process, the silicon substrate is immersed in the BOE solution for 30 s to ensure the complete removal of the native oxide layer and is subsequently directly installed in the Loadlock of the Ultradisk sputtering system within a time frame of approximately two minutes to avoid reoxidization. Consequently, our resonator optimization study aims in particular to mitigate TLS losses at these interfaces by using different substrates and performing BOE sample treatments prior to deposition.

6.1.2 Optimization series of our superconducting resonators

In detail, our superconducting planar microwave resonators are patterned into NbTiN thin films grown by sputter deposition on both pristine (001) oriented high-resistivity Si substrates ($\rho > 10^4 \Omega\text{cm}$) and on thermally oxidized SiO₂ (1 μm) on Si substrates ($\rho > 4 \cdot 10^3 \Omega\text{cm}$). The Nb₇₀Ti₃₀N thin films with a layer thickness of $d = 150 \text{ nm}$ were grown on both thermally oxidized and bare Si (100) substrates in the Ultradisk using reactive dc magnetron sputtering in a mixed N₂/Ar-atmosphere with a gas flow ratio of 3.8/36.2, a deposition temperature of $T_{\text{depo}} = 500 \text{ }^\circ\text{C}$, a pressure of $p_{\text{depo}} = 5 \text{ } \mu\text{bar}$, and a deposition power of $P_s = 95 \text{ W}$ using a 4" Nb₇₀Ti₃₀ target. These sputtering parameters are the result of a growth optimization series [186] to maximize the superconducting transition temperature of NbTiN reaching a maximum of $T_c = 16.3 \text{ K}$. For this study, the Ultradisk sputtering machine is used, as Ref. [186] had previously observed higher quality factors in a comparative study using the Ultradisk sputtering chamber compared to the Superbowls cluster potentially due to magnetic contaminants in the latter. In this study, NbTiN thin films made from three differently processed substrates and different materials have been fabricated at WMI and characterized in terms of their quality factors: (i) NbTiN grown on a SiO₂ (1 μm) on Si substrate labeled *SiO₂*, (ii) NbTiN grown on a pristine Si substrate ($\rho > 4 \cdot 10^3 \Omega\text{cm}$) with a native oxide layer, which we will refer to as *Si* and (iii) NbTiN grown on a pristine Si substrate ($\rho > 4 \cdot 10^3 \Omega\text{cm}$, where the surface oxide layer is removed with a buffered oxide etch labeled BOE [193, 404, 408]).

We compare the performance of the resonators of these three samples to (iv) one resonator chip patterned with the identical geometry from NbTiN thin films, which have been deposited on 300 nm thick thermally oxidized SiO₂ on

Si substrate ($\rho = 1 - 10 \Omega\text{cm}$) at the *Physikalisch-Technischen Bundesanstalt* (PTB), which we label as *PTB*. There, the NbTiN was grown with a layer thickness of 150 nm at a N_2/Ar gas flow ratio of 2.6/20 without any substrate heating and thermalization, a pressure of $p_{\text{depo}} = 5 \mu\text{bar}$ and at a deposition power of $P_s = 320 \text{ W}$ using a 6'' Nb₇₀Ti₃₀ target.

Atomic force microscopy (AFM) surface roughness scans displayed in Fig. 6.2 indicate low root mean square (RMS) surface roughness values of less than 1 nm for (a) the sample *SiO₂* (RMS roughness = 0.6 nm), (b) the *Si*-sample, where NbTiN is grown on a Si substrate with native oxide layer (RMS roughness = 0.7 nm) and (c) the *PTB* sample (RMS roughness = 0.8 nm). These AFM scans are representative for the whole sample area, as a uniform roughness of the NbTiN thin films throughout the substrate area of $6 \times 10 \text{ mm}^2$ has been confirmed by performing several AFM scans at varying positions on the chip. Interestingly, the NbTiN film grown on a Si substrate at the WMI, where the native oxide was stripped off prior to the deposition using a BOE treatment, *BOE* in panel (d), exhibits a higher roughness (RMS roughness = 1.5 nm) and large visible grains. We attribute this to the highly textured growth of NbTiN induced by the removal of the native amorphous oxide layer, as exclusively this NbTiN thin film exhibited diffraction peaks in x-ray scans along the (002) plane of the cubic phase oriented parallel to the substrate surface [409,410]. A detailed analysis of the x-ray diffraction of this sample has been added to the Appendix F. We note, that a low surface roughness

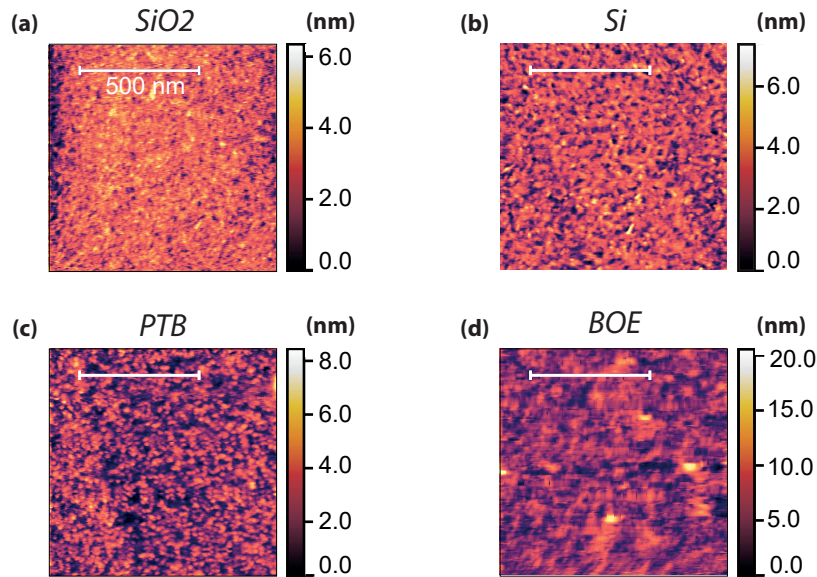


Fig. 6.2. – Atomic force microscopy surface scans of a $1 \mu\text{m}^2$ -area for the 150 nm thick NbTiN film deposited on (a) a SiO_2 -substrate (*SiO₂*) (b) *Si*-substrate (*Si*), (c) a SiO_2 -substrate from the PTB (*PTB*), (d) a BOE treated *Si*-substrate (*BOE*). The extracted RMS surface roughnesses are (a) 0.6 nm, (b) 0.7 nm, (c) 0.8 nm and (d) 1.5 nm, respectively.

is desirable to reduce losses in the planar microwave resonators at the metal-air (MA) interface [411].

Resonator	f_r (GHz)	Q ($\times 10^3$)	Q_{int} ($\times 10^3$)	Q_{ext} ($\times 10^3$)
R1	4.672	84.7 ± 1.4	215.2 ± 9.0	139.7 ± 0.1
R2	4.806	61.0 ± 0.1	152.2 ± 5.3	101.9 ± 0.1
R3	4.924	84.3 ± 0.6	207.8 ± 3.8	141.9 ± 0.1
R4	5.026	69.4 ± 2.3	161.7 ± 12.0	121.5 ± 0.1
R5*	5.133	17.9 ± 0.1	50.6 ± 0.1	27.9 ± 0.1

Tab. 6.1. – Extracted fitting parameters for resonance frequency f_r , the quality factors Q , Q_{int} and Q_{ext} for the five on-chip NbTiN resonators of the *BOE*-sample. Measurements are performed at $T = 2.2\text{ K}$, $\mu_0 H_{\text{ext}} = 0\text{ mT}$ and at a microwave power corresponding to the high power regime. Resonator R5 is marked with a *, as it has been omitted from the statistical analysis due to its uncharacteristically bad performance.

Using the micropatterning fabrication procedure using electron beam lithography and reactive ion etching in a mixed SF_6/Ar -atmosphere as outlined in detail in Sec. 3.2, all of the NbTiN films are patterned into planar lumped element resonators. The used chip layout includes a microwave transmission or feedline coupled in a hanger-type configuration to five lumped element microwave resonators, which slightly differ in their capacitance C and hence their resonance frequency f_r . This configuration allows for a multiplexed readout of the on-chip resonators (see also Fig. 3.3 for the geometry of the resonator layout). For our initial characterization measurements, the finalized chip is mounted in a gold plated oxygen free high thermal conductivity copper sample box and inserted into the 17T cryostat using the measurement configuration depicted in Fig. 3.6(a). In our initial resonator performance characterization experiments, we connect the two ends of the central feed line to the two ports of a VNA and record the complex transmission parameter $S_{21}(f)$ at the lowest experimentally accessible temperature $T = 2.2\text{ K}$ and $\mu_0 H_{\text{ext}} = 0\text{ mT}$ close to the resonance frequency f_r for each of the five resonators using microwave powers that correspond to the high-photon limit of the resonators ($\langle n_{\text{ph}} \rangle \simeq 10^7$).

The quality factors Q , Q_{ext} and Q_{int} as well as resonance frequency f_r for each resonator is then extracted individually by fitting the recorded complex transmission data to $S_{21}(f)$ using the ‘circle fit method’ via Eq. (3.18). Exemplary fitted Q , Q_{ext} and Q_{int} and f_r of the *BOE*-sample are listed in Tab. 6.1. The fitted parameters for all resonators of this study are listed in the Appendix F2 in Tabs. F1-F4.

Being primarily interested in the typically achievable performance of our resonators, we choose to omit resonators with uncharacteristically low Q_{int} from our analysis. Hence, resonator R5 in Tab. 6.1, highlighted with an asterisk, is omitted from our statistical analysis. To enable the reliable comparison for the average resonator performance on different substrates, we calculate the mean Q -factors for each of the four samples, while accounting for the deviations between the resonators by setting the value for the net error of the Q -values as the sum

of the fitting uncertainty and a statistical error σ/\sqrt{N} , where σ is the standard deviation of the extracted Q -values and N is the number of resonators. The extracted average quality factors for all investigated NbTiN films grown on different substrates are listed in Tab. 6.2. Additionally, we add the resonance frequency of the third resonator with the middle resonance frequency f_r^{R3} to discuss the varying dielectric properties for the different resonators.

Substrate	$Q (\times 10^3)$	$Q_{\text{int}} (\times 10^3)$	$Q_{\text{ext}} (\times 10^3)$	$f_r^{\text{R3}} (\text{GHz})$
<i>SiO₂</i>	9.3 ± 1.8	13.2 ± 3.6	38.7 ± 10.7	5.525
<i>PTB</i>	11.7 ± 1.6	21.3 ± 4.5	45.2 ± 15.0	4.697
<i>Si</i>	28.5 ± 7.9	208.3 ± 70.4	37.8 ± 11.6	4.927
<i>BOE</i>	74.6 ± 7.0	182.5 ± 22.7	126.3 ± 9.8	4.924

Tab. 6.2. – Mean quality factors Q , Q_{int} and Q_{ext} and resonance frequency of resonator 3 f_r^{R3} of the NbTiN resonators, deposited on the different substrates. Measurements are performed at $T = 2.2 \text{ K}$, $\mu_0 H_{\text{ext}} = 0 \text{ mT}$ and at a microwave power corresponding to the high power regime.

For the NbTiN films grown on SiO_2 at the WMI denoted as *SiO₂*, we obtain an average internal quality factor of $Q_{\text{int}} = (13.2 \pm 3.6) \cdot 10^3$, which is about 1.5 times lower than that of the PTB film [$Q_{\text{int}} = (21.3 \pm 4.5) \cdot 10^3$], despite the a larger surface roughness of this film [see Fig. 6.2(a) and (b)]. As the NbTiN resonators from the PTB are patterned on substrates with a lower SiO_2 layer thickness ($d_{\text{SiO}_2}^{\text{PTB}} = 150 \text{ nm}$) compared to the NbTiN resonators grown on SiO_2 at the WMI ($d_{\text{SiO}_2}^{\text{WMI}} = 1 \mu\text{m}$), this result suggests that the thickness of the thermally grown oxide layer has a strong impact on Q_{int} . We interpret this as the TLS losses scaling with the thickness of the oxide layer. The increased f_r^{R3} of the *SiO₂*-sample with respect to the other samples can be understood from the reduced dielectric constant ϵ of the SiO_2 -layer compared to elementary Si [86], whereas the comparatively reduced f_r^{R3} of the *PTB*-sample is attributed to the reduced layer thickness of the used Si substrate. Note, that the third resonators has been designed to exhibit an $f_r \approx 5 \text{ GHz}$ on Si substrates by using finite element simulations [412]. Hence, we can confirm a decent frequency targeting for the resonators on samples *Si* and *BOE*, where NbTiN is grown on bare Si substrates. Furthermore, the precise deposition conditions play an important role on the obtained quality factors. In particular, the selected deposition power P_{depo} governs the deposition rate r_{depo} , which has been found to have a crucial impact on the disorder in superconductors with higher deposition rates being desirable [413]. The comparatively higher deposition power used for the films grown at PTB can hence also give rise to NbTiN thin films with reduced disorder-induced TLS, though no clear correlation between P_{depo} and Q_{int} has been observed for our films in Ref. [186]. For the resonators of the *Si*-sample, we find one order of magnitude higher average internal quality factors $Q_{\text{int}} = (208.3 \pm 70.4) \cdot 10^3$ compared to samples *SiO₂* and

PTB. We attribute this to increased TLS losses from the MS interface induced by the diffusion of oxygen from the SiO₂-layer into the NbTiN layer in these samples. The resonators for the NbTiN thin films grown on BOE-treated Si achieved internal quality factors $Q_{\text{int}} = (182.5 \pm 22.7) \cdot 10^3$, comparable to those of the untreated Si-substrate. This finding indicates, that the TLS at the MS-interface from the remaining native SiO₂-layer are not the limiting factor for the resonator performance. The slightly lower average Q_{int} for the *BOE*-sample compared to the *Si*-sample are attributed to its larger surface roughness (see Fig. 6.2) and the resulting enhanced losses from oxidized Nb₂O₅ and TiO₂-phases [414] at the roughened MA-interface. Notably, the enhanced crystalline texturing of the *BOE*-sample does not result in higher internal quality factors, indicating that TLS losses in the bulk of the superconductor, induced for example from lattice interstitials or dangling bonds in the reactively sputtered NbTiN compound, do not significantly contribute to Q_{int} . In summary, we find in our sample series, that losses from TLS at the MS-interface constitute the dominant loss mechanism in our resonators, which can be greatly mitigated by using bare Si substrates. We identify TLS from the Nb₂O₅- and TiO₂-phases at the MA-interface as a secondary source of losses, whereas the crystalline quality of the bulk does not impact the performance of our resonators in contrast to the results of Ref. [404]. By fitting our raw data for $S_{21}(f)$ to equation (3.18), we are also able to extract the external quality factors Q_{ext} of our resonators. Here, we find in Tab. 6.2, that the resonators of the samples *SiO₂*, *PTB* and *Si* share an external quality factor of $Q_{\text{ext}} \approx 4 \cdot 10^4$ within the margin of error. This is expected as we have used the identical layout for all chips (see Fig. 3.3) with an equal spacing of $w_{\text{gs}} = 40 \mu\text{m}$ between feed line and resonators, except for those of the *BOE* samples. Here, we have used $w_{\text{TL}} = 70 \mu\text{m}$ to avoid large uncertainties in Q_{int} for overcoupled resonators resulting in $Q_{\text{ext}} \approx 1.3 \cdot 10^5$ for this case. In comparison to existing results for planar microwave resonators made from elementary Nb at the WMI [382,415], our NbTiN resonators grown on Si exhibit an one order of magnitude higher the Q_{int} at liquid helium temperatures and are now used as the base material platform for ongoing research towards the implementation of quantum memory based on spin donors in Si [416] and EPR spectroscopy on 2d materials.

6.1.3 Performance of NbTiN resonators at elevated temperatures and at applied magnetic fields

Having developed an optimal recipe for the fabrication of superconducting planar microwave NbTiN resonators with a high $Q_{\text{int}} \simeq 2 \cdot 10^5$ at $T = 2.2 \text{ K}$, we now study the robustness of our resonators to elevated temperatures, which is of particular interest in ESR experiments to identify the various possible spin-lattice and spin-spin interaction mechanisms, which govern the spin-lattice- and spin-spin relaxation rates T_1 and T_2 [191,417]. To exemplify the typical performance of

our NbTiN resonators, we focus on R1 from Tab. 6.1 of the BOE-sample. Figure 6.3 shows the relative change in its resonance frequency and internal Q -factor in the temperature range ($2.2 \leq T \leq 13$) K. The superconducting transition temperature $T_c = 16.3$ K for this NbTiN thin film was determined by recording the transmission parameter $|S_{21}(T)|$ as function of temperature using the same method as in Ch. 5, which is described in the appendix C. We also attempted to characterize the performance of this resonator in the range ($13 \text{ K} \leq T_c$), but found that when approaching T_c the steep dependence of f_r with temperature limited the reliable determination of Q_{int} due to finite temperature fluctuations. As shown

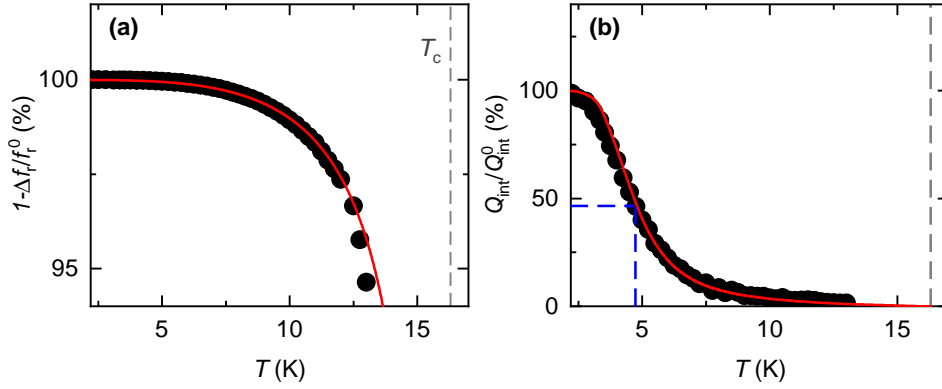


Fig. 6.3. – Internal quality factor of a NbTiN resonator (R1 of the BOE-sample from Tab. 6.1) as function of temperature T . (a) Normalized change in resonance frequency $1 - \Delta f_r(T)/f_r^0$ as a function of temperature T . The black dashed vertical line indicates $T_c = 16.3$ K and the red curve represents a fit following the imaginary part of Eq. (6.3). (b) Internal quality factor Q_{int} normalized by its value at $T = 2.2$ K. The red curve represents a fit to the real part of Eq. (6.3) to the data with a finite residual quality factor. The blue dashed lines in panel (b) indicate where Q_{int} drops below 10^5 .

in Fig. 6.3(a), the resonance frequency f_r remains roughly constant in the range $T \leq 7$ K, and then rapidly drops with increasing T , reaching a maximum relative change of 5.5% at $T = 13$ K. For the Q_{int} of this resonator, plotted in Fig. 6.3(b), we observe a much stronger reduction with increasing T , approaching only about 1.5% of its low temperature value at $T = 13$ K. We model the temperature dependence of the resonance frequency $f_r(T)$ and the internal quality factor $Q_{\text{int}}(T)$ of the resonators with that of the surface reactance $X_s(T)$ and surface resistance $R_s(T)$ of the superconducting NbTiN using the relation [192, 418]

$$\frac{1}{Q_{\text{int}}(T)} + 2i \frac{\Delta f_r(T)}{f_r^0} = \frac{\beta}{\mu_0 \omega_r^0 \lambda_L(0)} (R_s(T) + i \delta X_s(T)). \quad (6.3)$$

Here, β denotes the contribution of the kinetic inductance to the total inductance, μ_0 is the vacuum permeability and $\delta X_s(T)$ represents the change in surface reac-

tance with temperature [$\delta X_S(T) = X_S(T) - X_S(0)$]. The temperature dependence of $R_S(T)$ and $\delta X_S(T)$ is given by [258,419]

$$\begin{aligned} R_S(T) &= \frac{1}{2} \mu_0^2 \lambda_L^3(T) \omega^2 \sigma_0 \frac{n_n(T)}{n} \\ \delta X_S(T) &= \mu_0 \omega [\lambda_L(T) - \lambda_L(0)], \end{aligned} \quad (6.4)$$

where σ_0 is the normal state conductivity, $n_n(T)$ is the density of unpaired charge carriers and n the total charge carrier density. As previously used in Ch. 5, we determine $n_n(T/T_c)/n = 1 - 2n_s(T/T_c)/n$, where n_s is the cooper pair density, using BCS theory [319,320]. Equation (6.3) can be divided into a real and an imaginary part, which respectively correspond to the temperature evolution of the resonance frequency f_r and the internal quality factor Q_{int} . The resulting fit using Eq. (6.3) is presented as a red line in Fig. 6.3(a). By using the relation $\lambda_L(T) = \lambda_L(0) / \sqrt{1 - (T/T_c)^4}$ [361], with $\lambda_L(0) = 200$ nm for NbTiN [420] and $T_c = 16.3$ K, we obtain $\beta = 0.124 \pm 0.001$. This value of β falls into the expected range for planar 2D-resonators ($10^{-2} \leq \beta \leq 1$) [421–423]. In the following step, we fit the internal quality factor $Q_{\text{int}}(T)$ in Fig. 6.3(b) using the real part of Eq. (6.3) and the previously used parameters for T_c and λ_L and the extracted value β . The fitting curve is shown as a red line in Fig. 6.3(b). We obtain a normal state conductivity of $\sigma_0 = (11 \pm 4) \cdot 10^6 \Omega^{-1} \text{m}^{-1}$, which is in good agreement with the results of Van-der-Pauw transport experiments [226] on our unpatterned films, where we detected varying σ_0 in the low $10^6 \Omega^{-1} \text{m}^{-1}$ -range. The dashed blue line in Fig. 6.3(b) represents the temperature, where the Q_{int} of R1 decays below 10^5 . We find a $Q_{\text{int}} > 10^5$ for temperatures $T \leq 4.8$ K, which greatly outperforms the “high-quality” temperature range of comparable resonators made from elementary Nb [424].

As a next step, we investigate the performance of our resonators in an external in-plane magnetic field to test their suitability for ESR- and FMR-applications. In Fig. 6.4(a) and (b), we plot the normalized shift in resonance frequency $1 - \Delta f_r(T)/f_r^0$ and internal quality factor Q_{int} of resonator R1 of the BOE-sample at $T = 2.2$ K as function of applied external in-plane magnetic field $\mu_0 H_{\text{ext}}$ in the range ($0 \text{ mT} \leq \mu_0 H_{\text{ext}} \leq 440 \text{ mT}$). For higher $\mu_0 H_{\text{ext}} > 440 \text{ mT}$, the fitting of the $S_{21}(f)$ spectra of this resonator becomes unreliable.

For f_r , we observe a weak reduction with increasing $\mu_0 H_{\text{ext}}$ due to the depletion of the superconducting condensate due to a reduction of the free enthalpy of the superconductor due to the magnetic field repulsion, which can be fitted with a quadratic relation [$\Delta f_r(\mu_0 H_{\text{ext}}) \propto (\mu_0 H_{\text{ext}})^2$, red line in Fig. 6.4] in agreement with Refs. [425,426]. For the internal quality factor Q_{int} in Fig. 6.4(b), we observe a nearly constant Q_{int} until $\mu_0 H_{\text{ext}} \approx 130 \text{ mT}$ and a strong decrease in Q_{int} for higher $\mu_0 H_{\text{ext}}$. For the magnetic field performance of this resonator, a $Q_{\text{int}} > 10^5$ is achieved for $\mu_0 H_{\text{ext}} \leq 180 \text{ mT}$ as indicated by the blue dashed lines in Fig. 6.4(b). For comparison to elementary Nb, in Ref. [424] a reduction of Q_{int} by a factor

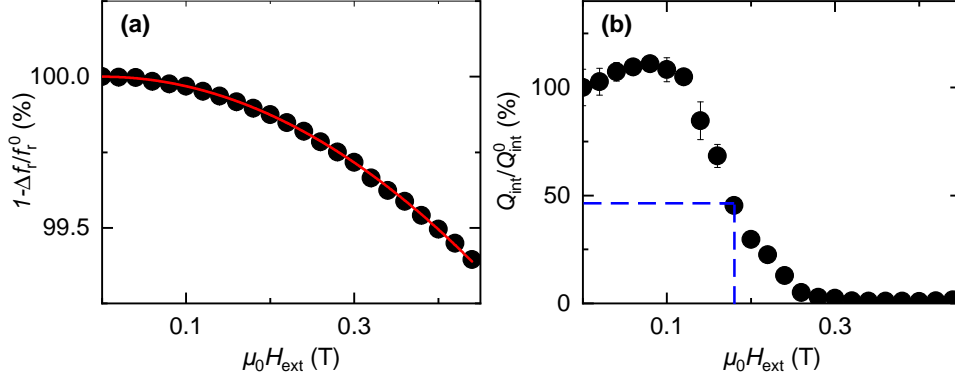


Fig. 6.4. – Internal quality factor of a NbTiN resonator (R1 of the *BOE*-sample from Tab. 6.1) in an external in-plane magnetic field $\mu_0 H_{\text{ext}}$. (a) Normalized change in resonance frequency $1 - \Delta f_r(\mu_0 H_{\text{ext}}) / f_r^0$ as a function of $\mu_0 H_{\text{ext}}$. The red curve represents a quadratic fit. (b) Internal quality factor Q_{int} normalized by its value at $\mu_0 H_{\text{ext}} = 0$ mT. The blue dashed lines in panel (b) indicate where Q_{int} drops below 10^5 .

of ≈ 20 between zero-field and $\mu_0 H_{\text{ip}} = 180$ mT was observed for Nb resonators, whereas within the same field range, the internal quality factor of our NbTiN resonators in Fig. 6.4(b) only reduce by a factor of ≈ 2 . These results underpin the better suitability of NbTiN compared to elementary Nb as a materials platform for ESR and FMR experiments as it offers a good resonator performance over both a larger magnetic field- and temperature range.

6.1.4 Performance of NbTiN resonators at mK temperatures for quantum science applications

To characterize the performance of our resonators for quantum applications, we install the *BOE*-sample in a Bluefors LD-400 dry dilution refrigerator [see Fig. 3.6(b)] using the same sample package as used for the 17 T setup and characterize its resonator R1 at the cryostat's base temperature of < 7 mK by recording the complex transmission parameter $S_{21}(f)$ as function of frequency around $f_r^{\text{R1}} = 4.672$ GHz. We then repeat this experiment for varying microwave spectroscopy powers P to investigate the impact of the TLS on Q_{int} . Here, P can be translated into an average photon occupancy $\langle n_{\text{ph}} \rangle$ by using

$$\langle n_{\text{ph}} \rangle = P \left(\frac{1}{h \cdot f_r} \cdot \frac{2\kappa_{\text{ext}}}{\kappa} \right). \quad (6.5)$$

The measured Q_{int} as function of $\langle n_{\text{ph}} \rangle$ is plotted in Fig. 6.5.

We observe a continuous increase in Q_{int} with increasing resonator photon population from $\approx 2 \cdot 10^5$ in the single photon limit at $\langle n_{\text{ph}} \rangle \simeq 1$ to $\approx 5.2 \cdot 10^5$ in the high power range at $\langle n_{\text{ph}} \rangle \simeq 10^7$. However, we do not observe a saturation in Q_{int} at high average photon numbers, suggesting that TLS-induced losses still constitute a substantial loss channel even at these high $\langle n_{\text{ph}} \rangle$ in agreement to

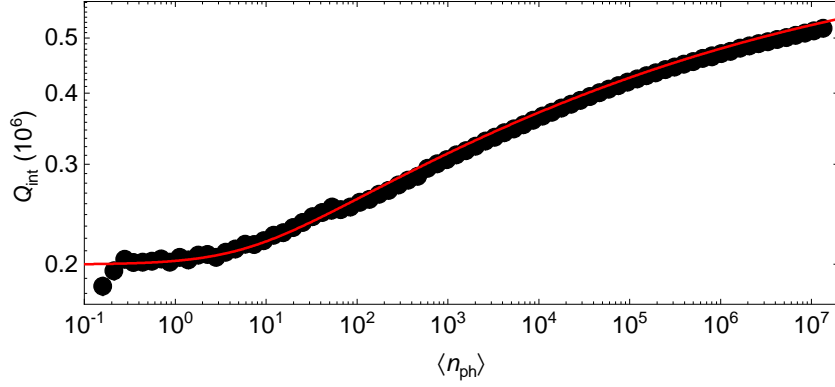


Fig. 6.5. – Intrinsic quality factor of a NbTiN resonator grown on BOE-treated Si (R1 from Tab. 6.1) and measured in the Bluefors LD-400 dry dilution refrigerator [see Fig. 3.6(b)] at $T < 7$ mK as function of photon number $\langle n_{\text{ph}} \rangle$. The resonator Q -factors and f_r are extracted by fitting the $S_{21}(f)$ -spectra to Eq. (3.18) and are then used to convert the calibrated input power P to $\langle n_{\text{ph}} \rangle$ using Eq. (6.5). The continuous red line represents a fit to Eq. (6.6).

previous reports on the power-dependence of Q_{int} in NbTiN in Refs. [402, 427]. The net Q_{int} at millikelvin temperatures is about a factor of two higher compared to the peak performance at $T = 2.2$ K in the 17T-setup in Tab. 6.1. We attribute this disparity to the mitigation of thermal-, magnetic field- and radiation-induced losses [192, 193]. The power dependence of $Q_{\text{int}}(\langle n_{\text{ph}} \rangle)$ is fitted using [428, 429]

$$\frac{1}{Q_{\text{int}}(\langle n_{\text{ph}} \rangle)} = F \tan \delta_{\text{TLS}}^0 \left(1 + \frac{\langle n_{\text{ph}} \rangle}{\langle n_{\text{ph}}^c \rangle} \right)^{-\alpha} + \frac{1}{Q^*}, \quad (6.6)$$

where $F \tan \delta_{\text{TLS}}^0 = 1/Q_{\text{TLS}}$ represents the total TLS loss at $\langle n_{\text{ph}} \rangle = 0$ and $T = 0$ K, $\langle n_{\text{ph}}^c \rangle$ denote the critical mean photon number above which the TLS defects are saturated and α is an exponent indicating the deviation from the standard TLS model (in the standard model $\alpha = 0.5$). Finally, the offset $1/Q^*$ accounts for all other (non-TLS associated) loss channels.

From the fit using Eq. (6.6) to the experimentally extracted Q_{int} , shown as a red line in Fig. 6.5, we extract the total TLS loss $F \tan \delta_{\text{TLS}}^0 = (3.6 \pm 0.1) \cdot 10^{-6}$, $\langle n_{\text{ph}}^c \rangle = (6.1 \pm 0.7) \cdot 10^3$, $\alpha = 0.14 \pm 0.03$ and $Q^* = (7.2 \pm 0.2) \cdot 10^5$. The fitted magnitude of α deviates from $\alpha = 0.5$ expected within the conventional TLS model, but is in agreement with values found for Al [428]. The total TLS losses consist of contributions originating from the dielectric losses at the MA, MS and SA-interface as well as the impact of the loss tangent of the substrate (S). Assuming that these are known factors and accounting for the geometry of the resonator, we compute $F \tan \delta_{\text{TLS}}^0$ using *Ansys HFSS (Ansys Electronics Desktop 2020 R2)* finite element simulation software (for details see Appendix Sec. F3). We use the same loss tangents $\tan(\delta_i)$, layer thicknesses d_i and dielectric constants ϵ_i/ϵ_0 of the four dielectric regions as for TiN in Ref. [401], we obtain $F \tan \delta_{\text{TLS}}^0 \approx 0.5 \cdot 10^{-6}$ with dominant losses from the substrate and SA-interface. This value

is approximately one order of magnitude smaller than the experimentally fitted $F \tan \delta_{\text{TLS}}^0 = (3.6 \pm 0.1) \cdot 10^{-6}$. This disparity suggests that either the NbTiN/Si interface is not well described within our model or that other contributions play a more dominant role. A detailed study disentangling and identifying the source of this discrepancy is necessary in the future. The large value for the critical photon number $\langle n_{\text{ph}}^c \rangle$ extracted from the fit in Fig. 6.5 results from the continuous rise in Q_{int} with $\langle n_{\text{ph}} \rangle$ as previously observed for NbTiN in Refs. [402, 427], but also for other materials such as elementary Nb [430, 431], NbN [425, 432] and TiN [401] and is the object of active research. One potential explanation is that NbTiN is considered an extreme ‘dirty superconductor’ with a large defect density, which may constitute an additional source of TLS in our NbTiN thin films.

Notably, the Q_{int} observed in our resonators is comparable to NbTiN resonators fabricated with similar processes [i.e. without deep reactive ion etching (DRIE) or hexamethyldisilazane (HMDS) surface passivation] in Ref. [427]. This demonstrates the state-of-the-art performance of our sputter-deposited NbTiN thin films and furthermore also suggests that defects within the material might represent a limiting factor for our resonators. To investigate the metallic bulk loss channel, future investigations of the impact on stoichiometry of NbTiN films as well as crystalline growth modes are required [404]. In literature, higher quality factors ($Q_{\text{int}} \simeq 10^6$) for NbTiN have been achieved for coplanar waveguide NbTiN resonators in Ref. [402]. Here, Bruno *et al.* have additionally performed deep reactive ion etching (DRIE) and used hexamethyldisilazane (HMDS) surface passivation to further reduced losses from TLS at the MS substrate interface and boost the performance of their resonators. Hence, future studies on NbTiN deposited on surface-passivated substrates and resonator patterning using DRIE to reduce oxygen-related TLS at the metal/substrate-interface are desirable [402, 428].

6.2 Magnon-Photon coupling in thin-film devices

To characterize magnon-photon coupling in our heterostructures, we fabricate NbTiN resonators with the same layout (see Fig. 3.3) and our optimized deposition recipe including the buffered oxide etch and deposit a rectangular ferromagnetic bar made from the ultralow damping alloy $\text{Co}_{25}\text{Fe}_{75}$ (CoFe) [135, 389, 390] with a width of $w_{\text{FM}} = 11 \mu\text{m}$, a length of $l_{\text{FM}} = 400 \mu\text{m}$ and a thickness of $d_{\text{FM}} = 30 \text{ nm}$ on top of the inductive element of the resonators (see Fig. 6.6) by performing an ex situ deposition in the Superbowl sputtering machine. The rectangular structure is processed via the lift-off technique using the resist procedure outlined in Sec. 3.2. In detail, we pattern our resonators using different deposition recipes:

(i) We deposit a trilayer of $\text{CoFe}(30 \text{ nm})/\text{Cu}(3 \text{ nm})/\text{Ta}(3 \text{ nm})$ directly on the NbTiN layer of the resonator and thereby generate a direct SC/FM-interface, which is expected to deteriorate the magnetic properties of the CoFe layer as oxides are present at the NbTiN/CoFe-interface due to the ex-situ deposition

process [414]. Here, we aim to investigate, how the ferromagnetic exchange bias at the direct SC/FM-interface impacts the magnon-photon coupling.

(ii) In analogy to the experiments in Refs. [79,80], for our second deposition process, we insert an insulating buffer layer between resonator and FM bar. Here, we select AlN [161] due to the expected good magnetic properties of CoFe grown on nitrides [122] in contrast to CoFe grown on oxides like e.g. SiO₂. Again, we deposit a trilayer comprising CoFe(30 nm)/Cu(3 nm)/Ta(3 nm) on top of the insulating layer. (iii) As a reference, one superconducting on-chip NbTiN resonator is not covered with a magnetic bar.

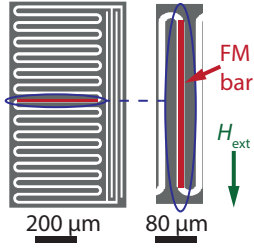


Fig. 6.6. – Illustration of the FM-bar deposited on the inductive element of the superconducting resonator. In our experiments, an external magnetic field H_{ext} is applied along the long axis of the FM bar (green arrow).

To characterize the magnetic properties of CoFe ex-situ grown on NbTiN and in-situ grown on AlN, we deposit the CoFe(30 nm)/Cu(3 nm)/Ta(3 nm) on unpatterned NbTiN reference chips from the UD with and without the insertion of the AlN buffer layer. These chips are fabricated within the same deposition run as the FM bars of our magnon-photon hybrid samples and hence allow for the characterization of magnetic loss rate κ_s , though micropatterning of the FM bars might deteriorate the magnetic properties [79]. The reference chips are then investigated in ip-bbFMR experiments at room temperature. Their resulting H_{res} and ΔH is plotted in Fig. 6.7(a)

and (b), respectively.

For the resonance field H_{res} in panel (a), we find a slightly different evolution with frequency for the two reference samples, which indicates that the different used seedlayers have affected their magnetic properties. We fit $H_r(f)$ to the ip-Kittel equation via Eq. (2.26) and find a reduced $\mu_0 M_{\text{eff}} \simeq 2.0$ T for the sample, where CoFe has been ex-situ deposited on NbTiN compared to the $\mu_0 M_{\text{eff}} \simeq 2.3$ T for the sample, where CoFe has been in-situ deposited on the protective AlN buffer layer. We note that the M_{eff} of the latter is in good agreement to literature values [135, 389, 390]. We attribute the reduced M_{eff} of the CoFe on NbTiN sample to the diffusion of oxygen into the CoFe layer. From the inset in panel (a), we find a different expected resonance field for the superconducting resonator resonance frequency $\mu_0 H_{\text{res}}(f_r)$ of the two samples [see star symbols of the inset in Fig. 6.7(a)]. For the FMR linewidth ΔH in Fig. 6.7(b), we observe a non-linear evolution in $\Delta H(f)$ for both samples. This can be attributed to a temperature dependent magnetic relaxation process (see Sec. 2.3.3) or two-magnon scattering processes [114–116]. At f_r , we extract magnetic relaxation rates $\kappa_s = \gamma \Delta H / (4\pi)$ of $\kappa_s^{\text{NbTiN/CoFe}} / (2\pi) \approx (231 \pm 3)$ MHz and $\kappa_s^{\text{AlN/CoFe}} / (2\pi) \approx (108 \pm 2)$ MHz [see star symbols in Fig. 6.7(b)].

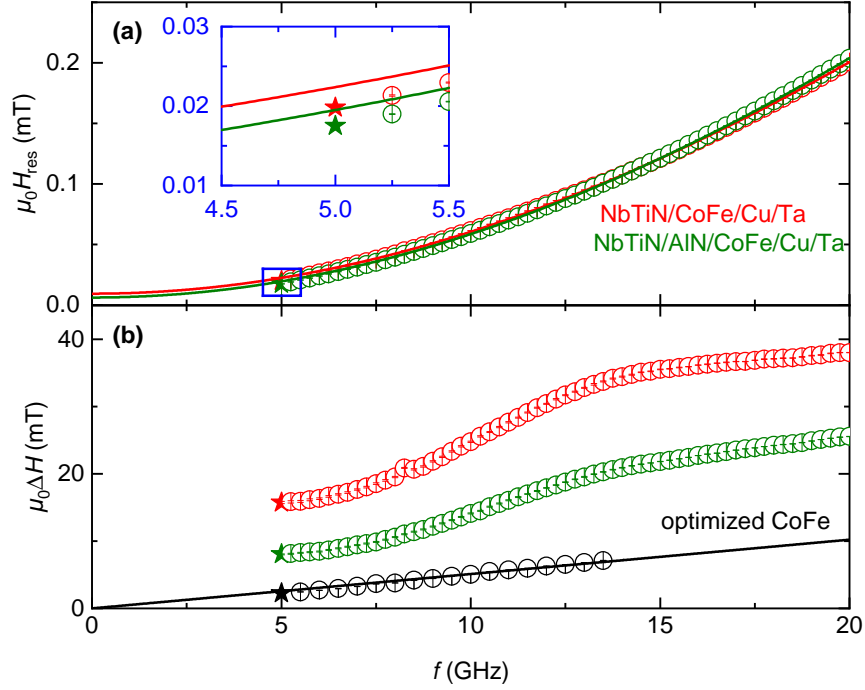


Fig. 6.7. – Ferromagnetic resonance field H_{res} (a) and linewidth ΔH of the CoFe thin films deposited on NbTiN grown in the Ultradisk (red) and the AlN buffer layer (green) as function of frequency recorded at RT in an external magnetic field applied in the sample plane along the long axis of the magnetic bar. In panel (a), the inset displays the range around $f_r \simeq 5$ GHz. Continuous lines represent fits to Eq. (2.26). To compare the observed FMR-linewidth in panel (b) to that of CoFe grown under optimized growth conditions following Ref. [135] (black dots). Star symbols in panels (a) and (b) represent the data points at the frequency of the superconducting microwave resonator ($f_r \simeq 5$ GHz).

These magnetic relaxation rates are comparable to those of Py in Refs. [79,80] but are higher than what would be expected for CoFe grown under optimal conditions [135,389,390]. The black data points in Fig. 6.7(b) represent the RT-ip FMR-linewidth of a 30 nm thick CoFe film grown in a Pt/Cu/CoFe/Cu/Ta layer stack, which has been found to exhibit ultralow Gilbert damping in Ref. [135] together with a linear fit to Eq. (2.28) (black line) yielding a Gilbert damping of $\alpha \approx 5 \cdot 10^{-3}$. For this sample, we extract an optimal magnetic relaxation rate of $\kappa_s^{\text{opt.CoFe}} / (2\pi) \approx 33 \pm 2$ MHz at $f_r = 5$ GHz. Since it is possible to grow CoFe with good magnetic properties on nitrides [122], we attribute the deteriorated magnetic properties of our thin films to a roughening of the NbTiN base layer due to oxidization (see also Fig. 6.2). While oxidized 3d transition metals can exhibit a more complicated temperature-dependence due to antiferromagnetic phases [137], we nonetheless assume a temperature-robust κ_s for these samples in agreement with our experiments in Refs. [122,433].

For the superconducting resonator/ferromagnetic bar hybrid sample discussed in the following, we did not deposit any FM bar on the NbTiN resonator R1 (acting as the reference) and deposited the FM bars made from AlN/CoFe on two resonators R2 and R4 as well as CoFe on resonators R3 and R5. The finalized

chip is mounted in a copper sample box and inserted into the 17T cryostat using the measurement configuration depicted in Fig. 3.6(a). An overview scan for the recorded microwave transmission $|S_{21}|(f)$ as function of f at $T = 3$ K in the unordered state of the magnetic CoFe layer at a microwave power corresponding to the high power regime is shown in Fig. 6.8.

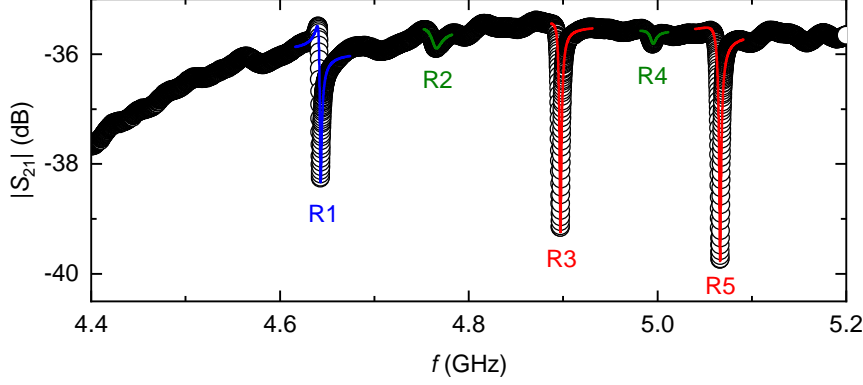


Fig. 6.8. – Microwave transmission spectra of the five on-chip NbTiN superconducting resonators recorded at $T = 3.0$ K, $\mu_0 H_{\text{ext}} = 0$ mT and at a microwave power corresponding to the high power regime. Continuous lines represent fits to Eq. (3.18). R1 is the bare reference resonator (blue), resonators R2 and R4 are coupled to CoFe strips grown on AlN (green), whereas resonators R3 and R5 are coupled to CoFe strips grown directly on the NbTiN layer (red).

Three distinct absorption dips can be identified for both the bare NbTiN resonator R1 (blue) and the resonators R3 and R5, which are directly coupled to the CoFe bar (red), whereas the resonators R2 and R4 exhibit weak absorption dip indicative of undercoupled resonators with $Q_{\text{ext}} \gg Q_{\text{int}}$. We interpret this as a reduced Q_{int} for all resonators due to the additional performed micropatterning steps deteriorating the MA-interface. In this picture, the resonators R3 and R5 remain critically coupled to the transmission line despite the reduced Q_{int} due to a strong reduction in Q_{ext} from the ferromagnetic exchange-field-mediated direct coupling between FM bar and superconducting resonator constituting an additional external loss channel for the microwave photons in the resonator. The individual resonators are fitted to Eq. (3.18) to extract the quality factors. The fitting results, depicted as continuous lines in Fig. 6.8, are listed in Tab. 6.3.

We observe in Tab. 6.3 strongly reduced $Q_{\text{int}} \simeq 2 \cdot 10^3$ of our resonators compared to those in Sec. 6.1. Besides the additional losses from the roughened MA interface due to the additional fabrication steps, we note that a degradation of the used NbTiN sputtering target in the Ultradisk has been found in Ref. [434], which strongly reduced the achievable Q_{int} values and thus the achieved results in this section. As discussed previously, the reduced Q_{ext} of resonators R3 and R5 originates from external losses induced by the exchange bias in the FM bar, whereas the strong variation between the Q_{ext} of the resonators R1, R2 and R4 is attributed to the imprecise fitting of undercoupled resonators to Eq. (3.18).

Resonator	f_r (GHz)	Q ($\times 10^3$)	Q_{int} ($\times 10^3$)	Q_{ext} ($\times 10^3$)
R1 (bare)	4.642	2.11 ± 0.01	2.49 ± 0.01	12.00 ± 0.01
R2 (AlN/CoFe)	4.762	0.62 ± 0.02	0.64 ± 0.02	31.40 ± 0.42
R3 (NbTiN/CoFe)	4.897	1.54 ± 0.01	2.32 ± 0.01	4.55 ± 0.01
R4 (AlN/CoFe)	4.997	1.32 ± 0.08	1.35 ± 0.08	72.31 ± 1.59
R5 (NbTiN/CoFe)	5.066	1.33 ± 0.06	2.14 ± 0.01	3.53 ± 0.01

Tab. 6.3. – Extracted fitting parameters for resonance frequency f_r , the quality factors Q , Q_{int} and Q_{ext} for the five on chip NbTiN resonators coupled to the magnetic CoFe bars. Measurements are performed at $T = 3.0$ K, $\mu_0 H_{\text{ext}} = 0$ mT and at a microwave power corresponding to the high power regime.

To characterize the magnon-photon coupling of our resonators, we record S_{21} for frequencies around the f_r of the individual resonators at varying in-plane external magnetic field H_{ext} applied along the long axis of the FM bars [see Fig. 3.6(a)] sweeping from positive to negative field values through the ferromagnetic resonance field of the ferromagnetic CoFe bar. The resulting microwave absorption spectra for resonators R1 to R5 are plotted as colormaps as function of f and H_{ext} in Fig. 6.9(a)-(e). The corresponding range in $|S_{21}|$ for each resonator is listed in Tab. 6.4.

	R1 (a)	R2 (b)	R3 (c)	R4 (d)	R5 (e)
$\min(S_{21}) (10^{-3})$	13.2	13.0	12.5	12.8	12.9
$\max(S_{21}) (10^{-3})$	15.6	15.3	15.0	14.9	14.9

Tab. 6.4. – Minimum and maximum transmission parameter $\min(|S_{21}|)$ and $\max(|S_{21}|)$ for the panels (a)-(e) of in Fig. 6.9.

For the uncoupled resonator R1 in Fig. 6.9(a), we observe a slight reduction in f_r and a roughly constant microwave absorption magnitude in $|S_{21}|$ indicating a weakly affected Q_{int} within the investigated magnetic-field range. These findings are agreement with the robustness of our NbTiN resonators observed in Fig. 6.4. Notably, the observed dispersion in $f_r(H_{\text{ext}})$ is not symmetric in H_{ext} [see Fig. 6.11(a)], which we attribute to a finite trapped flux Φ_{tr} in the superconducting magnetic coils. For the resonators R2 and R4 in panels (b) and (d), where the CoFe bar is deposited on top of an insulating AlN layer, we observe an anticrossing feature resonator mode at small positive fields for $\mu_0 H_{\text{ext}} \simeq +10$ mT (white dashed line), which we attribute to the resonator mode coupling to the positive branch of the magnetic Kittel mode as accounting for the trapped flux $\Phi_{\text{tr}} \approx -5$ mT, this $\mu_0 H_{\text{ext}}$ roughly corresponds to the expected resonance field at $f \simeq 5$ GHz [i.e. $\mu_0 H_{\text{ext}} \approx \mu_0 H_{\text{res}} + \Phi_{\text{tr}}$, see also Fig. 6.7(a)].

For negative fields smaller than $\mu_0 H_{\text{ext}} \simeq -28$ mT, the unperturbed resonator mode is restored, however no anticrossing from the resonator mode coupling

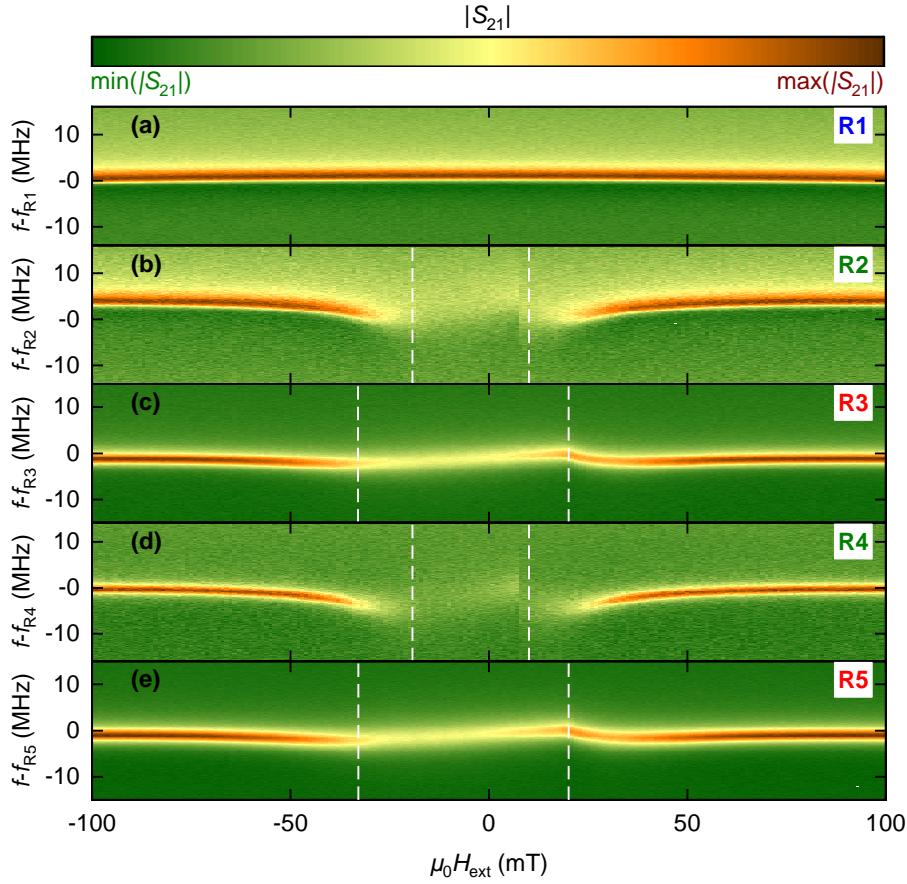


Fig. 6.9. – Microwave transmission spectra of the NbTiN superconducting resonators coupled to the CoFe strips as a function of external magnetic field $\mu_0 H_{\text{ext}}$ applied in the sample plane along the long axis of the FM bar (cf. Fig. 6.6) and frequency f around the respective f_{Ri} of the individual resonators (see Tab. 6.3) recorded at $T = 3$ K and a power corresponding to the high power range. (a) Spectrum of a bare NbTiN resonator (indicated with blue color). In (b) and (d), resonators R2 and R4 (green color) are coupled to CoFe(30 nm)/Cu(3 nm)/Ta(3 nm) deposited on top of a 30 nm thick AlN layer. Resonators R3 and R5 (red color) in (c) and (e) are coupled to a CoFe(30 nm)/Cu(3 nm)/Ta(3 nm)-bar, which is ex-situ deposited directly on the NbTiN resonator. The corresponding range in $|S_{21}|$ for each resonator is listed in Tab. 6.4. Vertical white dashed lines indicate the positive and negative resonance field positions $\mu_0 H_{\text{res}}$ of the CoFe bar. These are offset by about $\simeq -5$ mT from the zero-field position due to trapped flux Φ_{tr} in the superconducting magnet coils.

to the negative branch of the Kittel mode is observed. We attribute this to a hysteresis in the magnetic order of the FM bar induced by the field-sweep direction of our measurement routine, where H_{ext} is swept from positive to negative fields. Consequently, the magnetization of CoFe is in an ordered state at positive fields, which can coherently couple with the resonator mode but, when reversing the magnetic field polarity, its magnetic moments do not fully align along the external magnetic field at low negative fields due to the shape anisotropy of the magnetic bars, which gives rise to a much lower coupling strength for the negative branch and thereby to an asymmetry in the evolution of the resonator mode with respect to H_{ext} . Note that such an asymmetry in the resonator modes of hybrid magnon-photon systems as function of magnetic field sweep direction has also been observed in Ref. [79]. For the resonators R3 and R5, where the CoFe is deposited directly on top of the NbTiN layer, we observe in Fig. 6.9(c) and (e), continuous uninterrupted resonator modes, which do however exhibit a kink at $\mu_0 H_{\text{ext}} \simeq +20$ mT (white dashed line). We again attribute this feature to the microwave photons of the resonator coupling with the ferromagnetic Kittel mode of the CoFe bar [see $\mu_0 H_{\text{ext}}$ of this sample in Fig. 6.7(a)]. However, for these samples, the enhanced magnetic relaxation rate appears to exceed the effective coupling rate g_{eff} between magnons and phonons and hence no anticrossing between magnon and photon mode is observed.

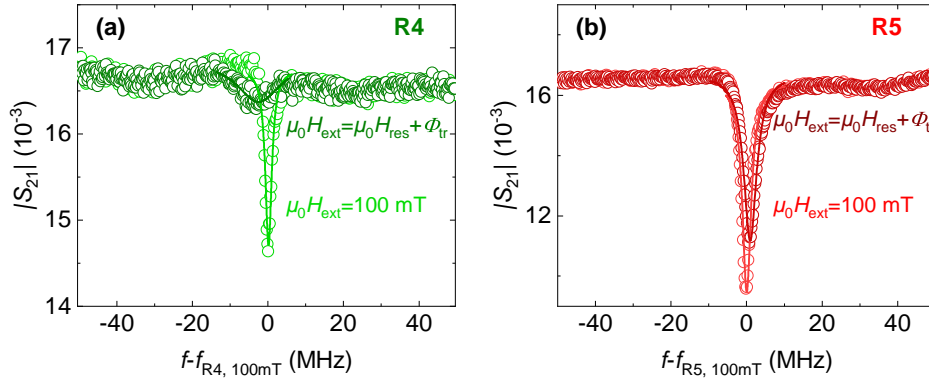


Fig. 6.10. – Vertical cuts for $|S_{21}(f)|$ from the colormaps in Fig. 6.9 for resonators R4 (a) and R5 (b) for magnetic fields, which are on/off-resonant with the magnetic Kittel mode. Light (Dark) coloring represent data for magnetic fields, which are on (off)-resonant with the magnetic Kittel mode. Continuous lines represent fits to a Lorentzian function.

In Fig. 6.10, we plot exemplary raw data cuts through $|S_{21}(f)|$ from the colormaps in Fig. 6.9 for the resonators R4 [panel (a)] and R5 [panel (b)] for magnetic fields, which are off-resonant ($\mu_0 H_{\text{ext}} = 100$ mT, light colors) and on-resonant ($\mu_0 H_{\text{ext}} = \mu_0 H_{\text{res}} + \Phi_{\text{tr}}$, dark colors) with the magnetic Kittel mode. We find, that in particular for resonator R4, the linewidth of the observed Lorentzian around f_{R4} is greatly enhanced for $\mu_0 H_{\text{ext}} = \mu_0 H_{\text{res}} + \Phi_{\text{tr}}$ and a strong shift in resonance frequency is apparent. Due to this strongly enhanced linewidth of the resonator mode in resonance with the magnetic Kittel mode, the fitting of the

raw $|S_{21}(f)|$ -spectra with Eq. (3.18) yielded unreliable fitting result. Hence, to reduce the amount of fitting parameter we decided to fit the data with a simple Lorentzian function (see continuous lines in Fig. 6.10) to extract f_r and κ as function of H_{ext} for our individual resonators. The resulting resonance frequency and net relaxation rates as function of external magnetic field are plotted in Fig. 6.11 for the resonators R1, R4 and R5, which represent the three different investigated resonator types. Here, the net quality factor Q is related to the relaxation rate of the magnon-photon hybrid devices κ via Eq. (3.14).

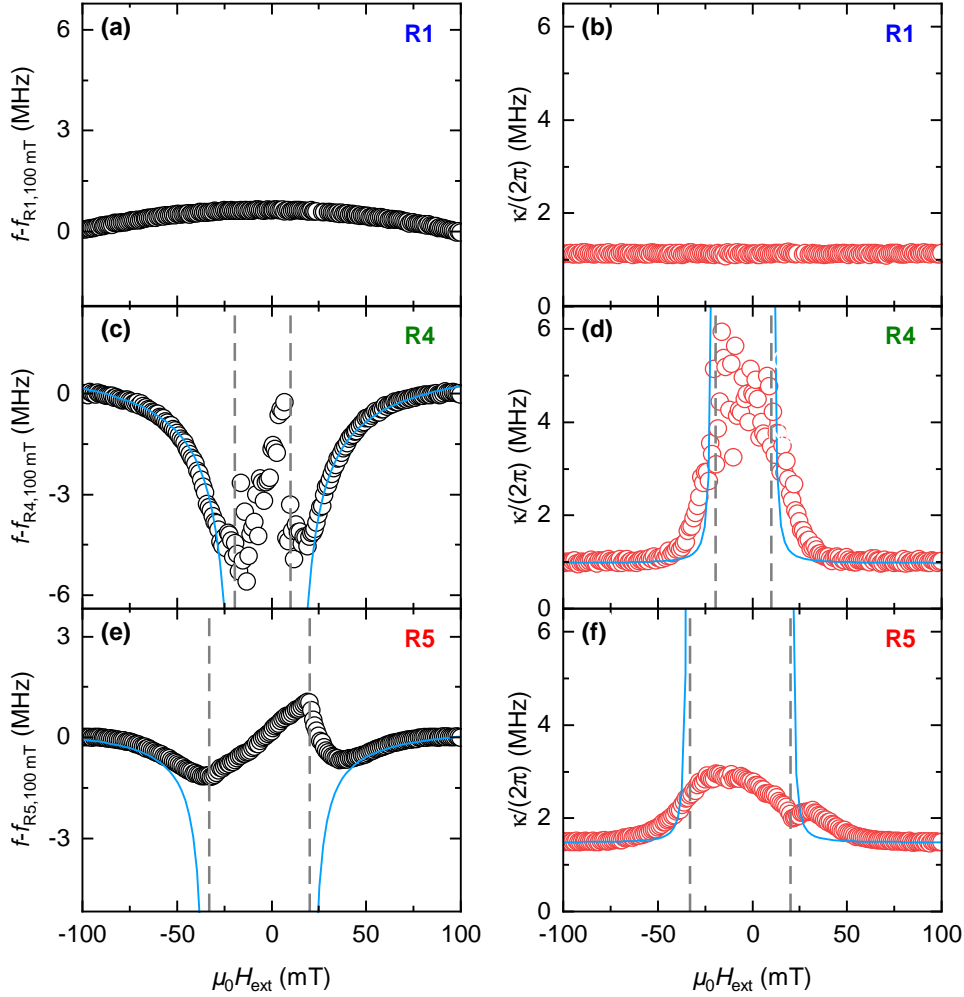


Fig. 6.11. – Resonance frequency f_r and relaxation rate κ of the three different resonator heterostructure types as function of the external magnetic field H_{ext} . Panels (a) and (b) depict f_r and κ of the bare NbTiN resonator. Panels (c) and (d) show f_r and κ for the hybrid device, where the CoFe bar has been grown on an AlN buffer layer. Around $\pm H_{\text{res}} + \Phi_{\text{tr}}$ of the Kittel mode for the CoFe bar (gray dashed lines), we observe a discontinuity in f_r and a large increase in κ generated by the mode hybridization due to magnon-photon coupling. A similar behavior is observed for the f_r and κ of the CoFe on NbTiN hybrid device in panels (e) and (f). Light blue lines in panels (c), (e) and (d), (f) represent fits to Eqs.(2.48) and (2.49), respectively.

For the uncoupled resonator in Fig. 6.11, we observe a quadratic reduction of f_r with H_{ext} in panel (a) and an approximately constant κ in panel (b). This

behavior is in agreement with our observations in Fig. 6.4. For the NbTiN/AlN/CoFe hybrid sample R₄, we observe discontinuities in f_r in panel (c), where the resonator mode intersects the positive and negative branch of the ferromagnetic Kittel mode, as indicated by the gray dashed lines in Fig. 6.11. At the same H_{ext} , we observe the strong increase of its relaxation rate κ in panel (d). The raw data for f_r and κ of R₄ are fitted to Eqs.(2.48) and (2.49), respectively, to extract the effective magnon-photon coupling rate g_{eff} . The resulting fits are shown as continuous light blue lines in Fig. 6.11(c) and (d). Using $\kappa_s^{\text{AlN/CoFe}}/(2\pi) \approx (108 \pm 2)$ MHz [see Fig. 6.7(b)], $\kappa_r^{\text{AlN/CoFe}}/(2\pi) \approx (0.99 \pm 0.01)$ MHz [see Fig. 6.11(d)] and $f_r = 4.997$ GHz (see Tab.6.3), we extract an effective coupling rate of $g_{\text{eff}}/(2\pi) = (120 \pm 4)$ MHz indicating, that the magnon-photon coupling of resonator R₄ is situated in the strong coupling regime with $g_{\text{eff}} > \kappa_r, \kappa_s$, though κ_s is just slightly lower than g_{eff} . We extract a cooperativity of $C = g_{\text{eff}}^2/(\kappa_r\kappa_s) \approx 136$. Both the values of g_{eff} and C of R₄ are in good agreement to findings on the magnon-photon coupling between superconducting resonators and nanomagnets in Refs. [79,80]. Notably, in our experiments, we benefit from the enhanced temperature-robustness of NbTiN and achieve strong magnon-photon coupling at $T = 3$ K in a liquid helium cryostat, whereas both Refs. [79,80] have performed their experiments at $T \simeq 1.5$ K. The coupling strength g_0 of photons to a single Bohr magneton is given by $g = g_0/\sqrt{N}$, where N is the number of spins in our micropatterned CoFe strip. We use a molar mass $M_{\text{CoFe}} = 0.25M_{\text{Co}} + 0.75M_{\text{Fe}} \approx 58.2$ u [435], where u is the atomic mass unit, a density of $\rho_{\text{CoFe}} = 8110$ kg/m³ [436] and a volume of the FM microstrip of $V = 400 \times 11 \times 0.03$ μm³ and thereby obtain a number of spins of $N = 1.14 \cdot 10^{13}$ resulting in a coupling rate per Bohr magneton μ_B of $g_0 \approx 223$ Hz⁵, which is in good agreement with the lumped element Nb resonators in Ref. [80] and one order of magnitude larger than the g_0 for coplanar resonators in Ref. [79] due to the reduced mode volume of lumped-element resonators. For the resonator R₅, where the FM bar is directly deposited on the NbTiN resonator, we observe in Figs. 6.11(e) and (f) peak-dip features in f_r and minor enhancements in κ around 20/−30 mT, which we attribute to the microwave photons in the resonator coupling with the two branches of the magnonic Kittel mode. Notably, in comparison to R₄, these coupling features manifest at larger H_{ext} , which we attribute to the reduced M_{eff} and correspondingly the enhanced H_{res} of CoFe ex-situ grown on NbTiN [see Fig. 6.7(a)]. Due to the enhanced $\kappa_s^{\text{NbTiN/CoFe}}/(2\pi) \approx (231 \pm 3)$ MHz of the CoFe in NbTiN/CoFe hybrid devices, we expect to operate the device in the Purcell-enhanced regime [149] with $\kappa_r < g_{\text{eff}} < \kappa_s$. In this regime, we expect the magnon-photon coupling to manifest as an effectively Purcell enhanced relaxation rate κ and a peak-dip dispersion in f_r [78,437], which is in agreement with what we observe for resonator R₅ in Figs. 6.11(e) and (f). A fit of f_r and κ

⁵Note, that in literature, g_0 is commonly referred to as the coupling rate per spin [79,80]. However, since in this work we are working with 3d transition metal itinerant ferromagnets, the term coupling rate per Bohr magneton is the physically sound term for our experiments.

to Eqs.(2.48) and (2.49) using $\kappa_s^{\text{NbTiN/CoFe}}/(2\pi) \approx (231 \pm 3)$ MHz [see Fig. 6.7(b)], $\kappa_r = 1.50$ MHz [see Fig. 6.11(f)] and $f_r = 5.066$ GHz (see Tab.6.3) yields a reduced $g_{\text{eff}} = (67 \pm 8)$ MHz. We note, that the evolution of κ in Fig. 6.11(f) is not well described by the performed fit and the broad and asymmetric evolution of $\kappa(H_{\text{ext}})$ cannot be described with Eq. (2.49). Hence, we expect the out-of-plane flux and exchange-coupling of the domain state in the CoFe bar at low magnetic fields H_{ext} to enhance the losses and increase the loss rate κ in resonator R5. In this picture, the asymmetrically enhanced κ in particular for small negative H_{ext} is caused by the measurement routine, where H_{ext} is swept from positive to negative values and the corresponding positive trapped flux Φ_{tr} in the superconducting coils shifts the peak in κ at the domain state of the CoFe bar to negative H_{ext} . Overall, the enhanced $\kappa_s^{\text{NbTiN/CoFe}}$ and reduced g_{eff} for resonator R5 renders the performance of the NbTiN/CoFe-hybrid devices to be inferior to the NbTiN/AlN/CoFe-hybrids. Hence, we infer, that a direct SC/FM contact layer cannot enhance coupling between magnetic moments and microwave photons potentially due to the formation of an interfacial dead layer at the NbTiN/CoFe-interface, which would explain the deteriorated magnetic properties for this sample.

6.3 Summary and Outlook

In summary, in this chapter, we have optimized the fabrication process of planar microwave resonators made from the dirty type II superconductor NbTiN, which exhibits a high $T_c \simeq 16$ K and robustness to external magnetic field ($\kappa_{\text{GL}} > 50$). The NbTiN thin films for our resonators are grown via reactive sputtering deposition in the Ultradisk sputtering machine on thermally oxidized Si and highly resistive Si (001) substrates using different substrate surface treatment procedures to mitigate TLS losses from the metal-substrate interface MS. The finalized resonators are then compared for their internal quality factors Q_{int} at $T = 2.2$ K. We find $Q_{\text{int}} \simeq 2 \cdot 10^5$ for resonators grown on Si-substrates, regardless of the performance of a buffered oxide etch substrate treatment prior to the NbTiN deposition and a strongly reduced $Q_{\text{int}} \simeq 1 \cdot 10^4$ for resonators grown on the thermally oxidized Si-substrates. These results demonstrate, that dielectric TLS losses from the MS-interface constitute the dominant loss channels that limits Q_{int} in our resonators. The obtained Q_{int} for NbTiN grown on Si are one order of magnitude higher than those reported in previous publications from the WMI for comparable resonator layouts based on superconducting Nb [382,415]. Regarding ESR and FMR applications, we demonstrated the usability of our resonators at elevated temperatures of up to $T \leq 13$ K and magnetic in-plane fields up to $\mu_0 H_{\text{ext}} \leq 440$ mT with a $Q_{\text{int}} > 10^5$ for $T \leq 4.8$ K and $\mu_0 H_{\text{ext}} \leq 180$ mT. For their integration in qubit devices operating at millikelvin temperatures, our NbTiN resonators exhibit $Q_{\text{int}} \approx 5 \cdot 10^5$ in the high power limit and $Q_{\text{int}} \approx 2 \cdot 10^5$ in the single photon limit. Using the optimized fabrication recipe, we couple

our superconducting resonators to the magnons of a micropatterned CoFe strip and characterize the resulting magnon-photon coupling for two types of hybrid devices, where 30 nm of the low damping ferromagnetic metal $\text{Co}_{25}\text{Fe}_{75}$ (CoFe) is deposited (i) on top of an AlN insulating layer to avoid direct exchange coupling between FM and SC, (ii) directly on the NbTiN resonator. For the former, we observe magnon-photon in the strong coupling regime with a coupling rate of $g_{\text{eff}}/(2\pi) = (120 \pm 4)$ MHz resulting in an estimated vacuum coupling rate per μ_{B} of $g_0 \approx 223$ Hz and a cooperativity of a cooperativity of $C = g_{\text{eff}}^2/(\kappa_{\text{r}}\kappa_{\text{s}}) \approx 136$. Due to an enhanced magnetic relaxation rate κ_{s} from the deteriorated growth of CoFe on NbTiN for the latter type, we find the signatures of coupling in the Purcell-enhanced regime ($\kappa_{\text{r}} < g_{\text{eff}} < \kappa_{\text{s}}$), where the magnon-photon coupling manifests primarily as an enhanced relaxation rate κ in our hybrid. The observed coupling rates g_{eff} and cooperativities C of our NbTiN/AlN/CoFe hybrid devices are in good agreement with contemporary research in Refs. [79, 80]. However, our experiments have been performed at higher base temperatures $T = 3$ K and using the temperature- and magnetic field-robust superconductor NbTiN with a high g_0 due to the small volume of the used lumped element resonator layout. Magnon-photon hybrid systems are discussed as high-speed coherent transducers for circuit quantum electrodynamics [79, 438] and for the transmission of spin excitations via photons [439, 440]. Our results help to push these hybrids to higher operating temperatures and smaller volumes. Working with metallic ferromagnets, future efforts should attempt to reduce the observed sizable κ_{s} for CoFe in hybrid devices for example by inserting a buffer layer between the AlN and CoFe or by omitting the buffered oxide etch before NbTiN deposition to obtain resonators with reduced surface roughness (see Fig. 6.1) as the base layer for the growth of CoFe.

Magnon-Phonon coupling in bulk acoustic wave resonator/ magnetic thin films hybrids

Having investigated the coupling of magnons in magnetic thin films to microwave photons in superconducting resonators in the previous chapter, we here investigate the coupling of magnons to a different kind of quasiparticle excitations, namely to transverse acoustic phonons in bulk acoustic wave (BAW) resonators. The coupling can be realized by the finite magnetoelastic coupling in magnetic materials. Here, our introduction to this field is oriented towards the one in our recent article entitled *Chiral phonons and phononic birefringence in ferromagnetic metal - bulk acoustic resonator hybrids* [71]. Phonons, the quantized excitations of elastic waves in solids, are of relevance for a vast variety of solid-state phenomena. Recently, they have in particular drawn attention in the field of quantum sciences due to the prospect to use phonons in hybrid quantum memory [441–444], quantum transducer [445–450], and quantum sensor devices [451–455]. Currently, the main research focus is oriented towards use of standing elastic waves generated in mechanical resonators with high quality factors [375, 456]. These standing elastic waves can be viewed as analog to standing electromagnetic waves in resonators. They are most commonly realized in the form of high harmonic overtone bulk acoustic wave (BAW) [457, 458] or surface acoustic wave (SAW) resonators [441, 442, 459, 460]. These acoustic wave resonators support both linearly polarized longitudinal and transversal (shear) elastic standing waves carrying no angular momentum. However, suitable superpositions of shear waves can also mediate angular momentum [461–463]. This allows for the transfer of spin information by phonons as well as the conversion between circularly polarized and linearly polarized shear waves. In analogy to the utilization of electron spins in electrical spin valve devices, spin currents carried by phonons allow for the realization of phononic spin valves [77, 158]. Experiments aiming to investigate the concept of phononic spin currents require schemes for the excitation and detection of phonons with circular polarization. To this end, the intrinsic chirality of the magnetic Kittel mode (see e.g. Fig. 2.2) in combination with the magnetoelastic interaction represents an experimentally simple approach for the generation and detection of phonons [464–467]. Here, in particular magnetic thin films with a sizable magnetostriction constant λ , while retaining a low Gilbert

damping α^6 coupled to a BAW resonator with low elastic relaxation rate η_a , allowing to carry long-lived excitations at high overtone frequencies, constitute an ideal experimental platform to study the excitation of phonons with angular momentum [64,77,112,157–159,468,469]. While early experiments [77,158,159] have used the ultra-low magnetization damping material yttrium iron garnet (YIG) grown lattice matched on gadolinium gallium garnet ($\text{Gd}_3\text{Ga}_5\text{O}_{12}$, GGG) substrates, the following experimental aspects have not yet been investigated: (i) What requirements must the phonon dispersion relations of a given crystalline symmetry of the host BAW material fulfill to allow for the transport of angular momentum or the interconversion between chiral to linear polarized phonons? (ii) Can the individual phonon modes participating in the phonon spin transport be experimentally resolved? (iii) Is the excitation concept using the ferromagnetic Kittel mode unique for epitaxial YIG films on GGG substrates, which are excellently matched in terms of their acoustic impedance Z , or can it be generalized to other material systems irrespective of the presence of epitaxial FM/BAW substrate interface, for example polycrystalline metallic thin films coupled to arbitrary crystalline substrates including materials such as silicon (Si) and sapphire (Al_2O_3), which are commonly used in the semiconductor industry, irrespective of the acoustic impedance matching at the FM/BAW substrate interface?

These are the central questions, we aim to answer in this chapter, where we investigate the magnetoelastic coupling between polycrystalline ferromagnetic metallic (FM) $\text{Co}_{25}\text{Fe}_{75}$ (CoFe) thin films and several crystalline BAW substrate materials. In Section 7.1, we experimentally demonstrate that, besides YIG on GGG, magnon-phonon hybrid devices incorporating polycrystalline metallic magnetic thin films are well suited for the excitation of high overtone BAWs in crystalline Al_2O_3 , GGG and Si substrates. This finding provides clear evidence that the excitation scheme of using the chirality of the Kittel mode to inject phonons in magnetostrictive materials is generic. In detail, in our experiments, we study the coupling between the resonant interaction of the ferromagnetic excitations with the standing elastic waves of the BAW resonators by performing cryogenic bbFMR (see Sec. 3.3.1). Using this method, we find that at least two propagation velocities or phonon modes must be considered in our substrates, which suggests that the phonon propagation direction with respect to crystallographic axes of the host substrate is of key importance for the efficient transport and conversion of angular momentum via phonons in the host substrate. In analogy to optics, we call this process phononic birefringence [470], which establishes novel concepts for the transformation and control of chiral phonon modes.

Our initial bbFMR-experiments on ferromagnetic metal/BAW resonator hybrids using various substrate materials and observing the manifestation of

⁶Note, that a large λ enables an efficient transfer of excitations from the spin to the phononic system resulting in an increased Gilbert damping [110,112,468]. Hence, a compromise between these contradicting requirements for the FM material needs to be found.

phononic birefringence, which are presented in Sec. 7.1, are available on the arxiv:

M. Müller, J. Weber, F. Engelhardt, V.A.S.V. Bittencourt, T. Luschmann, M. Cherkasski, S.T.B. Goennenwein, S. Viola Kusminskiy, S. Geprägs, R. Gross, M. Althammer, H. Huebl *Chiral phonons and phononic birefringence in ferromagnetic metal - bulk acoustic resonator hybrids*, arxiv: 2303.08429, (2023) [71].

Having experimentally demonstrate the suitability of polycrystalline metallic thin films for magnon-phonon hybrid devices, in the following Sec. 7.2, we provide a detailed study on the frequency and temperature dependence of the effective magnetoelastic coupling rate g_{eff} as well as the relaxation rates of the magnetic and elastic systems κ_s and η_a for the magnetic thin film/ Al_2O_3 host crystal hybrid sample.

Here, the performance of our magnon-phonon hybrids at cryogenic temperatures is of particular interest, as the reduced acoustic loss rates [471, 472] in combination with the increased magnetoelastic coupling constant B [473] allow to push these devices into stronger coupling regimes such as the Purcell-enhanced- or potentially even the strong coupling regime [149]. Furthermore, a strong frequency dependence of the effective magnetoelastic coupling rate has been demonstrated in Refs. [159, 160]. Consequently, a study of both these experimental parameters allow for the identification of an optimal working point for these hybrid devices. Finally, we also assess the potential of the phononic signatures in the FMR for the realization of highly sensitive strain and stress sensing applications.

The presented results for the temperature and frequency dependence of the magnetic thin film/ Al_2O_3 host crystal hybrid sample, presented in Sec. 7.2, constitute the basis of a manuscript, which is under preparation at the writing of this thesis. M. Müller, J. Weber, F. Engelhardt, M. Cherkasski, S. Sharma, S.T.B. Goennenwein, S. Viola Kusminskiy, R. Gross, M. Althammer, H. Huebl *temperature dependence of magnon-phonon-polarons in a ferromagnetic metal with low Gilbert damping*, (202X).

7.1 Chiral phonons and phononic birefringence in ferromagnetic metal - bulk acoustic resonator hybrids

In this section, we experimentally investigate the magnetoelastic coupling between the ferromagnetic resonance (FMR) modes in a metallic $\text{Co}_{25}\text{Fe}_{75}$ thin film and standing transverse elastic phonon modes in crystalline Al_2O_3 , Si and GGG substrates serving as the BAW resonators by performing cryogenic bbFMR spectroscopy (see Sec. 3.3.1). For all of these substrate materials, we observe an interaction between the resonant acoustic and magnetic modes. The acoustic

modes correspond to specific propagation directions with respect to the crystallographic axes. We identify these phonon modes as two orthogonal transverse shear waves propagating with slightly different velocities with relative differences in the range $\Delta v/v \simeq 10^{-5}$. In other words, in analogy to optics, we observe a phononic birefringence for all substrate materials.

7.1.1 Qualitative discussion

We consider ferromagnetic metallic CoFe thin films deposited on crystalline substrates with a hexagonal or cubic symmetry [see Fig. 7.1 (a)]. We then apply a magnetic field H_{ext} oriented along the film normal [z-direction in Fig. 3.4(a)] and using a microwave drive, we resonantly excite the oop Kittel mode of the CoFe layer. Due to the sizable magnetoelastic coupling (MEC) [55, 56, 77, 158, 159] in CoFe, the magnetization dynamics generates a high frequency stress field and thereby drives elastic modes exhibiting the same frequency and helicity as the magnonic mode. As the magnetic thin film is elastically coupled to the substrate serving as the BAW resonator, they can be considered as a singular elastic object in which elastic waves are excited by the magnetization dynamics in the FM layer. This process is called phonon pumping [112]. For the used sample oop-geometry chosen for our experiment [see Fig. 7.1(a)], the excited phonons are exclusively transverse acoustic phonons. This is due to the fact that the projection of the magnetization vector M onto the field direction is constant in the linear regime and as a result no longitudinal acoustic phonons are excited along the out-of-plane direction z [112, 157]. Due to our experimental setting with a thin magnetic film acting as transducer on top of a substrate, the properties of the standing waves are dominated by the phonon dispersion relation of the substrate material, which in turn are governed by the crystal structure of the substrate [86, 474, 475].

Owing to this acoustic wave excitation scheme, the generated phonons exhibit frequencies in the GHz range corresponding to wave numbers close to the center of the Brillouin zone of the substrate, where the dispersion relation is to a good approximation linear. Hence, phonon group and phase velocities can be assumed to be identical and in the following, we will refer to the phonon group velocity, when discussing the phonon velocities of the individual modes. However, depending on the symmetry of the crystal, these velocities are usually anisotropic, i.e., they depend on the propagation direction (z-direction in our setting) relative to the crystallographic axis [see Fig. 7.1(b)], as described by the Christoffel equation [476, 477] and the polarization. Figures 7.1(b) and (c) show the calculated longitudinal and transverse phonon propagation velocities of hexagonal Al_2O_3 [478], which is calculated by solving the Christoffel equation [477]. We find that the observed anisotropy of the velocities in the hexagonal lattice vector planes reflects the symmetry of the underlying crystal structure. Notably, in Fig. 7.1(b), the velocities of the two shear waves with a propagation direction z along the

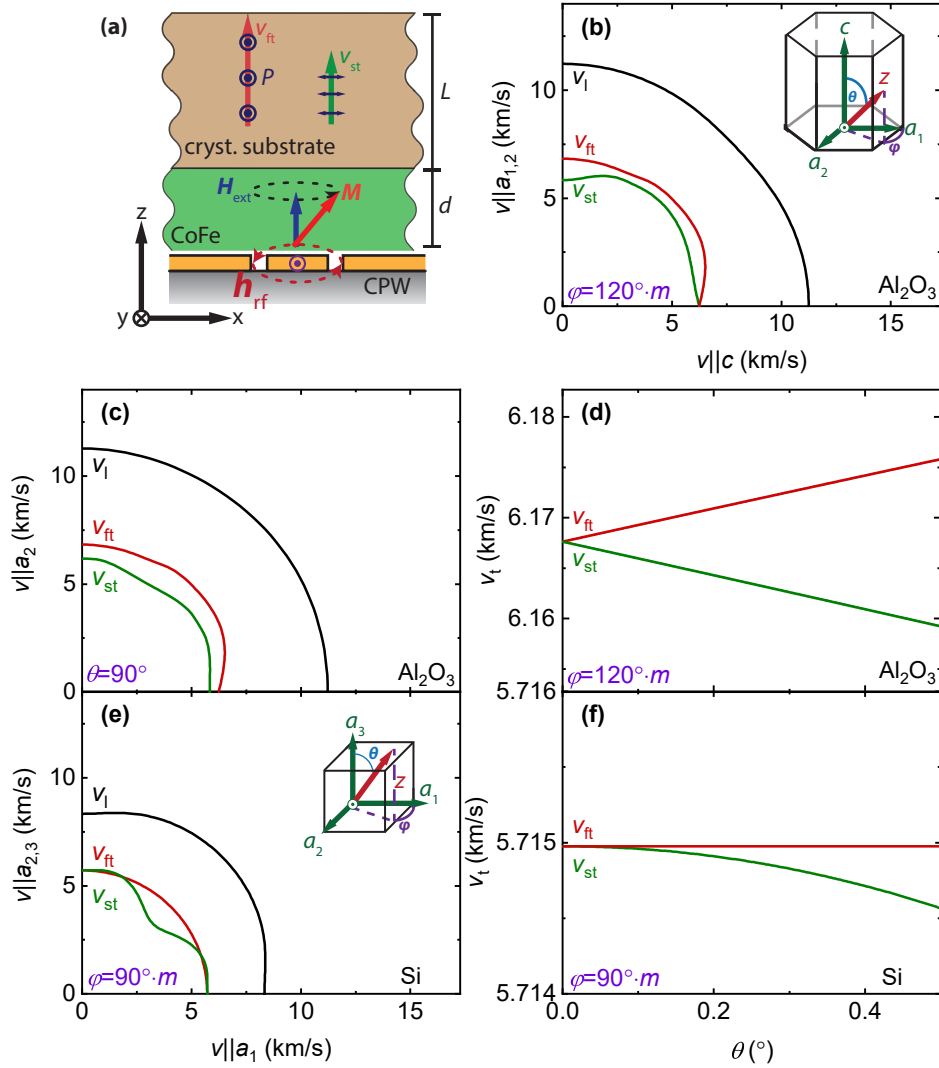


Fig. 7.1. – (a) Schematic of the magnon-phonon hybrid sample composed of a metallic CoFe thin film grown on a crystalline substrate mounted on a coplanar waveguide. The transverse acoustic waves can split into fast and slow modes with velocities v_{ft} and v_{st} , respectively (red and green arrows), and different polarization direction \mathbf{P} (blue arrows). (b) Group velocities of the longitudinal and transverse acoustic phonons of hexagonal Al_2O_3 in the $\mathbf{a}_{1,2}$ - c -plane ($\varphi = 120^\circ \cdot m$, $m \in [0, 2]$). The length of the vector from the origin to the colored lines gives the magnitude of the velocities and its direction the propagation direction in the \mathbf{a}_1 - c -plane. The vector \mathbf{z} defines the phonon propagation direction with θ and φ representing the azimuthal and polar angles of \mathbf{z} with respect to the hexagonal lattice vectors \mathbf{c} and \mathbf{a}_1 . (c) Phonon group velocities of Al_2O_3 in the \mathbf{a}_1 - \mathbf{a}_2 -plane for $\theta = 90^\circ$. (d) Calculated splitting of the fast and slow transverse mode velocities v_{ft} and v_{st} in Al_2O_3 as a function of azimuthal angle θ ($\varphi = 120^\circ \cdot m$, $m \in [0, 2]$). (e) Group velocities of the longitudinal and transverse acoustic phonons of cubic Si in the \mathbf{a}_1 - $\mathbf{a}_{2,3}$ -plane. The vector \mathbf{z} defines the phonon propagation direction with respect to the cubic lattice vectors \mathbf{a}_i ($\varphi = 90^\circ \cdot m$, $m \in [0, 3]$). (f) Calculated splitting of v_{st} and v_{ft} as a function of θ ($\varphi = 90^\circ \cdot m$, $m \in [0, 3]$).

hexagonal c -direction are identical. However, if z is not parallel to the c -axis, this degeneracy is lifted for arbitrarily small azimuthal angles θ between z and c as plotted in Fig. 7.1(d). Here, we neglect the φ -dependence of v_{ft} and v_{st} for small θ -angles. However, note that this lifting in the degeneracy of phonon velocities is not unique to hexagonal crystals. As an example for the transverse velocity splitting in cubic crystals, we plot in Figures 7.1(e) and (f) the phonon velocity anisotropy for Si (diamond structure) [479] and the small angle θ dependence, respectively. Analytical expressions for the velocity splitting Δv_t as function of θ of hexagonal and cubic crystals are derived in the Appendix G2.

As is depicted in Fig. 7.1(a), the propagating phonons meet reflective boundary conditions imposed by the finite thickness $L + d \simeq L$ of the sample composed of substrate (L) and magnetic thin film (d). This leads to the formation of standing waves with frequencies in the MHz range and hence the whole sample consisting of substrate and film can serve as a BAW resonator, which at GHz frequencies is driven in the high-overtone regime. Here, the resonance frequency of an elastic standing wave mode with mode number n can be well approximated by Eq. (2.50). As we have established in Sec. 2.3.5, for FMR frequencies, which are in resonance with one of the standing wave modes of the BAW resonator, it can excite the elastic mode via MEC, which leads to a change of the FMR linewidth due to phonon pumping [112, 157] at f_n . Thus, we expect the FMR absorption line to show a frequency-periodic modification, where the periodicity is given by the free spectral range $f_{\text{FSR}} = f_{n+1} - f_n = f_1$ [77, 158, 159]. Notably, in this way, the FMR absorption line is sensitive to all elastic modes, which can be excited with the stress field created via MEC in the FM film. This fact is of relevance as commercial substrate materials generally have a small but finite miscut angle θ_m between its surface normal z and respective crystallographic axis.

Therefore, in principle, we expect to observe two non-degenerate propagation velocities v_{ft} and v_{st} along z , which manifest themselves as a superposition of frequency periodic intersections of the FMR with periods given by the respective free spectral ranges $f_{1,\text{ft}}$ and $f_{1,\text{st}}$, respectively, given that the linewidths of both phononic modes are sufficiently narrow to resolve them. Notably, previous works [77, 158, 159] did not account for this phenomenon and due to the increased phononic linewidths at room temperature did not observe two individual phonon modes. The experimental observation of two phonon modes via bbFMR experiments allows to determine the resonance spectra of the BAW resonator and, hence, according to Eq. (2.50) the group velocities of both of the excited acoustic phonon modes. Thus, this technique represents a technologically simple, but sensitive tool for the characterization of these substrate BAW-resonators.

7.1.2 Experimental detection of phononic birefringence

Using the Superbowls sputtering system (see Sec. 3.1.2), we sputter deposit a Pt(3 nm)/Cu(3 nm)/CoFe(30 nm)/Cu(3 nm)/Ta(3 nm) multilayer stack on a 510 μm thick (0001)-oriented Al_2O_3 substrate, a 675 μm thick (001)-oriented high-resistivity Si substrate, and a 380 μm (111)-oriented GGG substrate, which are each polished on both sides. The seed layer of the CoFe film, composed of a Pt(3 nm)/Cu(3 nm)-bilayer is required to generate optimal magnetization damping properties of CoFe [135, 389, 390], whereas the top Cu(3 nm)/Ta(3 nm) capping bilayer protects the CoFe thin film from oxidation. To analyze the MEC, we perform cryogenic bbFMR experiments in the Moria cryostat (see Sec. 3.3.1), as we require magnetic fields of up to $\simeq 4.5\text{ T}$ in the oop-direction. The samples are mounted face-down onto a coplanar waveguide and we record the frequency-dependent complex microwave transmission parameter S_{21} as a function of the out-of-plane magnetic field H_{ext} at a temperature of $T = 5\text{ K}$ using a VNA.

Fig. 7.2(a) shows the magnitude of the complex transmission parameter $|S_{21}|$ as a function of external magnetic field H_{ext} around $\mu_0 H_{\text{res}}(f_0) \approx 3.005\text{ T}$ and microwave frequency f around $f_0 = 18\text{ GHz}$ recorded at $T = 5\text{ K}$ for the CoFe multilayer stack deposited on an Al_2O_3 substrate. We observe the characteristic FMR of the CoFe layer (brown color), which shows distinct, frequency periodic horizontal features. We attribute these features to the magnon mode interacting with the high overtone BAW mediated by MEC and elastic coupling at the interface to the substrate (see Refs. [77, 159]). Regarding the frequency periodicity of the features, we clearly observe a double peak structure at a free spectral range of $f_{\text{FSR}} \approx 6.04\text{ MHz}$, which is in good agreement with the expected $f_{\text{FSR}} \approx 6.05\text{ MHz}$ from Eq. (2.50) in Al_2O_3 using the material parameters of CoFe and Al_2O_3 ($d = 30\text{ nm}$, $L = 510\text{ }\mu\text{m}$, $v_{\text{ft,st}} \approx 6.17\text{ km/s}$ and $\tilde{v}_t = 3.17\text{ km/s}$ [436]). As we are in the linear regime of the phonon dispersion close to the center of the Brillouin zone, the BAW resonance condition reads as $f_n = v_t/\lambda_n$, where λ_n is the wavelength of the acoustic mode, which is fixed by the geometrical size of the BAW resonator. The observation of two frequency-periodic modes suggests the coupling of the magnonic Kittel mode with two non-degenerate transverse acoustic phonon with a difference in velocity of $\Delta v_t \propto \Delta f \simeq 0.5\text{ m/s}$. That is, the velocities v_{ft} and v_{st} of the two transverse acoustic phonon modes are not degenerate but show a finite splitting. In our experiments, we are able to resolve this small difference in the propagation velocities due to the narrow linewidth of the acoustic modes at low temperatures. Hence, this mode splitting can also be observed in YIG on GGG BAW resonators at cryogenic temperatures as confirmed by Johannes Weber in his Master's thesis [433]. In accordance to Ref. [159], we extract the uncoupled linewidth of the two elastic modes from a linecut through $S_{21}(f - f_0)$ at a constant external field $\mu_0 H_{\text{ext}} = 3.011\text{ T}$, which is detuned from the FMR in the plotted frequency range [orange vertical line in Fig. 7.2(a)]. Likewise, the uncoupled

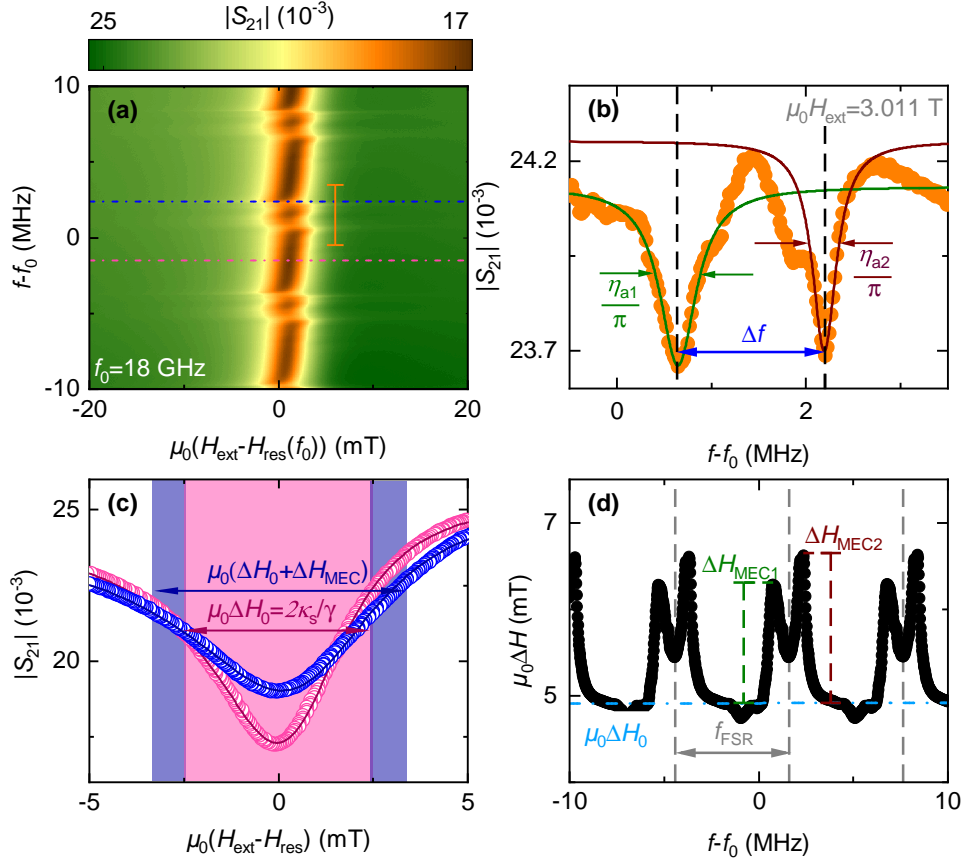


Fig. 7.2. – (a) Microwave transmission parameter $|S_{21}|$ as a function of frequency $f - f_0$ around $f_0 = 18$ GHz and external magnetic field H_{ext} around $\mu_0 H_{\text{res}}(f_0) = 3.005$ T recorded at $T = 5$ K. Panel (b) shows a vertical cut through $|S_{21}(f)|$ along the orange vertical line in (a) at the off-resonant external magnetic field $\mu_0 H_{\text{ext}} = 3.011$ T to analyze the unperturbed linewidth of the elastic modes. From this cut, we obtain the BAW resonator decay rates $\eta_{a1,2}$ by fitting two Lorentzian lines to the data (green and brown lines). The blue arrow indicates the spacing of the two MEC features in the FMR-linewidth Δf . Panel (c) shows horizontal cuts $|S_{21}(H_{\text{ext}})|$ for the blue (magenta) horizontal dashed lines in (a), which correspond to the resonant (off-resonant) case of the n^{th} bulk elastic resonance interacting with the Kittel mode. In resonance, we observe a linewidth broadening ΔH_{MEC} due to the MEC. In panel (d), the FMR-linewidth $\Delta H(f)$ is plotted as a function of f . The gray dashed lines mark the free spectral range f_{FSR} , the green and brown dashed lines indicate the magnitude of the ΔH_{MEC} and the light blue dashed line represents the linear dispersion of ΔH with an offset H_{inh} (see Appendix G1).

FMR linewidth is extracted from a fixed frequency linescan detuned from the acoustic modes [dashed horizontal magenta line in Fig. 7.2(a)]. The respective data are presented in Fig. 7.2(b) and (c). We find the elastic relaxation rates $\eta_{a1,2}/(2\pi) \approx (0.23 \pm 0.02) \text{ MHz}$, $(0.16 \pm 0.01) \text{ MHz}$ and the magnetic relaxation rate $\kappa_s/(2\pi) \approx (69.0 \pm 0.1) \text{ MHz}$ from the half-width at half maximum linewidth of the elastic resonances and FMR, respectively. Notably, from the BAW decay rates, we calculate an BAW decay length of $\delta_{1,2} = 2\pi v_t/\eta_{a1,2} \approx 0.4 \text{ cm}$, $0.6 \text{ cm} > 2L$ at $f_0 = 18 \text{ GHz}$ which allows for the formation of standing waves in the Al_2O_3 substrate. In Fig. 7.2(d), we plot the FMR-linewidth ΔH as function of f around f_0 . We observe an enhanced ΔH , when the magnetic Kittel mode is in resonance with the elastic modes. Therefore, the study of the frequency-dependence of ΔH provides a very sensitive probe to detect phonon modes in our experiments [$\Delta v_t/v_t = \eta_a/(2\pi f_0) \simeq 10^{-5}$ comparable to Brillouin light spectroscopy [480]]. In addition, the analysis of $\Delta H(f)$ allows us to investigate the intrinsic magnetization damping mechanisms in CoFe as will be discussed in Sec. 7.2. The light blue dashed line represents the uncoupled FMR-linewidth ΔH_0 with Gilbert damping $\alpha = (2.8 \pm 0.1) \cdot 10^{-3}$ and inhomogeneous broadening $H_{\text{inh}} = (1.6 \pm 0.3) \text{ mT}$. Both α and H_{inh} are extracted from broadband FMR experiments on our hybrid sample (see Appendix G1).

To quantify the effective coupling rate g_{eff} , we use Eq. (2.56) in combination with the fitted elastic relaxation rates $\eta_{a,i}$ of the two modes from Fig. 7.2(b) and their observed resonant enhancement of the FMR-linewidth $\mu_0 \Delta H_{\text{MEC}1,2}$ from Fig. 7.2(d). We obtain $g_{\text{eff}1,2}/(2\pi) = (4.02 \pm 0.62) \text{ MHz}$, $(4.55 \pm 0.47) \text{ MHz}$ at $f_0 = 18 \text{ GHz}$ and the corresponding cooperativities $C_{1,2} = g_{\text{eff}}^2/(2\kappa_s \eta_{a1,2}) = (0.63 \pm 0.09)$, (0.76 ± 0.10) . To test the validity of our coupled harmonic oscillator model from Sec. 2.3.5 for our magnon-phonon hybrid sample, we compare a zoom-in of the experimentally recorded absorption spectrum from Fig. 7.2(a) in Fig. 7.3(a) together with the calculated power absorption $P_{\text{abs}} \propto |m^x + m^y|^2$ using Eq. (2.52) and the fitted elastic and magnetic loss rates $\eta_{a1}/(2\pi) = 0.23 \text{ MHz}$, $\eta_{a2}/(2\pi) = 0.16 \text{ MHz}$, $\kappa_s/(2\pi) = 69.0 \text{ MHz}$ from Fig. 7.2, the effective coupling rates of $g_{\text{eff}1,2}/(2\pi) = 4.55 \text{ MHz}$, 4.02 MHz , the resonance frequencies $f_{n1} = 18.0008 \text{ GHz}$ and $f_{n2} = 18.0023 \text{ GHz}$ as well as $\zeta = 1 \text{ MHz}$ and $h^+ = 1$, which is plotted in Fig. 7.3(b). We observe in Fig. 7.3 a good agreement between theory model and the experimental data, demonstrating that the used model together with the estimated effective coupling rate can well describe the experimentally recorded spectrum. For the experimental spectrum, we observe a small dispersion in the acoustic modes as function of $\mu_0 H_{\text{ext}}$, which we attribute to a weak indirect coupling of the two elastic modes via the ferromagnetic Kittel mode. Likewise, a

⁷Note that in this model we need to divide the circular excitation of m^+ into m^x and m^y , which exclusively couple to the two degenerate transverse phonons modes. This modification to the model from Sec. 2.3.5 is valid, as we are free to define the x - y -coordinate system of the FMR with respect to the polarization of the acoustic modes.

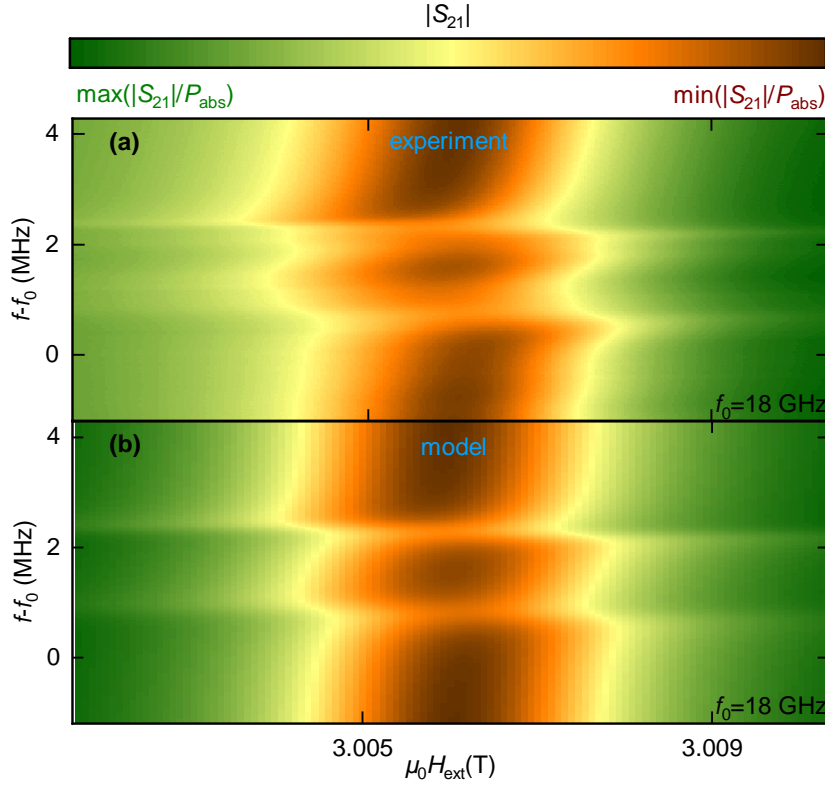


Fig. 7.3. – (a) $|S_{21}|$ recorded at $T = 5$ K and plotted as a function of f and H_{ext} in the range of H_{res} for $f_0 = 18$ GHz. (b) Simulation of P_{abs} obtained by solving Eq. (2.51) by $m^x + m^y$ and plotted as a function of f and H_{ext} in the range of H_{res} for $f_0 = 18$ GHz using the parameters listed above. A good agreement between experiment and theory is observed. The plotted power absorption range is (a) from $\min(|S_{21}|) = 0.016$ to $\max(|S_{21}|) = 0.025$ and (b) from $\min(P_{\text{abs}}) = 0.24 \cdot 10^6$ to $\max(P_{\text{abs}}) = 2.52 \cdot 10^6$.

magnetic-field dependence of cavity modes via the ferromagnetic Kittel mode of a YIG single crystal has been observed in Ref. [481].

As we find $\eta_{a,i} < g_{\text{eff},i} < \kappa_s$, we operate our hybrid devices in a regime analogous to the Purcell enhanced regime [149], where we can understand the observed enhanced ΔH of the FMR mode in resonance with the elastic modes as an effectively Purcell enhanced damping [78, 437].

In the following, we investigate the frequency dependence of the splitting of the acoustic modes originating from the two different group velocities of the transverse modes on a broader frequency scale. To this end, we plot in Fig. 7.4(a) and (b) the microwave transmission magnitude $|S_{21}|$ for CoFe thin films grown on two both-sides polished, nominally c-axis oriented Al_2O_3 substrates with varying miscut specifications from two different suppliers [(a) *Crystec* $\theta_m < 0.1^\circ$ and (b) *UniversityWafer* $\theta_m < 0.2^\circ$] as function of frequency $f - f_0$ and $H_{\text{ext}}(f_0)$ at $T = 5$ K for varying f_0 ranging from 12 GHz to 30 GHz in steps of 6 GHz.

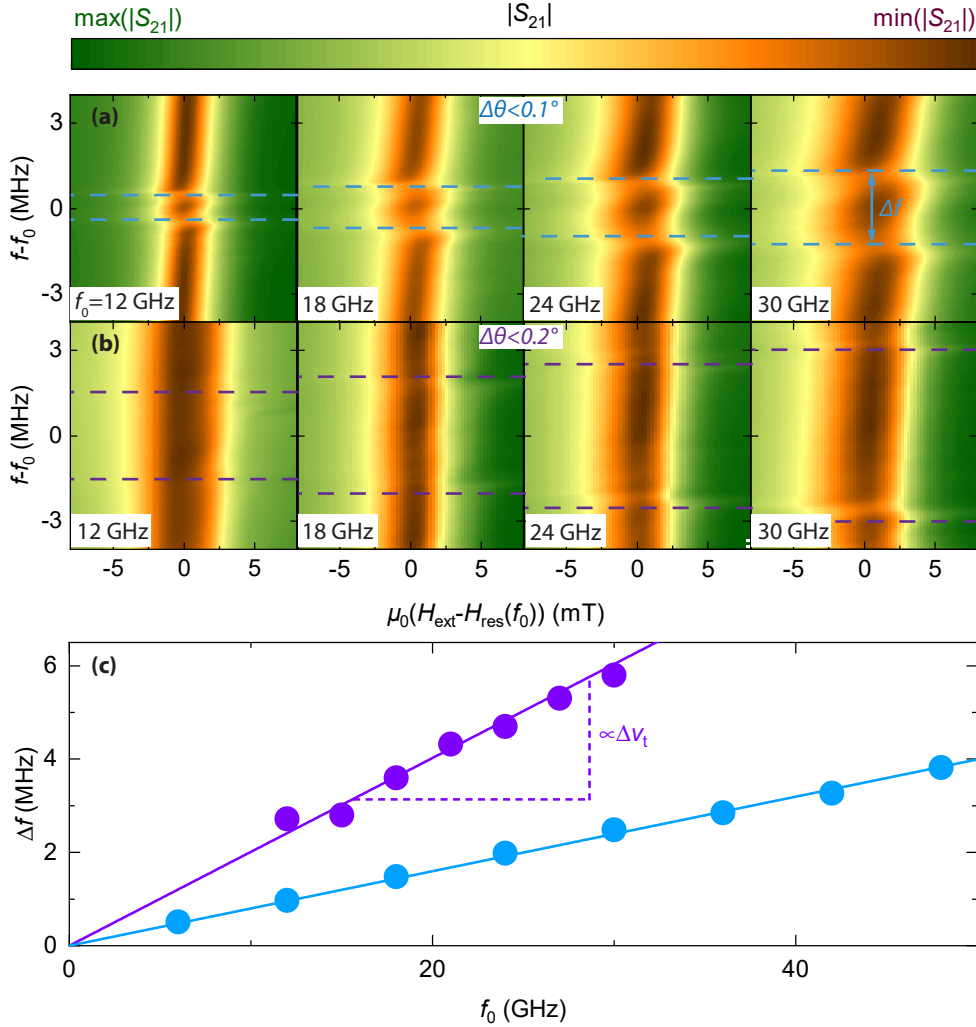


Fig. 7.4. – (a) Microwave transmission magnitude $|S_{21}|$ as a function of frequency $f - f_0$ and $H_{\text{ext}}(f_0)$ in narrow intervals around f_0 and $H_{\text{res}}(f_0)$ recorded at $T = 5$ K for a CoFe thin film deposited on a c -axis Al_2O_3 substrate with a miscut $\theta_m < 0.1^\circ$. Panel (b) shows a second sample of CoFe on a c -axis Al_2O_3 substrate with a specified miscut of $\theta_m < 0.2^\circ$. The values of $H_{\text{res}}(f_0)$ as well as $\min(|S_{21}|)$ and $\max(|S_{21}|)$ at the respective f_0 for both samples are given in Tab. 7.1. Note that the frequency spacing of the panels in (a) and (b) is 6 GHz. Panel (c) displays the observed frequency splitting Δf for both samples as a function of f_0 (blue and purple circles) together with linear fits to extract the velocity difference of the two transverse modes Δv_t .

CoFe/Al ₂ O ₃ -sample from Fig. 7.4(a)				
f_0 (GHz)	12	18	24	30
$\mu_0 H_{\text{res}}$ (T)	2.80	3.01	3.21	3.42
$\min(S_{21})$ (10^{-3})	55	16	5.1	2.2
$\max(S_{21})$ (10^{-3})	75	26	8.6	4.0

CoFe/Al ₂ O ₃ -sample from Fig. 7.4(b)				
f_0 (GHz)	12	18	24	30
$\mu_0 H_{\text{res}}$ (T)	2.78	3.00	3.21	3.41
$\min(S_{21})$ (10^{-3})	140	72	36	18
$\max(S_{21})$ (10^{-3})	156	86	46	24

Tab. 7.1. – Plot parameters of the colormaps in Fig. 7.4(a) and (b). Frequency f , resonance field $\mu_0 H_{\text{res}}$ as well as minimum and maximum S_{21} -parameter $\min(|S_{21}|)$ and $\max(|S_{21}|)$.

We find that the frequency separation Δf of the BAW resonances from the two phonon velocities scales linearly with f_0 for both CoFe/Al₂O₃ hybrid devices. This is expected as

$$\Delta f = f_n^{\text{ft}} - f_n^{\text{st}} = \frac{\Delta v_t}{\lambda_n} \quad (7.1)$$

and λ_n decreases linearly with rising f_0 . The observed frequency-splitting Δf of the two CoFe/Al₂O₃ hybrid samples as function of f_0 is plotted in Fig. 7.4(c). From linear fits to $\Delta f(f_0)$ [continuous lines in Fig. 7.4(c)], we are able to extract the velocity splitting Δv_t of the two transverse modes. Note that we expect the Δv_t of the two modes to also manifest itself as two different f_{FSR} values for the two modes, but the difference in f_{FSR} of the two modes is too small to be experimentally visible in our experiments. Hence, we require high-overtone BAW resonances with modes numbers $n \simeq 1000$ to resolve the small velocity difference of the two transverse modes of $\Delta v_t \approx 0.44$ m/s observed here. From Fig. 7.1(b), we find that for sapphire v_{ft} is equal to v_{st} for elastic modes propagation along the c -axis. Hence the observed frequency-splitting of the transverse modes requires a small miscut angle θ_m between the propagation direction z and the c -axis of the sapphire crystal. Using the calculated velocity splitting of the transverse modes, we can respectively relate the observed velocity splitting $\Delta v_t \approx 0.44$ m/s to an estimated miscut angle of $\theta \approx 0.017^\circ$ for the first CoFe/Al₂O₃ sample in panel (a) and $\Delta v_t \approx 1.1$ m/s to an estimated miscut angle of $\theta \approx 0.037^\circ$ for the second hybrid sample in panel (b). Here, we neglect the φ -dependence, which is valid for small θ . The calculated θ -values of both samples are compatible with the suppliers miscut specifications of the sapphire substrate of $\theta_m < 0.1^\circ$ (a) and $\theta_m < 0.2^\circ$ (b).

To verify these misalignment angle values for the specific samples, we performed high-resolution x-ray diffraction experiments on the CoFe/Al₂O₃ sample with a miscut specification of $\theta_m < 0.1^\circ$. Specifically, we first utilize the total

reflection at grazing incidence and a sample tilt stage to align the sample surface before studying the change of the angle of incidence θ_{XRD} of the (0006)-reflection of the Al_2O_3 substrate originating from the finite miscut denoted as θ_m as function of the polar angle φ_{XRD} ⁸ [see Fig. 7.5(a) for the measurement geometry. Note, that in contrast to previous chapters, we here have used a high-resolution XRD setup, that operates in the θ - θ geometry with stationary goniometer and sample instead of the θ - 2θ geometry with stationary X-ray tube.]. The resulting tuning of the (0006)-reflection of the substrate as function of φ_{XRD} is plotted in Fig. 7.5(b).

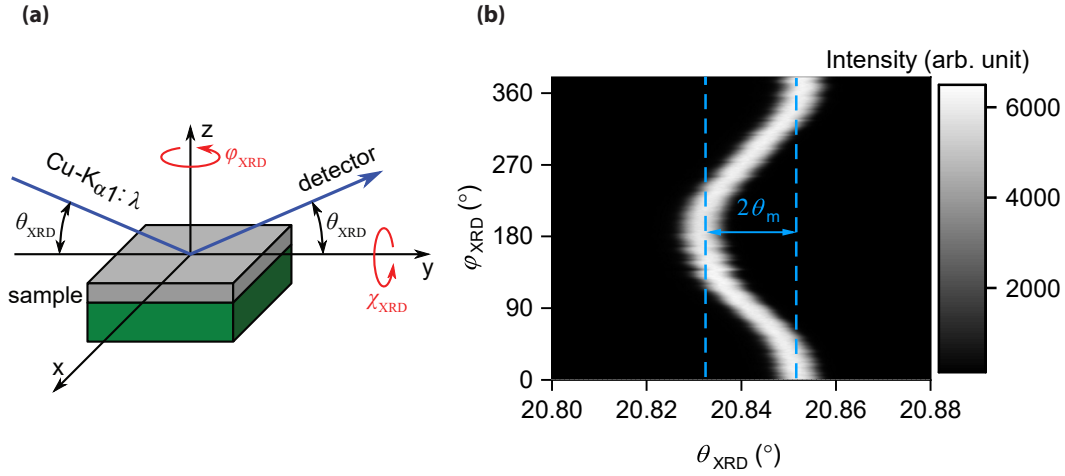


Fig. 7.5. – (a) Measurement geometry used for the XRD experiments using a θ - θ X-ray diffractometer with $\text{Cu-K}\alpha_1$ radiation. Prior to the measurements, the azimuthal rotation axis is aligned parallel to the surface normal of the sample. To determine the miscut angle, rocking curves around the Al_2O_3 (0006) substrate reflection at different azimuthal angles have been performed. (b) Colormap for the X-ray intensity of the (0006)-reflection of the Al_2O_3 substrate for the CoFe on a c-axis Al_2O_3 ($\Delta\theta < 0.1^\circ$) substrate as function of φ_{XRD} and θ_{XRD} . The deviation of (0006)-reflection from a constant θ_{XRD} is attributed to the sample miscut θ_m . We find $\theta_m = (0.011 \pm 0.002)^\circ$ (see blue dashed lines), which is in excellent agreement with the $\theta_m = 0.017^\circ$ determined via our FMR experiments.

We observe a tuning of the (0006)-reflection of $\approx 0.022^\circ$, which corresponds to a miscut angle of θ_m of $(0.011 \pm 0.002)^\circ$, which is in good agreement with the calculated value $\theta = 0.017^\circ$ for this sample determined via the frequency splitting of the two transverse modes and the related velocity splitting following the Christoffel equation.

As a next step, we demonstrate that these observations are not unique to CoFe on hexagonal Al_2O_3 . To this end, we deposit 30 nm thick CoFe films on both sides polished cubic GGG and Si substrates. Fig. 7.6 shows the fitted FMR linewidth $\Delta H(f)$ at these samples recorded at $T = 5$ K as a function of f around $f_0 = 18$ GHz. We choose to study the MEC coupling features by plotting $\Delta H(f)$ instead of from the raw colormap data for $|S_{21}(H_{\text{ext}}, f)|$ due to its enhanced sensitivity at low signal magnitudes.

⁸Here, we use the subscript "XRD" for the XRD-setup angles to avoid confusion with the sample geometry angles introduced in Fig. 7.1(a).

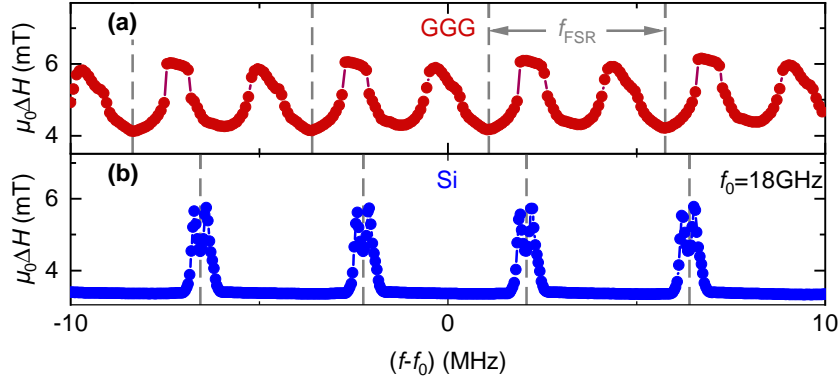


Fig. 7.6. – Fitted FMR linewidth $\Delta H(f)$ recorded at $T = 5$ K as a function of f around $f_0 = 18$ GHz for CoFe deposited on various substrate materials. Pronounced MEC peaks are observed for CoFe deposited on (a) a 380 μm thick GGG (111) substrate ($\theta_m < 1.0^\circ$) and (b) a 675 μm thick Si (100) substrate ($\theta_m < 0.5^\circ$). Gray dashed lines indicate the free spectral range f_{FSR} of the BAW resonances in the individual substrates.

We find that the MEC double peak features in $\Delta H(f)$ are not unique to hexagonal Al_2O_3 substrates [see Fig. 7.2(d)] but are also observed for CoFe grown on (a) 380 μm thick (111)-oriented cubic GGG- and (b) on 675 μm thick (100) oriented cubic Si substrates. Note that we nominally expect the two transverse phonon modes to be degenerate for the crystal directions of these two substrates [see Fig. 7.1(e)]. Hence, we again require a small miscut angle θ_m in these cubic substrate to give rise to a detectable splitting in the phonon modes [see Fig. 7.1(f)]. In Fig. 7.6, the splitting Δf and the free spectral range f_{FSR} of the overtone resonances differ for the various substrates, as the absolute values of v_{st} and v_{ft} are different for these various material systems. Furthermore, we find that the magnitude of both the off- and on-resonant FMR linewidth is comparable for all substrates. This finding suggests that (i) the magnetization damping and thus the magnetic properties of the CoFe film remain unchanged for the various used substrates, (ii) that the elastic relaxation rates of the used substrates are similarly low, and (iii) that the underlying phonon excitation mechanism is governed by the material parameters of CoFe [157,436].

As a last step, we verify the linear frequency-splitting of the transverse phonon modes for all of the used substrate materials by plotting the observed $\Delta f(f)$ of the MEC features recorded at $T = 5$ K as function of f for CoFe deposited on the individual substrate materials in Fig. 7.7. The observed behavior in $\Delta f(f)$ can be well fitted with a linear function without a y-axis intercept following Eq. (7.1). As a general trend, the slope of the fits in Fig. 7.7 is larger for substrate materials with a larger margin of miscut angle θ_m and larger transverse velocities v_t [77,479] in agreement with our expectations.

To briefly summarize the results of this section, we investigate the magnetoelastic coupling between the ferromagnetic resonance mode in a ferromagnetic metallic CoFe thin film and the transverse acoustic phonon modes of high-overtone

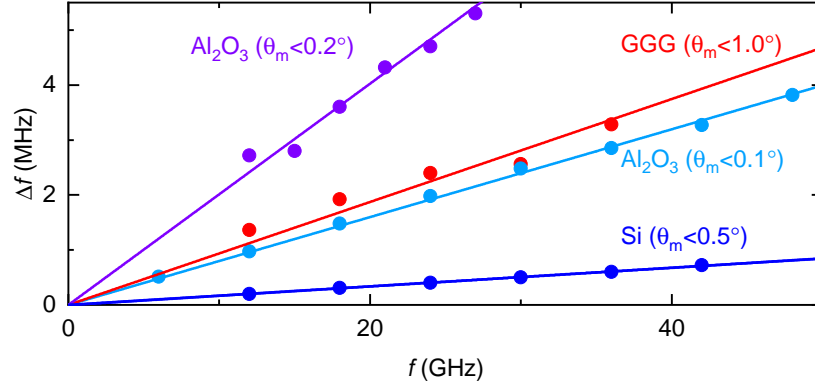


Fig. 7.7. – Frequency splitting $\Delta f(f)$ of the MEC double peak features recorded at $T = 5$ K as function of f around $f_0 = 18$ GHz for CoFe deposited on various substrate materials. A linear evolution as function of f following Eq. (7.1) is confirmed for all substrate materials studied in this work.

bulk acoustic resonators made from crystalline Al_2O_3 , Si, and GGG substrates as phononic host materials. As the chirality of the ferromagnetic resonance modes excites circularly polarized elastic shear waves in the substrates, this excitation scheme is of interest for the investigation of phononic angular momentum transport. However, the two transverse shear wave velocities can also differ depending on the crystallographic symmetry and the phonon propagation direction with respect to the crystal axes. As a small miscut angle θ_m between crystallographic axis and propagation direction is commonly observed for commercially available substrate materials, we find twofold MEC features in our experiments, which can be mapped velocity differences in the m/s range of the two transverse phonon modes and the corresponding substrate miscut angle is experimentally corroborated by XRD experiments. Thus these substrates can be considered as birefringent for phonons [470]. However, we note that cryogenic temperatures and the corresponding strongly reduced acoustic loss rates η_a are a basic requirement to resolve the splitting of the two transverse BAW modes. The temperature dependence of this birefringence effect will be discussed in detail in the following section.

7.2 Temperature dependence of magnon-phonon-polarons in a ferromagnetic metal with low Gilbert damping

In section 7.1, we have stated the importance of cryogenic environments for the detection of phononic birefringence in the host crystal arising from a small but finite miscut introduced in its formatting process, as at low temperatures the elastic loss rates are reduced and the two phonon modes can be resolved as high overtone modes of the BAW resonator in the GHz regime. Hence room temperature measurements in Refs. [77, 158, 159] were not able to detect this effect.

Furthermore, the used YIG on GGG BAW resonator material combination has significant drawbacks at cryogenic temperatures due to an enhanced magnetization damping of YIG [140, 142] and high microwave losses in GGG [482, 483]. Consequently, the implementation of MEC using CoFe grown on arbitrary crystalline substrates has advantages in this regard to benefit from the reduced acoustic losses [471, 472] combined with the increased magnetoelastic coupling [473], which result in improved cooperativities C at cryogenic temperatures. This motivates us to explore both the frequency- and temperature dependence of the acoustic and magnetic damping properties η_a and κ_s as well the magneto-elastic coupling rate g_{eff} of the CoFe grown on c-axis Al_2O_3 bilayer system from Sec. 7. We find, that the results for both κ_s and η_a can be well understood in terms of the models of Gilbert damping in 3d metals [119, 484] and Landau-Rumer theory [471, 472], respectively. Furthermore, by investigating the frequency- and temperature dependence of the magnetoelastic coupling rate g_{eff} and cooperativity C , we are able to identify optimal operation conditions of our hybrid devices for mode hybridization. Finally, we also assess the potential of the phononic signatures in the FMR for strain and stress sensing applications.

7.2.1 temperature dependence of the raw $|S_{21}|$ -data spectra

The frequency-dependence of the raw $|S_{21}|$ -spectra of the CoFe/ Al_2O_3 hybrid sample at cryogenic temperatures has already been briefly discussed in the interpretation of Fig. 7.4(a), where we clearly observe phononic resonances up to $f_0 = 30$ GHz at $T = 5$ K, which indicate the low elastic damping at cryogenic temperatures. Regarding the temperature dependence, its strong impact on the magnetoelastic coupling in our hybrid sample is immediately evident from the temperature dependence raw data transmission spectra $|S_{21}|$ recorded as function of external magnetic field H_{ext} around $H_{\text{res}}(T)$ and f in a range of 20 MHz around a center frequency of $f_0 = 18$ GHz, which are plotted in Fig. 7.8 for low ($T = 5$ K, $l = 1$), intermediate ($T = 100$ K, $l = 2$) and elevated temperatures ($T = 300$ K, $l = 3$). The resonance field H_{res} and plotted $|S_{21}|$ -range of the sub-panels are listed in Tab. 7.2.

Superimposed on the Kittel mode in dark brown color, we observe the distinct frequency periodic pattern of the two phononic resonances induced by the two transverse elastic modes for both low and intermediate temperatures. As previously discussed in Sec. 7.1, the observed $f_{\text{FSR}} \approx 6.04$ MHz agrees well with the expectation for a standing elastic wave pattern in a bulk acoustic resonator via Eq.(2.50). Furthermore, the detection of two neighboring phonon resonances with a frequency splitting of $\Delta f \approx 1.40$ MHz is attributed to the non-degeneracy of the velocities of the fast and slow transverse modes v_{ft} and v_{st} due to a small but finite angle between the c-axis of sapphire and the propagation direction of the shear waves which is parallel to the surface normal \mathbf{z} (see Sec. 7.1). Comparing

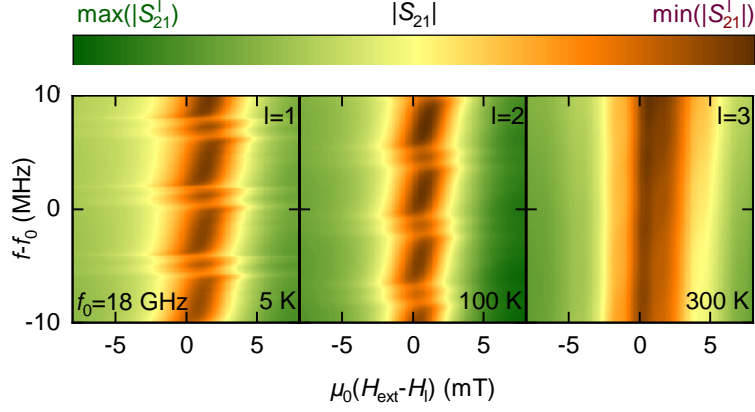


Fig. 7.8. – $|S_{21}|$ recorded at varying temperatures and plotted as a function of frequency f and external magnetic field H_{ext} in the range of H_{res} for $f_0 = 18$ GHz. The H_{res} and $|S_{21}|$ -range of the individual panels are listed in Tab. 7.2. The phononic double peak features are apparent for low ($T = 5$ K, $l = 1$) and intermediate temperature ($T = 100$ K, $l = 2$) but vanish at elevated temperatures ($T = 300$ K, $l = 3$).

panels $l = 1$ and $l = 2$, we find, that for elevated temperatures the phonon resonances decrease in frequency due to the thermal expansion of the sample and also become less pronounced due to the increased elastic damping, which results in a broadening of the phononic resonances. Consequently, at $T = 300$ K ($l = 3$), the interaction between magnons and the bulk acoustic resonator modes is no longer directly visible in the raw $|S_{21}|$ -spectra and we therefore need to process the raw data to visualize the weak and smeared out coupling features at elevated temperatures.

l	1	2	3
T (K)	5	100	300
$\mu_0 H_{\text{res}}$ (T)	3.01	3.00	2.94
$\min(S_{21}^l) (10^{-3})$	16	14	14
$\max(S_{21}^l) (10^{-3})$	25	21	18

Tab. 7.2. – Plot parameters of Fig. 7.8. Temperature T , resonance field $\mu_0 H_{\text{res}}$ as well as minimum and maximum S_{21} -parameter $\min(|S_{21}^l|)$ and $\max(|S_{21}^l|)$ for $l \in [1, 3]$, $l \in \mathbb{N}$.

7.2.2 Frequency and temperature dependence of the magnetic and elastic relaxation rate

As previously done in the data analysis procedure of Fig. 7.2, we analyze the magnonic and phononic relaxation rates as function of T and f by fitting the fixed frequency $S_{21}(H_{\text{ext}})$ -cuts, which are off-resonant with the phononic modes and fixed $|S_{21}(f)|$ -cuts for fixed H_{ext} , which are detuned from the Kittel mode with Lorentzian functions. The resulting half-width at half maximum of these fits are

the magnetic and elastic relaxation rates κ_s and η_a , respectively. In Fig. 7.9(a) and (b), we plot κ_s and the $\eta_{a,i}$ as function of microwave driving frequency f .

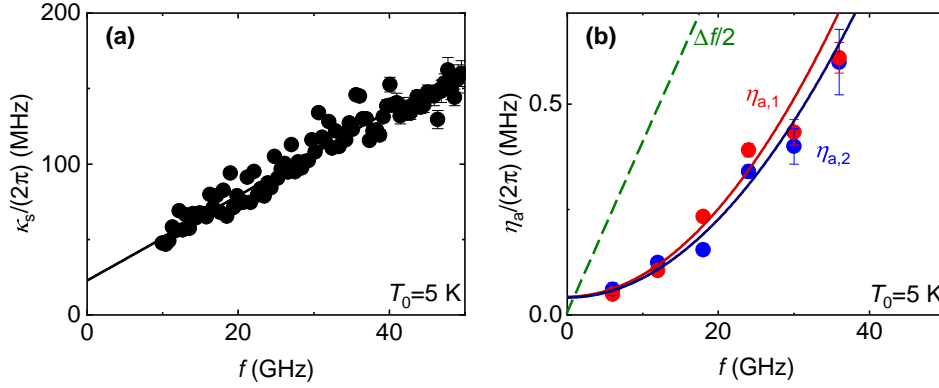


Fig. 7.9. – Relaxation rates of the magnetic (a) and elastic (b) subsystems of the CoFe on Al_2O_3 hybrid sample at $T_0 = 5$ K as a function of frequency f . Continuous lines represent fits to the data with a linear (a) or quadratic (b) frequency dependence for the magnetic and elastic subsystems, respectively. The green dashed line indicates half of the frequency splitting of the two transverse elastic modes $\Delta f/2$ as a measure for the mode overlap of the two transverse elastic modes.

For the magnetic relaxation rate κ_s in panel (a), we observe a linear dispersion in the magnetic relaxation rate $\kappa_s(f)$ induced by the expected viscous Gilbert damping in the LLG [see Eq-(2.15)]. We fit the raw data to the expression $\kappa_s / (2\pi) = \kappa_{s0} / (2\pi) + 2\alpha f$, where κ_{s0} is the inhomogeneous linewidth of the FMR at $f = 0$ Hz and α is the Gilbert damping parameter, and obtain $\kappa_{s0} / (2\pi) = (48.0 \pm 2.4)$ MHz and a low $\alpha = (2.9 \pm 0.1) \cdot 10^{-3}$ comparable to the RT-values for CoFe in Refs. [135, 389]. This result demonstrates the temperature-robust low magnetic damping of CoFe. In the Appendix G1.1, we verify the roughly constant α of our CoFe thin film. The elastic damping of the two transverse modes $\eta_{a,i}$ in panel (b), we observe a non-linear increase with rising f . In analogy to the room-temperature attenuation of elastic modes in GGG in Ref. [159, 160], we fit the $\eta_{a,i}(f)$ with a quadratic expression of the form

$$\eta_a(f) = \eta_a^0 + 4\pi^2 \zeta f^2, \quad (7.2)$$

yielding the fit parameters $\eta_{a1,2}^0 / (2\pi) = (43 \pm 17)$ kHz, (41 ± 18) kHz and $\zeta_{1,2} / (2\pi) = (1.3 \pm 0.1) \cdot 10^{-8} / \text{GHz}$, $(1.2 \pm 0.1) \cdot 10^{-8} / \text{GHz}$, which are one order of magnitude lower to those for GGG in Refs. [159, 160] at room temperature. The greatly reduced $\eta_{a,i}^0$ and ζ_i compared to literature are attributed to both the excellent acoustic properties of Al_2O_3 and the strongly reduced elastic damping at 5 K compared to RT. The quadratic dependence of $\eta_a(f)$ can be naively attributed to phonon-phonon-scattering as the phonon density of states scales $\propto f^2$ for $hf/k_B T < 1$, where h is the Planck constant and k_B is the Boltzmann constant. To obtain an estimate of up to which frequencies we are able to detect the standing waves in our samples, we compare the acoustic decay length to the acoustic wave

propagation distance given by the substrate thickness L . Here, we naively expect to be able to detect standing waves if $\delta_{1,2} = 2\pi v_t / \eta_{a,1,2}(f) > 2L$, i.e. the acoustic wave amplitude is reduced by less than $1/e$ of its initial value after transmitting the substrate twice and interfering with the injected acoustic wave to form a standing wave mode. Using Eq. (7.2) together with our fitting parameters from Fig. 7.2(b), we find that this criterion is met for frequencies up to $f \simeq 50$ GHz. Hence, in agreement with our experimental observations, we expect the formation of standing waves in our sapphire substrate throughout the experimentally available frequency range.

The fitted elastic damping in Fig. 7.9(b) translates to a quality factor of our bulk elastic modes of approximately $Q \simeq (20 - 25) \cdot 10^3$ at $f = 1$ GHz, which is comparable in magnitude to those of high overtone bulk acoustic resonators in Refs. [485,486] demonstrating the expected good acoustic properties of the used Al_2O_3 substrates. Notably, the quadratic dependence of η_a with f can also be viewed as an asset as the generation of chiral phonons requires the controlled excitation of both orthogonal shear waves, which requires that their modes overlap in frequency. As the mode spacing of the two transverse modes Δf scales linear in f [see green dashed line in Fig. 7.2(b)], whereas their mode linewidth increases proportional to f^2 , the degree of mode overlap (relation between mode splitting Δf and the mode linewidths $\eta_{a,i}$, mode coupling for $\Delta f/2 > \eta_{a,1,2}$) can be controlled by appropriately choosing the microwave frequency. In particular, for the investigated sample a frequency overlap of the modes can be achieved at $T = 5$ K for $f < 0.8$ GHz in the investigated frequency range (note that due to the quadratic dependence of η_a , the mode overlap of the two transverse elastic modes is restored for frequencies above the investigated frequency range). Similarly, the tuning of η_a with temperature can also be explored for this purpose as will be discussed in the interpretation of Fig. 7.10(b).

Having discussed the evolution of the elastic and magnetic relaxation rates κ_s and $\eta_{a,i}$ with microwave frequency at a fixed $T = 5$ K, we now discuss their temperature dependence at fixed frequency. In Fig. 7.10, we plot κ_s and $\eta_{a,i}$ as function of temperature at fixed $f_0 = 18$ GHz.

The magnetic relaxation rate in panel (a) is approximately constant up to $T = 30$ K followed by the formation of a minimum in κ_s at $T = 100$ K and a continuous increase in damping for higher T . The regime 4 K $< T < 100$ K matches the expected behavior of 3d transition metals such as for example Permalloy in our previous studies [69,137] and theoretical predictions [117]. However, the increase of κ_s for higher T is too substantial in magnitude to be explained solely with an increased damping from magnon-magnon scattering at elevated temperatures [484]. The likeness of the strong increase in κ_s at elevated T s in panel (a) with the evolution of the $\eta_{a,i}$ in panel (b) indicates, that the increasing linewidth of the phonon modes results in a more effective phonon pumping contribution to the magnetization damping [112,157]. This increase in phonon pumping

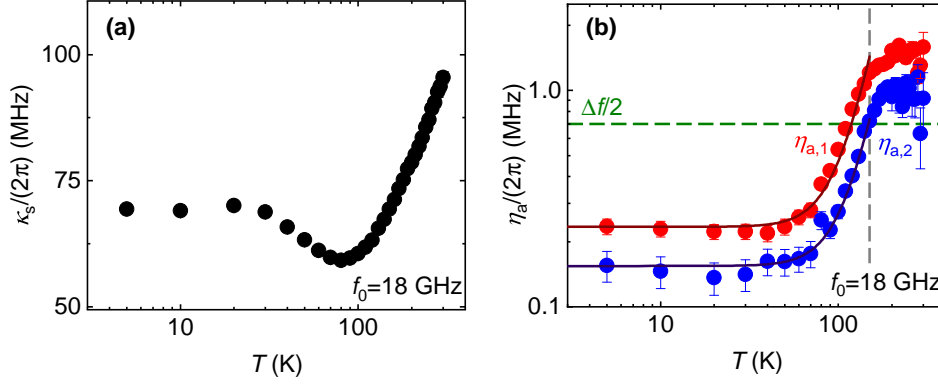


Fig. 7.10. – Relaxation rates of the magnetic (a) and elastic (b) subsystems of the CoFe on Al_2O_3 hybrid sample at $f_0 = 5$ K as a function of temperature T . The continuous lines in panel (b) represent fits to Eq. (7.3) and the green dashed line indicates half of the frequency splitting of the two transverse elastic modes $\Delta f/2$ as a measure for the mode overlap of these two modes.

also manifests itself as an increased inhomogeneous linewidth H_{inh} at elevated temperatures in bbFMR experiments in the Appendix G1.1.

For the elastic relaxation rates of the two transverse phononic modes in Fig. 7.10(b), we observe nearly constant $\eta_{a,i}$ from 300 K down to $T \approx 180$ K. Notably, the formation of standing acoustic waves can also be weakly detected in $|S_{21}(f)|$ spectra at elevated temperatures up to 300 K at $f_0 = 18$ GHz as the acoustic decay length remains comparable to $2L$ [$\delta_{1,2}(T = 300 \text{ K}) \approx 0.6 \text{ cm}/1.0 \text{ cm} \simeq 2L$]. For lower temperatures, the $\eta_{a,i}$ decrease strongly down to $T = 80$ K and remain roughly constant for lower T . The temperature dependence of the transverse acoustic modes in sapphire in the low temperature regime is governed by the Landau-Rumer mechanism [472] as experimentally observed in Ref. [471]. In this model, the acoustic wave is regarded as a parallel beam of low-energy phonons. Because of a finite anharmonicity of the crystal, interactions between different modes are possible. The rate at which the acoustic phonons are scattered can be calculated within perturbation theory. This model predicts a temperature dependence of the acoustic relaxation rate of the form [471]

$$\eta_{a,i}(T) = \eta_{a,i}^0 + \beta_{a,i}T^4. \quad (7.3)$$

A fit of Eq.(7.3) to our low temperature data for $T \leq 180$ K yields the parameters $\eta_{a1,2}^0/(2\pi) = (0.22 \pm 0.02) \text{ MHz}, (0.16 \pm 0.01) \text{ MHz}$ and $\beta_{1,2}/(2\pi) = (0.97 \pm 0.03) \cdot 10^{-3} \text{ Hz/K}^4, (2.28 \pm 0.16) \cdot 10^{-3} \text{ Hz/K}^4$, which are in rough agreement with the values in Ref. [471] as discussed in detail in the Appendix G3. For temperatures $T > 150$ K, all the phonon modes involved in the Landau-Rumer scattering process are excited and hence we observe a roughly constant η_a [487]. The strongly increased η_a at elevated temperatures translates to a stronger mode overlap of the two transverse elastic modes, which are split in frequency by Δf and thus the more efficient generation of helical phonons at elevated temperatures. To

indicate the degree of mode overlap, we added the green dashed line corresponding to $\Delta f/2$ in Fig. 7.10(b). When the individual $\eta_{a,i}$ of the two transverse elastic modes exceed $\Delta f/2$, the two modes overlap. Thus, from Fig. 7.10(b) we expect the generation of helical phonons for temperatures $T > 150$ K at $f_0 = 18$ GHz. The strong tuning of the $\eta_{a,i}$ with both frequency and temperature underlines the potential for controlling the helicity of the phonons by engineering the crystalline orientation with respect to the phonon propagation direction for suitable working points in f and T . However, here we have to account for the magnetoelastic coupling rate between magnons and phonons, which itself is also strongly frequency-dependent [159, 160] and expectedly to a lower degree also temperature dependent due to the expected reduction of magnetoelastic coupling constant B [473]. Hence, in the following section, we study the effective coupling rates g_{eff} and cooperativities C of the two phononic modes as function of both frequency and temperature.

7.2.3 Frequency- and temperature dependence of the effective coupling rate and cooperativity

To extract the effective magnetoelastic coupling rate, we use Eq. (2.56) in combination with the extracted elastic relaxation rates $\eta_{a,i}$ and modification of the FMR-linewidth for frequencies, which are in resonance with the BAW phonon modes ΔH_{MEC} [see Fig. 7.2(b) and (d)]. The resulting g_{eff} as function of f at $T_0 = 5$ K is plotted in Fig. 7.11(a).

We observe in Fig. 7.11(a) a continuous increase in g_{eff} with rising f , which is fitted using [77]

$$g_{\text{eff}}(\omega) = B \sqrt{\frac{2g\mu_B}{hfM_s\tilde{\rho}_t dL}} \left[1 - \cos\left(2\pi f \frac{d}{\tilde{v}_t}\right) \right], \quad (7.4)$$

where h is the Planck constant and $\tilde{\rho}_t$ is the volume density of the CoFe layer. Using $M_s = M_{\text{eff}} = 1.90 \cdot 10^6$ A/m, $g = 2.079$ (see Appendix Sec. G1), $L = 510$ μm , $d = 30$ nm, the transverse velocity $\tilde{v}_t = 3170$ m/s and the volume density $\tilde{\rho}_t = 8110$ kg/m³ for CoFe [436], we extract a fitted magnetoelastic constant $B_{1,2} = (13.5 \pm 0.6) \cdot 10^6$ J/m³, $(12.3 \pm 0.8) \cdot 10^6$ J/m³ for the two modes [continuous lines in Fig. 7.11(a)]. To compare our experimentally extracted B with literature values, we use the following definition for the magnetoelastic constant B in polycrystalline thin films [488]

$$B = \frac{3}{2} \frac{E}{1 + \nu} \lambda_s \quad (7.5)$$

where E is the Young's modulus, ν is the Poisson ratio and λ_s is the saturation magnetostriction. We insert $E = 220$ GPa [489], $\nu = 0.29$ (Sputtering target manufacturer's specification) and $\lambda_s = 0.25\lambda_s^{\text{Co}} + 0.75\lambda_s^{\text{Fe}} \approx 6.1 \cdot 10^{-5}$ [488] in

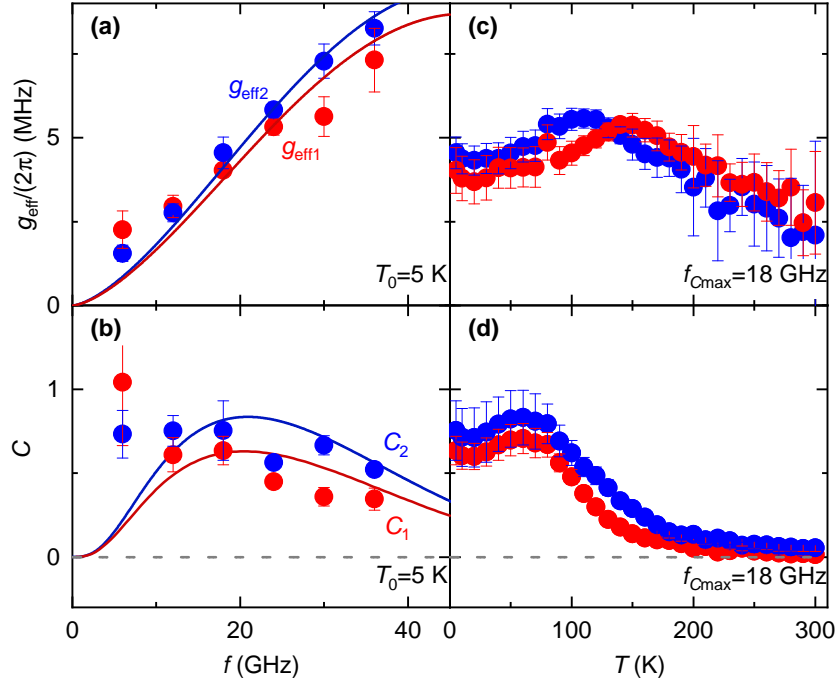


Fig. 7.11. – Left column: Magnetoelastic coupling g_{eff} (a) and cooperativity C (b) at $T_0 = 5$ K as function of f . Right column: Temperature dependence of g_{eff} (c) and C (d) at $f_{\text{Cmax}} = 18$ GHz as function of T . Continuous lines in panels (a) and (b) represent fitting curves to Eqs. (7.4) and $C = g_{\text{eff}}^2 / (2\eta_{a,i}\kappa_s)$ using the fitting results of Fig. 7.2.

Eq. (7.5) and obtain $B = 15.7 \cdot 10^6$ J/m³, which is in good agreement with our fitted $B_{1,2}$ -values from Fig. 7.11(a).

From a comparison of the $\kappa_s(f)$ in Fig. 7.9(a), $\eta_{a,i}(f)$ in Fig. 7.9(b) and the effective coupling rate $g_{\text{eff}}(f)$ in Fig. 7.11(a), we find we are operating the CoFe/Al₂O₃ sample in a regime analogous to the Purcell enhanced regime ($\eta_{a,i} < g_{\text{eff}} < \kappa_s$) throughout the experimentally investigated frequency range ($5 \text{ GHz} \leq f \leq 50 \text{ GHz}$) at $T_0 = 5$ K [149]. In Fig. 7.11(b), we plot the calculated cooperativity of our coupled system $C_{1,2} = g_{\text{eff}}^2 / (2\kappa_s\eta_{a,1,2})$ as function of f . Here, the continuous lines represent the calculated C from our fitted $\eta_{a,i}$ using Eq. (7.2), g_{eff} using Eq. (7.4) as well as the linear fit for κ_s from Fig. 7.9(a). Note that the maximum of the cooperativity is at approximately $f_{\text{Cmax}} = 18$ GHz and does not coincide with a maximum in g_{eff} from Eq. (7.4) due to the frequency dependence of the magnetic and elastic relaxation rates (see also Ref. [77]). We find a good agreement between theory curve and experimental data for $f > 15$ GHz, but do not observe the predicted reduction in C for lower frequencies. We attribute this disparity to the unexpectedly large g_{eff} at low f in Fig. 7.11(a). In Fig. 7.11(c), we plot the temperature dependence of g_{eff} at $f_{\text{Cmax}} = 18$ GHz. We observe a slight increase with rising T resulting in a peak at 150 K for mode 1 and at 110 K for mode 2. We attribute this peak in g_{eff} to the tuning of the acoustic properties of the CoFe thin film and sapphire substrate Al₂O₃, which at the peak temperature minimizes the interfacial acoustic impedance mismatch ($Z = \sqrt{\rho v_t}$) and thereby allows for

the more efficient injection of phonons for $Z_{\text{CoFe}} = Z_{\text{Al}_2\text{O}_3}$ [157]. The observed reduction in $g_{\text{eff}}(T)$ for higher temperatures in panel (c) is in agreement with the expected reduction of B for 3d transition metals at elevated T [473]. Comparing the evolution of $g_{\text{eff}}(T)$ in Fig. 7.11(c) with that of η_a in Fig. 7.10(b), we find Purcell enhanced coupling $g_{\text{eff}} > \eta_a$ for $T < 130$ K for mode 1 and for $T < 160$ K for mode 2 and weak coupling for higher temperatures. Regarding the temperature dependence of the cooperativity in Fig. 7.11(d), we observe a peak at around 60 K from the reduced κ_s in this temperature-range as apparent in Fig. 7.10(a). At higher temperatures, the strong decrease in C mirrors the increase in the $\eta_{a,i}$ in Fig. 7.10(b) for this temperature range.

7.2.4 Study of the tuning of the phononic resonances for sensing applications

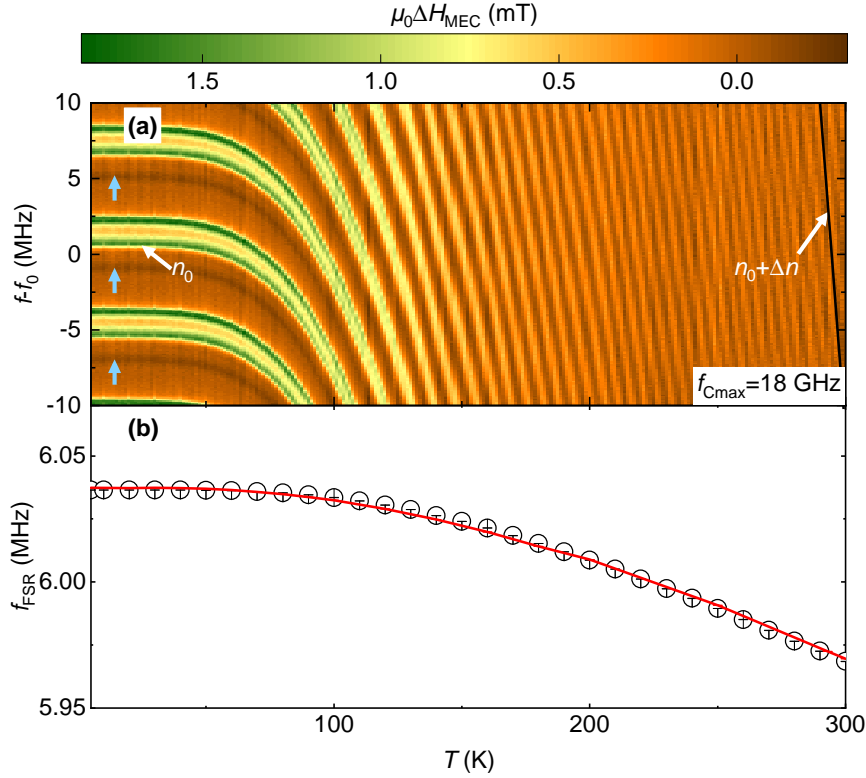


Fig. 7.12. – (a) Modulation of the FMR linewidth due to magnetoelastic coupling ΔH_{MEC} as function of T around $f_{\text{Cmax}} = 18$ GHz. White arrows indicate the acoustic modes n_0 , which are visible at around 18 GHz at $T = 5$ K and the mode $n_0 + \Delta n$ at around 18 GHz at RT. Light blue arrows indicate the unexpected third visible periodic feature, which is currently still the subject of active research. (b) Free spectral range f_{FSR} as function of T . The red continuous line represents a theory model for the temperature dependence of $f_{\text{FSR}}(T)$ using Eq. (7.6).

Finally, having mapped out the relaxation rates of both the magnetic and elastic subsystems as well as the effective magnetoelastic coupling rate as function of both frequency and temperature, in a last step, we investigate the tuning of the

BAW resonances with temperature. As for elevated temperatures, the phononic features are not directly visible in the raw $|S_{21}|$ -data (see Fig. 7.8), we instead investigate the modulation of the FMR-linewidth ΔH_{MEC} in resonance with the acoustic BAW modes, which is visible up to room-temperature and can hence serve as a very sensitive tool to probe MEC even at large κ_s and η_a . To this end, we plot in Fig. 7.12(a) the FMR linewidth change ΔH_{MEC} around $f_{\text{Cmax}} = 18$ GHz as function of temperature and frequency $f - f_{\text{Cmax}}$.

We observe in Fig. 7.12(a), that the two peaks in FMR-linewidth, induced by the coupling of the Kittel mode with the two transverse acoustic modes, broaden and overlap for increasing temperatures. Additionally, they shift to lower frequencies with the mode number of the phononic resonance increasing by $\Delta n = 35$ from $T = 5$ K to $T = 295$ K. Below the two prominent MEC features, which can be directly assigned to the two transverse acoustic modes, a weak frequency periodic feature with a negative ΔH_{MEC} can be identified for cryogenic temperatures. We attribute this feature to the coupling of the Kittel mode to standing waves in the substrate of an unexpected additional phononic branch with slightly altered propagation velocity to the two transverse phonon modes. The origin of this additional mode is currently still the subject of active research.

Note that owing to our excitation scheme, we cannot excite longitudinal modes in the linear regime, which would furthermore also exhibit a significantly larger group velocity and thereby also a different free spectral range [471]. From the evolution of the MEC features of $\Delta H - \Delta H_0$ in Fig. 7.12(a), we can extract the free spectral range $f_{\text{FSR}}(T)$, which is plotted in Fig. 7.12(b). This allows us to compare its tuning in temperature with a naive model via [157]

$$f_{\text{FSR}} = 1/[2(d/\tilde{v}_t + L(T)/v_t(T))]. \quad (7.6)$$

Here, $L(T)$ and $v_t(T)$ are governed by the thermal expansion coefficient $\alpha^*(T)$ [490] and the shear modulus $G(T)$ [478] of Al_2O_3 via $v_t(T) = \sqrt{(G(T)/\rho(T))}$. As the thickness of the FM layer ($d \approx 30$ nm) is thin compared to that of the substrate ($L \approx 510$ μm), we expect that the temperature dependence of the acoustic properties of the magnetic film can be neglected in Eq. (7.6). The expected behavior for $f_{\text{FSR}}(T)$ is plotted as a solid line in Fig. 7.12(b).

We observe a good agreement of our theory curve with the experimentally measured f_{FSR} , thus proving its validity. Hence, the monitoring of f_{FSR} as function of an external control parameter can serve as a sensitive tool to monitor the tuning of both shear modulus G and sample thickness L . Notably, we are able to resolve changes in f_{FSR} down to the kHz-range, which via Eq. (7.6) and using the parameters $L \simeq 510$ μm and $v \simeq 6.1$ km/s translates to a relative change in substrate thickness of $\Delta L/L \approx 1.7 \cdot 10^{-4}$, which is comparable with the sensitivity of state-of-the-art high precision strain sensors [491, 492].

7.3 Summary and Outlook

To summarize the results presented in this chapter, we have investigated the magnetoelastic coupling between the Kittel mode in a ferromagnetic metal and the transverse acoustic phonon modes of various high-overtone bulk acoustic wave resonators by performing cryogenic bbFMR (see Sec. 3.3.1). Using thin polycrystalline ferromagnetic CoFe films to drive the acoustic excitations, we have explored Al_2O_3 , Si, and GGG as host materials for phononic excitations. As the chirality of the ferromagnetic resonance mode can excite circularly polarized elastic shear waves carrying angular momentum in the substrate materials, this excitation scheme is suitable for the investigation of phononic angular momentum transport. Notably, the two transverse shear wave velocities can differ depending on the crystallographic symmetry and the phonon propagation direction with respect to the crystal axis, which we experimentally detect in our experiments for all of the investigated substrate materials as the manifestation of two frequency-periodic magnetoelastic coupling features at a frequency splitting Δf that linearly scales with f and can be translated to velocity differences of the two transverse modes in the m/s range. We attribute these features to a small miscut angle in the host crystals induced during the growth process. As a consequence, the BAW host substrate materials can be considered as birefringent for phonons [470]. The combination of an experimentally simple but efficient ferromagnetic excitation scheme using ferromagnetic resonance with crystalline substrates hosting long-lived phonons thus allows for the realization of phononic $\lambda/4$ -plates [470], to convert linear into circularly polarized phonons and vice-versa via phononic birefringence [493].

In a following step, we study the CoFe grown on crystalline sapphire hybrid sample in greater detail by performing by investigating the frequency- and temperature dependence of both the magnetic- and elastic loss rates κ_s and η_a as well as of its effective magnetoelastic coupling rate g_{eff} and cooperativity C to identify optimal working points for the realization of magnetoelastic devices. In particular the strong increase in the elastic loss rates η_a for rising T demonstrate the advantage of performing these experiments at cryogenic temperatures to push magnon-phonon hybrids to stronger coupling regimes such as the high cooperativity Purcell-enhanced regime [149]. From a different perspective, the strongly increasing η_a at elevated temperatures give rise to a substantial mode overlap of the two transverse elastic waves allowing for the injection of circularly polarized phonons. Hence in particular the sample temperature can be viewed as a control knob for the controlled pumping of either circular or linear phonons. Regarding the magnetic loss rate, we find a relatively temperature-robust Gilbert damping, which renders the CoFe/ Al_2O_3 material platform superior to the conventionally used YIG on GGG substrate [77, 158–160] hybrid devices regarding their performance at cryogenic temperatures. Furthermore, the usage of CoFe allows the free

choice of substrate material and its integration into more complex device layouts. Finally, the study of the tuning of the free spectral range f_{FSR} as function of temperature allows to study the thermal expansion coefficient and shear modulus with high sensitivity. A high sensitivity to relative changes in substrate thickness of the order of $\Delta L/L \simeq 10^{-4}$ of this CoFe/Al₂O₃ hybrid sample are of interest for the realization of magnetic micro-actuators and systems (MAGMAS) [494–497].

Summary and Outlook

In this thesis, we have investigated the magnetization dynamics of various magnetic thin films coupled to other systems. The resulting hybrid systems are of interest for the control and manipulation of the magnetization dynamics in the magnetic thin films. By coupling the magnetization dynamics to different elementary excitations of the solid-state system, various hybrid modes are generated, which allow to unlock novel functionalities of the hybrid system. The overarching goal is to harness the spin degree of freedom for information processing. In particular, collective excitations of the spin system such as spin waves are promising for the realization of more versatile and energy efficient logic circuits. The results presented in this thesis have been obtained using different magnetic materials and coupling the excitation of their spin system to a variety of other solid-state excitations. In detail, we have studied:

- (i) the magnetization dynamics in γ -Fe₂O₃ thin films and how magnetization damping is affected by the presence of paramagnetic impurities in these films in **Chapter 4**.
- (ii) the change of magnetization dynamics of permalloy thin films by the spin torques generated in adjacent superconducting NbN and high spin-orbit interaction TaN layers in **Chapter 5**.
- (iii) the coupling of magnons in ultra-low damping ferromagnetic Co₂₅Fe₇₅ thin films to photons in magnetic field-robust Nb₇₀Ti₃₀N microwave resonators in **Chapter 6**
- (iv) the coupling of magnons in ferromagnetic Co₂₅Fe₇₅ thin films to transverse acoustic phonons in various single-crystalline substrate materials in **Chapter 7**.

These hybrid systems have been characterized by performing either broadband ferromagnetic resonance experiments at cryogenic temperatures or microwave spectroscopy on superconducting resonators.

In the following, we provide a brief summary of the key experimental results for each of the studied hybrid systems. We discuss the main findings and give an outlook on the new questions and exciting prospects for further research triggered by these findings.

8.1 Slowly relaxing impurities in maghemite thin films

In **Chapter 4**, we characterize the epitaxial growth as well as static and dynamic magnetic properties of the room-temperature ferrimagnetic insulator γ - Fe_2O_3 (maghemite). Epitaxially strained maghemite thin films have been grown on MgO substrates via pulsed laser deposition (PLD). The x-ray diffraction (HR-XRD) scans confirm good crystalline quality and coherently strained growth of our thin films, while the results of SQUID magnetometry reveal the presence of a sizable density of antiphase boundaries in our γ - Fe_2O_3 thin films. By studying magnetization dynamics, we find a small negative effective magnetization M_{eff} , providing further evidence for a strain-induced perpendicular magnetic anisotropy in our samples. Most importantly, we observe a non-linear evolution of the ferromagnetic resonance linewidth as a function of the magnetization precession frequency. We can attribute this dependence to the finite coupling of the magnetization dynamics to paramagnetic Fe^{2+} impurities within the framework of a so-called slow relaxor mechanism at cryogenic temperatures and a valence exchange model for elevated temperatures.

The controlled tuning of the magnetization damping is of interest in the research field of magnetization damping engineering of magnetic materials [82]. Moreover, it allows one to tailor the magnetic damping to the specific requirement of device applications, for example, to enhance the sensitivity of magnetic sensors by increasing damping. Furthermore, the observed perpendicular magnetic anisotropy in γ - Fe_2O_3 is of interest for the realization of energy efficient data storage devices using magnetic textures such as magnetic bubbles, chiral domain walls, and magnetic skyrmions [212, 213]. Finally, the near-zero effective magnetization of γ - Fe_2O_3 induced by perpendicular magnetic anisotropy renders it an interesting material platform for magnonics applications using magnetically ordered insulators [106, 199, 214, 215].

8.2 Spin torques in Superconductor/Ferromagnet heterostructures

In **Chapter 5**, we study how the magnetization dynamics in ferromagnetic materials is affected by spin torques generated in adjacent materials using superconductor/ferromagnet heterostructures. First, we investigate NbN/ $\text{Ni}_{80}\text{Fe}_{20}$ (Py)-multilayers with and without a Pt spin sink layer by cryogenic bbFMR experiments using a coplanar waveguide both as signal detector and microwave transducer. By performing a phase sensitive detection of the transmission signal as a function of both temperature and frequency, we quantitatively extract the inductive coupling between sample and coplanar waveguide. The experimental results can

be consistently interpreted in terms of inverse current-induced torques in our heterostructures. In the superconducting state of NbN, we observe a negative damping-like spin torque σ_d , which can be mapped to the quasiparticle mediated inverse spin Hall effect [47]. Moreover, below T_c we find an unexpectedly large field-like current-induced torque σ_f . To gain more insight into the underlying physics, for comparison, we have optimized the growth of superconducting TaN thin films on SiO₂ substrates via reactive dc magnetron sputtering. We selected this material due to its strong spin-orbit interaction, which is expected to translate into the generation of larger spin torques in superconductor/ferromagnet heterostructures based on TaN. As a result of our growth optimization series, we obtained a maximum superconducting transition temperature of $T_c = 5$ K and a maximum critical field $\mu_0 H_{c2} = (13.8 \pm 0.1)$ T, which are comparable to literature [338, 341, 356]. With the optimized samples, we have investigated the impact of the strong spin-orbit interaction in TaN on the inductively detected spin torques in TaN/Py heterostructures. In the superconducting state of TaN, we again detect a negative damping-like spin torque attributed to the QMiSHE. Compared to the results for NbN/Py bilayers a larger amplitude is found due to the stronger spin-orbit interaction in TaN. Furthermore, we again observe the manifestation of a large positive field-like spin torque of unknown origin matching our results for NbN/Py-bilayers. The observed field-like σ_f in the superconducting state of TaN/Py-bilayers was considerably smaller than for the NbN/Py-bilayers, what indicates the crucial impact of the superconducting condensate density to σ_f . This observation points to charge currents with a field-like symmetry generated directly in the superconductor as proposed in Refs. [295, 362]. Future experiments are required to identify the precise physical mechanism giving rise to the enhanced σ_f in our heterostructures.

The experiments performed within this thesis allow one to investigate the spin transport in superconductors from a different angle by incorporating the inverse spin torque conductivities with existing methods, which solely rely on the study of the magnetization damping [49, 50, 256, 285, 287]. In particular, the damping-like σ_d in the superconducting state represents an alternative detection technique for the study of the quasiparticle-mediated inverse spin Hall effect in superconductors to the spin-current injection experiments performed in Ref. [47]. Furthermore, the observed large field-like spin torque σ_f provides clear evidence for the presence of frequency-dependent charge currents in the superconducting state apart from the Meißner screening currents. Notably, intrinsic charge currents with field-like symmetry in superconductors in the presence of spin-orbit interaction have been theoretically proposed in Refs. [295, 362]. Future research aims to exploit the sizable spin torques in the superconducting state to manipulate the magnetization dynamics of the magnetic thin film of a superconductor/ferromagnet heterostructures via the application of a charge current. As an experimental detection technique, we propose to perform the microfocused frequency-resolved

magneto-optic Kerr effect (μ FR-MOKE) technique outlined in Refs. [30, 365] on micropatterned SC/FM-bilayer samples at cryogenic temperatures. Aside from the study of how superconductivity impacts the magnetization dynamics in SC/FM-hybrids performed in this thesis, μ FR-MOKE-experiments could in principle also allow to probe the vice versa effect, i.e. how the magnetization dynamics in the FM layer impacts superconductivity. Research in this direction is motivated by recent theoretical works, which predict the formation of dynamical supercurrents [498] and spin-triplets [499, 500] in the SC layer induced by magnetization dynamics in an adjacent FM layer. To enable the characterization of the SC layer simultaneous to the magnetization dynamics in the FM layer, we propose the addition of electric DC lines on the coplanar waveguide used in the experimental μ FRMOKE setup.

8.3 Magnon-Photon coupling in superconducting microwave resonators/ferromagnetic microstructure hybrids

In **Chapter 6**, we have studied the coupling of magnons in micropatterned ferromagnetic strips to photons in superconducting microwave resonators. In a first step, we have investigated the performance of compact lumped element planar microwave resonators based on Nb₇₀Ti₃₀N (NbTiN) films grown on various substrate materials. The resonators have been studied in external in-plane magnetic fields up to 440 mT, a broad temperature regime from 2.2 K up to 13 K, as well as at mK temperatures. When operating the resonators in the multi-photon regime at $T = 2.2$ K, we find internal quality factors $Q_{\text{int}} \simeq 2 \cdot 10^5$ for NbTiN resonators grown on pristine Si substrates. Regarding their robustness to elevated temperatures and fields, we find a $Q_{\text{int}} > 10^5$ for $T \leq 4.8$ K and $\mu_0 H_{\text{ext}} \leq 180$ mT. These values are comparable to those reported recently for NbN resonators [425] and greatly exceed the performance of elementary Nb [382, 415, 424]. In addition, we have investigated the Q -factors of the resonators on pristine Si substrates at millikelvin temperatures to assess their applicability for quantum applications. Operating at $T = 7$ mK and $\mu_0 H_{\text{ext}} = 0$ mT in a dilution refrigerator with appropriate magnetic field and radiation shielding, we extract $Q_{\text{int}} \simeq 2 \cdot 10^5$ in the single photon regime and $Q_{\text{int}} \simeq 5 \cdot 10^5$ in the high power regime. In the future, we expect that these Q_{int} values can be further improved by using deep reactive ion etching (DRIE) or interface passivation treatments [402, 501, 502] in the resonator fabrication procedure. From the excellent performance of our resonators over a broad temperature and magnetic field range, we conclude that NbTiN deposited on Si (100) substrates constitutes an ideal material platform for field-robust magnon-photon hybrid devices. Consequently, in a second step, we use our optimized NbTiN resonators for the implementation of on-chip magnon-photon hybrid devices. We

realized such devices by fabricating a ferromagnetic $\text{Co}_{25}\text{Fe}_{75}$ (CoFe) on top of the superconducting microwave resonators. In our experiments, we have investigated two different types of hybrid devices, where the CoFe has been (i) coupled either directly to the NbTiN layer or (ii) grown on top of an insulating AlN layer to investigate the impact of the direct ferromagnetic exchange field on the magnon-photon coupling. While for devices of the former type we observed high magnetic loss rates and a reduced effective magnon-photon coupling rate g_{eff} , for samples of the latter type, we found strong coupling with an effective magnon-photon coupling rate of $g_{\text{eff}}/(2\pi) = (120 \pm 4)$ MHz, resulting in an estimated coupling rate per Bohr magneton of $g_0 \approx 223$ Hz and a cooperativity of $C \approx 136$ at a temperature of $T = 3$ K. Magnon-photon hybrid systems are of interest for the implementation of high-speed coherent transducers for circuit quantum electrodynamics [79, 438] and for the transmission of spin excitations via photons [439, 440]. Our results are comparable to state of the art magnon-photon devices [79, 80] and unite the high g_0 with the usage of a hard type-II-superconductor. This combination offers the perspective to push these devices to higher operating temperatures. For the fabrication of a new generation of NbTiN/CoFe magnon-photon hybrid devices, the observed sizable κ_s for CoFe in hybrid devices has to be reduced. To this end, for example an additional buffer layer between the AlN and CoFe could be inserted or alternatively, the impact of the buffered oxide etch before NbTiN deposition could be tested to obtain resonators with reduced surface roughness, which would likely translate to a CoFe growth on a less rough under layer. Furthermore, we note, that the realization of strong magnon-photon coupling using 3d magnetic materials such as CoFe in this thesis and Permalloy in Refs. [79, 80] could in principle allow to electrically control the magnetic properties of the thin film magnetic layer via voltage-controlled magnetic anisotropy [503–505] and thus to tune the achievable magnon-photon coupling rates. Finally, it is worth mentioning, that the realized planar on-chip magnon-photon hybrid devices can be straightforwardly integrated into existing planar superconducting Qubit architectures for example via flip-chip bonding [506–508].

8.4 Magnon-Phonon coupling in bulk acoustic wave resonator/ magnetic thin films hybrids

As discussed in **Chapter 7**, we have performed experiments to study the magnetoelastic coupling between the ferromagnetic resonance modes in a metallic $\text{Co}_{25}\text{Fe}_{75}$ thin film and standing transverse elastic waves in crystalline sapphire, silicon and gadolinium gallium garnet substrates. In our experiments, the single crystalline substrates serve as bulk acoustic wave resonators. Standing elastic waves in these resonators are excited by driving FMR in the ferromagnetic films deposited on them via magnetoelastic coupling. Altogether, this leads

to a finite coupling between the FMR mode in the ferromagnetic film and the transverse acoustic elastic modes (transverse acoustic phonons) in the substrate. The broadband ferromagnetic resonance experiments are performed at cryogenic temperatures. For all substrate materials, we observe an interaction between two resonant standing-wave modes with the magnetic Kittel mode. We identify these modes as the two orthogonally polarized transverse shear waves. As these waves propagated with slightly different velocities in particular directions, we observe phononic birefringence for all substrates. We note that the combination of an experimentally simple but efficient ferromagnetic excitation scheme using ferromagnetic resonance with crystalline substrates hosting long-lived phonons could allow for the realization of phononic $\lambda/4$ -plates [470], to convert linear into circularly polarized phonons and vice-versa by making use of this phononic birefringence [493]. However, to this end, optimal working points in frequency, driving field and overlap of the two transverse acoustic phonons modes need to be identified. Therefore, in a second step, we exemplarily study the frequency- and temperature-dependence of the magnetoelastic coupling of a CoFe thin film with the standing transverse elastic waves of a sapphire substrate. We observe a strong decrease in the relaxation rate of the elastic modes with decreasing T and correspondingly a considerable enhancement of the cooperativity C of the coupled magnon-phonon system, which highlight the importance of performing these experiments at cryogenic temperatures. However, the strongly increased elastic loss rate η_a at elevated temperatures gives rise to a substantial mode overlap of the two transverse elastic waves allowing for the injection of circularly polarized phonons into the host crystal. Hence, we find that in particular the sample temperature constitutes a control knob to select the chirality of the pumped phonons. Regarding the magnetic loss rate of the CoFe layer, we find a relatively constant Gilbert damping as function of T , which renders the CoFe/Al₂O₃ material platform a temperature-robust alternative to the commonly investigated YIG on GGG substrate hybrid devices [77, 158–160]. Most importantly, the usage of CoFe allows the free choice of substrate material and its integration into more complex device layouts. Finally, the sensitive tuning of f_{FSR} to relative changes in substrate thickness of the order of $\Delta L/L \simeq 10^{-4}$ of this CoFe/Al₂O₃ hybrid sample is of interest for the realization of Magnetic micro-actuators and systems (MAGMAS) [494–497]. Concepts to achieve higher effective magnetoelastic coupling rates for magnon-phonon hybrid devices operating in the strong and ultra-strong coupling regime revolve around realizing BAW resonators with lower mode volumes for example in the form of freestanding membranes [509, 510]. Notably, there already exist methods for the growth of ultrathin sapphire membranes [511, 512], which could be straightforwardly interfaced with thin film CoFe layers and characterized in terms of their coupling regimes in future experiments. On the other hand, the perspective to transport angular momentum via phonons could allow for the realization of phononic spin valve devices [77]. For an electrical control of the

phononic spin transport in such devices, the propagation velocities of the transverse acoustic phonon modes, piezoelectric materials such as Lithium niobate (LiNbO_3 , LNO) can be used as BAW resonators. Notably, the good acoustic properties of LNO and sizable coupling rates of CoFe on LNO BAW resonators has been realized under the guidance of the author by Keita Takahashi during his Bachelors' thesis [513], though in his experiments, a potential tuning of the BAW resonances in LNO under an applied gate voltage was masked by thermal effects. However, as the tuning of the resonances in piezoelectric BAW resonators via an applied gate voltage has recently been experimentally demonstrated in Ref. [514], we expect, that additional experiments in a thermally stable environment will also unambiguously reveal this effect in our CoFe on LNO BAW resonator devices thus paving the way towards the control of phononic spin transport in BAW resonators.

In conclusion, within this thesis, high sensitivity microwave spectroscopy experiments at cryogenic temperatures have been performed to characterize the magnetization dynamics of various hybrid systems. New materials have been grown and characterized and new data analysis methods as well as novel concepts have been developed to pave the way for the efficient manipulation and control of magnetization dynamics in hybrid systems. Most importantly, this includes the coherent transfer of angular momentum in these hybrid systems, which enables engineering of magnetization dynamics in and applying frequency conversion schemes to magnetic hybrid systems.

Appendix A: Additional experiments on the magnetic properties of $\gamma\text{-Fe}_2\text{O}_3$

In this section, we present the results of energy-dispersive X-ray spectroscopy (EDS) experiments on the $\gamma\text{-Fe}_2\text{O}_3$ thin film investigated in Ch. 4 the main text and FMR results of additional $\gamma\text{-Fe}_2\text{O}_3$ thin films.

A1 Identification of potential slowly relaxing impurities

To identify the potential present impurities in our samples, we perform energy-dispersive X-ray spectroscopy (EDS) using a scanning electron microscope (SEM). In Fig. A.1, we plot the integrated detected x-ray intensity as a function of x-ray energy E recorded for a scanned area of $50 \times 40 \mu\text{m}^2$ of the 52.6 nm thick $\gamma\text{-Fe}_2\text{O}_3$ thin film.

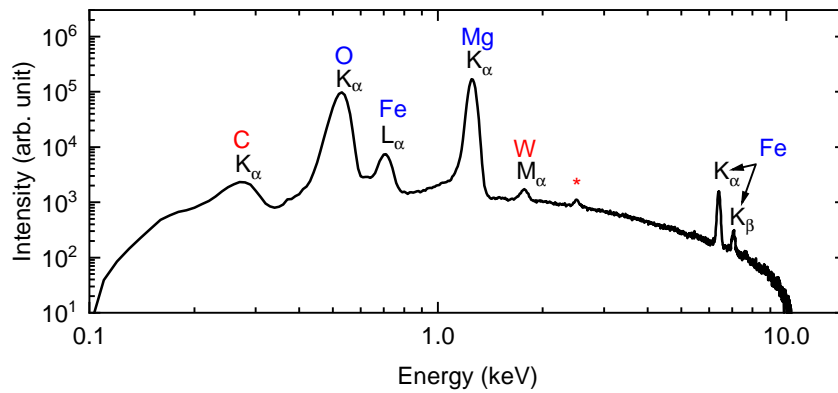


Fig. A.1. – EDS energy spectrum of the 52.6 nm thick $\gamma\text{-Fe}_2\text{O}_3$ thin film. Peaks are labeled with the corresponding element and energy shell. Blue labels correspond to peaks from elements, which comprise the MgO substrate and $\gamma\text{-Fe}_2\text{O}_3$ thin film, whereas red labels represent peaks from unexpected elements, which we attribute to contaminants present in the SEM.

The visible peaks in Fig. A.1 allow to identify the different atomic species present in our samples. Particularly pronounced are the signatures of oxygen, magnesium and iron atoms in agreement with the used MgO substrate and the $\gamma\text{-Fe}_2\text{O}_3$ thin film (blue labels). The observed small K_α peak from carbon is attributed to carbon impurities on the sample surface, whereas the tungsten M_α -peak most likely stems from the point source cathode of the SEM. The additional peak at $E \approx 2.504 \text{ keV}$ (cf. asterisk in Fig. A.1) can however not be directly matched

to the energy shell of any element. We speculate that it originates from the molybdenum $L_{\text{fi},2}$ -shell at $E \approx 2.518$ keV from abrasions of the tweezers used for sample handling. To our knowledge, neither C, Mo nor W impurities have been found to induce slowly relaxing impurity damping mechanisms. As we observe no additional peaks from elements, known to induce slowly relaxing impurity damping such as e.g. Si [147], Ir [246], Yb [245], Nd [247] and Ge [82], they constitute a mass fraction for our maghemite thin films below the detection limit of the used SEM setup ($w < 0.1$ wt%), which is too low to affect the magnetization dynamics in our samples. As discussed in the main text (see Sec. 4.3), an alternative candidate for slowly relaxing impurities are unpaired Fe^{2+} -ions [147, 235–237] caused by the oxygen deficiency in our samples.

A2 Additional data on magnetic properties of maghemite films

In addition to the data of the 52.6 nm thick maghemite thin film, we here present the results of our cryogenic bbFMR experiments for the magnetization dynamics and slowly relaxing impurity parameters of a 45.0 nm thick maghemite film as a function of temperature T in Fig. A2. Here, the parameters describing the slowly relaxing impurities are again derived under the assumption of a temperature independent g -factor $g = 2.022$ (see Sec. 4.3). For the effective magnetization in Fig. A2(a), we observe a continuous increase with decreasing T and M_{eff} exhibits a sign change at $T_{\text{cross}} = 25$ K. For the Gilbert damping α in panel (b), we find approximately constant values down to $T = 25$ K, followed by a steep increase at lower T . Similarly to Fig. 4.6 from the main text, this abrupt increase in damping coincides with the sign change in M_{eff} . This correspondence indicates, that the change in anisotropy from easy-axis to easy-plane in our samples affects the Gilbert damping in our thin films. Regarding the slowly relaxing impurity parameter $CF(T)$ in Fig. A2(c), we observe a strong reduction with increasing temperature. In contrast to Fig. A2(c) from the main, a peak-like feature in $CF(T)$ is not evident due to the reduced number of recorded data points in the low temperature regime. For higher temperatures, the behavior in $CF(T)$ is in agreement with the results in Fig. A2(c) of the main text. We perform a fit to the product of Eqs. (2.40) and (2.41) [red line in Fig. A2(c)] and extract the fitting parameters $E_{\text{slow}} = (0.55 \pm 0.07)$ meV and $C \cdot T = (78 \pm 12)$ GHz·K. These values coincide with fitting results for the 52.6 nm thick maghemite sample in the main text and thereby demonstrate that the FMR results presented in the main text are representative for our maghemite films. Finally, for the relaxation time τ in panel (d), we find an approximately constant τ for elevated temperatures and a strong increase for $T < 50$ K. We fit the τ values for $T \leq 50$ K to Eq. (4.1) and obtain $E_{\text{A}} = (6.2 \pm 0.3)$ meV and $\tau_0 = (19.3 \pm 0.2)$ ps. These fitting values are in

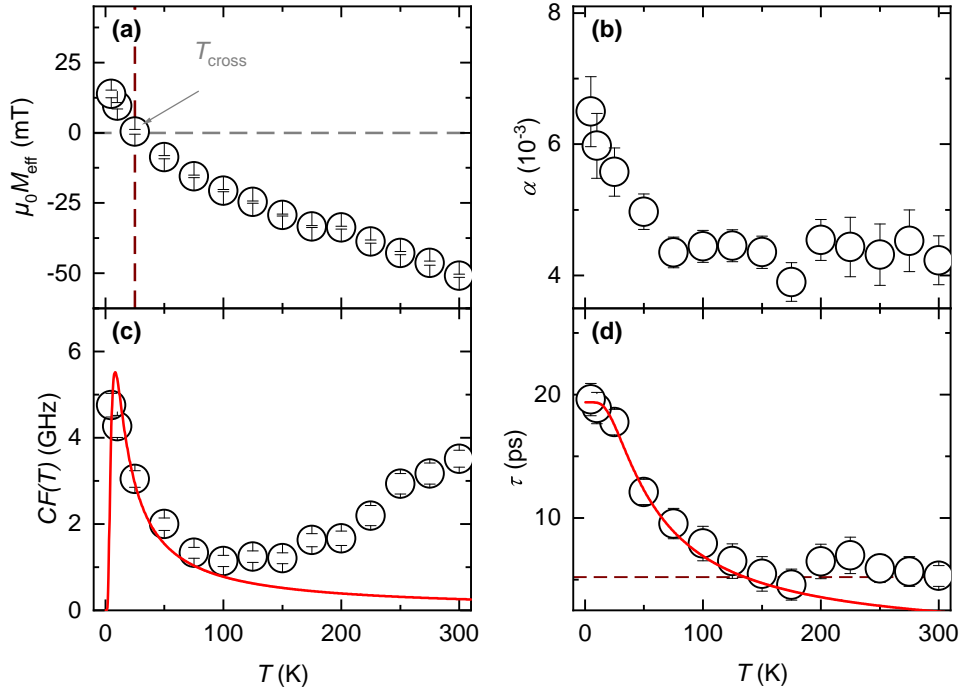


Fig. A2. – Magnetization dynamics and slowly relaxing impurity parameters of the 45.0 nm thick maghemite film as a function of temperature T . (a) Effective magnetization M_{eff} and (b) Gilbert damping parameter α as function of T . (c) Magnitude of the slowly relaxing impurity contribution $CF(T)$ together with a theoretical fitting curve for $F(T)$ following the product of Eqs. (2.40) and (2.41) (red line). We obtain the slowly relaxing impurity parameters $E_{\text{slow}} = (0.55 \pm 0.07)$ meV and $C \cdot T = (78 \pm 12)$ GHz·K. (d) Relaxation time τ as a function of T . The red line represents a fit to Eq. (4.1). We extract $E_A = (6.2 \pm 0.4)$ meV and $\tau_0 = (19.3 \pm 0.2)$ ps.

good agreement to the fitting results from Fig. A2(d) from the main text, while the fitted activation energy E_A is a factor or two larger than for the thicker maghemite sample.

A3 Additional FMR-results for $\gamma - \text{Fe}_2\text{O}_3$ thin films

In Fig. A3, we present additional room temperature FMR results for three $\gamma\text{-Fe}_2\text{O}_3$ thin films of varying thickness d (see Tab. A1). For these three films, we again observe a reduced effective magnetization attributed to a perpendicular magnetic anisotropy and a non-linear behavior in ΔH as function of frequency, which we interpret with the slow-relaxor model. The raw data for H_{res} and ΔH

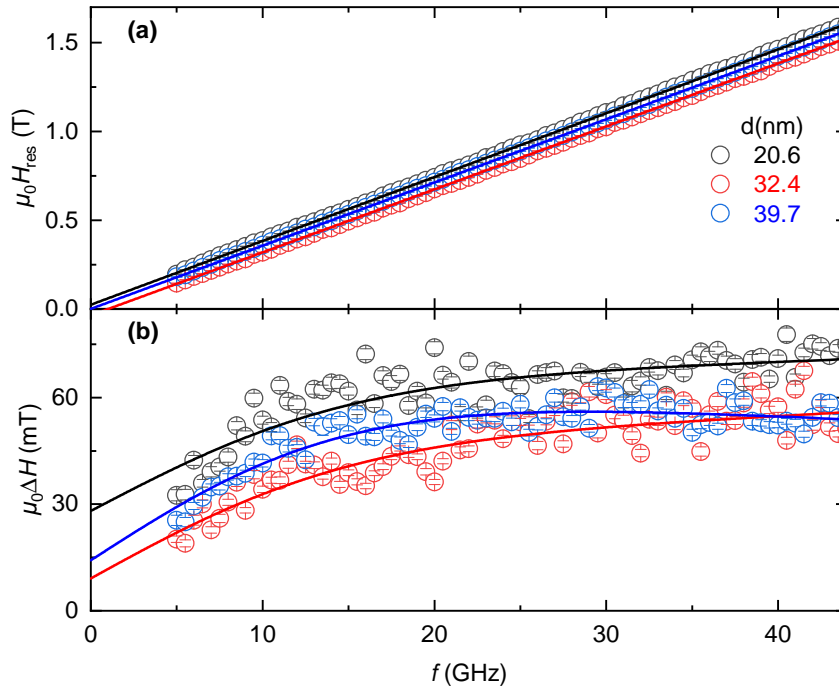


Fig. A3. – Room temperature FMR results for three $\gamma\text{-Fe}_2\text{O}_3$ thin films of varying thickness d (see Tab. A1). (a) Raw data of the extracted resonance field H_{res} together with a fit following Eq. (2.37). (b) Raw data of the extracted resonance linewidth ΔH together with a fit following Eq. (2.38).

are fitted with equations (2.37) and (2.38) under the assumption of a constant g -factor of $g = 2.022$. The resulting fitted magnetization dynamics and slow-relaxor parameters are listed in Table A1. They correspond well with the FMR-parameters of the 52.8 nm and 45.0 nm thick $\gamma\text{-Fe}_2\text{O}_3$ -samples at RT.

d (nm)	$\mu_0 M_{\text{eff}}$ (mT)	α (10^{-3})	$CF(T)$ (GHz)	τ (ps)
20.6	41 ± 2	5.6 ± 1.1	4.5 ± 0.4	6.1 ± 0.2
32.4	-30 ± 1	8.6 ± 0.6	4.7 ± 0.6	6.4 ± 0.3
39.7	14 ± 1	2.2 ± 0.8	6.5 ± 0.3	5.9 ± 0.2

Tab. A1. – FMR and slow-relaxor model parameters of the three additional $\gamma\text{-Fe}_2\text{O}_3$ thin films.

Appendix B: Sputter deposition parameters

In the following we summarize the deposition parameters used for the individual sputtered materials of the hybrid devices investigated in Chapters 5,6 and 7 using the Superbowls and Ultradisk sputtering systems (see Sec. 3.1).

B1 Sputter deposition parameters

B2 Superbowls

Target material	P/A [W/cm ²]	r [Å/s]	T [°C]	N ₂ /Ar-ratio
Cu	0.8	1.0	RT	-
Co ₂₅ Fe ₇₅	0.8	2.1	RT	-
NbN	2.1	4.0	400	1.9/18.1
Py	3.1	3.1	RT	-
Pt	1.2	4.2	RT	-
Pt in sample C	0.2	0.2	RT	-
Ta	1.2	0.5	RT	-
TaN (NC)	1.2	1.1	500	1.0/10
TaN (SC)	1.2	1.3	500	3.5/10

Tab. B1. – Sputtering parameters of the materials grown in the Superbowl. All materials were grown at a deposition pressure $p_{\text{depo}} = 5 \times 10^{-3}$ mbar.

B3 Ultradisk

Target material	P/A [W/cm ²]	r [Å/s]	T [°C]	N ₂ /Ar-ratio
Nb ₇₀ Ti ₃₀ N	0.9	0.8	500	3.8/36.2

Tab. B2. – Sputtering parameters of the materials grown in the Ultradisk. All materials were grown at deposition pressure $p_{\text{depo}} = 5 \times 10^{-3}$ mbar.

Appendix C: Determination of the superconducting transition temperature via microwave spectroscopy

This section outlines the method used to determine the superconducting transition temperature of the SC/FM-heterostructures investigated in Ch. 5.

To determine T_c of our samples from the microwave response in $|S_{21}|$ as function of T is derived in Refs. [68, 122]. we recorded $|S_{21}|$ at fixed frequencies as function of sample temperature. Exemplary data is shown in Fig. C1 at $f_0 = 30$ GHz for sample B from Ch. 5.

We observe a steep increase in $|S_{21}|$ below 9 K, which we attribute to the onset of superconductivity. For a quantitative description of the observed behavior, we used the following expression for $|S_{21}|$ normalized by the transmission parameter of an unloaded CPW $|S_{21}^0|$ [308].

$$\left| \frac{S_{21}}{S_{21}^0} \right| \propto \exp \left(- \frac{|\gamma_0 Z_{\text{eff}}| l}{2Z_0} \right). \quad (\text{C.1})$$

Here, l represents the sample's length on the CPW, Z_{eff} and Z_0 stand for the thin film surface impedance and unloaded CPW-impedance, respectively. Additionally, $\gamma_0 = \omega/v_{\text{ph}}$ is the complex propagation factor, where $f = \omega/2\pi$ and v_{ph} is the phase velocity of microwaves in the CPW. For Z_{eff} , we use the superconducting surface impedance [86]

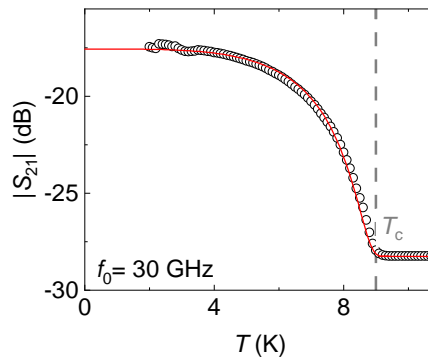


Fig. C1. – Microwave transmission $|S_{21}|$ recorded at a fixed microwave frequency $f_0 = 30$ GHz as a function of normalized temperature for sample B. The steep increase in T_c fitted using Eq. (C.4). We extract a London penetration depth of $\lambda_L = (1.12 \pm 0.06) \mu\text{m}$.

$$Z_{\text{eff}}(\omega) \approx -i \cdot \mu_0 \omega \lambda_{\text{eff}}. \quad (\text{C.2})$$

We note, that the T -dependence of $|S_{21}|$ is governed by that of the London penetration depth λ_L , most commonly described by the Casimir-Görter-model [361]

$$\lambda_L(T) = \frac{\lambda_L(0)}{\sqrt{1 - (T/T_c)^4}}. \quad (\text{C.3})$$

We insert Eq. (C.2) into (C.1) and obtain the result

$$|S_{21}| = |S_{21}^{\text{NC}}| + |\Delta S_{21}| \exp\left(-\frac{|\gamma_0| l \mu_0 \omega \lambda_L^2(0)}{2Z_0 d_{\text{SC}} (1 - (T/T_c)^4)}\right) \quad (\text{C.4})$$

for our fitting function, where $|S_{21}^{\text{NC}}|$ represents the complex transmission magnitude in the normal state and $|\Delta S_{21}|$ is the magnitude of the change in S_{21} below T_c . The resulting fitting curve is shown in Fig. C1 using the $d_{\text{SC}} = 16$ nm, $l = 6$ mm, $v_{\text{ph}} = 1.8 \cdot 10^8$ m/s (used by Schmidt et. al. in Ref. [308]) and $Z_0 = 50 \Omega$. We extract a London penetration depth of $\lambda_L = (1.12 \pm 0.06) \mu\text{m}$, which is considerably larger than literature values for NbN, ranging from 200 nm to 400 nm [314, 315]. We attribute this to disorder. In disordered superconductors, a correction factor is added to λ_L of the form [515]

$$\lambda_L(0) = \lambda_L^\infty(0) \left(1 + \frac{\zeta^\infty(0)}{l_0}\right)^{1/2}, \quad (\text{C.5})$$

where ζ^∞ and l_0 are the bulk superconducting coherence length and mean free path respectively. Using $l_0 = 3.96 \text{ \AA}$ [516], $\zeta^\infty = 5$ nm [257] and $\lambda_L^\infty(0) = 300$ nm, we obtain $\lambda_L(0) \approx 1 \mu\text{m}$, which agrees well with our experimental results. Furthermore, we note that an unusually large λ_L has also been observed for SC/FM-bilayers in [517], where it was attributed to the depletion of the superconducting fluid density n_s at the FM interface. The respective T_c and λ_L of the samples from Sec. 5.2 are listed in Tab. C1.

Sample	A	B	C	D
T_c [K]	11.5	9.0	10.0	10.2
λ_L [μm]	0.84	1.12	0.71	0.96

Tab. C1. – Superconducting transition temperature T_c and estimated London penetration depth λ_L of samples discussed in Sec. 5.2.

Appendix D: Raw data for the reduced inductance

In this section, we exemplarily present raw data for the complex reduced inductance of the SC/FM-heterostructures investigated in Ch. 5 for temperatures, where the used SC layer is in both the normal- and superconducting state.

D1 Reduced inductance at room temperature

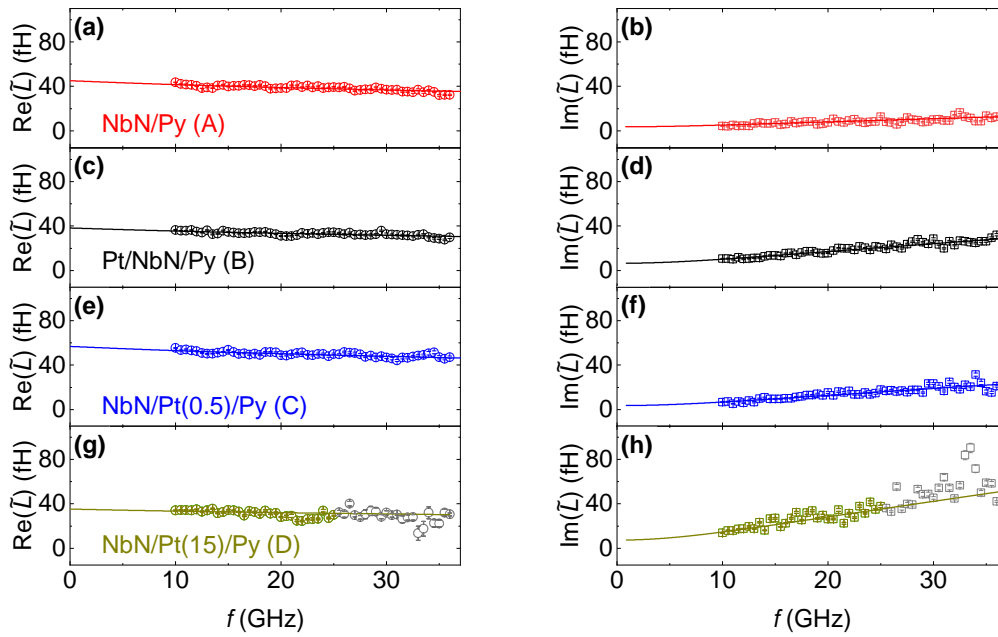


Fig. D1. – Real and imaginary part of the reduced inductance \tilde{L} at room temperature for samples A-D. Samples B and D exhibit an iSHE as apparent from the slopes of $\text{Im}(\tilde{L})$ in panels (d) and (h). Due to the enhanced damping in the NbN/thick Pt/Py-trilayer (sample D), the strongly broadened FMR-linewidth above 25 GHz leads to an imprecise fitting. Hence these data-points are omitted in the fitting of \tilde{L} [see gray data points in panels (g) and (h)]. Lines in the graphs are fits using Eq.(5.14).

In Fig. D1, we show raw data of the reduced complex inductance \tilde{L} for the four NbN/Py-heterostructures from Sec. 5.2 of the main text at room temperature in real and imaginary part. For all samples, $\text{Re}(\tilde{L})$ in Fig. D1 exhibits a similar y-axis intercept as well as a linear frequency dependence. For its imaginary part $\text{Im}(\tilde{L})$, the samples display different behaviors. Sample B and D exhibit a large positive slope, while sample A, devoid of platinum, exhibits only a minor positive slope. These results are in line with our expectations that the slope in $\text{Im}(\tilde{L})$ is governed by the iSHE from spin pumping into Pt. Hence, the slope in $\text{Im}(\tilde{L})$, is the largest in samples containing thick Pt-layers and absent in the red data points of sample A. All curves converge towards the origin for zero frequency, which is

expected as in the dc limit ($f = 0$ Hz), the inductance is a real value. This condition is well met in our samples. However, we refrain from rotating $\tilde{L} = (\text{Re}(\tilde{L}), \text{Im}(\tilde{L}))$ by a rotational matrix with angle β to ensure $\text{Im}(\tilde{L})(f = 0) = 0$ as performed in [40,84]. Our reasoning is that the inductive coupling \tilde{L}_0 changes slightly with temperature giving rise to artifacts in our temperature-dependent study, when rotating each data point with a slightly different angle β for each temperature.

D2 Reduced inductance in the superconducting state

We plot the reduced inductance of our samples at $T \approx 0.5 \times T_c$ in Fig. D2.

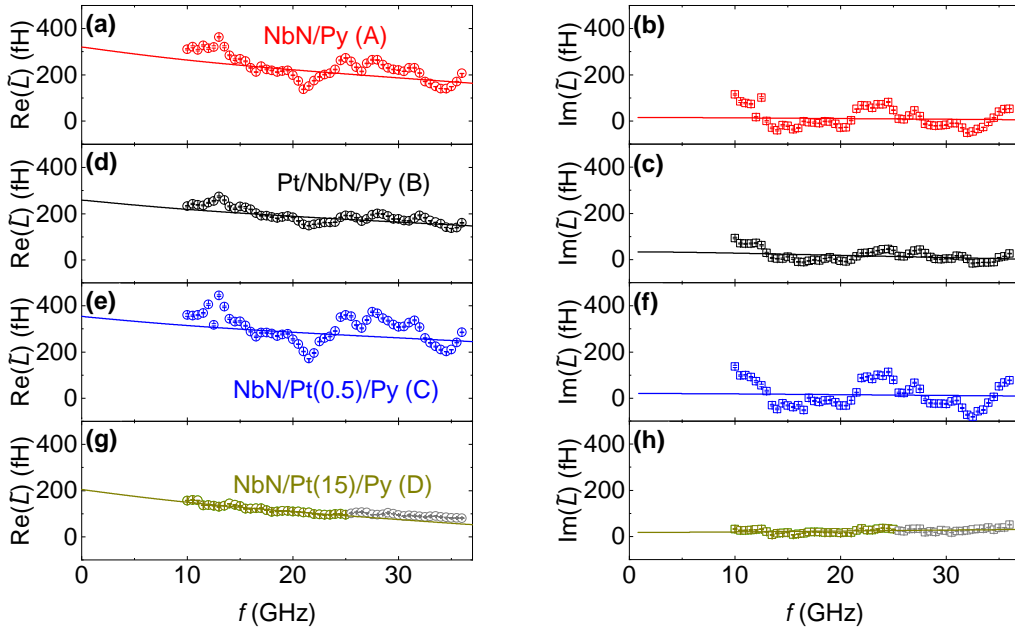


Fig. D2. – Real and imaginary part of the reduced inductance \tilde{L} for samples A-D below the superconducting transition temperature T_c . Dramatic changes in both \tilde{L}_0 and L_j are apparent. The omitted data points for the NbN/thick Pt/Pt-trilayer (sample D) are again shown as grey data points. Continuous lines represent fits to the data using Eq. (5.14).

We observe an enhancement in the inductive coupling strength \tilde{L}_0 , which can be well explained by superconducting image charge currents repelling the oscillatory driving field of the CPW h_{rf} (see Sec. 5.1). We observe a 6 to 7-times enhancement of \tilde{L}_0 in the SC-state. We observe a reduction and sign change for $\text{Im}(\tilde{L})$, which indicates the blocking of normal state spin currents and the quasiparticle mediated iSHE in the SC state as well as slightly negative $\text{Re}(\tilde{L})$ corresponding to a positive field-like spin torques σ_f of unknown origin. Moreover, an oscillatory behavior of \tilde{L} in both real and imaginary part is apparent, which is discussed in Sec. 5.2.

Appendix E: Sputter deposition parameters of the TaN thin films of the growth optimization study

In the following, we list the deposition parameters, superconducting properties and volume densities D_V for the TaN films deposited in the growth optimization study in Sec. 5.3.1.

E1 N_2/Ar -gas flow ratio series

N_2/Ar [%]	T_{depo} [°C]	P_{depo} [W]	p_{depo} [mbar]	T_c [K]	ΔT_c [K]	D_V [g/cm ³]
5	500	30	0.005	-	-	14.7
10	500	30	0.005	-	-	15.2
15	500	30	0.005	-	-	14.6
20	500	30	0.005	-	-	14.2
25	500	30	0.005	3.51	0.71	14.4
30	500	30	0.005	4.14	1.11	13.4
35	500	30	0.005	4.97	1.26	13.8
40	500	30	0.005	4.65	1.24	13.1
45	500	30	0.005	3.54	0.98	12.6
50	500	30	0.005	-	-	12.9

Tab. E1. – Deposition parameters, superconducting transition temperature T_c and width ΔT_c as well as volume density D_V for TaN films grown for varying N_2/Ar gas flow ratios.

E2 Deposition temperature series

N_2/Ar [%]	T_{depo} [°C]	P_{depo} [W]	p_{depo} [mbar]	T_c [K]	ΔT_c [K]	D_V [g/cm ³]
35	100	30	0.005	-	-	12.2
35	200	30	0.005	-	-	12.5
35	300	30	0.005	-	-	12.7
35	400	30	0.005	-	-	13.0
35	500	30	0.005	4.97	1.26	13.8
35	600	30	0.005	3.07	0.54	13.8
35	700	30	0.005	3.68	0.96	14.1
35	800	30	0.005	4.72	0.60	14.0

Tab. E2. – Deposition parameters, superconducting transition temperature T_c and width ΔT_c as well as volume density D_V for TaN films grown for varying deposition temperatures T_{depo} .

E3 Deposition power series

N_2/Ar [%]	T_{depo} [°C]	P_{depo} [W]	p_{depo} [mbar]	T_c [K]	ΔT_c [K]	D_V [g/cm ³]
35	500	15	0.005	-	-	13.0
35	500	30	0.005	4.97	1.26	13.8
35	500	45	0.005	3.81	0.78	14.3
35	500	60	0.005	-	-	14.4
35	500	75	0.005	-	-	14.8
35	500	90	0.005	-	-	15.0

Tab. E3. – Deposition parameters, superconducting transition temperature T_c and width ΔT_c as well as volume density D_V for TaN films grown for varying deposition powers P_{depo} .

E4 Deposition pressure series

N_2/Ar [%]	T_{depo} [°C]	P_{depo} [W]	p_{depo} [mbar]	T_c [K]	ΔT_c [K]	D_V [g/cm ³]
35	500	30	0.002	4.31	0.97	13.9
35	500	30	0.0035	4.45	1.02	13.8
35	500	30	0.005	4.97	1.26	13.8
35	500	30	0.007	3.49	0.92	13.0

Tab. E4. – Deposition parameters, superconducting transition temperature T_c and width ΔT_c as well as volume density D_V for TaN films grown for varying deposition pressures p_{depo} .

Appendix F: Superconducting NbTiN microwave resonators

In this subsection, we present x-ray diffraction results of NbTiN thin films deposited in the Ulatradisk, as well as a list of the individual quality factors and participation ratios of our NbTiN resonators investigated in Ch. 6.

F1 X-ray diffraction results of NbTiN thin film grown on HF-dipped Si

In this section of the Appendix, we present the results of x-ray diffraction experiments on the NbTiN thin films grown on the BOE treated Si-substrate in Fig. F1. Note, that all the other NbTiN thin films in the study of Ch. 6 did not exhibit crystalline reflections. The $2\theta - \omega$ x-ray diffraction scan in Fig. F1(a)

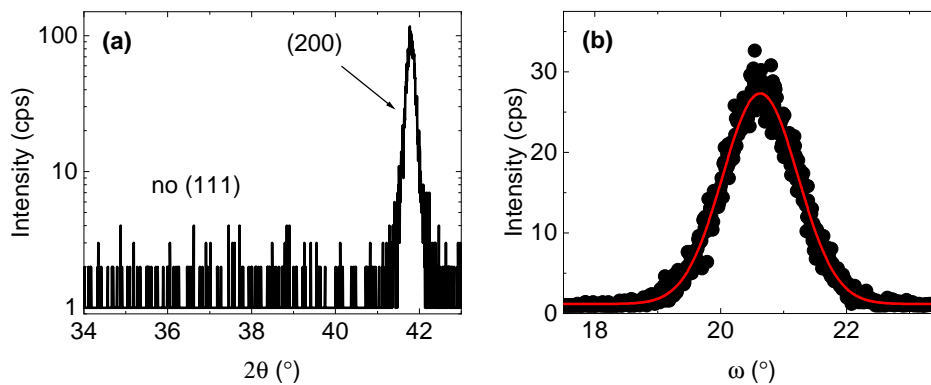


Fig. F1. – (a) $2\theta - \omega$ x-ray diffraction scan of the NbTiN film grown on HF-dipped (001)-oriented Si. We observe a peak originating from a preferential (200) orientation of cubic NbTiN but no evidence for a preferred (111) orientation. (b) Rocking curve of the (200)-reflection. The red line indicates a gaussian fit to the raw data. We extract a full-width at half maximum (FWHM) of $\text{FWHM} = (1.19 \pm 0.01)^\circ$.

shows the preferred cubic NbTiN growth in the (200) orientation on the Si (001) substrate. In Fig. F1(b), we fit the extracted rocking curve of the (200)-reflection of NbTiN to a gaussian fit and extract a full-width at half maximum (FWHM) of $\text{FWHM} = (1.19 \pm 0.01)^\circ$, which indicates a textured growth in agreement to literature (see Refs. [409, 518]).

As the (200)-reflection peak could only be detected for a NbTiN film grown on the BOE treated Si-substrate, we infer that the removal of the native SiO_2 -layer promotes the textured growth of cubic NbTiN.

F2 Quality factors of our NbTiN resonators

We here list the individual quality factors of the investigated resonators, which were used as a basis for the statistical mean values and standard deviations for the individual samples listed in Tab. 6.2. Resonators that have been excluded from the statistical evaluation are marked with an asterisk *.

- Nb₇₀Ti₃₀N on thermally oxidized Si:

Resonator	f_r (GHz)	Q ($\times 10^3$)	Q_{int} ($\times 10^3$)	Q_{ext} ($\times 10^3$)
R1	5.256	15.0 \pm 0.1	26.2 \pm 0.1	35.4 \pm 0.1
R2	5.398	8.0 \pm 0.1	9.4 \pm 0.1	54.9 \pm 1.0
R3	5.525	6.7 \pm 0.4	10.0 \pm 0.4	19.8 \pm 4.2
R4	5.689	6.1 \pm 0.5	7.7 \pm 0.6	29.4 \pm 1.4
R5	5.769	10.4 \pm 0.1	12.9 \pm 0.1	54.3 \pm 0.1

Tab. F1. – Extracted fitting parameters for resonance frequency f_r , quality factor Q , internal quality factor Q_{int} and external quality factor Q_{ext} for the on chip resonators of the chip, where NbTiN was grown on thermally oxidized Si. Measurements are performed at $T = 2.2$ K and at a microwave power corresponding to $\simeq 10^7$ photons on average in the resonator.

- Nb₇₀Ti₃₀N on thermally oxidized Si (PTB):

Resonator	f_r (GHz)	Q ($\times 10^3$)	Q_{int} ($\times 10^3$)	Q_{ext} ($\times 10^3$)
R1	4.485	16.5 \pm 0.1	29.7 \pm 0.2	37.4 \pm 0.1
R2	4.584	8.5 \pm 0.1	15.8 \pm 0.1	18.4 \pm 0.1
R3	4.697	13.2 \pm 0.8	16.6 \pm 0.8	66.0 \pm 2.8
R4	4.793	10.2 \pm 0.1	33.1 \pm 0.3	14.7 \pm 0.1
R5	4.870	10.0 \pm 0.1	11.3 \pm 0.2	89.4 \pm 0.4

Tab. F2. – Extracted fitting parameters for resonance frequency f_r , quality factor Q , internal quality factor Q_{int} and external quality factor Q_{ext} for the on chip resonators of the chip, where NbTiN was grown on thermalized Si at the PTB. Measurements are performed at $T = 2.2$ K and at a microwave power corresponding to $\simeq 10^7$ photons on average in the resonator.

- Nb₇₀Ti₃₀N on pristine Si:

Resonator	f_r (GHz)	Q ($\times 10^3$)	Q_{int} ($\times 10^3$)	Q_{ext} ($\times 10^3$)
R1	4.674	19.8 \pm 0.4	196.3 \pm 23.2	22.0 \pm 0.1
R2	4.803	48.9 \pm 1.5	262.5 \pm 26.2	60.1 \pm 0.4
R3	4.928	26.7 \pm 2.5	373.8 \pm 27.6	28.8 \pm 0.8
R4	5.034	9.3 \pm 0.2	123.8 \pm 15.2	10.1 \pm 0.1
R5	5.133	37.7 \pm 0.6	84.9 \pm 2.9	67.9 \pm 0.5

Tab. F3. – Extracted fitting parameters for resonance frequency f_r , quality factor Q , internal quality factor Q_{int} and external quality factor Q_{ext} for the on chip resonators of the chip, where NbTiN was grown on pristine Si. Measurements are performed at $T = 2.2$ K and at a microwave power corresponding to $\simeq 10^7$ photons on average in the resonator.

- Nb₇₀Ti₃₀N on Si + HF dip:

Resonator	f_r (GHz)	Q ($\times 10^3$)	Q_{int} ($\times 10^3$)	Q_{ext} ($\times 10^3$)
R1	4.672	84.7 \pm 1.4	215.2 \pm 9.0	139.7 \pm 0.1
R2	4.806	61.0 \pm 0.1	152.2 \pm 5.3	101.9 \pm 0.1
R3	4.924	84.3 \pm 0.6	207.8 \pm 3.8	141.9 \pm 0.1
R4	5.026	69.4 \pm 2.3	161.7 \pm 12.0	121.5 \pm 0.1
R5*	5.133	17.9 \pm 0.1	50.6 \pm 0.1	27.9 \pm 0.1

Tab. F4. – Extracted fitting parameters for resonance frequency f_r , quality factor Q , internal quality factor Q_{int} and external quality factor Q_{ext} for the on chip resonators of the chip, where NbTiN was grown on HF-treated Si. Measurements are performed at $T = 2.2$ K and at a microwave power corresponding to $\simeq 10^7$ photons on average in the resonator.

We attribute the unusually bad performance of resonator R5 for the sample, where NbTiN was grown on HF-treated Si to a small scratch on the meander structure of the resonator.

F3 Participation ratios and loss tangents extracted from simulation

The numerically calculated participation ratios of the four dielectric regions for our resonator layout are listed in Tab.F5. The total loss induced by TLS, $F \tan \delta_{\text{TLS}}^0 \approx 0.5 \cdot 10^{-6}$, is the sum of the listed $p_i \tan(\delta_i)$.

	metal-air	metal-substrate	substrate-air	substrate
p_i	3.4E-6	2.4E-4	1.6E-4	0.89
$\tan(\delta_i)$	3.3E-3	2.7E-4	1.2E-3	2.6E-7
$p_i \tan(\delta_i)$	1.1E-8	6.5E-8	2E-7	2.3E-7
d_i (nm)	2	2	2	2
ϵ_i / ϵ_0	10	11.4	11.4	11.9

Tab. F5. – Numerically calculated participation ratios p_i , assumed loss tangents $\tan(\delta_i)$, layer thicknesses d_i and dielectric constants ϵ_i / ϵ_0 of the four dielectric regions, following Ref. [401].

Appendix G: Magnetoelastic coupling in CoFe on Al₂O₃ substrates

In this section, we present additional MEC experiments for CoFe grown on Al₂O₃ BAW substrates as function of frequency, present simulation results for the MEC and discuss the frequency splitting Δf of the MEC features for other substrate materials as function of frequency.

G1 Determination of the parameters describing the magnetization dynamics in CoFe

To determine the magnetization dynamics parameters of the CoFe/Al₂O₃ sample investigated at cryogenic temperatures in Sec. 7.1, we perform broadband ferromagnetic resonance (FMR) experiments in the oop-geometry. We fit the raw data using Eq. (2.20) and extract the uncoupled FMR resonance frequency and linewidth in a frequency spacing in the GHz range, where the contributions from the elastic resonances average out. Fig. G1(a) and (b) show the raw data for the resonance field $H_{\text{res}}(f)$ and linewidth $\Delta H(f)$ of the Al₂O₃/CoFe sample at $T = 5$ K. To characterize the effective magnetization M_{eff} and the g -factor of the

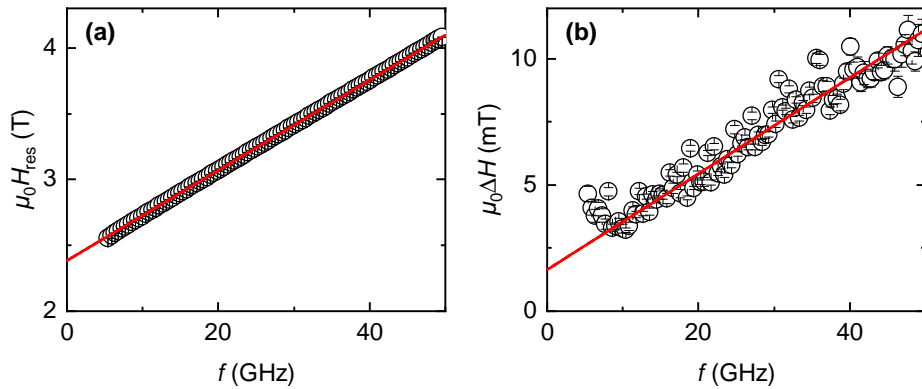


Fig. G1. – (a) Resonance field $\mu_0 H_{\text{res}}(f)$ of the Al₂O₃/CoFe sample at $T = 5$ K plotted versus frequency. The line shows a fit to Eq. (2.24). (b) Resonance linewidth $\mu_0 \Delta H(f)$ of the Al₂O₃/CoFe sample at $T = 5$ K together with a fit to Eq. (2.28) (red line).

magnetic system g , the frequency dependence of the resonance field $H_{\text{res}}(f)$ is fitted using Eq. (2.24). We extract a g -factor of $g = 2.079 \pm 0.001$ and an effective magnetization $\mu_0 M_{\text{eff}} = (2.381 \pm 0.004)$ T in agreement with the expected values for CoFe of this material composition (Co₂₅Fe₇₅) [135]. The frequency dependency of the FMR linewidth $\mu_0 \Delta H(f)$ is fitted with the linear model following Eq. (2.28)

to extract the Gilbert damping parameter α and the inhomogeneous broadening $\mu_0 H_{\text{inh}}$. We extract an inhomogeneous line broadening of $\mu_0 H_{\text{inh}} = (1.6 \pm 0.2)$ mT and a Gilbert damping $\alpha = (2.8 \pm 0.1) \cdot 10^{-3}$ in agreement with the values reported in Ref. [135].

G1.1 Magnetization dynamics parameters of the CoFe layer as function of temperature

In order to demonstrate the temperature-robust performance of the magnetization dynamics parameters of our CoFe thin films, we plot in Fig. G2 their temperature dependence for the CoFe thin film grown on a both sides polished c-axis Al_2O_3 -substrate investigated in Sec. 7. For the g -factor in Fig. G2(a), we observe no apparent temperature-dependence, while the effective magnetization M_{eff} in Fig. G2(b) decreases for increasing temperature due to the thermal excitation of magnons [86]. The Gilbert damping parameter α in Fig. G2(c) is roughly constant. However, the inhomogeneous linewidth H_{inh} in Fig. G2(d) increases for rising T , which we attribute to the phonon pumping [112].

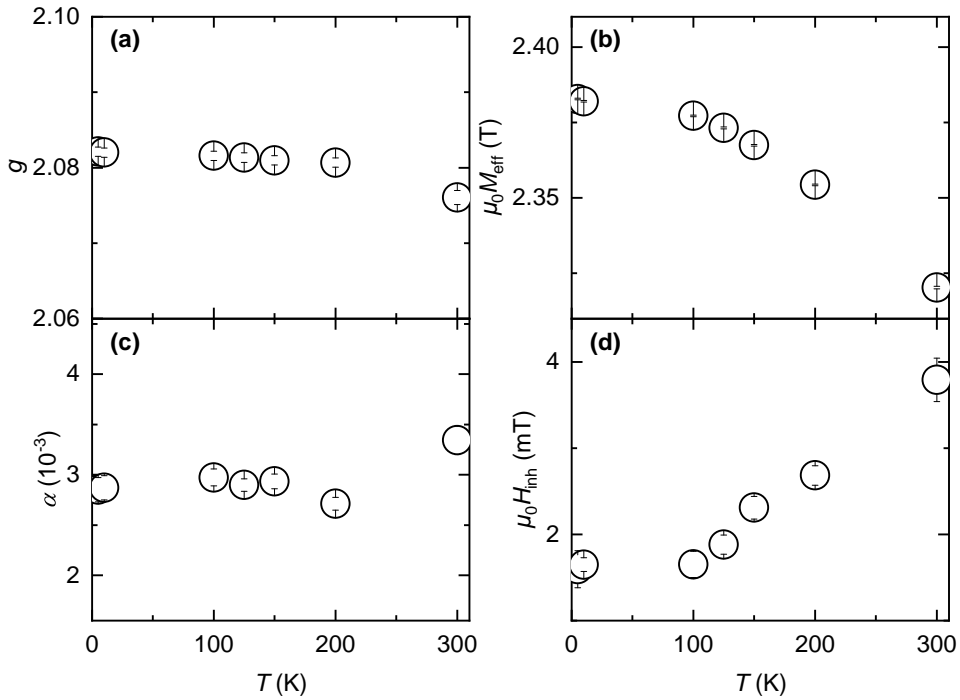


Fig. G2. – Temperature dependence of the magnetization dynamics parameters of the CoFe on Al_2O_3 hybrid sample. (a) The g -factor is constant as function of T . (b) The effective magnetization M_{eff} decreases with increasing T due to the thermal excitation of magnons. (c) The Gilbert damping α is roughly constant as function of temperatures. (d) The inhomogeneous linewidth broadening increases, which we attribute to the enhanced phonon pumping contribution to ΔH .

G2 Analytical expressions for the velocity splitting of the transverse modes in various crystal systems

In the following, we derive analytical expressions for the velocity splitting of the transverse elastic modes in both hexagonal and cubic BAW resonator substrates. We reshape the stress tensor in terms of displacement u using

$$\varepsilon_{i,j} = \frac{1}{2} \left(\frac{\partial u_i}{\partial x_j} + \frac{\partial u_j}{\partial x_i} \right), \quad (\text{G.1})$$

where coordinates are denoted as $\{x_x, x_y, x_z\}$. We rotate the strain tensor taking into account the deflection of c -axis by introducing an auxiliary cartesian coordinate system $\{x', y', z'\}$. The transformation of the strain tensor into $x'y'z'$ -system is given by

$$\varepsilon_{i',j'} = \sum_{k,j} \left(R^T \right)_{i',j} \varepsilon_{j,k} R_{k,j'}, \quad (\text{G.2})$$

where the Euler matrix reads

$$R = \begin{pmatrix} \cos \theta & 0 & \sin \theta \\ 0 & 1 & 0 \\ -\sin \theta & 0 & \cos \theta \end{pmatrix}. \quad (\text{G.3})$$

This matrix describes the rotation of the c -axis away from the z -axis by an azimuthal angle θ . In the following we omit prime superscripts in notations, since we do not discuss the $\varepsilon_{i,j}$ in the following equations. If we write the force density in the form

$$f_i = \sum_j \frac{\partial \sigma_{i,j}}{\partial x_j}, \quad (\text{G.4})$$

where the $\sigma_{i,j}$ represent the components of the stress tensor, then Hooke's equation of motion reads

$$\rho \frac{\partial^2 u_i}{\partial t^2} + \Xi \frac{\partial u_i}{\partial t} = f_i, \quad (\text{G.5})$$

where ρ is the mass density, and $\Xi = \eta_a \rho$ represents a measure of the elastic damping. As solutions for these differential equations, we use the plane wave ansatz of the form

$$u_{x,y,z} = u_{x,y,z} e^{i(\omega t - \mathbf{k} \cdot \mathbf{r})}. \quad (\text{G.6})$$

As we focus on standing waves along the thickness of the substrate, hence the wave vector has only one component $k = k_z = n\pi/L$. Thus, the Hooke's equation yields a dispersion equation, which can be written in matrix form

$$\det \begin{pmatrix} a_{11} & a_{12} & a_{13} \\ a_{21} & a_{22} & a_{23} \\ a_{31} & a_{32} & a_{33} \end{pmatrix} = 0, \quad (\text{G.7})$$

The remaining task is now to insert the respective stress tensor components for the individual crystal symmetries into Eq. (G.7) to derive the phononic dispersion relations $\omega(k, \theta)$ of the individual modes. The group velocities of the acoustic waves can then be calculated as

$$v_g(\theta) = \frac{\partial \omega}{\partial k}. \quad (\text{G.8})$$

Finally, we can subtract the results for the fast and slow transverse elastic modes v_{ft} and v_{st} to obtain an expression for the velocity splitting Δv_t as function of the miscut angle θ .

G2.1 Substrate with hexagonal crystallographic order

For the hexagonal Al_2O_3 , the stress tensor components can be written as [519]

$$\begin{aligned} \sigma_{x,x} &= c_{11}\varepsilon_{x,x} + c_{12}\varepsilon_{y,y} + 2c_{14}\varepsilon_{y,z} + c_{13}\varepsilon_{z,z} \\ \sigma_{y,y} &= c_{12}\varepsilon_{x,x} + c_{11}\varepsilon_{y,y} - 2c_{14}\varepsilon_{y,z} + c_{13}\varepsilon_{z,z} \\ \sigma_{z,z} &= c_{13}\varepsilon_{x,x} + c_{13}\varepsilon_{y,y} + c_{33}\varepsilon_{z,z} \\ \sigma_{y,z} &= \sigma_{z,y} = c_{14}\varepsilon_{x,x} - c_{14}\varepsilon_{y,y} + 2c_{44}\varepsilon_{y,z} \\ \sigma_{x,z} &= \sigma_{z,x} = 2c_{14}\varepsilon_{x,y} + 2c_{44}\varepsilon_{x,z} \\ \sigma_{x,y} &= \sigma_{y,x} = (c_{11} - c_{12})\varepsilon_{x,y} + 2c_{14}\varepsilon_{x,z}, \end{aligned} \quad (\text{G.9})$$

where the c_{pq} represent the components of the compliance tensor in Voigt notation. When inserting these $\sigma_{i,j}$ in Eq. (G.7), we obtain

$$\begin{aligned} a_{11} &= c_{44}k^2 \cos(2\theta) + i\omega\Xi - \rho\omega^2, \\ a_{12} &= -c_{14}k^2 \sin(\theta), \\ a_{13} &= -c_{44}k^2 \sin(2\theta), \\ a_{21} &= -c_{14}k^2 \sin(\theta) \cos(\theta), \\ a_{22} &= c_{44}k^2 \cos(\theta) + i\Xi\omega - \rho\omega^2, \\ a_{23} &= c_{14}k^2 \sin^2(\theta), \\ a_{31} &= (c_{13} - c_{33})k^2 \sin(\theta) \cos(\theta), \\ a_{32} &= 0, \\ a_{33} &= -k^2 (c_{13} \sin^2(\theta) + c_{33} \cos^2(\theta)) + \rho\omega^2 - i\Xi\omega. \end{aligned} \quad (\text{G.10})$$

The explicit form of the determinant of Eq. (G.7) is not elucidative, we therefore turn to numerical results for the exact solution. We find that the velocities

of two acoustic waves are almost the same $v_g \approx 6.17$ km/s for the parameters from Ref. [478] and the difference between them depends on the deflection angle θ away from the c -axis as shown in Fig. G3(a). For a miscut angle of $\theta = 0.017^\circ$, we obtain $\Delta v \approx 0.5$ m/s in agreement with the calculations in Sec. 7.1 using the numerical Christoffel equation solver tool from Ref. [477].

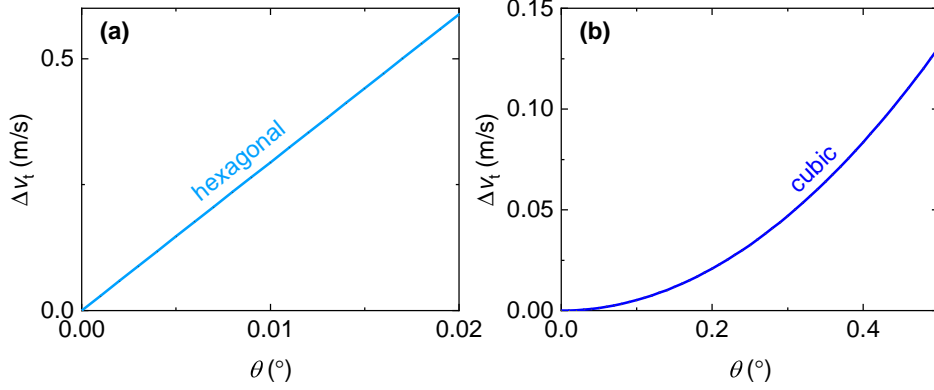


Fig. G3. – (a) The difference between velocities of two acoustic waves calculated for hexagonal Al_2O_3 . The calculation parameters are $k = 2\pi/L$ rad \cdot m $^{-1}$, $L = 510$ mm, $\rho = 3970$ kg/m 3 , $c_{11} = 5.00073 \times 10^{11}$ Pa, $c_{33} = 5.02385 \times 10^{11}$ Pa, $c_{44} = 1.51017 \times 10^{11}$ Pa, $c_{12} = 1.61672 \times 10^{11}$ Pa, $c_{13} = 1.11368 \times 10^{11}$ Pa, $c_{14} = -2.32604 \times 10^{10}$ Pa and $\eta_a/(2\pi) = 0.23$ MHz, which are given in Ref. [478]. (b) The difference between velocities of two acoustic waves calculated for cubic Si. The calculation parameters are $k = 2\pi/L$ rad \cdot m $^{-1}$, $L = 0.510$ m, $\rho = 3970$ kg/m 3 , $c_{11} = 161.8$ GPa, $c_{12} = 64$ GPa, $c_{44} = 76.1$ GPa and $\eta_a/(2\pi) = 0.23$ MHz, which are extracted from Ref. [479].

G2.2 Cubic crystallographic order

We employ the same formalism to derive the velocity difference Δv_t of acoustic waves in an elastic medium with cubic symmetry. In a cubic system, the stress tensor elements are given by [519]

$$\begin{aligned}
 \sigma_{x,x} &= c_{11}\varepsilon_{x,x} + c_{12}\varepsilon_{y,y} + c_{12}\varepsilon_{z,z}, \\
 \sigma_{y,y} &= c_{12}\varepsilon_{x,x} + c_{11}\varepsilon_{y,y} + c_{12}\varepsilon_{z,z}, \\
 \sigma_{z,z} &= c_{12}\varepsilon_{x,x} + c_{12}\varepsilon_{y,y} + c_{11}\varepsilon_{z,z}, \\
 \sigma_{y,z} &= \sigma_{z,y} = 2c_{44}\varepsilon_{y,z}, \\
 \sigma_{x,z} &= \sigma_{z,x} = 2c_{44}\varepsilon_{x,z}, \\
 \sigma_{x,y} &= \sigma_{y,x} = 2c_{44}\varepsilon_{x,y}.
 \end{aligned} \tag{G.11}$$

Performing the same procedure as for the hexagonal crystal, the dispersion equation is given by

$$\det \begin{pmatrix} a_{11} & a_{12} & a_{13} \\ a_{21} & a_{22} & a_{23} \\ a_{31} & a_{32} & a_{33} \end{pmatrix} = 0, \tag{G.12}$$

where

$$\begin{aligned}
a_{11} &= c_{44}k^2 \cos(2\theta) - \rho\omega^2 + i\Xi\omega, \\
a_{12} &= 0, \\
a_{13} &= -2c_{44}k^2 \sin(\theta) \cos(\theta), \\
a_{21} &= 0, \\
a_{22} &= c_{44}k^2 \cos(\theta) - \rho\omega^2 + i\Xi\omega, \\
a_{23} &= 0, \\
a_{31} &= (c_{11} - c_{12})k^2 \sin(\theta) \cos(\theta), \\
a_{32} &= 0, \\
a_{33} &= c_{12}k^2 \sin^2(\theta) + c_{11}k^2 \cos^2(\theta) - \rho\omega^2 + i\Xi\omega.
\end{aligned} \tag{G.13}$$

The calculated Δv_t obtained by solving this equation is plotted in Fig. G3(b). Again, we achieve a good likeness to the plot in Fig. 7.1(f).

G3 Temperature-dependence of the elastic damping by the Landau-Rumer-mechanism

In the Landau-Rumer damping mechanism of transverse phonons, the attenuation coefficient $\nu(T)$ of the transverse elastic waves is given by [471]

$$\nu(T) = 60\gamma_G^2 \frac{2\pi k_B}{Mv_t^3 \Theta_D^3} \cdot f \cdot T^4, \tag{G.14}$$

where Θ_D is the Debye temperature and γ_G is the Grüneisen parameter, whereas M is the average atomic mass. Using the attenuation coefficient $\nu(T)$ in combination with the characteristic decay length $\delta = 2\pi v_t / \eta_a$ [77], we can determine the elastic relaxation rate by using

$$\frac{|u(\delta)|}{|u(0)|} = \exp(-\nu\delta) = \exp(-1). \tag{G.15}$$

Here $|u(z')|$ is the magnitude of acoustic modes after propagating distance z' through the Al_2O_3 substrate in the z -direction. From Eq. (G.15), we obtain the relation $\eta_a = \nu v_t = \beta_a T^4$. By inserting $\gamma_G = 2$, $(Mv_t^2/k_B) = 135000 \text{ K}$ and $\Theta_D = 1000 \text{ K}$ from Ref. [471] and $v_t = 6.17 \text{ km/s}$ in Eq. (G.14), we obtain $\beta_a / (2\pi) \approx 3.2 \cdot 10^{-2} \text{ Hz/K}^4$, which roughly corresponds with the obtained fitting values for β_a in Sec. 7.2.

List of Publications

First author publications

- M. Müller, L. Liensberger, L. Flacke, H. Huebl, A. Kamra, W. Belzig, R. Gross, M. Weiler, M. Althammer, *Temperature-Dependent Spin Transport and Current-Induced Torques in Superconductor-Ferromagnet Heterostructures*, Physical Review Letters **126**, 087201 (2021).
- M. Müller, R. Hoepfl, L. Liensberger, S. Geprägs, H. Huebl, M. Weiler, R. Gross, M. Althammer, *Growth optimization of TaN for superconducting spintronics*, Materials for Quantum Technology **1**, 045001 (2021).
- M. Müller, T. Luschmann, A. Faltermeier, S. Weichselbaumer, L. Koch, G.B.P. Huber, H.W. Schumacher, N. Ubbelohde, D. Reifert, T. Scheller, F. Deppe, A. Marx, S. Filipp, M. Althammer, R. Gross, H. Huebl, *Magnetic field robust high quality factor NbTiN superconducting microwave resonators*, Materials for Quantum Technology **2**, 015002 (2022).
- M. Müller, M. Scheufele, J. Gückelhorn, L. Flacke, M. Weiler, H. Huebl, S. Gepraegs, R. Gross, M. Althammer, *Reduced effective magnetization and damping by slowly relaxing impurities in strained γ -Fe₂O₃ thin films*, Journal of Applied Physics **132**, 233905 (2022).
- M. Müller, J. Weber, F. Engelhardt, V.A.S.V. Bittencourt, T. Luschmann, M. Cherkasskii, S.T.B. Goennenwein, S.V. Kusminskiy, S. Gepraegs, R. Gross, M. Althammer, H. Huebl, *Chiral phonons and phononic birefringence in ferromagnetic metal - bulk acoustic resonator hybrids*, arxiv 2303.08429 (2023).

Co-author publications

- T.S. Suraj, M. Müller, S. Gelder, S. Geprägs, M. Opel, M. Weiler, K. Sethupathi, H. Huebl, R. Gross, M.S. Ramachandra Rao, M. Althammer, *Effect of interfacial oxidation layer in spin pumping experiments on $Ni_{80}Fe_{20}/SrIrO_3$ heterostructures*, Journal of Applied Physics **128**, 083903 (2020).
- G. Terrasanta, M. Müller, T. Sommer, S. Geprägs, R. Gross, M. Althammer, M. Poot, *Growth of aluminum nitride on a silicon nitride substrate for hybrid photonic circuits*, Materials for Quantum Technology **1**, 021002 (2021).
- J. Gückelhorn, T. Wimmer, M. Müller, S. Geprägs, H. Huebl, R. Gross, M. Althammer, *Magnon transport in $Y_3Fe_5O_{12}/Pt$ nanostructures with reduced effective magnetization*, Physical Review B **104**, L180410 (2021).
- L. Flacke, V. Ahrens, S. Mendisch, L. Körber, T. Böttcher, E. Meidinger, M. Yaqoob, M. Müller, L. Liensberger, A. Kákay, M. Becherer, P. Pirro, M. Althammer, S. Geprägs, H. Huebl, R. Gross, M. Weiler, *Robust formation of nanoscale magnetic skyrmions in easy-plane anisotropy thin film multilayers with low damping*, Physical Review B **104**, L100417 (2021).
- G. Terrasanta, T. Sommer, M. Müller, M. Althammer, R. Gross, M. Poot, *Aluminum nitride integration on silicon nitride photonic circuits: a hybrid approach towards on-chip nonlinear optics*, Optics Express **30**, 8537 (2022).
- R. Flaschmann, C. Schmid, L. Zugliani, S. Strohauer, F. Wietschorke, S. Grotowski, B. Jonas, M. Müller, M. Althammer, R. Gross, J.J. Finley, K. Müller, *Optimizing the growth conditions of Al mirrors for superconducting nanowire single-photon detectors*, Materials for Quantum Technology **3**, 035002 (2023).
- S. Strohauer, F. Wietschorke, L. Zugliani, R. Flaschmann, C. Schmid, S. Grotowski, M. Müller, B. Jonas, M. Althammer, R. Gross, K. Müller, J.J. Finley, *Site-Selective Enhancement of Superconducting Nanowire Single-Photon Detectors via Local Helium Ion Irradiation*, Advanced Quantum Technologies **6**, 2300139 (2023)

Bibliography

- [1] M.M. Waldrop, *The chips are down for Moore's law*, Nature **530**, 144 (2016).
- [2] J. Nathawat, K.K.H. Smithe, C.D. English, S. Yin, R. Dixit, M. Randle, N. Arabchigavkani, B. Barut, K. He, E. Pop, J.P. Bird, *Transient hot-carrier dynamics and intrinsic velocity saturation in monolayer MoS₂*, Physical Review Materials **4**, 014002 (2020).
- [3] S. Das, A. Sebastian, E. Pop, C.J. McClellan, A.D. Franklin, T. Grasser, T. Knobloch, Y. Illarionov, A.V. Penumatcha, J. Appenzeller, Z. Chen, W. Zhu, I. Asselberghs, L.J. Li, U.E. Avci, N. Bhat, T.D. Anthopoulos, R. Singh, *Transistors based on two-dimensional materials for future integrated circuits*, Nature Electronics **4**, 786 (2021).
- [4] W. Lu, P. Xie, C.M. Lieber, *Nanowire Transistor Performance Limits and Applications*, IEEE Transactions on Electron Devices **55**, 2859 (2008).
- [5] J.P. Colinge, C.W. Lee, A. Afzalian, N.D. Akhavan, R. Yan, I. Ferain, P. Razavi, B. O'Neill, A. Blake, M. White, A.M. Kelleher, B. McCarthy, R. Murphy, *Nanowire transistors without junctions*, Nature Nanotechnology **5**, 225 (2010).
- [6] A.M. Ionescu, H. Riel, *Tunnel field-effect transistors as energy-efficient electronic switches*, Nature **479**, 329 (2011).
- [7] K.R.N. Karthik, C.K. Pandey, *A Review of Tunnel Field-Effect Transistors for Improved ON-State Behaviour*, Silicon **15**, 1 (2023).
- [8] K. Amsalu, S. Palani, *A review on photonics and its applications*, Materials Today: Proceedings **33**, 3372 (2020).
- [9] I. Amiri, S. Azzuhri, M. Jalil, H. Hairi, J. Ali, M. Bunruangses, P. Yupapin, *Introduction to Photonics: Principles and the Most Recent Applications of Microstructures*, Micromachines **9**, 452 (2018).
- [10] N. Jiang, X. Zhuo, J. Wang, *Active Plasmonics: Principles, Structures, and Applications*, Chemical Reviews **118**, 3054 (2018).
- [11] T.W. Odom, G.C. Schatz, *Introduction to Plasmonics*, Chemical Reviews **111**, 3667 (2011).

- [12] T. Liew, I. Shelykh, G. Malpuech, *Polaritonic devices*, Physica E: Low-dimensional Systems and Nanostructures **43**, 1543 (2011).
- [13] W. Binasch, G. and Grünberg, P. and Saurenbach, F. and Zinn, *Enhanced magnetoresistance in layered magnetic structures with antiferromagnetic interlayer exchange*, Physical Review B **39**, 4828 (1989).
- [14] M.N. Baibich, J.M. Broto, A. Fert, F.N. Van Dau, F. Petroff, P. Eitenne, G. Creuzet, A. Friederich, J. Chazelas, *[Nanoscale Combination] Giant magnetoresistance of (001)Fe/(001)Cr magnetic superlattices*, Physical Review Letters **61**, 2472 (1988).
- [15] A. Fert, *Nobel Lecture: Origin, development, and future of spintronics*, Reviews of Modern Physics **80**, 1517 (2008).
- [16] S. Bhatti, R. Sbiaa, A. Hirohata, H. Ohno, S. Fukami, S. Piramanayagam, *Spintronics based random access memory: a review*, Materials Today **20**, 530 (2017).
- [17] H.S.P. Wong, S. Salahuddin, *Memory leads the way to better computing*, Nature Nanotechnology **10**, 191 (2015).
- [18] J. Åkerman, *Toward a Universal Memory*, Science **308**, 508 (2005).
- [19] J. von Neumann, *First draft of a report on the EDVAC*, IEEE Annals of the History of Computing **15**, 27 (1993).
- [20] Q.F. Ou, B.S. Xiong, L. Yu, J. Wen, L. Wang, Y. Tong, *In-Memory Logic Operations and Neuromorphic Computing in Non-Volatile Random Access Memory*, Materials **13**, 3532 (2020).
- [21] A. Hirohata, K. Yamada, Y. Nakatani, I.L. Prejbeanu, B. Diény, P. Pirro, B. Hillebrands, *Review on spintronics: Principles and device applications*, Journal of Magnetism and Magnetic Materials **509**, 166711 (2020).
- [22] S. Parkin, S.H. Yang, *Memory on the racetrack*, Nature Nanotechnology **10**, 195 (2015).
- [23] A. Hirohata, K. Takanashi, *Future perspectives for spintronic devices*, Journal of Physics D: Applied Physics **47**, 193001 (2014).
- [24] S.S.P. Parkin, M. Hayashi, L. Thomas, *Magnetic Domain-Wall Racetrack Memory*, Science **320**, 190 (2008).
- [25] A.V. Chumak, V.I. Vasyuchka, A.A. Serga, B. Hillebrands, *Magnon spintronics*, Nature Physics **11**, 453 (2015).
- [26] A.V. Chumak, A.A. Serga, B. Hillebrands, *Magnonic crystals for data processing*, Journal of Physics D: Applied Physics **50**, 244001 (2017).

- [27] A.V. Chumak, P. Kabos, M. Wu, C. Abert, C. Adelman, A.O. Adeyeye, J. Akerman, F.G. Aliev, A. Anane, A. Awad, C.H. Back, A. Barman, G.E.W. Bauer, M. Becherer, E.N. Beginin, V.A.S.V. Bittencourt, Y.M. Blanter, P. Bortolotti, I. Boventer, D.A. Bozhko, S.A. Bunyayev, J.J. Carmiggelt, R.R. Cheenikundil, F. Ciubotaru, S. Cotofana, G. Csaba, O.V. Dobrovolskiy, C. Dubs, M. Elyasi, K.G. Fripp, H. Fulara, I.A. Golovchanskiy, C. Gonzalez-Ballester, P. Graczyk, D. Grundler, P. Gruszecki, G. Gubbiotti, K. Guslienko, A. Haldar, S. Hamdioui, R. Hertel, B. Hillebrands, T. Hioki, A. Houshang, C.M. Hu, H. Huebl, M. Huth, E. Iacocca, M.B. Jungfleisch, G.N. Kakazei, A. Khitun, R. Khymyn, T. Kikkawa, M. Klaui, O. Klein, J.W. Klos, S. Knauer, S. Koraltan, M. Kostylev, M. Krawczyk, I.N. Krivorotov, V.V. Kruglyak, D. Lachance-Quirion, S. Ladak, R. Lebrun, Y. Li, M. Lindner, R. Macedo, S. Mayr, G.A. Melkov, S. Mieszczak, Y. Nakamura, H.T. Nembach, A.A. Nikitin, S.A. Nikitov, V. Novosad, J.A. Otalora, Y. Otani, A. Papp, B. Pigeau, P. Pirro, W. Porod, F. Porrati, H. Qin, B. Rana, T. Reimann, F. Riente, O. Romero-Isart, A. Ross, A.V. Sadovnikov, A.R. Safin, E. Saitoh, G. Schmidt, H. Schultheiss, K. Schultheiss, A.A. Serga, S. Sharma, J.M. Shaw, D. Suess, O. Surzhenko, K. Szulc, T. Taniguchi, M. Urbanek, K. Usami, A.B. Ustinov, T. van der Sar, S. van Dijken, V.I. Vasyuchka, R. Verba, S.V. Kusminskiy, Q. Wang, M. Weides, M. Weiler, S. Wintz, S.P. Wolski, X. Zhang, *Advances in Magnetism Roadmap on Spin-Wave Computing*, IEEE Transactions on Magnetism **58**, 0800172 (2022).
- [28] A. Mahmoud, F. Ciubotaru, F. Vanderveken, A.V. Chumak, S. Hamdioui, C. Adelman, S. Cotofana, *Introduction to spin wave computing*, Journal of Applied Physics **128**, 161101 (2020).
- [29] K. Zakeri, *Terahertz magnonics: Feasibility of using terahertz magnons for information processing*, Physica C: Superconductivity and its Applications **549**, 164 (2018).
- [30] L. Liensberger, *Magnon hybrid dynamics*, PhD Thesis (2021).
- [31] A.V. Chumak, A.A. Serga, B. Hillebrands, *Magnon transistor for all-magnon data processing*, Nature Communications **5**, 4700 (2014).
- [32] A. Khitun, M. Bao, K.L. Wang, *Magnonic logic circuits*, Journal of Physics D: Applied Physics **43**, 264005 (2010).
- [33] N. Sato, K. Sekiguchi, Y. Nozaki, *Electrical Demonstration of Spin-Wave Logic Operation*, Applied Physics Express **6**, 063001 (2013).
- [34] F. Freimuth, S. Blügel, Y. Mokrousov, *Direct and inverse spin-orbit torques*, Physical Review B **92**, 064415 (2015).

- [35] J. Sinova, S.O. Valenzuela, J. Wunderlich, C.H. Back, T. Jungwirth, *Spin Hall effects*, *Reviews of Modern Physics* **87**, 1213 (2015).
- [36] P.M. Haney, H.W. Lee, K.J. Lee, A. Manchon, M.D. Stiles, *Current induced torques and interfacial spin-orbit coupling: Semiclassical modeling*, *Physical Review B* **87**, 174411 (2013).
- [37] Y.A. Bychkov, É.I. Rashba, *Properties of a 2D electron gas with a lifted spectral degeneracy*, *JETP Letters* **39**, 78 (1984).
- [38] V. Edelstein, *Spin polarization of conduction electrons induced by electric current in two-dimensional asymmetric electron systems*, *Solid State Communications* **73**, 233 (1990).
- [39] I.M. Miron, K. Garello, G. Gaudin, P.J. Zermatten, M.V. Costache, S. Auffret, S. Bandiera, B. Rodmacq, A. Schuhl, P. Gambardella, *Perpendicular switching of a single ferromagnetic layer induced by in-plane current injection*, *Nature* **476**, 189 (2011).
- [40] A.J. Berger, E.R.J. Edwards, H.T. Nembach, O. Karis, M. Weiler, T.J. Silva, *Determination of the spin Hall effect and the spin diffusion length of Pt from self-consistent fitting of damping enhancement and inverse spin-orbit torque measurements*, *Physical Review B* **98**, 024402 (2018).
- [41] K. Garello, I.M. Miron, C.O. Avci, F. Freimuth, Y. Mokrousov, S. Blügel, S. Auffret, O. Boulle, G. Gaudin, P. Gambardella, *Symmetry and magnitude of spin-orbit torques in ferromagnetic heterostructures*, *Nature Nanotechnology* **8**, 587 (2013).
- [42] A.J. Berger, E.R.J. Edwards, H.T. Nembach, A.D. Karenowska, M. Weiler, T.J. Silva, *Inductive detection of fieldlike and dampinglike ac inverse spin-orbit torques in ferromagnet/normal-metal bilayers*, *Physical Review B* **97**, 94407 (2018).
- [43] A. Hoffmann, *Spin Hall Effects in Metals*, *IEEE Transactions on Magnetics* **49**, 5172 (2013).
- [44] L. Liu, C.F. Pai, Y. Li, H.W. Tseng, D.C. Ralph, R.A. Buhrman, *Spin-Torque Switching with the Giant Spin Hall Effect of Tantalum*, *Science* **336**, 555 (2012).
- [45] A. Manchon, J. Železný, I.M. Miron, T. Jungwirth, J. Sinova, A. Thiaville, K. Garello, P. Gambardella, *Current-induced spin-orbit torques in ferromagnetic and antiferromagnetic systems*, *Reviews of Modern Physics* **91**, 035004 (2019).
- [46] C. Song, R. Zhang, L. Liao, Y. Zhou, X. Zhou, R. Chen, Y. You, X. Chen, F. Pan, *Spin-orbit torques: Materials, mechanisms, performances, and potential applications*, *Progress in Materials Science* **118**, 100761 (2021).

- [47] T. Wakamura, H. Akaike, Y. Omori, Y. Niimi, S. Takahashi, A. Fujimaki, S. Maekawa, Y. Otani, *Quasiparticle-mediated spin Hall effect in a superconductor*, Nature Materials **14**, 675 (2015).
- [48] M. Umeda, Y. Shiomi, T. Kikkawa, T. Niizeki, J. Lustikova, S. Takahashi, E. Saitoh, *Spin-current coherence peak in superconductor/magnet junctions*, Applied Physics Letters **112**, 232601 (2018).
- [49] K.R. Jeon, C. Ciccarelli, A.J. Ferguson, H. Kurebayashi, L.F. Cohen, X. Montiel, M. Eschrig, J.W.A. Robinson, M.G. Blamire, *Enhanced spin pumping into superconductors provides evidence for superconducting pure spin currents*, Nature Materials **17**, 499 (2018).
- [50] K.R. Jeon, J.C. Jeon, X. Zhou, A. Migliorini, J. Yoon, S.S.P. Parkin, *Giant Transition-State Quasiparticle Spin-Hall Effect in an Exchange-Spin-Split Superconductor Detected by Nonlocal Magnon Spin Transport*, ACS Nano **14**, 15874 (2020).
- [51] S. Sharma, B.Z. Rameshti, Y.M. Blanter, G.E.W. Bauer, *Optimal mode matching in cavity optomagnonics*, Physical Review B **99**, 214423 (2019).
- [52] S. Viola Kusminskiy, H.X. Tang, F. Marquardt, *Coupled spin-light dynamics in cavity optomagnonics*, Physical Review A **94**, 033821 (2016).
- [53] J. Graf, S. Sharma, H. Huebl, S.V. Kusminskiy, *Design of an optomagnonic crystal: Towards optimal magnon-photon mode matching at the microscale*, Physical Review Research **3**, 013277 (2021).
- [54] J. Graf, H. Pfeifer, F. Marquardt, S. Viola Kusminskiy, *Cavity optomagnonics with magnetic textures: Coupling a magnetic vortex to light*, Physical Review B **98**, 241406 (2018).
- [55] M. Weiler, L. Dreher, C. Heeg, H. Huebl, R. Gross, M.S. Brandt, S.T.B. Goennenwein, *Elastically Driven Ferromagnetic Resonance in Nickel Thin Films*, Physical Review Letters **106**, 117601 (2011).
- [56] M. Weiler, H. Huebl, F.S. Goerg, F.D. Czeschka, R. Gross, S.T.B. Goennenwein, *Spin Pumping with Coherent Elastic Waves*, Physical Review Letters **108**, 176601 (2012).
- [57] P.G. Gowtham, G.M. Stiehl, D.C. Ralph, R.A. Buhrman, *Thickness-dependent magnetoelasticity and its effects on perpendicular magnetic anisotropy in Ta/CoFeB/MgO thin films*, Physical Review B **93**, 024404 (2016).
- [58] M. Küß, M. Heigl, L. Flacke, A. Hörner, M. Weiler, M. Albrecht, A. Wixforth, *Nonreciprocal Dzyaloshinskii–Moriya Magnetoacoustic Waves*, Physical Review Letters **125**, 217203 (2020).

- [59] M. Küß, M. Heigl, L. Flacke, A. Hefele, A. Hörner, M. Weiler, M. Albrecht, A. Wixforth, *Symmetry of the Magnetoelastic Interaction of Rayleigh and Shear Horizontal Magnetoacoustic Waves in Nickel Thin Films on LiTaO₃*, *Physical Review Applied* **15**, 034046 (2021).
- [60] M. Küß, M. Heigl, L. Flacke, A. Hörner, M. Weiler, A. Wixforth, M. Albrecht, *Nonreciprocal Magnetoacoustic Waves in Dipolar-Coupled Ferromagnetic Bilayers*, *Physical Review Applied* **15**, 034060 (2021).
- [61] T. Kikkawa, K. Shen, B. Flebus, R.A. Duine, K.i. Uchida, Z. Qiu, G.E. Bauer, E. Saitoh, *Magnon Polarons in the Spin Seebeck Effect*, *Physical Review Letters* **117**, 207203 (2016).
- [62] Y. Hashimoto, T.H. Johansen, E. Saitoh, *180°-Phase Shift of Magnetoelastic Waves Observed By Phase-Resolved Spin-Wave Tomography*, *Applied Physics Letters* **112** (2018).
- [63] X. Zhang, A. Galda, X. Han, D. Jin, V.M. Vinokur, *Broadband Nonreciprocity Enabled by Strong Coupling of Magnons and Microwave Photons*, *Physical Review Applied* **13**, 044039 (2020).
- [64] D. Hatanaka, M. Asano, H. Okamoto, Y. Kunihashi, H. Sanada, H. Yamaguchi, *On-Chip Coherent Transduction between Magnons and Acoustic Phonons in Cavity Magnomechanics*, *Physical Review Applied* **17**, 034024 (2022).
- [65] L. Liensberger, F.X. Haslbeck, A. Bauer, H. Berger, R. Gross, H. Huebl, C. Pfliederer, M. Weiler, *Tunable cooperativity in coupled spin-cavity systems*, *Physical Review B* **104**, L100415 (2021).
- [66] C. Lüthi, L. Flacke, A. Aqeel, A. Kamra, R. Gross, C. Back, M. Weiler, *Hybrid magnetization dynamics in Cu₂OSeO₃/NiFe heterostructures*, *Applied Physics Letters* **122**, 012401 (2023).
- [67] M. Müller, M. Scheufele, J. Gückelhorn, L. Flacke, M. Weiler, H. Huebl, S. Gepraegs, R. Gross, M. Althammer, *Reduced effective magnetization and damping by slowly relaxing impurities in strained γ -Fe₂O₃ thin films*, *Journal of Applied Physics* **132**, 233905 (2022).
- [68] M. Müller, L. Liensberger, L. Flacke, H. Huebl, A. Kamra, W. Belzig, R. Gross, M. Weiler, M. Althammer, *Temperature-Dependent Spin Transport and Current-Induced Torques in Superconductor-Ferromagnet Heterostructures*, *Physical Review Letters* **126**, 087201 (2021).
- [69] M. Müller, R. Hoepfl, L. Liensberger, S. Geprägs, H. Huebl, M. Weiler, R. Gross, M. Althammer, *Growth optimization of TaN for superconducting spintronics*, *Materials for Quantum Technology* **1**, 045001 (2021).

- [70] M. Müller, T. Luschmann, A. Faltermeier, S. Weichselbaumer, L. Koch, G.B.P. Huber, H.W. Schumacher, N. Ubbelohde, D. Reifert, T. Scheller, F. Deppe, A. Marx, S. Filipp, M. Althammer, R. Gross, H. Huebl, *Magnetic field robust high quality factor NbTiN superconducting microwave resonators*, *Materials for Quantum Technology* **2**, 015002 (2022).
- [71] M. Müller, J. Weber, F. Engelhardt, V.A.S.V. Bittencourt, T. Luschmann, M. Cherkasskii, S.T.B. Goennenwein, S.V. Kusminskiy, S. Gepraegs, R. Gross, M. Althammer, H. Huebl, *Chiral phonons and phononic birefringence in ferromagnetic metal - bulk acoustic resonator hybrids*, arxiv 2303.08429 (2023).
- [72] D. Polder, *On the theory of ferromagnetic resonance*, *Physica* **15**, 253 (1949).
- [73] C. Kittel, *On the Theory of Ferromagnetic Resonance Absorption*, *Physical Review* **73**, 155 (1948).
- [74] A. Gurevich, G. Melkov, *Magnetization Oscillations and Waves*, Taylor & Francis (1996).
- [75] D.D. Stancil, A. Prabhakar, *Spin Waves*, Springer US, Boston, MA (2009).
- [76] B. Lax, K.J. Button, H.J. Hagger, *Microwave Ferrites and Ferrimagnetics*, *Physics Today* **16**, 57 (1963).
- [77] K. An, A.N. Litvinenko, R. Kohno, A.A. Fuad, V.V. Naletov, L. Vila, U. Ebels, G. de Loubens, H. Hurdequint, N. Beaulieu, J. Ben Youssef, N. Vukadinovic, G.E.W. Bauer, A.N. Slavin, V.S. Tiberkevich, O. Klein, *Coherent long-range transfer of angular momentum between magnon Kittel modes by phonons*, *Physical Review B* **101**, 060407 (2020).
- [78] H. Huebl, C.W. Zollitsch, J. Lotze, F. Hocke, M. Greifenstein, A. Marx, R. Gross, S.T.B. Goennenwein, *High Cooperativity in Coupled Microwave Resonator Ferrimagnetic Insulator Hybrids*, *Physical Review Letters* **111**, 127003 (2013).
- [79] Y. Li, T. Polakovic, Y.L. Wang, J. Xu, S. Lendinez, Z. Zhang, J. Ding, T. Khaire, H. Saglam, R. Divan, J. Pearson, W.K. Kwok, Z. Xiao, V. Novosad, A. Hoffmann, W. Zhang, *Strong Coupling between Magnons and Microwave Photons in On-Chip Ferromagnet-Superconductor Thin-Film Devices*, *Physical Review Letters* **123**, 107701 (2019).
- [80] J.T. Hou, L. Liu, *Strong Coupling between Microwave Photons and Nanomagnet Magnons*, *Physical Review Letters* **123**, 107702 (2019).
- [81] S. Kosen, *Microwave Magnonics at Millikelvin Temperatures*, PhD Thesis (2019).

- [82] H.T. Nembach, T.J. Silva, J.M. Shaw, M.L. Schneider, M.J. Carey, S. Maat, J.R. Childress, *Perpendicular ferromagnetic resonance measurements of damping and Lande g-factor in sputtered $(\text{Co}_2\text{Mn})_{1-x}\text{Ge}_x$ thin films*, Physical Review B **84**, 054424 (2011).
- [83] M. Weiler, *Magnetization dynamics and spin torques in exchange-coupled spin systems*, Habilitation Thesis (2020).
- [84] A.J. Berger, E.R. Edwards, H.T. Nembach, A.D. Karenowska, M. Weiler, T.J. Silva, *Inductive detection of fieldlike and dampinglike ac inverse spin-orbit torques in ferromagnet/normal-metal bilayers*, Physical Review B **97**, 94407 (2018).
- [85] Y. Tserkovnyak, A. Brataas, G.E.W. Bauer, *Spin pumping and magnetization dynamics in metallic multilayers*, Physical Review B **66**, 224403 (2002).
- [86] R. Gross, A. Marx, *Festkörperphysik*, De Gruyter Oldenbourg, Berlin, Boston (2022).
- [87] W. Pauli, *Über den Zusammenhang des Abschlusses der Elektronengruppen im Atom mit der Komplexstruktur der Spektren*, Zeitschrift für Physik **31**, 765 (1925).
- [88] F. Hund, *Zur Deutung der Molekelspektren. I*, Zeitschrift für Physik **40**, 742 (1927).
- [89] W. Heisenberg, *Mehrkörperproblem und Resonanz in der Quantenmechanik*, Zeitschrift für Physik **38**, 411 (1926).
- [90] R. O'Handley, *Modern Magnetic Materials: Principles and Applications*, Wiley (1999).
- [91] M. Planck, *Ueber das Gesetz der Energieverteilung im Normalspectrum*, Annalen der Physik **309**, 553 (1901).
- [92] L. Flacke, *Spin-wave transport and skyrmion formation in CoFe-based thin film heterostructures*, PhD Thesis (2021).
- [93] A. Landé, *Über den anomalen Zeemaneffekt*, in *Selected Scientific Papers of Alfred Landé*, 156–158, Springer Netherlands, Dordrecht (1988).
- [94] R. Shankar, *Principles of Quantum Mechanics*, Springer-Verlag New York (1994).
- [95] J.M.D. Coey, *Magnetism and Magnetic Materials*, Cambridge University Press (2001).
- [96] L. Dreher, M. Weiler, M. Pernpeintner, H. Huebl, R. Gross, M.S. Brandt, S.T.B. Goennenwein, *Surface acoustic wave driven ferromagnetic resonance in nickel thin films: Theory and experiment*, Physical Review B **86**, 134415 (2012).

- [97] B. Lax, K. Button, *Microwave Ferrites and Ferrimagnetics*, Lincoln Laboratory publications, McGraw-Hill (1962).
- [98] T. Miyazaki, H. Jin, *The Physics of Ferromagnetism*, Vol. 158 von *Springer Series in Materials Science*, Springer Berlin Heidelberg, Berlin, Heidelberg (2012).
- [99] J.A. Osborn, *Demagnetizing Factors of the General Ellipsoid*, *Physical Review* **67**, 351 (1945).
- [100] A. Gurevich, G. Melkov, *Magnetization Oscillations and Waves*, CRC Press (2020).
- [101] J.G. Gay, R. Richter, *Spin anisotropy of ferromagnetic films*, *Physical Review Letters* **56**, 2728 (1986).
- [102] C. Chappert, K.L. Dang, P. Beauvillain, H. Hurdequint, D. Renard, *Ferromagnetic resonance studies of very thin cobalt films on a gold substrate*, *Physical Review B* **34**, 3192 (1986).
- [103] P.F. Carcia, *Perpendicular magnetic anisotropy in Pd/Co and Pt/Co thin-film layered structures*, *Journal of Applied Physics* **63**, 5066 (1988).
- [104] M. Wolloch, D. Suess, *Strain-induced control of magnetocrystalline anisotropy energy in FeCo thin films*, *Journal of Magnetism and Magnetic Materials* **522**, 167542 (2021).
- [105] L. Flacke, V. Ahrens, S. Mendisch, L. Körber, T. Böttcher, E. Meidinger, M. Yaqoob, M. Müller, L. Liensberger, A. Kákay, M. Becherer, P. Pirro, M. Althammer, S. Geprägs, H. Huebl, R. Gross, M. Weiler, *Robust formation of nanoscale magnetic skyrmions in easy-plane anisotropy thin film multilayers with low damping*, *Physical Review B* **104**, L100417 (2021).
- [106] J. Gückelhorn, T. Wimmer, M. Müller, S. Geprägs, H. Huebl, R. Gross, M. Althammer, *Magnon transport in $Y_3Fe_5O_{12}$ /Pt nanostructures with reduced effective magnetization*, *Physical Review B* **104**, L180410 (2021).
- [107] G.H.O. Daalderop, P.J. Kelly, F.J.A. den Broeder, *Prediction and confirmation of perpendicular magnetic anisotropy in Co/Ni multilayers*, *Physical Review Letters* **68**, 682 (1992).
- [108] F. Gimbert, L. Calmels, *First-principles investigation of the magnetic anisotropy and magnetic properties of Co/Ni(111) superlattices*, *Physical Review B* **86**, 184407 (2012).
- [109] L. Landau, E. Lifshitz, *On the theory of the dispersion of magnetic permeability in ferromagnetic bodies*, in *Perspectives in Theoretical Physics*, 51–65, Elsevier (1992).

- [110] W.K. Peria, X. Wang, H. Yu, S. Lee, I. Takeuchi, P.A. Crowell, *Magnetoelastic Gilbert damping in magnetostrictive Fe_{0.7}Ga_{0.3} thin films*, Physical Review B **103**, L220403 (2021).
- [111] H. Suhl, *Theory of the magnetic damping constant*, IEEE Transactions on Magnetics **34**, 1834 (1998).
- [112] S. Streib, H. Keshtgar, G.E. Bauer, *Damping of Magnetization Dynamics by Phonon Pumping*, Physical Review Letters **121**, 027202 (2018).
- [113] E. Rossi, O.G. Heinonen, A.H. MacDonald, *Dynamics of magnetization coupled to a thermal bath of elastic modes*, Physical Review B **72**, 174412 (2005).
- [114] M.J. Hurben, C.E. Patton, *Theory of two magnon scattering microwave relaxation and ferromagnetic resonance linewidth in magnetic thin films*, Journal of Applied Physics **83**, 4344 (1998).
- [115] S. Yoshii, K. Kato, E. Shigematsu, R. Ohshima, Y. Ando, K. Usami, M. Shiraishi, *Significant suppression of two-magnon scattering in ultrathin Co by controlling the surface magnetic anisotropy at the Co/nonmagnet interfaces*, Physical Review B **106**, 174414 (2022).
- [116] L. Zhu, D.C. Ralph, R.A. Buhrman, *Effective Spin-Mixing Conductance of Heavy-Metal-Ferromagnet Interfaces*, Physical Review Letters **123**, 57203 (2019).
- [117] K. Gilmore, Y.U. Idzerda, M.D. Stiles, *Identification of the Dominant Precession-Damping Mechanism in Fe, Co, and Ni by First-Principles Calculations*, Physical Review Letters **99**, 027204 (2007).
- [118] Z. Xu, K. Zhang, J. Li, *Disentangling intrinsic and extrinsic Gilbert damping*, Physical Review B **104**, 224404 (2021).
- [119] T. Gilbert, *Classics in Magnetism A Phenomenological Theory of Damping in Ferromagnetic Materials*, IEEE Transactions on Magnetics **40**, 3443 (2004).
- [120] L. Liensberger, *Spin-Orbit Torques and Magnetization Dynamics in Non-collinear Magnets*, Master's Thesis (2017).
- [121] L. Flacke, *Spin-Pumping and Spin Wave Damping in Co₂₅Fe₇₅ Thin-Film Heterostructures*, Master's Thesis (2018).
- [122] M. Müller, *Superconductor/Ferromagnet Heterostructures for Superconducting Spintronics*, Master's Thesis (2020).
- [123] J.A.C. Bland, B. Heinrich (Eds.), *Ultrathin Magnetic Structures III*, Springer-Verlag, Berlin/Heidelberg (2005).

- [124] W. Bailey, P. Kabos, F. Mancoff, S. Russek, *Control of magnetization dynamics in $Ni_{81}Fe_{19}$ thin films through the use of rare-earth dopants*, IEEE Transactions on Magnetism **37**, 1749 (2001).
- [125] J. Rantschler, B. Mar, J. Mallett, P. Chen, R. McMichael, W. Egelhoff, *Damping at normal metal/permalloy interfaces*, IEEE Transactions on Magnetism **41**, 3523 (2005).
- [126] J.M. Beaujour, D. Ravelosona, I. Tudosa, E.E. Fullerton, A.D. Kent, *Ferromagnetic resonance linewidth in ultrathin films with perpendicular magnetic anisotropy*, Physical Review B **80**, 180415 (2009).
- [127] M. Obstbaum, M. Härtinger, H.G. Bauer, T. Meier, F. Swientek, C.H. Back, G. Woltersdorf, *Inverse spin Hall effect in $Ni_{81}Fe_{19}$ /normal-metal bilayers*, Physical Review B **89**, 060407 (2014).
- [128] E. Saitoh, M. Ueda, H. Miyajima, G. Tatara, *Conversion of spin current into charge current at room temperature: Inverse spin-Hall effect*, Applied Physics Letters **88**, 182509 (2006).
- [129] A. Soumyanarayanan, N. Reyren, A. Fert, C. Panagopoulos, *Emergent phenomena induced by spin-orbit coupling at surfaces and interfaces*, Nature **539**, 509 (2016).
- [130] M. Weiler, J.M. Shaw, H.T. Nembach, T.J. Silva, *Phase-Sensitive Detection of Spin Pumping via the ac Inverse Spin Hall Effect*, Physical Review Letters **113**, 157204 (2014).
- [131] A. Barman, J. Sinha, *Spin Dynamics and Damping in Ferromagnetic Thin Films and Nanostructures*, Springer International Publishing, Springer Cham (2018).
- [132] M.A.W. Schoen, J.M. Shaw, H.T. Nembach, M. Weiler, T.J. Silva, *Radiative damping in waveguide-based ferromagnetic resonance measured via analysis of perpendicular standing spin waves in sputtered permalloy films*, Physical Review B **92**, 184417 (2015).
- [133] D. Huertas Hernando, Y.V. Nazarov, A. Brataas, G.E.W. Bauer, *Conductance modulation by spin precession in noncollinear ferromagnet normal-metal ferromagnet systems*, Physical Review B **62**, 5700 (2000).
- [134] B. Heinrich, C. Burrowes, E. Montoya, B. Kardasz, E. Girt, Y.Y. Song, Y. Sun, M. Wu, *Spin Pumping at the Magnetic Insulator (YIG)/Normal Metal (Au) Interfaces*, Physical Review Letters **107**, 066604 (2011).
- [135] L. Flacke, L. Liensberger, M. Althammer, H. Huebl, S. Geprägs, K. Schultheiss, A. Buzdakov, T. Hula, H. Schultheiss, E.R.J. Edwards, H.T. Nembach, J.M. Shaw, R. Gross, M. Weiler, *High spin-wave propagation length*

- consistent with low damping in a metallic ferromagnet*, Applied Physics Letters **115**, 122402 (2019).
- [136] M. Haertinger, C.H. Back, J. Lotze, M. Weiler, S. Geprägs, H. Huebl, S.T.B. Goennenwein, G. Woltersdorf, *Spin pumping in YIG/Pt bilayers as a function of layer thickness*, Physical Review B **92**, 054437 (2015).
- [137] T.S. Suraj, M. Müller, S. Gelder, S. Geprägs, M. Opel, M. Weiler, K. Sethupathi, H. Huebl, R. Gross, M.S. Ramachandra Rao, M. Althammer, *Effect of interfacial oxidation layer in spin pumping experiments on Ni₈₀Fe₂₀/SrIrO₃ heterostructures*, Journal of Applied Physics **128**, 083903 (2020).
- [138] C. Yu, H. Li, Y. Luo, L. Zhu, Z. Qian, T. Zhou, *Thickness-dependent magnetic order and phase-transition dynamics in epitaxial Fe-rich FeRh thin films*, Physics Letters A **383**, 2424 (2019).
- [139] C. Lüthi, L. Flacke, A. Aqeel, A. Kamra, R. Gross, C. Back, M. Weiler, *Hybrid magnetization dynamics in Cu₂OSeO₃/NiFe heterostructures*, Applied Physics Letters **122**, 012401 (2023).
- [140] H. Maier-Flaig, S. Klingler, C. Dubs, O. Surzhenko, R. Gross, M. Weiler, H. Huebl, S.T.B. Goennenwein, *Temperature-dependent magnetic damping of yttrium iron garnet spheres*, Physical Review B **95**, 214423 (2017).
- [141] E.G. Spencer, R.C. LeCraw, A.M. Clogston, *Low-Temperature Line-Width Maximum in Yttrium Iron Garnet*, Physical Review Letters **3**, 32 (1959).
- [142] C.L. Jermain, S.V. Aradhya, N.D. Reynolds, R.A. Buhrman, J.T. Brangham, M.R. Page, P.C. Hammel, F.Y. Yang, D.C. Ralph, *Increased low-temperature damping in yttrium iron garnet thin films*, Physical Review B **95**, 174411 (2017).
- [143] M. Sparks, *Ferromagnetic-relaxation Theory*, McGraw-Hill advanced physics monograph series, McGraw-Hill (1964).
- [144] J.H. Van Vleck, R. Orbach, *Ferrimagnetic Resonance of Dilute Rare-Earth Doped Iron Garnets*, Physical Review Letters **11**, 65 (1963).
- [145] H. Chen, P. De Gasperis, R. Marcelli, M. Pardavi-Horvath, R. McMichael, P.E. Wigen, *Wide-band linewidth measurements in yttrium iron garnet films*, Journal of Applied Physics **67**, 5530 (1990).
- [146] G. Woltersdorf, M. Kiessling, G. Meyer, J.U. Thiele, C.H. Back, *Damping by Slow Relaxing Rare Earth Impurities in Ni₈₀Fe₂₀*, Physical Review Letters **102**, 257602 (2009).
- [147] T.S. Hartwick, J. Smit, *Ferromagnetic Resonance in Si-Doped YIG*, Journal of Applied Physics **39**, 827 (1968).

- [148] A.M. Clogston, *Relaxation Phenomena in Ferrites*, Bell System Technical Journal **34**, 739 (1955).
- [149] X. Zhang, C.L. Zou, L. Jiang, H.X. Tang, *Strongly coupled magnons and cavity microwave photons*, Physical Review Letters **113**, 156401 (2014).
- [150] H. Maier-Flaig, M. Harder, S. Klingler, Z. Qiu, E. Saitoh, M. Weiler, S. Geprägs, R. Gross, S.T.B. Goennenwein, H. Huebl, *Tunable magnon-photon coupling in a compensating ferrimagnet—from weak to strong coupling*, Applied Physics Letters **110**, 132401 (2017).
- [151] Y. Li, W. Zhang, V. Tyberkevych, W.K. Kwok, A. Hoffmann, V. Novosad, *Hybrid magnonics: Physics, circuits, and applications for coherent information processing*, Journal of Applied Physics **128**, 130902 (2020).
- [152] Ö.O. Soykal, M.E. Flatté, *Size dependence of strong coupling between nanomagnets and photonic cavities*, Physical Review B **82**, 104413 (2010).
- [153] Ö.O. Soykal, M.E. Flatté, *Strong field interactions between a nanomagnet and a photonic cavity*, Physical Review Letters **104**, 077202 (2010).
- [154] D. Walls, G.J. Milburn (Eds.), *Quantum Optics*, Springer Berlin Heidelberg, Berlin (2008).
- [155] J. Zollitsch, *Single Excitation Transfer in the Quantum Regime: A Spin-Based Solid-State Approach*, PhD Thesis (2016).
- [156] I. Diniz, S. Portolan, R. Ferreira, J.M. Gérard, P. Bertet, A. Auffèves, *Strongly coupling a cavity to inhomogeneous ensembles of emitters: Potential for long-lived solid-state quantum memories*, Physical Review A **84**, 063810 (2011).
- [157] T. Sato, W. Yu, S. Streib, G.E.W. Bauer, *Dynamic magnetoelastic boundary conditions and the pumping of phonons*, Physical Review B **104**, 014403 (2021).
- [158] K. An, R. Kohno, A.N. Litvinenko, R.L. Seeger, V.V. Naletov, L. Vila, G. de Loubens, J. Ben Youssef, N. Vukadinovic, G.E.W. Bauer, A.N. Slavin, V.S. Tiberkevich, O. Klein, *Bright and Dark States of Two Distant Macrospins Strongly Coupled by Phonons*, Physical Review X **12**, 011060 (2022).
- [159] R. Schlitz, L. Siegl, T. Sato, W. Yu, G.E.W. Bauer, H. Huebl, S.T.B. Goennenwein, *Magnetization dynamics affected by phonon pumping*, Physical Review B **106**, 014407 (2022).
- [160] K. An, C. Kim, K.W. Moon, R. Kohno, G. Olivetti, G. de Loubens, N. Vukadinovic, J.B. Youssef, C. Hwang, O. Klein, *Optimizing the magnon-phonon cooperativity in planar geometries*, arxiv 1–11 (2023).

- [161] G. Terrasanta, M. Müller, T. Sommer, S. Geprägs, R. Gross, M. Althammer, M. Poot, *Growth of aluminum nitride on a silicon nitride substrate for hybrid photonic circuits*, *Materials for Quantum Technology* **1**, 021002 (2021).
- [162] R. Hoepfl, *Wachstumsoptimierung supraleitender Tantalnitrid (TaN) -Dünnschichten für fortgeschrittene Spinelektronik*, Bachelor's Thesis (2020).
- [163] R. Hoepfl, *Growth optimization and magnetotransport properties of ferromagnetic insulating gadolinium nitride thin films*, Master's Thesis (2023).
- [164] K. Wasa, I. Kanno, H. Kotera, *Handbook of Sputter Deposition Technology: Fundamentals and Applications for Functional Thin Films, Nano-Materials and MEMS*, Elsevier Science (2012).
- [165] D. Depla, S. Mahieu (Eds.), *Reactive Sputter Deposition*, Vol. 109 von *Springer Series in Materials Science*, Springer Berlin Heidelberg, Berlin (2008).
- [166] D. Mattox, *Handbook of Physical Vapor Deposition (PVD) Processing*, Online access with subscription: Proquest Ebook Central, Elsevier Science (2014).
- [167] A. Anders, *Tutorial: Reactive high power impulse magnetron sputtering (R-HiPIMS)*, *Journal of Applied Physics* **121**, 171101 (2017).
- [168] G. Betz, W. Husinsky, *Modelling of cluster emission from metal surfaces under ion impact*, *Philosophical Transactions of the Royal Society of London. Series A: Mathematical, Physical and Engineering Sciences* **362**, 177 (2004).
- [169] J.P. Biersack, J.F. Ziegler, *The Stopping and Range of Ions in Solids*, in *Ion Implantation Techniques*, 122–156, Springer Berlin Heidelberg, Berlin (1982).
- [170] Y. Yamamura, H. Tawara, *Energy dependence of ion-induced sputtering yields from monatomic solids at normal incidence*, *Atomic Data and Nuclear Data Tables* **62**, 149 (1996).
- [171] S. Wu, H. Chen, X. Du, Z. Liu, *Effect of deposition power and pressure on rate deposition and resistivity of titanium thin films grown by DC magnetron sputtering*, *Spectroscopy Letters* **49**, 514 (2016).
- [172] S. Schiller, G. Beister, W. Sieber, G. Schirmer, E. Hacker, *Influence of deposition parameters on the optical and structural properties of TiO₂ films produced by reactive d.c. plasmatron sputtering*, *Thin Solid Films* **83**, 239 (1981).
- [173] A. Karpuz, S. Colmekci, H. Kockar, H. Kuru, M. Uckun, *Impact of Deposition Rate on the Structural and Magnetic Properties of Sputtered Ni/Cu Multilayer Thin Films*, *Zeitschrift für Naturforschung A* **73**, 85 (2017).
- [174] Z. Ghorannevis, M.T. Hosseinejad, M. Habibi, P. Golmahdi, *Effect of substrate temperature on structural, morphological and optical properties of deposited Al/ZnO films*, *Journal of Theoretical and Applied Physics* **9**, 33 (2015).

- [175] R. Vidyasagar, S. Kitayama, H. Yoshitomi, T. Kita, T. Sakurai, H. Ohta, *Tuning optical and ferromagnetic properties of thin GdN films by nitrogen-vacancy centers*, The European Physical Journal B **86**, 52 (2013).
- [176] C. Ndoye, K. Tapily, M. Orłowski, H. Baumgart, D. Gu, *Silicidation of Niobium Deposited on Silicon by Physical Vapor Deposition*, Journal of The Electrochemical Society **158**, H897 (2011).
- [177] F. Schulz, R. Lawitzki, H. Głowiński, F. Lisiecki, N. Träger, P. Kuświk, E. Goering, G. Schütz, J. Gräfe, *Increase of Gilbert damping in Permalloy thin films due to heat-induced structural changes*, Journal of Applied Physics **129**, 153903 (2021).
- [178] K. Barmak, J. Liu, *Impact of deposition rate, underlayers, and substrates on β -tungsten formation in sputter deposited films*, Journal of Vacuum Science & Technology A: Vacuum, Surfaces, and Films **35**, A1944 (2017).
- [179] G.S. Jang, S.M. Ahn, N.M. Hwang, *Effects of Sputtering Power, Working Pressure, and Electric Bias on the Deposition Behavior of Ag Films during DC Magnetron Sputtering Considering the Generation of Charged Flux*, Electronic Materials Letters **18**, 57 (2022).
- [180] D.M. Mitin, A.A. Serdobintsev, *Effect of scattering of sputtered atoms on the growth rate of films fabricated by magnetron sputtering*, Technical Physics Letters **43**, 814 (2017).
- [181] C. Priestland, S. Hersee, *The effects of pressure on the deposition rate in rf sputtering processes*, Vacuum **22**, 103 (1972).
- [182] A. Engwall, L. Bayu Aji, A. Baker, S. Shin, J. Bae, S. McCall, J. Moody, S. Kucheyev, *Effect of substrate tilt on sputter-deposited AuTa films*, Applied Surface Science **547**, 149010 (2021).
- [183] R.C. Raju Nagiri, S.D. Yambem, Q. Lin, P.L. Burn, P. Meredith, *Room-temperature tilted-target sputtering deposition of highly transparent and low sheet resistance Al doped ZnO electrodes*, Journal of Materials Chemistry C **3**, 5322 (2015).
- [184] D.M. Glowacka, D.J. Goldie, S. Withington, H. Muhammad, G. Yassin, B.K. Tan, *Development of a NbN Deposition Process for Superconducting Quantum Sensors*, arxiv 1401.2292 (2014).
- [185] M. Reichert, *Hochwertige supraleitende Dünnschichten für fortgeschrittene Spinelektronik*, PhD thesis, TUM (2018).
- [186] A. Faltermeier, *Optimierung supraleitender Schichten aus Niob, Niobnitrid und Niobtitanitrid für den Einsatz in Mikrowellenresonatoren*, Master's Thesis (2019).

- [187] F. Hartz, *Herstellung eines Breitband-Messstabs zur Untersuchung ferromagnetischer Resonanz*, Bachelor's thesis, Technical University Munich (2014).
- [188] O. Karlqvist, *Calculation of the Magnetic Field in the Ferromagnetic Layer of a Magnetic Drum*, Acta polytechnica, Elanders boktr.; H. Lindståhls bokhandel i distribution (1954).
- [189] Z. Ma, D.G. Seiler, *Metrology and Diagnostic Techniques for Nanoelectronics*, Jenny Stanford Publishing (2017).
- [190] S. Weichselbaumer, *Spin dynamics in strongly coupled spin-photon hybrid systems*, PhD Thesis (2020).
- [191] C. Poole, *Electron Spin Resonance: A Comprehensive Treatise on Experimental Techniques*, Dover books on physics, Dover Publications (1996).
- [192] H. Wang, C.R. McRae, J. Gao, M.R. Vissers, T. Brecht, A. Dunsworth, D.P. Pappas, J. Mutus, *Materials loss measurements using superconducting microwave resonators*, Review of Scientific Instruments **91**, 091101 (2020).
- [193] J. Goetz, F. Deppe, M. Haeberlein, F. Wulschner, C.W. Zollitsch, S. Meier, M. Fischer, P. Eder, E. Xie, K.G. Fedorov, E.P. Menzel, A. Marx, R. Gross, *Loss mechanisms in superconducting thin film microwave resonators*, Journal of Applied Physics **119**, 015304 (2016).
- [194] D.S. Wisbey, J. Gao, M.R. Vissers, F.C.S. da Silva, J.S. Kline, L. Vale, D.P. Pappas, *Effect of metal/substrate interfaces on radio-frequency loss in superconducting coplanar waveguides*, Journal of Applied Physics **108**, 093918 (2010).
- [195] J. Gao, M. Daal, A. Vayonakis, S. Kumar, J. Zmuidzinas, B. Sadoulet, B.A. Mazin, P.K. Day, H.G. Leduc, *Experimental evidence for a surface distribution of two-level systems in superconducting lithographed microwave resonators*, Applied Physics Letters **92**, 152505 (2008).
- [196] J. Wenner, R. Barends, R.C. Bialczak, Y. Chen, J. Kelly, E. Lucero, M. Mariantoni, A. Megrant, P.J.J. O'Malley, D. Sank, A. Vainsencher, H. Wang, T.C. White, Y. Yin, J. Zhao, A.N. Cleland, J.M. Martinis, *Surface loss simulations of superconducting coplanar waveguide resonators*, Applied Physics Letters **99**, 113513 (2011).
- [197] M. Göppl, A. Fragner, M. Baur, R. Bianchetti, S. Filipp, J.M. Fink, P.J. Leek, G. Puebla, L. Steffen, A. Wallraff, *Coplanar waveguide resonators for circuit quantum electrodynamics*, Journal of Applied Physics **104**, 113904 (2008).
- [198] S. Probst, F.B. Song, P.A. Bushev, A.V. Ustinov, M. Weides, *Efficient and robust analysis of complex scattering data under noise in microwave resonators*, Review of Scientific Instruments **86**, 024706 (2015).

- [199] A. Brataas, B. van Wees, O. Klein, G. de Loubens, M. Viret, *Spin insulatronics*, Physics Reports **885**, 1 (2020).
- [200] G.E. Bauer, E. Saitoh, B.J. Van Wees, *Spin caloritronics*, Nature Materials **11**, 391 (2012).
- [201] P. Li, T. Liu, H. Chang, A. Kalitsov, W. Zhang, G. Csaba, W. Li, D. Richardson, A. DeMann, G. Rimal, H. Dey, J.S. Jiang, W. Porod, S.B. Field, J. Tang, M.C. Marconi, A. Hoffmann, O. Mryasov, M. Wu, *Spin-orbit torque-assisted switching in magnetic insulator thin films with perpendicular magnetic anisotropy*, Nature Communications **7**, 12688 (2016).
- [202] V. Cherepanov, I. Kolokolov, V. L'vov, *The saga of YIG: Spectra, thermodynamics, interaction and relaxation of magnons in a complex magnet*, Physics Reports **229**, 81 (1993).
- [203] H.B. Maier-Flaig, *Magnetic resonance of ferrimagnetic insulators*, PhD Thesis (2017).
- [204] A.A. Serga, A.V. Chumak, B. Hillebrands, *YIG magnonics*, Journal of Physics D: Applied Physics **43**, 264002 (2010).
- [205] T.S. Seifert, S. Jaiswal, J. Barker, S.T. Weber, I. Razdolski, J. Cramer, O. Gueckstock, S.F. Maehrlein, L. Nadvornik, S. Watanabe, C. Ciccarelli, A. Melnikov, G. Jakob, M. Münzenberg, S.T.B. Goennenwein, G. Woltersdorf, B. Rethfeld, P.W. Brouwer, M. Wolf, M. Kläui, T. Kampfrath, *Femtosecond formation dynamics of the spin Seebeck effect revealed by terahertz spectroscopy*, Nature Communications **9**, 2899 (2018).
- [206] A.V. Singh, B. Khodadadi, J.B. Mohammadi, S. Keshavarz, T. Mewes, D.S. Negi, R. Datta, Z. Galazka, R. Uecker, A. Gupta, *Bulk Single Crystal-Like Structural and Magnetic Characteristics of Epitaxial Spinel Ferrite Thin Films with Elimination of Antiphase Boundaries*, Advanced Materials **29**, 1701222 (2017).
- [207] S. Emori, B.A. Gray, H. Jeon, J. Peoples, M. Schmitt, K. Mahalingam, M. Hill, M.E. McConney, M.T. Gray, U.S. Alaani, A.C. Bornstein, P. Shafer, A.T. N'Diaye, E. Arenholz, G. Haugstad, K. Meng, F. Yang, D. Li, S. Mahat, D.G. Cahill, P. Dhagat, A. Jander, N.X. Sun, Y. Suzuki, B.M. Howe, *Coexistence of Low Damping and Strong Magnetoelastic Coupling in Epitaxial Spinel Ferrite Thin Films*, Advanced Materials **29**, 1701130 (2017).
- [208] S. Emori, D. Yi, S. Crossley, J.J. Wissler, P.P. Balakrishnan, B. Khodadadi, P. Shafer, C. Klewe, A.T. N'Diaye, B.T. Urwin, K. Mahalingam, B.M. Howe, H.Y. Hwang, E. Arenholz, Y. Suzuki, *Ultralow Damping in Nanometer-Thick Epitaxial Spinel Ferrite Thin Films*, Nano Letters **18**, 4273 (2018).

- [209] S. Tang, M.S. Sarker, K. Ma, H. Yamahara, H. Tabata, M. Seki, *Efficient spin-wave transmission in epitaxial thin films of defect spinel γ -Fe_{2x}Al_xO₃*, Applied Physics Letters **119**, 082402 (2021).
- [210] E.T. Lee, G.E. Jang, C.K. Kim, D.H. Yoon, *Fabrication and gas sensing properties of α -Fe₂O₃ thin film prepared by plasma enhanced chemical vapor deposition (PECVD)*, Sensors and Actuators B: Chemical **77**, 221 (2001).
- [211] L. Dghoughi, B. Elidrissi, C. Bernède, M. Addou, M.A. Lamrani, M. Regragui, H. Erguig, *Physico-chemical, optical and electrochemical properties of iron oxide thin films prepared by spray pyrolysis*, Applied Surface Science **253**, 1823 (2006).
- [212] K. Garello, C.O. Avci, I.M. Miron, M. Baumgartner, A. Ghosh, S. Auffret, O. Boulle, G. Gaudin, P. Gambardella, *Ultrafast magnetization switching by spin-orbit torques*, Applied Physics Letters **105**, 212402 (2014).
- [213] A. Fert, V. Cros, J. Sampaio, *Skyrmions on the track*, Nature Nanotechnology **8**, 152 (2013).
- [214] B. Divinskiy, H. Merbouche, V.E. Demidov, K.O. Nikolaev, L. Soumah, D. Gouéré, R. Lebrun, V. Cros, J.B. Youssef, P. Bortolotti, A. Anane, S.O. Demokritov, *Evidence for spin current driven Bose-Einstein condensation of magnons*, Nature Communications **12**, 6541 (2021).
- [215] M. Evelt, L. Soumah, A. Rinkevich, S. Demokritov, A. Anane, V. Cros, J. Ben Youssef, G. de Loubens, O. Klein, P. Bortolotti, V. Demidov, *Emission of Coherent Propagating Magnons by Insulator-Based Spin-Orbit-Torque Oscillators*, Physical Review Applied **10**, 041002 (2018).
- [216] M. Scheufele, *Tuning the Amplitude of the Spin Hall Magnetoresistance*, Master's Thesis (2021).
- [217] R. Grau-Crespo, A.Y. Al-Baitai, I. Saadoune, N.H. De Leeuw, *Vacancy ordering and electronic structure of γ -Fe₂O₃ (maghemite): a theoretical investigation*, Journal of Physics: Condensed Matter **22**, 255401 (2010).
- [218] J.E. Jørgensen, L. Mosegaard, L.E. Thomsen, T.R. Jensen, J.C. Hanson, *Formation of γ -Fe₂O₃ nanoparticles and vacancy ordering: An in situ X-ray powder diffraction study*, Journal of Solid State Chemistry **180**, 180 (2007).
- [219] M. Coduri, P. Masala, L. Del Bianco, F. Spizzo, D. Ceresoli, C. Castellano, S. Cappelli, C. Oliva, S. Checchia, M. Allietta, D.V. Szabo, S. Schlabach, M. Hagelstein, C. Ferrero, M. Scavini, *Local Structure and Magnetism of Fe₂O₃ Maghemite Nanocrystals: The Role of Crystal Dimension*, Nanomaterials **10**, 867 (2020).

- [220] R. Zboril, M. Mashlan, D. Petridis, *Iron(III) Oxides from Thermal Processes Synthesis, Structural and Magnetic Properties, Mössbauer Spectroscopy Characterization, and Applications*, Chemistry of Materials **14**, 969 (2002).
- [221] R. Dronskowski, *The Little Maghemite Story: A Classic Functional Material*, Advanced Functional Materials **11**, 27 (2001).
- [222] X. Huang, Y. Yang, J. Ding, *Epitaxial growth of γ -Fe₂O₃ thin films on MgO substrates by pulsed laser deposition and their properties*, Acta Materialia **61**, 548 (2013).
- [223] *MgO Crystal Structure: Datasheet from "PAULING FILE Multinaries Edition – 2012" in SpringerMaterials*, copyright 2016 Springer-Verlag Berlin Heidelberg & Material Phases Data System (MPDS), Switzerland & National Institute for Materials Science (NIMS), Japan (2012).
- [224] D. Chicot, J. Mendoza, A. Zaoui, G. Louis, V. Lepingue, F. Roudet, J. Lesage, *Mechanical properties of magnetite (Fe₃O₄), hematite (α -Fe₂O₃) and goethite (α -FeO·OH) by instrumented indentation and molecular dynamics analysis*, Materials Chemistry and Physics **129**, 862 (2011).
- [225] Y. He, L. Zhang, H.W. Xiong, X. Kang, *Evolution of lattice defects in nickel ferrite spinel: Oxygen vacancy and cation substitution*, Journal of Alloys and Compounds **917**, 165494 (2022).
- [226] L.J. van der Pauw, *A method of measuring specific resistivity and Hall effect of discs of arbitrary shape*, in *Semiconductor Devices: Pioneering Papers*, 174–182, World Scientific (1991).
- [227] F.J. Morin, *Magnetic Susceptibility of α -Fe₂O₃ and α -Fe₂O₃ with Added Titanium*, Physical Review **78**, 819 (1950).
- [228] E.J.W. Verwey, *Electronic Conduction of Magnetite (Fe₃O₄) and its Transition Point at Low Temperatures*, Nature **144**, 327 (1939).
- [229] S. Alraddadi, *The Electronic and Magnetic Properties of Ultrathin γ -Fe₂O₃ Films*, IOP Conference Series: Materials Science and Engineering **842**, 012012 (2020).
- [230] J. Bobo, D. Basso, E. Snoeck, C. Gatel, D. Hrabovsky, J. Gauffier, L. Ressier, R. Mamy, S. Visnovsky, J. Hamrle, J. Teillet, A. Fert, *Magnetic behavior and role of the antiphase boundaries in Fe₃O₄ epitaxial films sputtered on MgO (001)*, The European Physical Journal B **24**, 43 (2001).
- [231] P. Lubitz, M. Rubinstein, J.J. Krebs, S.F. Cheng, *Frequency and temperature dependence of ferromagnetic linewidth in exchange biased Permalloy*, Journal of Applied Physics **89**, 6901 (2001).

- [232] R.D. McMichael, C.G. Lee, M.D. Stiles, F.G. Serpa, P.J. Chen, W.F. Egelhoff, *Exchange bias relaxation in CoO-biased films*, Journal of Applied Physics **87**, 6406 (2000).
- [233] I. Knittel, J. Wei, Y. Zhou, S.K. Arora, I.V. Shvets, M. Luysberg, U. Hartmann, *Observation of antiferromagnetic coupling in epitaxial ferrite films*, Physical Review B **74**, 132406 (2006).
- [234] A.V. Ramos, S. Matzen, J.B. Moussy, F. Ott, M. Viret, *Artificial antiphase boundary at the interface of ferrimagnetic spinel bilayers*, Physical Review B **79**, 014401 (2009).
- [235] E.G. Spencer, R.C. LeCraw, R.C. Linares, *Low-Temperature Ferromagnetic Relaxation in Yttrium Iron Garnet*, Physical Review **123**, 1937 (1961).
- [236] P. Hansen, W. Tolksdorf, J. Schuldt, *Anisotropy and magnetostriction of germanium-substituted yttrium iron garnet*, Journal of Applied Physics **43**, 4740 (1972).
- [237] D.J. Epstein, L. Tocci, *High temperature resonance losses in silicon-doped Yttrium-iron garnet (YIG)*, Applied Physics Letters **11**, 55 (1967).
- [238] J.B. Youssef, C. Brosseau, *Magnetization damping in two-component metal oxide micropowder and nanopowder compacts by broadband ferromagnetic resonance measurements*, Physical Review B **74**, 214413 (2006).
- [239] R. Comstock, *Magnetoelastic coupling constants of the ferrites and garnets*, Proceedings of the IEEE **53**, 1508 (1965).
- [240] E. Popova, N. Keller, F. Gendron, L. Thomas, M.C. Brianso, M. Guyot, M. Tessier, S.S.P. Parkin, *Perpendicular magnetic anisotropy in ultrathin yttrium iron garnet films prepared by pulsed laser deposition technique*, Journal of Vacuum Science & Technology A: Vacuum, Surfaces, and Films **19**, 2567 (2001).
- [241] M. Takeda, T. Onishi, S. Nakakubo, S. Fujimoto, *Physical properties of iron-oxide scales on Si-containing steels at high temperature*, Materials Transactions **50**, 2242 (2009).
- [242] O. Madelung, U. Rössler, M. Schulz (Eds.), *II-VI and I-VII Compounds; Semimagnetic Compounds*, Vol. 41B von Landolt-Börnstein - Group III Condensed Matter, Springer-Verlag, Berlin/Heidelberg (1999).
- [243] D. Overview, *Part A*, Vol. 4a von Landolt-Börnstein - Group III Condensed Matter, Springer-Verlag, Berlin/Heidelberg (1970).
- [244] A.B. Drovosekov, N.M. Kreines, A.S. Barkalova, S.N. Nikolaev, A.V. Sitnikov, V.V. Rylkov, *Effect of Slow Ion Relaxation at Ferromagnetic Resonance in a CoFeB-LiNbO Metal-Insulator Nanocomposite*, JETP Letters **112**, 84 (2020).

- [245] B.H. Clarke, K. Tweedale, R.W. Teale, *Rare-Earth Ion Relaxation Time and G Tensor in Rare-Earth-Doped Yttrium Iron Garnet. I. Ytterbium*, Physical Review **139**, A1933 (1965).
- [246] P. Hansen, J. Schuldt, W. Tolksdorf, *Anisotropy and Magnetostriction of Iridium-Substituted Yttrium Iron Garnet*, Physical Review B **8**, 4274 (1973).
- [247] B.H. Clarke, *Rare-earth ion relaxation time and G tensor in rare-earth-doped yttrium iron garnet. II. Neodymium*, Physical Review **139**, A1944 (1965).
- [248] T. Kasuya, R.C. LeCraw, *Relaxation Mechanisms in Ferromagnetic Resonance*, Physical Review Letters **6**, 223 (1961).
- [249] M. Sparks, *Ferromagnetic-relaxation theory*, McGraw-Hill advanced physics monograph series, McGraw-Hill, New York (1964).
- [250] A. Krysztofik, S. Özoğlu, R.D. McMichael, E. Coy, *Effect of strain-induced anisotropy on magnetization dynamics in $Y_3Fe_5O_{12}$ films recrystallized on a lattice-mismatched substrate*, Scientific Reports **11**, 14011 (2021).
- [251] P. Jiménez-Cavero, I. Lucas, A. Anadón, R. Ramos, T. Niizeki, M.H. Aguirre, P.A. Algarabel, K. Uchida, M.R. Ibarra, E. Saitoh, L. Morellón, *Spin Seebeck effect in insulating epitaxial γFe_2O_3 thin films*, APL Materials **5**, 026103 (2017).
- [252] Y. Tabuchi, S. Ishino, A. Noguchi, T. Ishikawa, R. Yamazaki, K. Usami, Y. Nakamura, *Coherent coupling between a ferromagnetic magnon and a superconducting qubit*, Science **349**, 405 (2015).
- [253] M. Giraldo, Q.N. Meier, A. Bortis, D. Nowak, N.A. Spaldin, M. Fiebig, M.C. Weber, T. Lottermoser, *Magnetolectric coupling of domains, domain walls and vortices in a multiferroic with independent magnetic and electric order*, Nature Communications **12**, 3093 (2021).
- [254] K. Bhoi, H.S. Mohanty, Ravikant, M.F. Abdullah, D.K. Pradhan, S.N. Babu, A.K. Singh, P.N. Vishwakarma, A. Kumar, R. Thomas, D.K. Pradhan, *Unravelling the nature of magneto-electric coupling in room temperature multiferroic particulate $(PbFe_{0.5}Nb_{0.5}O_3)-(Co_{0.6}Zn_{0.4}Fe_{1.7}Mn_{0.3}O_4)$ composites*, Scientific Reports **11**, 3149 (2021).
- [255] V. Risinggård, I. Kulagina, J. Linder, *Electric field control of magnon-induced magnetization dynamics in multiferroics*, Scientific Reports **6**, 31800 (2016).
- [256] C. Bell, S. Milikisyants, M. Huber, J. Aarts, *Spin Dynamics in a Superconductor-Ferromagnet Proximity System*, Physical Review Letters **100**, 047002 (2008).
- [257] Y. Yao, Q. Song, Y. Takamura, J.P. Cascales, W. Yuan, Y. Ma, Y. Yun, X.C. Xie, J.S. Moodera, W. Han, *Probe of spin dynamics in superconducting NbN thin films via spin pumping*, Physical Review B **97**, 224414 (2018).

- [258] M. Tinkham, *Introduction to Superconductivity*, Dover Books on Physics Series, Dover Publications (2004).
- [259] J. Annett, *Superconductivity, Superfluids and Condensates*, Oxford Master Series in Physics, OUP Oxford (2004).
- [260] R. Kleiner, W. Buckel, R. Huebener, *Superconductivity: An Introduction*, Wiley (2016).
- [261] S. Pittard, P. Feenan, W. Vennart, *Superconducting magnets for magnetic resonance imaging*, Applied Superconductivity **1**, 1827 (1993).
- [262] M. Lakrimi, A.M. Thomas, G. Hutton, M. Kruip, R. Slade, P. Davis, A.J. Johnstone, M.J. Longfield, H. Blakes, S. Calvert, M. Smith, C.A. Marshall, *The principles and evolution of magnetic resonance imaging*, Journal of Physics: Conference Series **286**, 012016 (2011).
- [263] H. Thomas, A. Marian, A. Chervyakov, S. Stückrad, D. Salmieri, C. Rubbia, *Superconducting transmission lines – Sustainable electric energy transfer with higher public acceptance?*, Renewable and Sustainable Energy Reviews **55**, 59 (2016).
- [264] J. Jin, L. Wang, R. Yang, T. Zhang, S. Mu, Q. Zhou, *A composite superconducting energy pipeline and its characteristics*, Energy Reports **8**, 2072 (2022).
- [265] M. Cullinane, F. Judge, M. O'Shea, K. Thandayutham, J. Murphy, *Subsea superconductors: The future of offshore renewable energy transmission?*, Renewable and Sustainable Energy Reviews **156**, 111943 (2022).
- [266] J. Bardeen, L.N. Cooper, J.R. Schrieffer, *Theory of Superconductivity*, Physical Review **108**, 1175 (1957).
- [267] J. Linder, J.W.A. Robinson, *Superconducting spintronics*, Nature Physics **11**, 307 (2015).
- [268] G. Yang, C. Ciccarelli, J.W.A. Robinson, *Boosting spintronics with superconductivity*, APL Materials **9**, 050703 (2021).
- [269] D. Beckmann, *Spin manipulation in nanoscale superconductors*, Journal of Physics Condensed Matter **28**, 163001 (2016).
- [270] M. Inoue, M. Ichioka, H. Adachi, *Spin pumping into superconductors: A new probe of spin dynamics in a superconducting thin film*, Physical Review B **96**, 024414 (2017).
- [271] T. Kato, Y. Ohnuma, M. Matsuo, J. Rech, T. Jonckheere, T. Martin, *Microscopic theory of spin transport at the interface between a superconductor and a ferromagnetic insulator*, Physical Review B **99**, 144411 (2019).

- [272] J.P. Morten, A. Brataas, G.E.W. Bauer, W. Belzig, Y. Tserkovnyak, *Proximity-effect-assisted decay of spin currents in superconductors*, Europhysics Letters **84**, 57008 (2008).
- [273] R.S. Keizer, S.T.B. Goennenwein, T.M. Klapwijk, G. Miao, G. Xiao, A. Gupta, *A spin triplet supercurrent through the half-metallic ferromagnet CrO₂*, Nature **439**, 825 (2006).
- [274] K.R. Jeon, C. Ciccarelli, H. Kurebayashi, L.F. Cohen, X. Montiel, M. Eschrig, S. Komori, J.W.A. Robinson, M.G. Blamire, *Exchange-field enhancement of superconducting spin pumping*, Physical Review B **99**, 024507 (2019).
- [275] K.R. Jeon, X. Montiel, S. Komori, C. Ciccarelli, J. Haigh, H. Kurebayashi, L.F. Cohen, A.K. Chan, K.D. Stenning, C.M. Lee, M.G. Blamire, J.W. Robinson, *Tunable Pure Spin Supercurrents and the Demonstration of Their Gateability in a Spin-Wave Device*, Physical Review X **10**, 31020 (2020).
- [276] A. Vargunin, M. Silaev, *Flux flow spin Hall effect in type-II superconductors with spin-splitting field*, Scientific Reports **9**, 5914 (2019).
- [277] R. Asaoka, H. Tsuchiura, M. Sigrist, *Spin-current induced around half-quantum vortices in chiral p-wave superconducting states*, Journal of Physics: Conference Series **871**, 012025 (2017).
- [278] T. Taira, Y. Kato, M. Ichioka, H. Adachi, *Spin Hall effect generated by fluctuating vortices in type-II superconductors*, Physical Review B **103**, 1 (2021).
- [279] K. Rogdakis, A. Sud, M. Amado, C.M. Lee, L. McKenzie-Sell, K.R. Jeon, M. Cubukcu, M.G. Blamire, J.W.A. Robinson, L.F. Cohen, H. Kurebayashi, *Spin transport parameters of NbN thin films characterized by spin pumping experiments*, Physical Review Materials **3**, 14406 (2019).
- [280] A. Hoffmann, *Spin Hall Effects in Metals*, IEEE Transactions on Magnetism **49**, 5172 (2013).
- [281] J. Gückelhorn, A. Kamra, T. Wimmer, M. Opel, S. Geprägs, R. Gross, H. Huebl, M. Althammer, *Influence of low-energy magnons on magnon Hanle experiments in easy-plane antiferromagnets*, Physical Review B **105**, 094440 (2022).
- [282] N. Poli, J.P. Morten, M. Urech, A. Brataas, D.B. Haviland, V. Korenivski, *Spin Injection and Relaxation in a Mesoscopic Superconductor*, Physical Review Letters **100**, 136601 (2008).
- [283] H. Yang, S.H. Yang, S. Takahashi, S. Maekawa, S.S.P. Parkin, *Extremely long quasiparticle spin lifetimes in superconducting aluminium using MgO tunnel spin injectors*, Nature Materials **9**, 586 (2010).

- [284] J.Y. Gu, J.A. Caballero, R.D. Slater, R. Loloee, W.P. Pratt, *Direct measurement of quasiparticle evanescent waves in a dirty superconductor*, Physical Review B **66**, 140507 (2002).
- [285] K.R. Jeon, C. Ciccarelli, H. Kurebayashi, J. Wunderlich, L.F. Cohen, S. Komori, J.W.A. Robinson, M.G. Blamire, *Spin-Pumping-Induced Inverse Spin Hall Effect in Nb/Ni₈₀Fe₂₀ Bilayers and its Strong Decay Across the Superconducting Transition Temperature*, Physical Review Applied **10**, 014029 (2018).
- [286] K.R. Jeon, C. Ciccarelli, H. Kurebayashi, L.F. Cohen, X. Montiel, M. Eschrig, S. Komori, J.W.A. Robinson, M.G. Blamire, *Exchange-field enhancement of superconducting spin pumping*, Physical Review B **99**, 024507 (2019).
- [287] K.R. Jeon, C. Ciccarelli, H. Kurebayashi, L.F. Cohen, X. Montiel, M. Eschrig, T. Wagner, S. Komori, A. Srivastava, J.W. Robinson, M.G. Blamire, *Effect of Meissner Screening and Trapped Magnetic Flux on Magnetization Dynamics in Thick Nb/Ni₈₀Fe₂₀/Nb Trilayers*, Physical Review Applied **11**, 014061 (2019).
- [288] K.R. Jeon, C. Ciccarelli, H. Kurebayashi, L.F. Cohen, S. Komori, J.W.A. Robinson, M.G. Blamire, *Abrikosov vortex nucleation and its detrimental effect on superconducting spin pumping in Pt/Nb/Ni₈₀Fe₂₀/Nb/Pt proximity structures*, Physical Review B **99**, 144503 (2019).
- [289] S.H. Jacobsen, J.A. Ouassou, J. Linder, *Critical temperature and tunneling spectroscopy of superconductor-ferromagnet hybrids with intrinsic Rashba-Dresselhaus spin-orbit coupling*, Physical Review B **92**, 024510 (2015).
- [290] F.S. Bergeret, I.V. Tokatly, *Spin-orbit coupling as a source of long-range triplet proximity effect in superconductor-ferromagnet hybrid structures*, Physical Review B **89**, 134517 (2014).
- [291] S. Nadj-Perge, I.K. Drozdov, J. Li, H. Chen, S. Jeon, J. Seo, A.H. MacDonald, B.A. Bernevig, A. Yazdani, *Observation of Majorana fermions in ferromagnetic atomic chains on a superconductor*, Science **346**, 602 (2014).
- [292] E. Sajadi, T. Palomaki, Z. Fei, W. Zhao, P. Bement, C. Olsen, S. Luescher, X. Xu, J.A. Folk, D.H. Cobden, *Gate-induced superconductivity in a monolayer topological insulator*, Science **362**, 922 (2018).
- [293] V. Fatemi, S. Wu, Y. Cao, L. Bretheau, Q.D. Gibson, K. Watanabe, T. Taniguchi, R.J. Cava, P. Jarillo-Herrero, *Electrically tunable low-density superconductivity in a monolayer topological insulator*, Science **362**, 926 (2018).
- [294] X. Zhang, J. Wang, Y. Liu, W. Zheng, J. Wang, *Superconductivity in large spin-orbit coupled material IrTe₂*, Journal of Physics and Chemistry of Solids **128**, 245 (2019).

- [295] J.J. He, K. Hiroki, K. Hamamoto, N. Nagaosa, *Spin supercurrent in two-dimensional superconductors with Rashba spin-orbit interaction*, Communications Physics **2**, 128 (2019).
- [296] M. Sato, *Majorana fermions in topological superconductors with spin-orbit interaction*, Journal of Physics: Conference Series **391**, 012150 (2012).
- [297] M. Sato, S. Fujimoto, *Existence of Majorana Fermions and Topological Order in Nodal Superconductors with Spin-Orbit Interactions in External Magnetic Fields*, Physical Review Letters **105**, 217001 (2010).
- [298] M.M. Desjardins, L.C. Contamin, M.R. Delbecq, M.C. Dartiailh, L.E. Bruhat, T. Cubaynes, J.J. Viennot, F. Mallet, S. Rohart, A. Thiaville, A. Cottet, T. Kontos, *Synthetic spin-orbit interaction for Majorana devices*, Nature Materials **18**, 1060 (2019).
- [299] K.M.D. Hals, *Supercurrent-induced spin-orbit torques*, Physical Review B **93**, 115431 (2016).
- [300] M. Alishahi, F. Mahboubi, S.M. Mousavi Khoie, M. Aparicio, E. Lopez-Elvira, J. Méndez, R. Gago, *Structural properties and corrosion resistance of tantalum nitride coatings produced by reactive DC magnetron sputtering*, RSC Advances **6**, 89061 (2016).
- [301] K. Baba, R. Hatada, *Synthesis and properties of tantalum nitride films formed by ion beam assisted deposition*, Surface and Coatings Technology **84**, 429 (1996).
- [302] J.H. Han, H.Y. Kim, S.C. Lee, D.H. Kim, B.K. Park, J.S. Park, D.J. Jeon, T.M. Chung, C.G. Kim, *Growth of tantalum nitride film as a Cu diffusion barrier by plasma-enhanced atomic layer deposition from bis((2-(dimethylamino)ethyl)(methyl)amido)methyl(tert-butylimido)tantalum complex*, Applied Surface Science **362**, 176 (2016).
- [303] S. Cho, K. Kim, S. Min, H. Shin, S. Kimd, *Diffusion Barrier Properties of Metallorganic Chemical Vapor Deposited Tantalum Nitride Films Against Cu Metallization*, Journal of The Electrochemical Society **146**, 3724 (1999).
- [304] T. Laurila, K. Zeng, J. Kivilahti, J. Molarius, T. Riekkinen, I. Suni, *Tantalum carbide and nitride diffusion barriers for Cu metallisation*, Microelectronic Engineering **60**, 71 (2002).
- [305] E.B. Rosa, *The self and mutual-inductances of linear conductors*, Bulletin of the Bureau of Standards **4**, 301 (1908).
- [306] F. London, H. London, *The electromagnetic equations of the supraconductor*, Proceedings of the Royal Society of London. Series A - Mathematical and Physical Sciences **149**, 71 (1935).

- [307] W. Meissner, R. Ochsenfeld, *Ein neuer Effekt bei Eintritt der Supraleitfähigkeit*, Die Naturwissenschaften **21**, 787 (1933).
- [308] H. Głowiński, M. Schmidt, I. Gościańska, J.P. Ansermet, J. Dubowik, *Coplanar waveguide based ferromagnetic resonance in ultrathin film magnetic nanostructures: Impact of conducting layers*, Journal of Applied Physics **116**, 053901 (2014).
- [309] B. Huang, M.A. McGuire, A.F. May, D. Xiao, P. Jarillo-Herrero, X. Xu, *Emergent phenomena and proximity effects in two-dimensional magnets and heterostructures.*, Nature Materials **19**, 1276 (2020).
- [310] Q.H. Wang, A. Bedoya-Pinto, M. Blei, A.H. Dismukes, A. Hamo, S. Jenkins, M. Koperski, Y. Liu, Q.C. Sun, E.J. Telford, H.H. Kim, M. Augustin, U. Vool, J.X. Yin, L.H. Li, A. Falin, C.R. Dean, F. Casanova, R.F.L. Evans, M. Chshiev, A. Mishchenko, C. Petrovic, R. He, L. Zhao, A.W. Tsen, B.D. Gerardot, M. Brotons-Gisbert, Z. Guguchia, X. Roy, S. Tongay, Z. Wang, M.Z. Hasan, J. Wrachtrup, A. Yacoby, A. Fert, S. Parkin, K.S. Novoselov, P. Dai, L. Balicas, E.J.G. Santos, *The Magnetic Genome of Two-Dimensional van der Waals Materials*, ACS Nano **16**, 6960 (2022).
- [311] C.W. Zollitsch, S. Khan, V.T.T. Nam, I.A. Verzhbitskiy, D. Sagkovits, J. O'Sullivan, O.W. Kennedy, M. Strungaru, E.J.G. Santos, J.J.L. Morton, G. Eda, H. Kurebayashi, *Probing spin dynamics of ultra-thin van der Waals magnets via photon-magnon coupling*, Nature Communications **14**, 2619 (2023).
- [312] A.I. Gubin, K.S. Il'in, S.A. Vitusevich, M. Siegel, N. Klein, *Dependence of magnetic penetration depth on the thickness of superconducting Nb thin films*, Physical Review B **72**, 064503 (2005).
- [313] G. Horn, E. Saur, *Präparation und Supraleitungseigenschaften von Niobnitrid sowie Niobnitrid mit Titan-, Zirkon- und Tantalzusatz*, Zeitschrift für Physik A Hadrons and nuclei **210**, 70 (1968).
- [314] D. Hazra, N. Tsavdaris, S. Jebari, A. Grimm, F. Blanchet, F. Mercier, E. Blanquet, C. Chapelier, M. Hofheinz, *Superconducting properties of very high quality NbN thin films grown by high temperature chemical vapor deposition*, Superconductor Science and Technology **29**, 105011 (2016).
- [315] M. Chand, A. Mishra, Y.M. Xiong, A. Kamlapure, S.P. Chockalingam, J. Jesudasan, V. Bagwe, M. Mondal, P.W. Adams, V. Tripathi, P. Raychaudhuri, *Temperature dependence of resistivity and Hall coefficient in strongly disordered NbN thin films*, Physical Review B **80**, 134514 (2009).
- [316] I. Golovchanskiy, N. Abramov, V. Stolyarov, V. Chichkov, M. Silaev, I. Shchetinin, A. Golubov, V. Ryazanov, A. Ustinov, M. Kupriyanov, *Magnetization Dynamics in Proximity-Coupled Superconductor-Ferromagnet-Superconductor Multilayers*, Physical Review Applied **14**, 024086 (2020).

- [317] C. Luo, Z. Feng, Y. Fu, W. Zhang, P.K.J. Wong, Z.X. Kou, Y. Zhai, H.F. Ding, M. Farle, J. Du, H.R. Zhai, *Enhancement of magnetization damping coefficient of permalloy thin films with dilute Nd dopants*, Physical Review B **89**, 184412 (2014).
- [318] A. Ghosh, J.F. Sierra, S. Auffret, U. Ebels, W.E. Bailey, *Dependence of nonlocal Gilbert damping on the ferromagnetic layer type in ferromagnet/Cu/Pt heterostructures*, Applied Physics Letters **98**, 052508 (2011).
- [319] D. Einzel, *Universal Parameters in the Response of Unconventional Superconductors*, Journal of Low temperature physics **126**, 867 (2002).
- [320] D. Einzel, *Interpolation of BCS response functions*, Journal of Low Temperature Physics **130**, 493 (2003).
- [321] A.J. Annunziata, D.F. Santavicca, L. Frunzio, G. Catelani, M.J. Rooks, A. Frydman, D.E. Prober, *Tunable superconducting nanoinductors*, Nanotechnology **21**, 445202 (2010).
- [322] Y. Sun, *Superconducting spintronics with magnetic insulators*, Master's Thesis (2023).
- [323] W. Yan, E. Sagasta, M. Ribeiro, Y. Niimi, L.E. Hueso, F. Casanova, *Large room temperature spin-to-charge conversion signals in a few-layer graphene/Pt lateral heterostructure*, Nature Communications **8**, 661 (2017).
- [324] T. Kimura, Y. Otani, T. Sato, S. Takahashi, S. Maekawa, *Room-Temperature Reversible Spin Hall Effect*, Physical Review Letters **98**, 156601 (2007).
- [325] S. Takahashi, S. Maekawa, *Spin Hall Effect in Superconductors*, Japanese Journal of Applied Physics **51**, 010110 (2012).
- [326] S. Takahashi, S. Maekawa, *Spin Current in Metals and Superconductors*, Journal of the Physical Society of Japan **77**, 031009 (2008).
- [327] H. Kontani, J. Goryo, D.S. Hirashima, *Intrinsic Spin Hall Effect in the s-Wave Superconducting State: Analysis of the Rashba Model*, Physical Review Letters **102**, 086602 (2009).
- [328] S. Takahashi, S. Maekawa, *Hall Effect Induced by a Spin-Polarized Current in Superconductors*, Physical Review Letters **88**, 116601 (2002).
- [329] S. Takahashi, T. Yamashita, H. Imamura, S. Maekawa, *Spin-relaxation and magnetoresistance in FM/SC/FM tunnel junctions*, Journal of Magnetism and Magnetic Materials **240**, 100 (2002).
- [330] L. Berger, *Side-Jump Mechanism for the Hall Effect of Ferromagnets*, Physical Review B **2**, 4559 (1970).

- [331] A. Fert, A. Friederich, *Skew scattering by rare-earth impurities in silver, gold, and aluminum*, Physical Review B **13**, 397 (1976).
- [332] S. Onoda, N. Sugimoto, N. Nagaosa, *Intrinsic Versus Extrinsic Anomalous Hall Effect in Ferromagnets*, Physical Review Letters **97**, 126602 (2006).
- [333] S. Mironov, A. Buzdin, *Spontaneous Currents in Superconducting Systems with Strong Spin-Orbit Coupling*, Physical Review Letters **118**, 077001 (2017).
- [334] S. Mironov, A.S. Mel'nikov, A. Buzdin, *Electromagnetic proximity effect in planar superconductor-ferromagnet structures*, Applied Physics Letters **113**, 022601 (2018).
- [335] O.V. Dobrovolskiy, R. Sachser, M. Huth, V.A. Shklovskij, R.V. Vovk, V.M. Bevz, M.I. Tsindlekht, *Radiofrequency generation by coherently moving fluxons*, Applied Physics Letters **112**, 152601 (2018).
- [336] A.A. Awad, F.G. Aliev, G.W. Ataklti, A. Silhanek, V.V. Moshchalkov, Y.M. Galperin, V. Vinokur, *Flux avalanches triggered by microwave depinning of magnetic vortices in Pb superconducting films*, Physical Review B **84**, 224511 (2011).
- [337] J.A. Ouassou, W. Belzig, J. Linder, *Prediction of a Paramagnetic Meissner Effect in Voltage-Biased Superconductor–Normal-Metal Bilayers*, Physical Review Letters **124**, 047001 (2020).
- [338] K. Il'in, M. Hofherr, D. Rall, M. Siegel, A. Semenov, A. Engel, K. Inderbitzin, A. Aeschbacher, A. Schilling, *Ultra-thin TaN Films for Superconducting Nanowire Single-Photon Detectors*, Journal of Low Temperature Physics **167**, 809 (2012).
- [339] K.S. Il'in, D. Rall, M. Siegel, A. Semenov, *Critical current density in thin superconducting TaN film structures*, Physica C: Superconductivity **479**, 176 (2012).
- [340] C.S. Shin, D. Gall, Y.W. Kim, P. Desjardins, I. Petrov, J.E. Greene, M. Odén, L. Hultman, *Epitaxial NaCl structure δ -TaNx(001): Electronic transport properties, elastic modulus, and hardness versus N/Ta ratio*, Journal of Applied Physics **90**, 2879 (2001).
- [341] S. Chaudhuri, I.J. Maasilta, L. Chandernagor, M. Ging, M. Lahtinen, *Fabrication of superconducting tantalum nitride thin films using infrared pulsed laser deposition*, Journal of Vacuum Science & Technology A: Vacuum, Surfaces, and Films **31**, 061502 (2013).
- [342] C.R.A. Catlow, J.M. Thomas, C.M. Freeman, P.A. Wright, R.G. Bell, *Simulating and Predicting Crystal Structures*, Proceedings of the Royal Society A: Mathematical, Physical and Engineering Sciences **442**, 85 (1993).

- [343] N.P. Breznay, K. Michaeli, K.S. Tikhonov, A.M. Finkel'stein, M. Tendulkar, A. Kapitulnik, *Hall conductivity dominated by fluctuations near the superconducting transition in disordered thin films*, Physical Review B **86**, 014514 (2012).
- [344] K. Wakasugi, M. Tokunaga, T. Sumita, H. Kubota, M. Nagata, Y. Honda, *Superconductivity of reactivity sputtered TaN film for ULSI process*, Physica B: Condensed Matter **239**, 29 (1997).
- [345] T. Hashizume, A. Saiki, K. Terayama, *Fabrication of Tantalum nitride thin film using the low vacuum magnetron sputtering system*, IOP Conference Series: Materials Science and Engineering **18**, 092032 (2011).
- [346] R.M. Hill, *Variable-range hopping*, Physica Status Solidi (a) **34**, 601 (1976).
- [347] N.F. Mott, *Conduction in non-crystalline materials*, Philosophical Magazine **19**, 835 (1969).
- [348] N.P. Breznay, M. Tendulkar, L. Zhang, S.C. Lee, A. Kapitulnik, *Superconductor to weak-insulator transitions in disordered tantalum nitride films*, Physical Review B **96**, 134522 (2017).
- [349] W. Schoepe, *Variable-range hopping conduction in doped germanium at very low temperatures and high magnetic fields*, Zeitschrift für Physik B Condensed Matter **71**, 455 (1988).
- [350] D. Yu, C. Wang, B.L. Wehrenberg, P. Guyot-Sionnest, *Variable Range Hopping Conduction in Semiconductor Nanocrystal Solids*, Physical Review Letters **92**, 216802 (2004).
- [351] S. Arrhenius, *Über die Reaktionsgeschwindigkeit bei der Inversion von Rohrzucker durch Säuren*, Zeitschrift für Physikalische Chemie **4U**, 226 (1889).
- [352] S. Arrhenius, *Über die Dissociationswärme und den Einfluss der Temperatur auf den Dissociationsgrad der Elektrolyte*, Zeitschrift für Physikalische Chemie **4U**, 96 (1889).
- [353] G. Counil, T. Devolder, J.V. Kim, P. Crozat, C. Chappert, S. Zoll, R. Fournel, *Temperature Dependences of the Resistivity and the Ferromagnetic Resonance Linewidth in Permalloy Thin Films*, IEEE Transactions on Magnetics **42**, 3323 (2006).
- [354] A. Zaman, E. Meletis, *Microstructure and Mechanical Properties of TaN Thin Films Prepared by Reactive Magnetron Sputtering*, Coatings **7**, 209 (2017).
- [355] M. Silaev, *Anderson-Higgs Mass of Magnons in Superconductor-Ferromagnet-Superconductor Systems*, Physical Review Applied **18**, L061004 (2022).

- [356] P.W. Swatek, X. Hang, Y. Fan, W. Jiang, H. Yun, D. Lyu, D. Zhang, T.J. Peterson, P. Sahu, O.J. Benally, Z. Cresswell, J. Liu, R. Pahari, D. Kukla, T. Low, K.A. Mkhoyan, J.p. Wang, *Room temperature spin-orbit torque efficiency in sputtered low-temperature superconductor δ -TaN*, *Physical Review Materials* **6**, 074206 (2022).
- [357] T. Wakamura, N. Hasegawa, K. Ohnishi, Y. Niimi, Y. Otani, *Spin Injection into a Superconductor with Strong Spin-Orbit Coupling*, *Physical Review Letters* **112**, 036602 (2014).
- [358] A.I. Buzdin, *Proximity effects in superconductor-ferromagnet heterostructures*, *Reviews of Modern Physics* **77**, 935 (2005).
- [359] J.S. Jiang, D. Davidović, D.H. Reich, C.L. Chien, *Oscillatory Superconducting Transition Temperature in Nb/Gd Multilayers*, *Physical Review Letters* **74**, 314 (1995).
- [360] M.G. Khusainov, Y.N. Proshin, *Possibility of periodically reentrant superconductivity in ferromagnet/superconductor layered structures*, *Physical Review B* **56**, R14283 (1997).
- [361] C. Gorter, H. Casimir, *On supraconductivity I*, *Physica* **1**, 306 (1934).
- [362] L. Chirulli, M.T. Mercaldo, C. Guarcello, F. Giazotto, M. Cuoco, *Colossal Orbital Edelstein Effect in Noncentrosymmetric Superconductors*, *Physical Review Letters* **128**, 217703 (2022).
- [363] S.J. Carreira, D. Sanchez-Manzano, M.W. Yoo, K. Seurre, V. Rouco, A. Sander, J. Santamaría, A. Anane, J.E. Villegas, *Spin pumping in d-wave superconductor-ferromagnet hybrids*, *Physical Review B* **104**, 144428 (2021).
- [364] Y. Yao, R. Cai, T. Yu, Y. Ma, W. Xing, Y. Ji, X.C. Xie, S.H. Yang, W. Han, *Giant oscillatory Gilbert damping in superconductor/ferromagnet/superconductor junctions*, *Science Advances* **7**, eabh3686 (2021).
- [365] L. Liensberger, L. Flacke, D. Rogerson, M. Althammer, R. Gross, M. Weiler, *Spin-Wave Propagation in Metallic $\text{Co}_{25}\text{Fe}_{75}$ Films Determined by Microfocused Frequency-Resolved Magneto-Optic Kerr Effect*, *IEEE Magnetics Letters* **10**, 5503905 (2019).
- [366] A. Blais, A.L. Grimsmo, S.M. Girvin, A. Wallraff, *Circuit quantum electrodynamics*, *Reviews of Modern Physics* **93**, 025005 (2021).
- [367] I. Chiorescu, P. Bertet, K. Semba, Y. Nakamura, C.J.P.M. Harmans, J.E. Mooij, *Coherent dynamics of a flux qubit coupled to a harmonic oscillator*, *Nature* **431**, 159 (2004).

- [368] A. Wallraff, D.I. Schuster, A. Blais, L. Frunzio, R.S. Huang, J. Majer, S. Kumar, S.M. Girvin, R.J. Schoelkopf, *Strong coupling of a single photon to a superconducting qubit using circuit quantum electrodynamics*, *Nature* **431**, 162 (2004).
- [369] Y.P. Korneeva, D.Y. Vodolazov, A.V. Semenov, I.N. Florya, N. Simonov, E. Baeva, A.A. Korneev, G.N. Goltsman, T.M. Klapwijk, *Optical Single-Photon Detection in Micrometer-Scale NbN Bridges*, *Physical Review Applied* **9**, 064037 (2018).
- [370] S.N. Dorenbos, P. Forn-Díaz, T. Fuse, A.H. Verbruggen, T. Zijlstra, T.M. Klapwijk, V. Zwiller, *Low gap superconducting single photon detectors for infrared sensitivity*, *Applied Physics Letters* **98**, 251102 (2011).
- [371] G. Reithmaier, S. Lichtmanecker, T. Reichert, P. Hasch, K. Müller, M. Bichler, R. Gross, J.J. Finley, *On-chip time resolved detection of quantum dot emission using integrated superconducting single photon detectors*, *Scientific Reports* **3**, 1901 (2013).
- [372] N. Bergeal, R. Vijay, V.E. Manucharyan, I. Siddiqi, R.J. Schoelkopf, S.M. Girvin, M.H. Devoret, *Analog information processing at the quantum limit with a Josephson ring modulator*, *Nature Physics* **6**, 296 (2010).
- [373] M.A. Castellanos-Beltran, K.W. Lehnert, *Widely tunable parametric amplifier based on a superconducting quantum interference device array resonator*, *Applied Physics Letters* **91**, 083509 (2007).
- [374] E.A. Tholén, A. Ergül, E.M. Doherty, F.M. Weber, F. Grégis, D.B. Haviland, *Nonlinearities and parametric amplification in superconducting coplanar waveguide resonators*, *Applied Physics Letters* **90**, 253509 (2007).
- [375] M. Aspelmeyer, T.J. Kippenberg, F. Marquardt, *Cavity optomechanics*, *Reviews of Modern Physics* **86**, 1391 (2014).
- [376] Y. Li, T. Polakovic, Y.L. Wang, J. Xu, S. Lendinez, Z. Zhang, J. Ding, T. Khairé, H. Saglam, R. Divan, J. Pearson, W.K. Kwok, Z. Xiao, V. Novosad, A. Hoffmann, W. Zhang, *Strong Coupling between Magnons and Microwave Photons in On-Chip Ferromagnet-Superconductor Thin-Film Devices*, *Physical Review Letters* **123**, 107701 (2019).
- [377] Y. Tabuchi, S. Ishino, T. Ishikawa, R. Yamazaki, K. Usami, Y. Nakamura, *Hybridizing Ferromagnetic Magnons and Microwave Photons in the Quantum Limit*, *Physical Review Letters* **113**, 083603 (2014).
- [378] D.I. Schuster, A.P. Sears, E. Ginossar, L. DiCarlo, L. Frunzio, J.J.L. Morton, H. Wu, G.A.D. Briggs, B.B. Buckley, D.D. Awschalom, R.J. Schoelkopf, *High-*

Cooperativity Coupling of Electron-Spin Ensembles to Superconducting Cavities, Physical Review Letters **105**, 140501 (2010).

- [379] Y. Kubo, C. Grezes, A. Dewes, T. Umeda, J. Isoya, H. Sumiya, N. Morishita, H. Abe, S. Onoda, T. Ohshima, V. Jacques, A. Dréau, J.F. Roch, I. Diniz, A. Auffeves, D. Vion, D. Esteve, P. Bertet, *Hybrid Quantum Circuit with a Superconducting Qubit Coupled to a Spin Ensemble*, Physical Review Letters **107**, 220501 (2011).
- [380] J. Majer, J.M. Chow, J.M. Gambetta, J. Koch, B.R. Johnson, J.A. Schreier, L. Frunzio, D.I. Schuster, A.A. Houck, A. Wallraff, A. Blais, M.H. Devoret, S.M. Girvin, R.J. Schoelkopf, *Coupling superconducting qubits via a cavity bus*, Nature **449**, 443 (2007).
- [381] S. Weichselbaumer, M. Zens, C.W. Zollitsch, M.S. Brandt, S. Rotter, R. Gross, H. Huebl, *Echo Trains in Pulsed Electron Spin Resonance of a Strongly Coupled Spin Ensemble*, Physical Review Letters **125**, 137701 (2020).
- [382] C.W. Zollitsch, K. Mueller, D.P. Franke, S.T.B. Goennenwein, M.S. Brandt, R. Gross, H. Huebl, *High cooperativity coupling between a phosphorus donor spin ensemble and a superconducting microwave resonator*, Applied Physics Letters **107**, 142105 (2015).
- [383] R. Narkowicz, D. Suter, R. Stonies, *Planar microresonators for EPR experiments*, Journal of Magnetic Resonance **175**, 275 (2005).
- [384] W.J. Wallace, R.H. Silsbee, *Microstrip resonators for electron-spin resonance*, Review of Scientific Instruments **62**, 1754 (1991).
- [385] S. Kim, H. Terai, T. Yamashita, W. Qiu, T. Fuse, F. Yoshihara, S. Ashhab, K. Inomata, K. Semba, *Enhanced coherence of all-nitride superconducting qubits epitaxially grown on silicon substrate*, Communications Materials **2**, 98 (2021).
- [386] M. Lyatti, M.A. Wolff, I. Gundareva, M. Kruth, S. Ferrari, R.E. Dunin-Borkowski, C. Schuck, *Energy-level quantization and single-photon control of phase slips in $\text{YBa}_2\text{Cu}_3\text{O}_{7-x}$ nanowires*, Nature Communications **11**, 763 (2020).
- [387] R. Di Leo, A. Nigro, G. Nobile, R. Vaglio, *Niobium-titanium nitride thin films for superconducting rf accelerator cavities*, Journal of Low Temperature Physics **78**, 41 (1990).
- [388] C.M. Yen, L.E. Toth, Y.M. Shy, D.E. Anderson, L.G. Rosner, *Superconducting $H_c - J_c$ and T_c Measurements in the Nb-Ti-N, Nb-Hf-N, and Nb-V-N Ternary Systems*, Journal of Applied Physics **38**, 2268 (1967).
- [389] E.R. Edwards, H.T. Nembach, J.M. Shaw, *$\text{Co}_{25}\text{Fe}_{75}$ Thin Films with Ultralow Total Damping of Ferromagnetic Resonance*, Physical Review Applied **11**, 054036 (2019).

- [390] M.A.W. Schoen, D. Thonig, M.L. Schneider, T.J. Silva, H.T. Nembach, O. Eriksson, O. Karis, J.M. Shaw, *Ultra-low magnetic damping of a metallic ferromagnet*, *Nature Physics* **12**, 839 (2016).
- [391] C. Müller, J.H. Cole, J. Lisenfeld, *Towards understanding two-level-systems in amorphous solids: insights from quantum circuits*, *Reports on Progress in Physics* **82**, 124501 (2019).
- [392] M.V.P. Altoé, A. Banerjee, C. Berk, A. Hajr, A. Schwartzberg, C. Song, M. Alghadeer, S. Aloni, M.J. Elowson, J.M. Kreikebaum, E.K. Wong, S.M. Griffin, S. Rao, A. Weber-Bargioni, A.M. Minor, D.I. Santiago, S. Cabrini, I. Siddiqi, D.F. Ogletree, *Localization and Mitigation of Loss in Niobium Superconducting Circuits*, *PRX Quantum* **3**, 020312 (2022).
- [393] J. Goetz, *The Interplay of Superconducting Quantum Circuits and Propagating Microwave States*, PhD Thesis (2017).
- [394] I. Nsanzineza, B.L.T. Plourde, *Trapping a Single Vortex and Reducing Quasiparticles in a Superconducting Resonator*, *Physical Review Letters* **113**, 117002 (2014).
- [395] G. Stan, S.B. Field, J.M. Martinis, *Critical Field for Complete Vortex Expulsion from Narrow Superconducting Strips*, *Physical Review Letters* **92**, 097003 (2004).
- [396] M. Sandberg, M.R. Vissers, T.A. Ohki, J. Gao, J. Aumentado, M. Weides, D.P. Pappas, *Radiation-suppressed superconducting quantum bit in a planar geometry*, *Applied Physics Letters* **102**, 072601 (2013).
- [397] H. Paik, D.I. Schuster, L.S. Bishop, G. Kirchmair, G. Catelani, A.P. Sears, B.R. Johnson, M.J. Reagor, L. Frunzio, L.I. Glazman, S.M. Girvin, M.H. Devoret, R.J. Schoelkopf, *Observation of High Coherence in Josephson Junction Qubits Measured in a Three-Dimensional Circuit QED Architecture*, *Physical Review Letters* **107**, 240501 (2011).
- [398] J.M. Martinis, K.B. Cooper, R. McDermott, M. Steffen, M. Ansmann, K.D. Osborn, K. Cicak, S. Oh, D.P. Pappas, R.W. Simmonds, C.C. Yu, *Decoherence in Josephson Qubits from Dielectric Loss*, *Physical Review Letters* **95**, 210503 (2005).
- [399] W.A. Phillips, *Two-level states in glasses*, *Reports on Progress in Physics* **50**, 1657 (1987).
- [400] H. Wang, M. Hofheinz, J. Wenner, M. Ansmann, R.C. Bialczak, M. Lenander, E. Lucero, M. Neeley, A.D. O'Connell, D. Sank, M. Weides, A.N. Cleland, J.M. Martinis, *Improving the coherence time of superconducting coplanar resonators*, *Applied Physics Letters* **95**, 233508 (2009).

- [401] A. Melville, G. Calusine, W. Woods, K. Serniak, E. Golden, B.M. Niedzielski, D.K. Kim, A. Sevi, J.L. Yoder, E.A. Dauler, W.D. Oliver, *Comparison of dielectric loss in titanium nitride and aluminum superconducting resonators*, Applied Physics Letters **117**, 124004 (2020).
- [402] A. Bruno, G. de Lange, S. Asaad, K.L. van der Enden, N.K. Langford, L. DiCarlo, *Reducing intrinsic loss in superconducting resonators by surface treatment and deep etching of silicon substrates*, Applied Physics Letters **106**, 182601 (2015).
- [403] A.M. Holder, K.D. Osborn, C.J. Lobb, C.B. Musgrave, *Bulk and Surface Tunneling Hydrogen Defects in Alumina*, Physical Review Letters **111**, 065901 (2013).
- [404] D. Bunch, *Minimizing Losses in Superconducting Coplanar Waveguide Resonators*, Master's Thesis (2022).
- [405] K. Agarwal, I. Martin, M.D. Lukin, E. Demler, *Polaronic model of two-level systems in amorphous solids*, Physical Review B **87**, 144201 (2013).
- [406] H. Kikyuama, N. Miki, K. Saka, J. Takano, I. Kawanabe, M. Miyashita, T. Ohmi, *Principles of Wet Chemical Processing in ULSI Microfabrication*, IEEE Transactions on Semiconductor Manufacturing **4**, 26 (1991).
- [407] N.E. Grant, J.D. Murphy, *Temporary Surface Passivation for Characterisation of Bulk Defects in Silicon: A Review*, physica status solidi (RRL) - Rapid Research Letters **11**, 1700243 (2017).
- [408] M.R. Vissers, J. Gao, D.S. Wisbey, D.A. Hite, C.C. Tsuei, A.D. Corcoles, M. Steffen, D.P. Pappas, *Low loss superconducting titanium nitride coplanar waveguide resonators*, Applied Physics Letters **97**, 232509 (2010).
- [409] L. Zhang, W. Peng, L.X. You, Z. Wang, *Superconducting properties and chemical composition of NbTiN thin films with different thickness*, Applied Physics Letters **107**, 122603 (2015).
- [410] H. Myoren, T. Shimizu, T. Iizuka, S. Takada, *Properties of NbTiN thin films prepared by reactive DC magnetron sputtering*, IEEE Transactions on Applied Superconductivity **11**, 3828 (2001).
- [411] A. Megrant, C. Neill, R. Barends, B. Chiaro, Y. Chen, L. Feigl, J. Kelly, E. Lucero, M. Mariantoni, P.J.J. O'Malley, D. Sank, A. Vainsencher, J. Wenner, T.C. White, Y. Yin, J. Zhao, C.J. Palmstrøm, J.M. Martinis, A.N. Cleland, *Planar superconducting resonators with internal quality factors above one million*, Applied Physics Letters **100**, 113510 (2012).
- [412] P. Natzkin, *Superconducting Microwave Resonator Designs for Electron Spin Resonance Applications*, Master's thesis, Technical University Munich (2017).

- [413] O.V. Dobrovolskiy, M. Huth, *Crossover from dirty to clean superconducting limit in dc magnetron-sputtered thin Nb films*, Thin Solid Films **520**, 5985 (2012).
- [414] L. Zhang, L. You, L. Ying, W. Peng, Z. Wang, *Characterization of surface oxidation layers on ultrathin NbTiN films*, Physica C: Superconductivity and its Applications **545**, 1 (2018).
- [415] S. Weichselbaumer, P. Natzkin, C.W. Zollitsch, M. Weiler, R. Gross, H. Huebl, *Quantitative Modeling of Superconducting Planar Resonators for Electron Spin Resonance*, Physical Review Applied **12**, 024021 (2019).
- [416] C. Grezes, B. Julsgaard, Y. Kubo, M. Stern, T. Umeda, J. Isoya, H. Sumiya, H. Abe, S. Onoda, T. Ohshima, V. Jacques, J. Esteve, D. Vion, D. Esteve, K. Mølmer, P. Bertet, *Multimode storage and retrieval of microwave fields in a spin ensemble*, Physical Review X **4**, 1 (2014).
- [417] P. Rinck, *Magnetic Resonance in Medicine: A Critical Introduction*, Books on Demand (2019).
- [418] M. Reagor, H. Paik, G. Catelani, L. Sun, C. Axline, E. Holland, I.M. Pop, N.A. Masluk, T. Brecht, L. Frunzio, M.H. Devoret, L. Glazman, R.J. Schoelkopf, *Reaching 10 ms single photon lifetimes for superconducting aluminum cavities*, Applied Physics Letters **102**, 192604 (2013).
- [419] T. Van Duzer, C. Turner, *Principles of Superconductive Devices and Circuits*, Bibliyografya Ve Indeks, Prentice Hall (1999).
- [420] L. Yu, R. Singh, H. Liu, S. Wu, R. Hu, D. Durand, J. Bulman, J. Rowell, N. Newman, *Fabrication of Niobium Titanium Nitride Thin Films With High Superconducting Transition Temperatures and Short Penetration Lengths*, IEEE Transactions on Applied Superconductivity **15**, 44 (2005).
- [421] H.G. Leduc, B. Bumble, P.K. Day, B.H. Eom, J. Gao, S. Golwala, B.A. Mazin, S. McHugh, A. Merrill, D.C. Moore, O. Noroozian, A.D. Turner, J. Zmuidzinas, *Titanium nitride films for ultrasensitive microresonator detectors*, Applied Physics Letters **97**, 102509 (2010).
- [422] Z.K. Mineev, I.M. Pop, M.H. Devoret, *Planar superconducting whispering gallery mode resonators*, Applied Physics Letters **103**, 142604 (2013).
- [423] P.K. Day, H.G. LeDuc, B.A. Mazin, A. Vayonakis, J. Zmuidzinas, *A broadband superconducting detector suitable for use in large arrays*, Nature **425**, 817 (2003).
- [424] S.E. de Graaf, A.V. Danilov, A. Adamyan, T. Bauch, S.E. Kubatkin, *Magnetic field resilient superconducting fractal resonators for coupling to free spins*, Journal of Applied Physics **112**, 123905 (2012).

- [425] C.W. Zollitsch, J. O'Sullivan, O. Kennedy, G. Dold, J.J.L. Morton, *Tuning high-Q superconducting resonators by magnetic field reorientation*, AIP Advances **9**, 125225 (2019).
- [426] M. Xu, X. Han, W. Fu, C.L. Zou, H.X. Tang, *Frequency-tunable high- Q superconducting resonators via wireless control of nonlinear kinetic inductance*, Applied Physics Letters **114**, 192601 (2019).
- [427] R. Barends, N. Vercruyssen, A. Endo, P.J. de Visser, T. Zijlstra, T.M. Klapwijk, P. Diener, S.J.C. Yates, J.J.A. Baselmans, *Minimal resonator loss for circuit quantum electrodynamics*, Applied Physics Letters **97**, 023508 (2010).
- [428] C.T. Earnest, J.H. Béjanin, T.G. McConkey, E.A. Peters, A. Korinek, H. Yuan, M. Mariantoni, *Substrate surface engineering for high-quality silicon/aluminum superconducting resonators*, Superconductor Science and Technology **31**, 125013 (2018).
- [429] J. Burnett, L. Faoro, T. Lindström, *Analysis of high quality superconducting resonators: consequences for TLS properties in amorphous oxides*, Superconductor Science and Technology **29**, 044008 (2016).
- [430] J. Verjauw, A. Potočnik, M. Mongillo, R. Acharya, F. Mohiyaddin, G. Simion, A. Pacco, T. Ivanov, D. Wan, A. Vanleenhove, L. Souriau, J. Jussot, A. Thiam, J. Swerts, X. Piao, S. Couet, M. Heyns, B. Govoreanu, I. Radu, *Investigation of Microwave Loss Induced by Oxide Regrowth in High- Q Niobium Resonators*, Physical Review Applied **16**, 014018 (2021).
- [431] M.V.P. Altoé, A. Banerjee, C. Berk, A. Hajr, A. Schwartzberg, C. Song, M. Alghadeer, S. Aloni, M.J. Elowson, J.M. Kreikebaum, E.K. Wong, S.M. Griffin, S. Rao, A. Weber-Bargioni, A.M. Minor, D.I. Santiago, S. Cabrini, I. Siddiqi, D.F. Ogletree, *Localization and Mitigation of Loss in Niobium Superconducting Circuits*, PRX Quantum **3**, 020312 (2022).
- [432] C.X. Yu, S. Zihlmann, G. Troncoso Fernández-Bada, J.I. Thomassin, F. Gustavo, É. Dumur, R. Maurand, *Magnetic field resilient high kinetic inductance superconducting niobium nitride coplanar waveguide resonators*, Applied Physics Letters **118**, 054001 (2021).
- [433] J. Weber, *Magnetoelastic coupling with metallic materials*, Master's Thesis (2023).
- [434] J. Franz, *Superconducting Microwave Resonators for Spin-Based Quantum Memories*, Master's Thesis (2023).
- [435] C.E. Mortimer, J. Beck, U. Müller, *Chemie : das Basiswissen der Chemie*, Thieme, Stuttgart [u.a.] (2014).

- [436] D. Schwienbacher, M. Pernpeintner, L. Liensberger, E.R.J. Edwards, H.T. Nembach, J.M. Shaw, M. Weiler, R. Gross, H. Huebl, *Magnetoelasticity of $\text{Co}_{25}\text{Fe}_{75}$ thin films*, Journal of Applied Physics **126**, 103902 (2019).
- [437] P.F. Herskind, A. Dantan, J.P. Marler, M. Albert, M. Drewsen, *Realization of collective strong coupling with ion Coulomb crystals in an optical cavity*, Nature Physics **5**, 494 (2009).
- [438] D. Lachance-Quirion, Y. Tabuchi, S. Ishino, A. Noguchi, T. Ishikawa, R. Yamazaki, Y. Nakamura, *Resolving quanta of collective spin excitations in a millimeter-sized ferromagnet*, Science Advances **3**, e1603150 (2017).
- [439] L. Bai, M. Harder, P. Hyde, Z. Zhang, C.M. Hu, Y.P. Chen, J.Q. Xiao, *Cavity Mediated Manipulation of Distant Spin Currents Using a Cavity-Magnon Polariton*, Physical Review Letters **118**, 217201 (2017).
- [440] X. Zhang, C.L. Zou, N. Zhu, F. Marquardt, L. Jiang, H.X. Tang, *Magnon dark modes and gradient memory*, Nature Communications **6**, 8914 (2015).
- [441] Y. Chu, P. Kharel, W.H. Renninger, L.D. Burkhardt, L. Frunzio, P.T. Rakich, R.J. Schoelkopf, *Quantum acoustics with superconducting qubits*, Science **358**, 199 (2017).
- [442] Y. Chu, P. Kharel, T. Yoon, L. Frunzio, P.T. Rakich, R.J. Schoelkopf, *Creation and control of multi-phonon Fock states in a bulk acoustic-wave resonator*, Nature **563**, 666 (2018).
- [443] C.T. Hann, C.L. Zou, Y. Zhang, Y. Chu, R.J. Schoelkopf, S.M. Girvin, L. Jiang, *Hardware-Efficient Quantum Random Access Memory with Hybrid Quantum Acoustic Systems*, Physical Review Letters **123**, 250501 (2019).
- [444] A. Wallucks, I. Marinković, B. Hensen, R. Stockill, S. Gröblacher, *A quantum memory at telecom wavelengths*, Nature Physics **16**, 772 (2020).
- [445] X. Han, C.L. Zou, W. Fu, M. Xu, Y. Xu, H.X. Tang, *Superconducting Cavity Electromechanics: The Realization of an Acoustic Frequency Comb at Microwave Frequencies*, Physical Review Letters **129**, 107701 (2022).
- [446] T.P. McKenna, J.D. Witmer, R.N. Patel, W. Jiang, R. Van Laer, P. Arrangoiz-Arriola, E.A. Wollack, J.F. Herrmann, A.H. Safavi-Naeini, *Cryogenic microwave-to-optical conversion using a triply resonant lithium-niobate-on-sapphire transducer*, Optica **7**, 1737 (2020).
- [447] F. Engelhardt, V. Bittencourt, H. Huebl, O. Klein, S.V. Kusminskiy, *Optimal Broadband Frequency Conversion via a Magnetomechanical Transducer*, Physical Review Applied **18**, 044059 (2022).

- [448] M. Shen, J. Xie, C.L. Zou, Y. Xu, W. Fu, H.X. Tang, *High frequency lithium niobate film-thickness-mode optomechanical resonator*, Applied Physics Letters **117**, 131104 (2020).
- [449] W. Jiang, C.J. Sarabalis, Y.D. Dahmani, R.N. Patel, F.M. Mayor, T.P. McKenna, R. Van Laer, A.H. Safavi-Naeini, *Efficient bidirectional piezo-optomechanical transduction between microwave and optical frequency*, Nature Communications **11**, 1166 (2020).
- [450] G. Arnold, M. Wulf, S. Barzanjeh, E.S. Redchenko, A. Rueda, W.J. Hease, F. Hassani, J.M. Fink, *Converting microwave and telecom photons with a silicon photonic nanomechanical interface*, Nature Communications **11**, 4460 (2020).
- [451] A. Bienfait, Y.P. Zhong, H.S. Chang, M.H. Chou, C.R. Conner, É. Dumur, J. Grebel, G.A. Peairs, R.G. Povey, K.J. Satzinger, A.N. Cleland, *Quantum Erasure Using Entangled Surface Acoustic Phonons*, Physical Review X **10**, 021055 (2020).
- [452] V. Jain, V.D. Kurilovich, Y.D. Dahmani, C.U. Lei, D. Mason, T. Yoon, L. Frunzio, P.T. Rakich, L. Glazman, R.J. Schoelkopf, *Acoustic radiation from a superconducting qubit : From spontaneous emission to Rabi oscillations*, arxiv 1–7 (2022).
- [453] P. Delsing, A.N. Cleland, M.J.A. Schuetz, J. Knörzer, G. Giedke, J.I. Cirac, K. Srinivasan, M. Wu, K.C. Balram, C. Bäuerle, T. Meunier, C.J.B. Ford, P.V. Santos, E. Cerda-Méndez, H. Wang, H.J. Krenner, E.D.S. Nysten, M. Weiß, G.R. Nash, L. Thevenard, C. Gourdon, P. Rovillain, M. Marangolo, J.Y. Duquesne, G. Fischerauer, W. Ruile, A. Reiner, B. Paschke, D. Denysenko, D. Volkmer, A. Wixforth, H. Bruus, M. Wiklund, J. Reboud, J.M. Cooper, Y. Fu, M.S. Brugger, F. Rehfeldt, C. Westerhausen, *The 2019 surface acoustic waves roadmap*, Journal of Physics D: Applied Physics **52**, 353001 (2019).
- [454] K.J. Satzinger, Y.P. Zhong, H.S. Chang, G.A. Peairs, A. Bienfait, M.H. Chou, A.Y. Cleland, C.R. Conner, É. Dumur, J. Grebel, I. Gutierrez, B.H. November, R.G. Povey, S.J. Whiteley, D.D. Awschalom, D.I. Schuster, A.N. Cleland, *Quantum control of surface acoustic-wave phonons*, Nature **563**, 661 (2018).
- [455] C.A. Potts, E. Varga, V.A.S.V. Bittencourt, S.V. Kusminskiy, J.P. Davis, *Dynamical Backaction Magnomechanics*, Physical Review X **11**, 031053 (2021).
- [456] A.D. O’Connell, M. Hofheinz, M. Ansmann, R.C. Bialczak, M. Lenander, E. Lucero, M. Neeley, D. Sank, H. Wang, M. Weides, J. Wenner, J.M. Martinis, A.N. Cleland, *Quantum ground state and single-phonon control of a mechanical resonator*, Nature **464**, 697 (2010).

- [457] M. Goryachev, D.L. Creedon, E.N. Ivanov, S. Galliou, R. Bourquin, M.E. Tobar, *Extremely low-loss acoustic phonons in a quartz bulk acoustic wave resonator at millikelvin temperature*, Applied Physics Letters **100**, 243504 (2012).
- [458] M. Goryachev, Z. Kuang, E.N. Ivanov, P. Haslinger, H. Muller, M.E. Tobar, *Next Generation of Phonon Tests of Lorentz Invariance Using Quartz BAW Resonators*, IEEE Transactions on Ultrasonics, Ferroelectrics, and Frequency Control **65**, 991 (2018).
- [459] G. Andersson, S.W. Jolin, M. Scigliuzzo, R. Borgani, M.O. Tholén, J. Rivera Hernández, V. Shumeiko, D.B. Haviland, P. Delsing, *Squeezing and Multimode Entanglement of Surface Acoustic Wave Phonons*, PRX Quantum **3**, 010312 (2022).
- [460] M.K. Ekström, T. Aref, J. Runeson, J. Björck, I. Boström, P. Delsing, *Surface acoustic wave unidirectional transducers for quantum applications*, Applied Physics Letters **110**, 073105 (2017).
- [461] A. Rückriegel, R.A. Duine, *Long-Range Phonon Spin Transport in Ferromagnet–Nonmagnetic Insulator Heterostructures*, Physical Review Letters **124**, 117201 (2020).
- [462] A.T. Levine, *A note concerning the spin of the phonon*, Il Nuovo Cimento **26**, 190 (1962).
- [463] S.V. Vonsovskii, M.S. Svirskii, *Phonon Spin*, Soviet Physics, Solid State **3**, 1568 (1962).
- [464] B. Flebus, K. Shen, T. Kikkawa, K.i. Uchida, Z. Qiu, E. Saitoh, R.A. Duine, G.E.W. Bauer, *Magnon-polaron transport in magnetic insulators*, Physical Review B **95**, 144420 (2017).
- [465] S. Sharma, V. S V Bittencourt, S. Viola Kusminskiy, *Protocol for generating an arbitrary quantum state of the magnetization in cavity magnonics*, Journal of Physics: Materials **5**, 034006 (2022).
- [466] V.A.S.V. Bittencourt, I. Liberal, S. Viola Kusminskiy, *Optomagnonics in Dispersive Media: Magnon-Photon Coupling Enhancement at the Epsilon-near-Zero Frequency*, Physical Review Letters **128**, 183603 (2022).
- [467] V. Wachter, V.A.S.V. Bittencourt, S. Xie, S. Sharma, N. Joly, P.S. Russell, F. Marquardt, S.V. Kusminskiy, *Optical signatures of the coupled spin-mechanics of a levitated magnetic microparticle*, Journal of the Optical Society of America B **38**, 3858 (2021).
- [468] W.K. Peria, D.L. Zhang, Y. Fan, J.P. Wang, P.A. Crowell, *Anomalous temperature dependence of phonon pumping by ferromagnetic resonance in Co/Pd*

- multilayers with perpendicular anisotropy*, Physical Review B **106**, L060405 (2022).
- [469] H. Keshtgar, M. Zareyan, G.E. Bauer, *Acoustic parametric pumping of spin waves*, Solid State Communications **198**, 30 (2014).
- [470] M. Born, E. Wolf, A.B. Bhatia, P.C. Clemmow, D. Gabor, A.R. Stokes, A.M. Taylor, P.A. Wayman, W.L. Wilcock, *Principles of Optics*, Cambridge University Press (1999).
- [471] J. de Klerk, *Behavior of Coherent Microwave Phonons at Low Temperatures in Al₂O₃ using Vapor-Deposited Thin-Film Piezoelectric Transducers*, Physical Review **139**, A1635 (1965).
- [472] L. Landau, G. Rumer, *Absorption of sounds in solids*, Physiklische Zeitschrift der Sowjetunion **11** (1937).
- [473] M. Barangi, P. Mazumder, *Effect of temperature variations and thermal noise on the static and dynamic behavior of straintronics devices*, Journal of Applied Physics **118**, 173902 (2015).
- [474] N. Ashcroft, N. Mermin, *Solid State Physics*, Cengage Learning (2011).
- [475] J.P. Wolfe, *Imaging Phonons*, Cambridge University Press (1998).
- [476] F.I. Fedorov, *Theory of Elastic Waves in Crystals*, Springer US, Boston, MA (1968).
- [477] J.W. Jaeken, S. Cottenier, *Solving the Christoffel equation: Phase and group velocities*, Computer Physics Communications **207**, 445 (2016).
- [478] W.E. Tefft, *Elastic constants of synthetic single crystal corundum*, Journal of Research of the National Bureau of Standards Section A: Physics and Chemistry **70A**, 277 (1966).
- [479] C. Malica, A.D. Corso, *Quasi-harmonic temperature dependent elastic constants: applications to silicon, aluminum, and silver*, Journal of Physics: Condensed Matter **32**, 315902 (2020).
- [480] Y. Minami, T. Yogi, K. Sakai, *Thermal Phonon Resonance in Solid Glass*, Japanese Journal of Applied Physics **45**, 4469 (2006).
- [481] P. Hyde, L. Bai, M. Harder, C. Match, C.M. Hu, *Indirect coupling between two cavity modes via ferromagnetic resonance*, Applied Physics Letters **109**, 152405 (2016).
- [482] L. Mihalceanu, V.I. Vasyuchka, D.A. Bozhko, T. Langner, A.Y. Nechiporuk, V.F. Romanyuk, B. Hillebrands, A.A. Serga, *Temperature-dependent relaxation*

- of dipole-exchange magnons in yttrium iron garnet films*, Physical Review B **97**, 1 (2018).
- [483] S. Knauer, K. Davidková, D. Schmoll, R.O. Serha, A. Voronov, Q. Wang, R. Verba, O.V. Dobrovolskiy, M. Lindner, T. Reimann, C. Dubs, M. Urbánek, A.V. Chumak, *Propagating spin-wave spectroscopy in a liquid-phase epitaxial nanometer-thick YIG film at millikelvin temperatures*, Journal of Applied Physics **133**, 143905 (2023).
- [484] Y. Zhao, Q. Song, S.H. Yang, T. Su, W. Yuan, S.S.P. Parkin, J. Shi, W. Han, *Experimental Investigation of Temperature-Dependent Gilbert Damping in Permalloy Thin Films*, Scientific Reports **6**, 22890 (2016).
- [485] H. Zhang, W. Pang, H. Yu, E.S. Kim, *High-tone bulk acoustic resonators on sapphire, crystal quartz, fused silica, and silicon substrates*, Journal of Applied Physics **99**, 124911 (2006).
- [486] V.J. Gokhale, B.P. Downey, D.S. Katzer, N. Nepal, A.C. Lang, R.M. Stroud, D.J. Meyer, *Epitaxial bulk acoustic wave resonators as highly coherent multiphonon sources for quantum acoustodynamics*, Nature Communications **11**, 2314 (2020).
- [487] C. Herring, *Role of Low-Energy Phonons in Thermal Conduction*, Physical Review **95**, 954 (1954).
- [488] E. Klokholm, J. Aboaf, *The saturation magnetostriction of thin polycrystalline films of iron, cobalt, and nickel*, Journal of Applied Physics **53**, 2661 (1982).
- [489] M. Yamamoto, *Young's Modulus of Elasticity and Its Change with Magnetization in Iron-Cobalt Alloys*, Physical Review **59**, 768 (1941).
- [490] G.K. White, M.L. Minges, *Thermophysical properties of some key solids: An update*, International Journal of Thermophysics **18**, 1269 (1997).
- [491] Y.G. Kim, J.H. Song, S. Hong, S.H. Ahn, *Piezoelectric strain sensor with high sensitivity and high stretchability based on kirigami design cutting*, npj Flexible Electronics **6**, 52 (2022).
- [492] H. Wang, J. Liu, H. Cui, Y. Liu, J. Zhu, H. Wang, G. Song, Z. Li, D. Chen, *Strain Sensor with High Sensitivity and Large Response Range Based on Self-Assembled Elastic-Sliding Conductive Networks*, ACS Applied Electronic Materials **3**, 1758 (2021).
- [493] I.E. Psarobas, D.A. Exarchos, T.E. Matikas, *Birefringent phononic structures*, AIP Advances **4**, 124307 (2014).

- [494] T. Ueno, J. Qiu, J. Tani, *Self-sensing magnetic force control by composite of giant magnetostrictive and piezoelectric materials*, The Proceedings of the International Conference on Motion and Vibration Control **6.2**, 1081 (2002).
- [495] R.G. Qhobosheane, M.R.P. Elenchezian, P.P. Das, M. Rahman, M.M. Rabby, V. Vadlamudi, K. Reifsnider, R. Raihan, *Smart Self-Sensing Composite: Piezoelectric and Magnetostrictive FEA Modeling and Experimental Characterization Using Wireless Detection Systems*, Sensors **20**, 6906 (2020).
- [496] O. Cugat, J. Delamare, G. Reyne, *Magnetic micro-actuators and systems (MAGMAS)*, IEEE Transactions on Magnetics **39**, 3607 (2003).
- [497] G. Reyne, J. Delamare, O. Cugat, *Magnetic Micro-actuators (MAGMAS)*, in *Encyclopedia of Materials: Science and Technology*, 1–5, Elsevier (2005).
- [498] R. Fermin, D. van Dinter, M. Hubert, B. Woltjes, M. Silaev, J. Aarts, K. Lahabi, *Superconducting Triplet Rim Currents in a Spin-Textured Ferromagnetic Disk*, Nano Letters **22**, 2209 (2022).
- [499] I.V. Bobkova, A.M. Bobkov, A. Kamra, W. Belzig, *Magnon-cooperons in magnet-superconductor hybrids*, Communication Materials **3**, 95 (2022).
- [500] I.V. Bobkova, A.M. Bobkov, M.A. Silaev, *Dynamic Spin-Triplet Order Induced by Alternating Electric Fields in Superconductor-Ferromagnet-Superconductor Josephson Junctions*, Physical Review Letters **127**, 147701 (2021).
- [501] M. Alghadeer, A. Banerjee, A. Hajr, H. Hussein, H. Fariborzi, S.G. Rao, *Surface Passivation of Niobium Superconducting Quantum Circuits Using Self-Assembled Monolayers*, ACS Applied Materials & Interfaces **15**, 2319 (2023).
- [502] K. Zheng, D. Kowsari, N.J. Thobaben, X. Du, X. Song, S. Ran, E.A. Henriksen, D.S. Wisbey, K.W. Murch, *Nitrogen Plasma Passivated Niobium Resonators for Superconducting Quantum Circuits* **120**, 102601 (2022).
- [503] B. Rana, Y. Otani, *Towards magnonic devices based on voltage-controlled magnetic anisotropy*, Communication Physics **2**, 90 (2019).
- [504] T. Nozaki, J. Okabayashi, S. Tamaru, M. Konoto, T. Nozaki, S. Yuasa, *Understanding voltage-controlled magnetic anisotropy effect at Co/oxide interface*, Scientific Reports **13**, 10640 (2023).
- [505] J. Zhang, P.V. Lukashev, S.S. Jaswal, E.Y. Tsybal, *Model of orbital populations for voltage-controlled magnetic anisotropy in transition-metal thin films*, Physical Review B **96**, 014435 (2017).
- [506] S. Kosen, H.X. Li, M. Rommel, D. Shiri, C. Warren, L. Grönberg, J. Salonen, T. Abad, J. Biznárová, M. Caputo, L. Chen, K. Grigoras, G. Johansson, A.F.

- Kockum, C. Križan, D.P. Lozano, G.J. Norris, A. Osman, J. Fernández-Pendás, A. Ronzani, A.F. Roudsari, S. Simbierowicz, G. Tancredi, A. Wallraff, C. Eichler, J. Govenius, J. Bylander, *Building blocks of a flip-chip integrated superconducting quantum processor*, Quantum Science and Technology **7**, 035018 (2022).
- [507] C.R. Conner, A. Bienfait, H.S. Chang, M.H. Chou, É. Dumur, J. Grebel, G.A. Pears, R.G. Povey, H. Yan, Y.P. Zhong, A.N. Cleland, *Superconducting qubits in a flip-chip architecture*, Applied Physics Letters **118**, 232602 (2021).
- [508] J. Yu, Y. Zheng, S. Zhou, Q. Wang, S. Wu, H. Wu, T. Li, J. Cai, *Indium-based Flip-chip Interconnection for Superconducting Quantum Computing Application*, in *2022 23rd International Conference on Electronic Packaging Technology (ICEPT)*, 1–6, IEEE (2022), ISBN 978-1-6654-9905-7.
- [509] P. Trempler, R. Dreyer, P. Geyer, C. Hauser, G. Woltersdorf, G. Schmidt, *Integration and characterization of micron-sized YIG structures with very low Gilbert damping on arbitrary substrates*, Applied Physics Letters **117**, 232401 (2020).
- [510] F. Heyroth, C. Hauser, P. Trempler, P. Geyer, F. Syrowatka, R. Dreyer, S. Ebbinghaus, G. Woltersdorf, G. Schmidt, *Monocrystalline Freestanding Three-Dimensional Yttrium-Iron-Garnet Magnon Nanoresonators*, Physical Review Applied **12**, 054031 (2019).
- [511] D. Moon, J. Jang, D. Choi, I.S. Shin, D. Lee, D. Bae, Y. Park, E. Yoon, *An ultra-thin compliant sapphire membrane for the growth of less strained, less defective GaN*, Journal of Crystal Growth **441**, 52 (2016).
- [512] S. Lee, J. Kim, J. Oh, J. Ryu, K. Hwang, J. Hwang, S. Kang, J.H. Choi, Y.C. Sim, Y.H. Cho, T.H. Chung, T. Jeong, Y. Park, E. Yoon, *A discrete core-shell-like micro-light-emitting diode array grown on sapphire nano-membranes*, Scientific Reports **10**, 7506 (2020).
- [513] K. Takahashi, *Magnon-phonon coupling in symmetric magneto-metallic thin film/bulk acoustic wave resonator heterostructures*, Bachelor's Thesis (2023).
- [514] W. Campbell, S. Galliou, M.E. Tobar, M. Goryachev, *Electro-mechanical tuning of high-Q bulk acoustic phonon modes at cryogenic temperatures*, Applied Physics Letters **122**, 032202 (2023).
- [515] B. Mühlshlegel, *Die thermodynamischen Funktionen des Supraleiters*, Zeitschrift für Physik **155**, 313 (1959).
- [516] S.P. Chockalingam, M. Chand, J. Jesudasan, V. Tripathi, P. Raychaudhuri, *Superconducting properties and Hall effect of epitaxial NbN thin films*, Physical Review B **77**, 214503 (2008).

- [517] E. Silva, N. Pompeo, O.V. Dobrovolskiy, *Vortices at Microwave Frequencies*, Physical Sciences Reviews **2**, 1 (2017).
- [518] H. Ge, Y.R. Jin, X.H. Song, *High quality NbTiN films fabrication and rapid thermal annealing investigation*, Chinese Physics B **28**, 077402 (2019).
- [519] J.F. Nye, *et al.*, *Physical properties of crystals*, Oxford university press (1985).
- [520] G. Terrasanta, T. Sommer, M. Müller, M. Althammer, R. Gross, M. Poot, *Aluminum nitride integration on silicon nitride photonic circuits: a hybrid approach towards on-chip nonlinear optics*, Optics Express **30**, 8537 (2022).
- [521] R. Flaschmann, C. Schmid, L. Zugliani, S. Strohauer, F. Wietschorke, S. Grotowski, B. Jonas, M. Müller, M. Althammer, R. Gross, J.J. Finley, K. Müller, *Optimizing the growth conditions of Al mirrors for superconducting nanowire single-photon detectors*, Materials for Quantum Technology **3**, 035002 (2023).
- [522] S. Strohauer, F. Wietschorke, L. Zugliani, R. Flaschmann, C. Schmid, S. Grotowski, M. Müller, B. Jonas, M. Althammer, R. Gross, K. Müller, J.J. Finley, *Site-Selective Enhancement of Superconducting Nanowire Single-Photon Detectors via Local Helium Ion Irradiation*, Advanced Quantum Technologies **6**, 2300139 (2023).

Acknowledgements - Danksagung

The past three years of my PhD have been an intense formative experience, in which I have dealt with a vast variety of different research topics and scientific methods ranging from fixing UHV setups over experimental setup assembly to data processing and manuscript writing. I hope, that this thesis will lay the groundwork for future scientific endeavors at the WMI and that my research has provided useful input for the field of spintronics. Importantly, I also got to know many different personalities with varying mindsets, work ethics and ideas. In the following, I want to thank the countless people, which have made my writing of this thesis possible.

Prof. Dr. Rudolf Gross for giving me the opportunity to conduct my doctoral thesis at the Walther-Meißner-Institut, for the very helpful comments on various manuscripts and the present doctoral thesis, and for always having a simple 'Bierdeckel' explanation to describe difficult physical concepts.

Dr. Matthias Althammer as my direct supervisor for your continuous support throughout my entire time as a PhD student. Thank you very much for your help and time in interpreting measurement data, proofreading the present thesis and manuscripts, and for your continuous interest in my progress with new measurements/projects and idea. Thank you also for giving me the freedom to independently explore and implement my own ideas and for pushing me to see them through, even when I was doubting them myself after less than favorable reviews. I wish you all the best for both your private life and your scientific career.

PD Dr. habil. Hans Huebl for tasking and enabling me to work on various projects outside of the field of spintronics such as the optimization of superconducting resonators or hybrid coupling phenomena. Thanks to you, I feel, I have become a more versatile and open-minded scientist. Furthermore, with your critical evaluation of all of my manuscripts, you have always revealed their flaws and open question, which we could then account for and discuss before submission.

Prof. Dr. Mathias Weiler for your continued interest in my research despite

the many tasks, you faced with your move to and professorship in Kaiserslautern. Thanks to our weekly Friday meetings, I could benefit from your helpful input and vast knowledge long after you had left the WMI.

Dr. Stephan Geprägs for your continuous support and advice in material science and XRD experiments. I could always talk to you and get advice about my latest material optimization issues. Also, I could always annoy you with the exercise sheets for the solid state physics tutorials, despite your busy schedule.

Dr. Matthias Opel for always helping me out with the various SQUID-magnetometry-related issues. As a member of the IT team, you also always helped me out with managing the LRZ-accounts of my various students.

Regarding experimental work, I in particular benefited from the advice on bbFMR from *Dr. Lukas Liensberger* and *Dr. Luis Flacke*. Without you two guys teaching me this experimental method and laying the experimental groundwork, this thesis would not have been possible. Also thanks to *Lukas* for introducing me to the μ FR-MOKE-technique.

For my research on superconducting resonators I could always rely on helpful advice from *Dr. Thomas Luschmann* regarding both fabrication and measurements. Naturally, the same also applies for the various issues with the nanobeam e-beam lithography system, where you always knew the solution for the various problems I encountered.

For cleanroom fabrication tasks in general, '*Fab God*' *Leon Koch* and *Niklas Bruckmoser* could always help me out with my various issues.

Of course, I also want to thank my PhD colleagues *Dr. Tobias Wimmer*, *Dr. Janine Gückelhorn*, *Monika Scheufele* and *Matthias 'Matze' Grammer* in general for the productive work atmosphere, where we always showed mutual interest for our research and also helped each other out.

Furthermore, I want to thank *Kedar Honasoge* for introducing me to EDS and SEM-spectroscopy.

I want to thank the students, who I have supervised during this thesis:

Raphael Hoepfl, who was both my first bachelor's student and second master's student. Thank you for the countless TaN and GdN thin films, you have grown and the corresponding countless hours, you had to spend in the Superbowls sputtering system. Also, thank you for skimming through loads of papers from

the sixties on the different TaN-phases, which made our detailed density analysis and TaN-phase identification possible.

Vincent Haueise, my second bachelor's student and briefly also my working student, who mastered the art of fitting noisy FMR-spectra. I could always load all the spectra with horrible signal-to-noise ratio on you and you would fit 100+ spectra without a word of complaint.

Yuhao Sun, my second master's student for fabricating the various non-local spin transport devices during your Master's thesis. While the experiments, though interesting, ended up being non-conclusive in terms of the physics at play, you did an outstanding job in the complicated multi-step fabrication process of these devices.

Thank you also to *Johannes Weber*, my third master's student for all the help on the magnon-phonon coupling experiments as my working- and master's student. I am always amazed at the speed with which you manage to implement my silly ideas on different CoFe/substrate heterostructures in the lab.

Franz Weidenhiller my reluctant fourth master's student (thanks to *Janine* for dumping this guy on me by the way). I learned a lot on magnon transport experiments by discussing your data and proof-reading your thesis.

Keita Takahashi, my third bachelor's student for your resilient work attitude, which allowed us to make great progress on our research on magnon-phonon coupling in symmetric trilayer structures, which allowed us to indirectly verify the presence of chiral phonons in our CoFe/Si-BAW-heterostructures.

Also thank you to *Luca Schmidt* for fabricating the $\text{Al}_{1-x}\text{Sc}_x\text{N}$ alloys. I learned a lot by working with you on a project, which was completely outside the field of magnetism.

I also want to give honorary mention to two master's students, who showed up in my office asking for help so much, one could be tempted to also consider them as mine, namely *Christian Mang* and *Julian Franz*. Starting with the latter, *Julian*, it was always fun to exchange our pleasant experiences in working with the amazingly engineered Ultradisk machine, which exhibits no flaws whatsoever. '*Nobody expects the shitty deposition.*' Also thank you the *Christian Mang* for giving me the opportunity to work on spin-wave spectroscopy in non-reciprocal devices.

Besides the WMI scientists, I also benefited greatly from the technical staff:

In particular, I want to thank *Thomas Brenninger* for always helping me out with issues regarding the UHV clusters.

Furthermore, I want to thank *Sebastian Kammerer* and *Astrid Habel* for their great help with supplying and managing the clean room equipment and chemistry.

From the technical workshop, I want to thank *Georg Nitschke*, *Mario Nodes*, *Christian Reichlmeier* and *Alexander Röß* for helping out with the realization of the various technical designs for the sample holders and resonator boxes.

From the Helium liquefaction team, I thank Peter Binkert, Harald Schwaiger and Jan Naundorf for the supply with cryogenic liquids for my experiments.

Furthermore, I thank Andreas Russo for electrical engineering support.

I also want to thank our administration team: *Emel Dönertas*, *Andrea Person*, *Martina Meven*, and *Carola Siegmayer* for always helping out with orders and administrative issues.

Finally, I thank the cleaning staff *Maria Botta* and *Sybilla Plöderl* for keeping the institute clean and neatly. Also, it was always nice to gossip with you.

For the various past and ongoing cooperations during this thesis I would like to thank in particular the following people:

For the many helpful discussions and theory input for the manuscript on the inductive detection of spin torques in superconductor/ferromagnet heterostructures, I want to thank *Prof. Dr. Wolfgang Belzig* and *Dr. Akashdeep Kamra*.

From the *Physikalische-Technische Bundesanstalt*, I would like to thank *PD Dr. Hans Werner Schumacher* and *Dr. Niels Ubbelohde* for your helpful input for the NbTiN resonator manuscript.

I want to thank the 'black team' of *Prof. Dr. Silvia Viola Kusminskiy*, *Fabian Engelhardt*, *Dr. Victor A.S.V. Bittencourt* and *Dr. Mikhail Cherkasskii* for the many useful discussions and theoretical input on the Magnon-Phonon coupling manuscript.

Prof. Dr. Friedemann Reinhard and *Paul Weinbrenner* from Rostock for our cooperation on NV center magnetometry. In particular, thank you to *Paul Weinbrenner* for remembering me from our shared lectures at TUM and for messaging me all

these years later, thus making this nice shared project possible.

Furthermore, I want to thank *Prof. Dr. Sebastian Gönnerwein* from Konstanz for his helpful input on the Magnon-Phonon coupling manuscript.

From our partners in Madras, I in particular want to thank *Dr. T.S. Suraj* for the fun times, we had together during my first real scientific cooperation project. Also, I want to acknowledge *Mayank Sharma* for the many interesting and silly philosophical talks we have had. I am glad, I could somewhat help you in your scientific career by correcting your application presentation for San Sebastian. Finally, I want to thank *Prof. M. S. Ramachandra Rao* for permitting your students to stay abroad, thus enabling these pleasant experiences for me.

The same goes for our cooperation with *Prof. Mashashi Shiraishi* from Kyoto. During your three month stay at WMI, I had the chance to work with and personally get to know *Shugo Yoshii*, which has been a valuable experience for me.

Furthermore, I got the chance to work in an interesting collaboration with *Prof. Dr. Haiming Yu, Hanchen Wang* and *Jilei Chen* from Beijing. I learned a lot in my experiences on the non-reciprocal spin propagation devices, you sent us and truly hope, you can benefit from the CoFe thin films, I have deposited in the Superbowls.

Having been responsible for the superbowls and partially also for the Ultra-disk sputtering system, I got to work in particular with many students from the *Walter Schottky institute* being 'the guy, who yells at you, when you break something'. Here, I have worked with many people and must shamefully admit, that I probably don't remember everybody. From the people, I have worked with regularly, I in particular want to thank *Rasmus Flaschmann, Lucio Zugliani, Christian Schmid, Fabian Becker, Stefanie Grotowski, Simone Spedicato, Stefan Strohauer, and Fabian Wietschorke*. I apologize for the people, I have worked with but are not listed here.

From the EQT group, I want to thank *Prof. Dr. Menno Poot, Timo 'you can still sputter according to Manu' Sommer* and *Giulio Terrasanta* for our nice work together on the integration of Aluminum nitride in photonic circuits. In particular, I enjoyed working with *Giulio Terrasanta* in the Superbowls and XRD lab. You had many great ideas and your continuous efforts made the two resulting publications from this cooperation possible.

Finally, from MPQ, I want to thank *Stephan Rinner*. I enjoyed our joined XRD experiments on the Er-doped Si on SiO₂ samples. Also, it was nice to catch up with you after our shared studies at TUM. I am glad, you could use our results

for your research.

Being an inmate of office mates WMI 136 aka the 'grumpy office' (also called the 'moaning office' by *Maria-Teresa Handschuh*), I want to thank my cellmates over the past three years: *Dr. Philip Schmidt*, *Dr. Stefan Pogorzalek*, *Dr. Michael Renger*, the elusive *Ivan Tsitsilin*, *Florian Fesquet* and *Matthias Grammer*.

In particular *Florian Fesquet* for all of our countless late night working sessions, Dice Throne duels, coffee breaks, jogs at Isar as well as the visits to Honghong. Without you, my PhD at WMI would have been way less fun.

Furthermore, I want to thank *Dr. Michael Renger*, my ranting partner in crime. You were always around the institute and willing to share your vast knowledge on bureaucracy-, IT, or science-related issues. Also, you were always willing to listen to my frequent lamentations without complaints.

I also want to thank *Dr. Leander Peis* ('*Dr. Pnice*') for all our countless coffee breaks and scientific discussions. Working in a different field, you always allowed me to view my work critically from an outside perspective. My coffee discussions have declined significantly since you left the institute.

Of course, this acknowledgments section would not be complete, without me thanking *Kedar Honasoge* again for making sure, I stayed 'hydrated' during my PhD. We have spent countless fun evenings together be it at the Institute or at Honghong.

The same also applies to *Daniil Bazulin*. Also thank you for giving me the nickname 'Professor Muller', which is following me around the institute with even new people I had never met calling me that.

Thanks also to *Niklas Bruckmoser* and *Monika Scheufele* for sometimes even allowing me to attend your exclusive 'Eispause' events. Also shout out to *Niklas Bruckmoser*, who decided, my face should just be pasted on every meme template in existence and filling my desk with hilarious memes.

In order to not further blow this acknowledgment section out of proportion, I will abstain from thanking other people in a full dedicated text segment. For many fun evenings and experiences, I want to thank *Dr. Yuki Noijiri*, '*Fab God*' *Leon Koch*, *David Bunch*, *Dr. Thomas Luschmann*, *Maria-Teresa Handschuh*, *Malay Singh*, *Ramona Stumberger* and *Philipp Schwenke*.

Honorary mention to the Quantum computing group. I hope, you guys will

find *Ivan* one day.

My grandfather *Dietrich 'Eirik' Radspieler*. I know, you would have loved to bind also this thesis and show off to your siblings about your 'Hundling' grandson. I miss you every day.

My sister *Elena Hergenreider* and her husband *Sergej Hergenreider* for our many board game evenings and all the trips, we met together. I must admit, it was also nice to get out of the Institute every once in a while.

My parents, *Heike* and *Michael Müller*, for your unconditional support throughout my life and for being there for me, when I need you.

Now the trouble is over, everybody got paid
Everybody is happy, they are glad that they came
Then you go to the place where you've finally found
You can look at yourself sleep the clock around
— 'Sleep the clock around', Belle and Sebastian